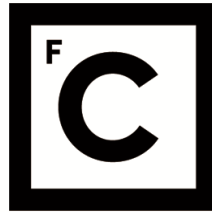UNIVERSIDADE DE LISBOA

FACULDADE DE CIÊNCIAS

Tsunamis from source to coast

" Documento Definitivo"

Doutoramento em Ciências Geofísicas e da Geoinformação

Especialidade de Geofísica

Martin Wronna

Tese orientada por:

Maria Ana Baptista, Utku Kânoğlu

Documento especialmente elaborado para a obtenção do grau de doutor

2021

UNIVERSIDADE DE LISBOA

FACULDADE DE CIÊNCIAS

Tsunamis from source to coast

Doutoramento em Ciências Geofísicas e da Geoinformação
Especialidade de Geofísica

Martin Wronna

Tese orientada por:

Maria Ana Baptista, Utku Kânoğlu

Júri:

Presidente:

● Doutor João Manuel de Almeida Serra, Professor Catedrático e Presidente do Departamento de Engenharia Geográfica, Geofísica e Energia da Faculdade de Ciências da Universidade de Lisboa,

Vogais:

● Doutor Alberto Armigliato, Professore Associato do Dipartimento di Fisica e Astronomia "Augusto Righi" da Università di Bologna Alma Mater Studiorum, Itália

● Doutora Hélène Hébert, do Commissariat à l`Énergie Atomique et aux Energies Alternatives, França, na qualidade de individualidade de reconhecida competência na área científica

● Doutor Joaquim Manuel Freire Luis, Professor Auxiliar da Faculdade de Ciências e Tecnologia da Universidade do Algarve

● Doutor Rui Pires de Matos Taborda, Professor Associado com Agregação da Faculdade de Ciências da Universidade de Lisboa

● Doutora Maria Ana de Carvalho Viana Baptista, Professora Associada Convidada com Agregação da Faculdade de Ciências da Universidade de Lisboa, (Orientadora)

Documento especialmente elaborado para a obtenção do grau de doutor

2021

ABSTRACT

Tsunami disasters pose a significant threat to coastal communities. In the last decades, tsunamis caused enormous destruction and exceeding 250000 fatalities. International efforts led to significant advances in tsunami science and research, but recent events demonstrated some limitations. Thus, it is essential to increase our knowledge of the source to coast tsunami phenomenon. A better understanding of potential tectonic structures and other generation mechanisms is needed, especially in complex geologic domains or where sources are unknown. Furthermore, we need to improve Tsunami Warning Systems (TWSs) to provide timely alerts for communities in the near field.

Therefore, potential tsunamigenic sources in the diffuse plate boundary setting and the near field of the southwest Iberian margin (SWIM) are investigated. For the March 31, 1761, transatlantic tsunami, numerical modelling has been used to propose a structure that agrees with tsunami travel times, tsunami observations, macroseismic data, and kinematic plate modelling. Since there exists a description of a tsunami for the November 11, 1858, Sétubal earthquake, its source has been investigated using macroseismic analysis. The analysis suggests a local structure in a compressive regime with weak to moderate tsunamigenic potential. Future tsunami hazard assessments need to include the sources of the investigated events.

To quickly estimate the tsunami impact, the Tsunami Runup Predictor (TRP), an empirical source-to-coast method to instantly provide first-order estimates of the tsunami runup based on waveform parameters has been developed. The TRP is helpful for emergency managers and evacuation planning for near-field events. Moreover, the author of this thesis contributed to the tsunami impact assessment of September 28, 2018, Palu tsunami, where tsunamis generated by multiple sources caused runup heights up to 9.2 m. However, for local sources, tsunami warning remains challenging; thus, communities need to be prepared how to respond appropriately to earthquakes and tsunamis with or without warning.

Keywords: Tsunami hazard   Tsunami early warning systems   Analytical runup computation Nonlinear shallow water-wave modelling · Rapid tsunami runup estimation

RESUMO

Os tsunamis são desastres naturais pouco frequentes, cujo impacto pode ser catastrófico. Os tsunamis são gerados por um deslocamento abrupto da superfície livre do mar, causados por sismos submarinos, erupções vulcânicas, deslizamentos de massa e meteoritos. A causa mais frequente são os terramotos submarinos. Nas últimas décadas os tsunamis causaram mais do que duzentos e cinquenta mil mortos e devastaram zonas costeiras. De entre os eventos mais devastadores destacam-se o tsunami de 26 de dezembro de 2004 no oceano Índico e o de 11 de março de 2011 no Japão. Na sequência destes eventos a comunidade internacional reconheceu a necessidade de implementação de sistemas de alertas em todo o globo.

Atualmente, apenas alguns destes sistemas incluem previsões de inundação por um lado porque estas simulações são computacionalmente pesadas e por outro lado os dados topo-batimétricos necessários ao seu cálculo nem sempre estão disponíveis. Alguns eventos recentes relembraram as limitações destes sistemas no que diz ao conhecimento das zonas fonte e mecanismos de geração bem como dos impactos costeiros e das medidas de mitigação.

A eficácia destes sistemas passa, assim, pela deteção rápida da geração do tsunami e pela previsão quase em tempo real do impacto costeiro.

Especialmente preocupantes são os eventos que impactam o campo próximo ou os que são gerados em condições de geologia complexa onde as fontes são pouco conhecidas. As costas de Portugal, Espanha e Marrocos encontram-se expostas ao perigo de tsunamis a partir de fontes ativas locais e regionais no Atlântico nordeste. Esta é uma zona de geologia complexa designada por SWIM (Margem sudoeste da Península Ibérica). Aqui, existem evidências geológicas que confirmam eventos importantes desde 218 BC e os relatos históricos referem eventos em 60 BC e 382 AD. A zona SWIM é considerada uma fronteira de placas difusa uma vez que não se identificou (até agora) um limite de placas bem definido, sendo uma zona de deformação distribuída por uma área de grande extensão incluindo várias falhas inversas. Estudos de diferentes autores sugerem que o evento mais importante da história recente, o grande terremoto de Lisboa de 1755, ocorreu na SWIM. A este evento que causou mais do que dez mil vítimas mortais foi atribuída uma magnitude estimada de 8.5. O tsunami foi observado no oceano Atlântico norte, até no Brasil mas com impacto extremo na Península Ibérica e Marrocos. No século 20, a 28 de Fevereiro de 1969 um terremoto com magnitude 7.9 gerou outro tsunami no Atlântico que foi registado marégrafos de Marrocos, Espanha e França. O

tsunami atingiu Portugal Continental perto das 3 horas da madrugada (cerca de 35 minutos depois do sismo) e em condições de maré vazia. As evidências geológicas, os relatos históricos e os eventos recentes sublinham a urgência de conhecer melhor as fontes associadas a eventos passados.

Esta tese contribui para:

- Conhecimento da perigosidade de tsunamis nesta zona do globo, através da reavaliação de eventos do catálogo português de tsunamis;
- Estimação do impacto de tsunamis (cálculo do "runup" ou espraio dos tsunamis)
- Avaliação do impacto de tsunamis na costa

Na avaliação da perigosidade de tsunamis nesta zona do globo, utilizou-se uma abordagem fonte-a-costa para melhor caracterizar os eventos históricos 31 de Março de 1761, que gerou um tsunami transatlântico e o evento sísmico de 11 de novembro 1858 de Setúbal. Desta investigação resultaram duas publicações nos jornais Natural Hazards and Earth Systems Science and Pure and Applied Geophysics.

O estudo do sismo e do tsunami de 31 de março de 1761 que foi sentido em grandes partes da Europa e gerou um tsunami que foi observado na bacia inteira do norte do atlântico propõe uma fonte com um mecanismo inverso predominante com o centro da falha localizado aproximadamente nas coordenadas 12.5W, 35N, sudoeste de uma zona com várias estruturas em regime compressivo situada no zona do Banco do Coral Patch.

O estudo de 11 de novembro 1858 é particularmente importante por ter sido o sismo mais forte, com uma magnitude estimada de ~ 7, que ocorreu no continente português no século 19 e por haver referência à ocorrência de um tsunami local em Setúbal. Estudos anteriores localizaram este sismo a sul de Setúbal no Oceano Atlântico. O estudo agora desenvolvido sugere uma fonte concluída muito próxima da costa cujo tsunami atinge a costa em menos de meia hora.

Atualmente, os sistemas de alerta na região Noroeste Atlântico e Mediterrâneo e mares adjacentes (NEAM) não incluem estimativas do impacto de tsunamis. Se a fonte for conhecida ou o tsunami quantificado uma estimativa rápida do impacto do tsunami é útil para o sistema de alerta, gestores de emergência ou planeamento de evacuação. No âmbito desta tese foram utilizados modelos numéricos e soluções analíticas para estudar o runup um parâmetro costeiro de impacto de um tsunami. O runup é definido como a cota topográfica mais alta, relativa ao nível médio do mar, atingida pelo tsunami ao nível do mar na altura do tsunami. Compilamos uma base de deslocamentos iniciais de tsunamis utilizando fontes sísmicas e aplicando a teoria

de elasticidade. Utilizamos os deslocamentos iniciais para calcular o runup para cada fonte numa batimetria para várias inclinações constantes com o modelo numérico NSWING (Non-linear Shallow Water Model with Nested Grids). Paralelamente, tiramos as formas de onda dos deslocamentos iniciais para avaliar o runup analiticamente. Com os resultados do runup desenvolvemos um método empírico, o Tsunami Runup Predictor (TRP) baseado em parâmetros da forma da onda do tsunami em relação ao runup. Com os parâmetros, máxima amplitude, mínima amplitude, distância entre crista e cava, a profundidade e o ângulo da inclinação se pode estimar instantaneamente o runup para LEN (ondas com crista precedente) e LDN (ondas com cava precedente). Depois aplicamos a metodologia TRP a alguns tsunamis passados e comparamos com medições do campo. Os resultados mostram que se consegue dar uma rápida estimativa do runup médio. Além disso descobrimos que também o runup extremo segue a fórmula do TRP só com um factor de multiplicação de 2.5. No entanto, é preciso validar este factor com mais tsunamis passados. Os resultados deste estudo foram publicados no jornal Natural Hazards.

No decorrer desta tese, ocorreu o tsunami de 28 de Setembro de 2018 na Indonesia, Sulawesi, Palu. Um sismo de magnitude 7.5 com um mecanismo de ruptura em deslizamento causou um tsunami de dimensão inicialmente subestimada que destruiu grande parte da costa na baía do Palu quase imediatamente após o sismo. Houve assim, a oportunidade do autor da tese integrar o International Tsunami Survey Team (ITST) (Equipa internacional do estudo do tsunami no campo) da UNESCO. Houve assim oportunidade para avaliar in situ o impacto na costa que contribui para uma melhor compreensão da fonte deste evento. O resultado deste trabalho foi publicado na revista Pure and Applied Geophyiscs (Omira et al., 2019).

Concluindo, esta tese contribui para uma melhor caracterização do perigo de tsunami na zona SWIM do Atlântico nordeste. Além disso, foi desenvolvido uma metodologia que permite estimar o runup imediatamente após detecção e parametrização do tsunami, que pode ser especificamente útil para tsunami no campo próximo e para fontes locais. A avaliação do impacto do tsunami na costa foi feita através da participação no post-tsunami-field survey na Indonesia. Deste trabalho resultaram três artigos como primeiro autor em revistas indexadas internacionais e um artigo como co-autor.

Palavras-chave: Caracterização de perigo de tsunami · Sistemas de alerta de tsunami · Cálculo analítico de tsunami runup · Modelo de equações de águas pouco profundas não-lineares · Estimativas rápidas do tsunami runup

ACKNOWLEDGEMENTS

TABLE OF CONTENTS

List of Figures

List of Tables

List of Publications

The list of publications, based on which the thesis has been prepared:

1. Wronna, M., Baptista, M.A., Miranda, J.M. (2019a) Reanalysis of the 1761 transatlantic tsunami, Nat. Hazards Earth Syst. Sci., 19, 337–352, https://doi.org/10.5194/nhess-19-337-2019

2. Wronna, M., Baptista, M.A., Kânoğlu, U. (2020) A new tsunami runup predictor. Nat Hazards 105, 1571–1585, https://doi.org/10.1007/s11069-020-04366-1

3. Wronna, M., Baptista, M.A., Miranda, J.M. (2021) Reevaluation of the 11 November 1858 Earthquake and Tsunami in Setúbal: A Contribution to the Seismic and Tsunami Hazard Assessment in Southwest Iberia. Pure Appl. Geophys. https://doi.org/10.1007/s00024-021-02885-x

Author's Contribution to the Publications

Contribution to the papers in this thesis are:

***   major contribution (> 90%)

**   leading contribution (> 50%)

*   supporting contribution (< 50%)

Publication	1 Wronna et al. (2019a)	2 Wronna et al. (2020)	3 Wronna et al. (2021)
Concept	**	**	***
Data Processing	***	***	***
Manuscript Preparation	***	***	***

Summary

Despite the recent advances in tsunami warning and forecast tools and capabilities, it is of utmost importance to enlarge our knowledge about the sources and triggers of tsunami events in complex geological environments, such as diffuse plate boundary environments and in near-source conditions.

Most of the approaches developed so far are increasingly effective in the case of subduction areas but are less effective in diffuse plate boundaries domains. Current studies characterize the tsunami hazard using deterministic (Heidarzadeh et al., 2009; Baptista et al., 2011; Wijetunge, 2014) or probabilistic approaches (Sarri et al., 2012; Omira et al., 2015). These approaches use seismic hazard, geological or historical evidence of past tsunami events or tsunami catalogues. These studies indicate differences between tsunami hazards in discrete or diffuse tectonic settings. After determining the tsunami source, the non-linear shallow water (NSW) models are used to model tsunami propagation and inundation (Titov and Synolakis, 1995; Liu et al., 1998; Tinti and Tonini, 2013). However, high-resolution inundation modelling is time-consuming and currently used only for far-field events in TWS (Bernard and Titov, 2015). Tsunami early warning needs: quick tsunami detection and quick and accurate source estimation. Most operational TWS use pre-computed scenario databases. Estimation of the seismic source uses w-phase inversion (Duputel et al., 2011), whereas tsunami source estimation uses joint inversion of various data sets (space geodetic data or tsunami waveforms through deep ocean measurements) (Melgar and Bock, 2015).

It is proposed to review existing methodologies and provide new approaches for the improvement of tsunami early warning systems. This thesis contributes to (a) a better characterization of the tsunami hazard in diffuse plate boundary domains, (b) a better understanding of the tsunami genesis in these conditions, (c) the development of new methods for quick run-up estimation.

The main goals of these study are:

1.)   The real-time evaluation of tsunami source in near-shore conditions, namely the implications of the fast evaluation of seismic sources to compute the co-seismic deformation. Recent tsunamis will be analyzed involving both seismic, mareograph and DART data.

2.)   Fast evaluation of tsunami impact, namely a review of methods to forecast inundation parameters based on NSW estimation; use of inundation scenario databases; use of statistical simulators; the use of regularized extreme learning machine algorithms; new approaches on the combination of 2D numerical based on NSW or combining pre-calculated empirical Green's functions + 1D analytical solution for inundation.

Acronym list

ATJ	Azores Triple Junction
BIG	Badan Informasi Geospatial, (Agency for Geospatial Information Indonesia)
BMKG	Badan Meteorologi, Klimatologi, dan Geofisika
CFL	Courant-Friedrichs-Lewy
DART	Deep-ocean Assessment and Reporting of Tsunamis
DEM	Digital Elevation Model
DTHA	Deterministic Tsunami Hazard Assessment
GEBCO	General Bathymetric Chart of the Oceans
IDL	Instituto Dom Luiz
IPMA	Instituto Português do Mar e da Atmosfera
ITST	International Tsunami Survey Team
JMA	Japan Meteorological Agency
JRC	Joint Research Center
LDN	Leading Depression N-waves
LEN	Leading Elevation N-waves
LTV	Lower Tagus Valley
MDP	Macro Seismic Data Points
MIH	Maximum Inundation Height
MTR	Madeira Torre Rise
NEAM	North-Eastern Atlantic and Mediterranean
NEAMTWS	North-Eastern Atlantic, the Mediterranean and Connected Seas Tsunami Early Warning and Mitigation System
NLSW	NonLinear Shallow Water
PNAF	Pinhal Novo - Alcochete Fault
PTHA	Probabilistic Tsunami Hazard Assessment
SCR	Stable Continente Region
SWIM	Southwest Iberian Margin
TTT	Tsunami Travel Time

TWS	Tsunami Early Warning System
UNESCO	United Nations Educational, Scientific and Cultural Organization
USGS	United States Geological Survey

1. Introduction

Worldwide, approximately 10% of the world's population live in coastal areas with increasing tendencies (Rangel-Buitrago et al., 2020) and thus they are at risk of coastal hazards such as sea-level rise, tsunamis, etc. (Bevacqua et al., 2019; Marcos et al., 2019). While climate change-related events and sea-level rise are somewhat forecastable, tsunamis are sudden events and therefore hardly predictable, at least in their timing.

In the last decades, a couple of tsunami events distressingly demonstrated the vulnerability of lives and assets, hosting some of the worst tsunami events in modern history. On December 26, 2004, the ocean-wide Indian Ocean tsunami caused over 225000 casualties, with about 40000 still missing, according to Emergency Events Database (EM-DAT, 2017). Besides the enormous loss of lives and assets, the tragedy displaced 1.74 million people from ten countries (Chakrabarti, 2018). On March 11, 2011, the Tohoku-Oki tsunami was the costliest natural disaster in history, causing over 15000 casualties, with around 2500 still missing (Kim, 2011, Zhang, 2011). Especially after the 2004 Indian Ocean tsunami, international efforts led to the development of warning systems (Rudloff et al., 2009) and some effective operational forecasting systems in the far-field (Titov et al., 2016; Greenslade et al., 2019). Now, oceanwide events may be forecasted in real-time once the earthquake is detected, allowing for timely alerts for distant coasts, such as with the National Oceanic and Atmospheric Administration (NOAA)'s forecasting system (Titov et al., 2016). Contrary, coastal populations close to the tsunami source often have almost no time or short time to evacuate. The only warning could be the tremor itself.

Tsunami warnings based on the earthquake data take about 5 - 10 minutes to be issued and might be not conclusive immediately. For example, the Japan Meteorological Agency (JMA, 2013) issued a major tsunami warning for the nearest three prefectures based on a magnitude estimate of 7.9 after 3 minutes for the Tohoku-Oki event. However, at that time of the first evaluation the rupture was still ongoing, omitting to evaluate the real magnitude that was upgraded to Mw 9 posterior to the rupture (Hoechner et al., 2013).

Moreover, present Tsunami Warning Systems (TWS) only work for earthquake-induced-tsunamis because the earthquake can be detected with seismic networks. This is not the case for landslide- and volcanic- induced tsunamis. Examples are the Greenland, June 17, 2017, earthquake-landslide tsunami (Butler, 2019; Paris et al., 2019) or the Sunda Strait, December 22, 2018, Anak Krakatoa flank collapse tsunami, Indonesia. The stratovolcano Anak Krakatoa

entered an eruptive phase in June 2018. Although the volcano was under surveillance, an explosive eruption caused a flank collapse (Walter et al., 2019; Grilli et al., 2019; Williams et al., 2019; Borrero et al., 2020; Heidarzadeh et al., 2020; Omira and Ramalho, 2020) that generated an undetected tsunami hitting the coast of the Sunda Strait without any warning (Thandlam et al., 2019).

For TWS, rapid impact estimation is crucial. After detection and localization of the earthquake, the tsunami source can be inferred. The initial sea surface displacement is used as input in the tsunami numerical models (Titov and Synolakis, 1995; Liu et al., 1998; Tinti and Tonini, 2013; Miranda et al., 2014). However, high-resolution tsunami simulation is often not feasible in an emergency situation. TWS currently uses tsunami inundation modelling only for far-field events (Bernard and Titov, 2015). Estimation of the runup height quickly after a tsunami detection is helpful for coastal emergency managers.

In the Northeast Atlantic, the Mediterranean and Connected Seas Tsunami Early Warning and Mitigation System (NEAMTWS) are based on earthquake data. National Tsunami Warning Centers commonly use earthquake data to rapidly assess the earthquake's, location, magnitude, and depth. Decision matrices then define whether an event is evaluated as possibly tsunamigenic and the level of alert to be issued (ICG/NEAMTWS, 2011). Different levels of alerts are required since tsunami threats vary on geographical and temporal scales and may demand adequate emergency responses. Tsunami warnings may need to be updated, adjusted geographically, downgraded, or cancelled depending on the tsunami's intensity and evolution.

One area in the Northeast Atlantic, the Mediterranean (NEAM) region that caused basin-wide tsunamis in the past is the Southwest Iberia Margin (SWIM). In the SWIM the tectonic regime offshore is compressive but without the presence of a discrete plate boundary. In this area, the seismicity is scarce, but some very strong magnitude events generated tsunamis observed in the entire Northeast Atlantic (Martínez Solares and Arroyo, 2004; Baptista et al., 2006; Baptista and Miranda, 2009; Kaabouben et al., 2009; Wronna et al., 2019a; Baptista, 2019). Among them are for example, the devastating November 1, 1755, Lisbon tsunami, the March 31, 1761, transatlantic tsunami, the November 25, 1941, North Atlantic tsunami, the February 28, 1969, Horseshoe tsunami and the May 26, 1975, Gloria Fault tsunami. In the SWIM, the geological and tectonic setting is complex, and deformation occurs over a large area. Moreover, the known tectonic structures in the SWIM are close to the shore and communities. On the other hand, local moderate magnitude events shook Iberia in recent history. Those events occurred within

the stable continental regime. Thus, any contribution to a better understanding of the tsunami genesis, hazard and impact in the area are of utmost importance.

For a better implementation and refinement of TWS the tsunami hazard needs to be assessed and characterized for areas at risk. Tsunami hazard characterization and assessment generally lead to a better understanding of the tsunami genesis and hazard in source and target areas. The tsunami hazard can be assessed through Deterministic Tsunami Hazard Assessment (DTHA) (Heidarzadeh et al., 2009; Baptista et al., 2011; Wijetunge, 2014; Wronna et al., 2015) or Probabilistic Tsunami Hazard Assessment (PTHA) (González et al., 2009; Sarri et al., 2012; Sørensen et al., 2012; Omira et al., 2015; Grezio et al., 2017; Behrens et al., 2021). Deterministic studies use sets of pre-assumed source parameters (e.g. seismic source, landslide parameters) to assess the tsunami hazard in given impact areas whereas probabilistic methods estimate the mean annual frequency of the exceedance of a chosen tsunami intensity measure. DTHA and PTHA methods include hydrodynamic modelling to assess the hazard and thus, both approaches need reasonable estimates of the tsunami source parameters. DTHA and PTHA often rely on historic or paleo, earthquake or tsunami catalogues. However, the completeness and quality of these catalogues varies greatly (Albini et al., 2014). Those catalogues only represent a short period of the seismic cycle and may be too short to be representative for source variability, especially in areas with long recurrence periods of large magnitude earthquakes. Thus, the earthquake recurrence and frequency-magnitude distribution of tsunami sources may include large uncertainties in PTHA (Geist and Parsons, 2014; Bommer and Stafford, 2016). That highlights the need to investigate pre-instrumental events to contribute to the completeness of paleoseismic and paleo-tsunami catalogues (Priest et al., 2017; Paris et al., 2021). That is especially important for tsunami sources in complex tectonic settings. The analysis of past events therefore contributes to a better understanding of the tsunami hazard and genesis, especially in source areas with low seismicity which is important for both DTHA and PTHA approaches since earthquake and tsunami catalogues are almost inherently incomplete. Thus, the study of historical and less known causes contributes to a better overall tsunami hazard assessment.

Recent events, like the September 28, 2018, tsunami in the bay of Palu, Sulawesi Island, Indonesia, following a Mw 7.5 strike-slip earthquake (USGS, 2018; Socquet et al., 2019) are reminder, about the limitations of operational systems, lack of knowledge on the sources and tsunami impact. For a better understanding the impact needs to be assessed after each event. After the disaster in Palu, international efforts led to the UNESCO international tsunami survey to assess the impact around Palu bay. In the case of the Palu tsunami, it is of particular

importance since the initially estimated generation mechanisms were incapable of explaining a tsunami of that size. The tsunami source is still under debate, but field data and coastal observations support the scientific community to identify the generating mechanisms.

Despite the advances in tsunami warning and forecast tools and capabilities, it is important to increase our knowledge about the sources of tsunami events, especially in complex geological environments and in near-source conditions. Recent events are a reminder of the limitations and lack of knowledge of the tsunami phenomenon. The United Nations Decade of Ocean Science for Sustainable Development Goals (2021 - 2030), for a safe ocean, aims to protect communities from ocean hazards. To contribute to this goal a better understanding of tsunamis from Source-to-Coast is needed.

1.1. Objectives of the thesis

The goal of this thesis is to contribute to a better understanding of the tsunami from its source to the impact on the coast. Hazard assessments are crucial to understand tsunami risk. Methods to understand tsunami hazard include deterministic and probabilistic approaches that depend on knowledge of past events and completeness of tsunami and earthquake catalogues. It is especially important to increase our knowledge in areas where large magnitude events are scarce, as it is the case of the SWIM.

1. In this thesis the sources of two less known historical events in the SWIM are investigated. Two events that are not well understood are the March 31, 1761, which generated a transatlantic tsunami and a possibly tsunamigenic earthquake on November 11, 1858, in the southwest of Iberia.

2. Tsunami propagation can be solved using state of the art tsunami modelling codes. While the propagation is relatively well understood the tsunami impact such as runup remains challenging, especially if there is only a little amount of time. Thus, there is a need for rapid impact estimation tools allowing for a quick source-to-coast impact assessment. Within the framework of this thesis the impact parameter runup has been studied.

3. The tsunami impact needs to be assessed after each event. Within the timeframe of this thesis international efforts led to the formation of the UNESCO International Tsunami Survey Team (ITST) to study the tsunami impact in the bay of Palu in the aftermath of the September 28, 2018, Palu, Sulawesi earthquake and tsunami. The author of this thesis participated in the post-tsunami field survey to assess the tsunami impact in Palu and adapted the work plan of the thesis accordingly.

1.2. Structure of the thesis

The thesis therefore contributes to (a) the investigation of past tsunamigenic sources, (b) a source-to-coast approach to quickly estimate the runup and (c) the investigation of the tsunami impact at the coast. The three components therefore contribute to a better understanding of the tsunami from source-to-coast phenomenon.

The thesis therefore is structured as follows:

The methods for the principal studies within this thesis are presented and discussed in Chapter 2. Those methods are (a) the application of the numerical model Nonlinear Shallow Water Model wIth Nested Grids (NSWING), which is explained in section 2.2 and (b) the analytical solution is explained in section 2.3.

Chapter 3 presents the contribution to the characterization of the tsunami hazard in southwest Iberia. The reanalysis the March 31, 1761, transatlantic tsunami (Wronna et al., 2019a) is presented in section 3.2, and the study on the November 11, 1858, Setúbal earthquake and tsunami (Wronna et al., 2021) is outlined in section 3.3.

Chapter 4 presents a new method for tsunami impact estimation. Section 4.1 briefly introduces the study on the Tsunami Runup Predictor (TRP) and section 4.2, presents the paper (Wronna et al., 2020).

Chapter 5 focuses on the tsunami impact assessment. Within the timeframe of this thesis, the author was given the opportunity to join the UNESCO-IOC International Tsunami Survey Team (ITST) to study the tsunami impact in the bay of Palu, following the September 28, 2018, event in Sulawesi, Indonesia. The field survey took place from November 7 – 11, 2018. The results of the coastal tsunami impact assessment of the UNESCO-IOC ITST field survey are published in Omira et al. (2019). The study is attached in Appendix 4.

Finally, Chapter 6 summarizes the main conclusions and achievements of the thesis.

2. Methods

This chapter introduces the main methods used in the thesis. The nonlinear shallow-water numerical tsunami model NSWING (Nonlinear Shallow Water Model with Nested Grids) is employed (Miranda et al., 2014). NSWING has been used for publication 1, 'Reanalysis of the 1761 transatlantic tsunami' (Wronna et al., 2019a), publication 2, 'A new tsunami runup predictor' (Wronna et al., 2020) and publication 3, 'Reevaluation of the 11 November 1858 earthquake and tsunami in Setúbal – A contribution to the seismic and tsunami hazard assessment in southwest Iberia' (Wronna et al., 2021). Section 2.1 presents an introduction to tsunami modelling. Here, exclusively earthquake-generated waveforms and free surface deformations are considered as initial conditions for the tsunami model. So, the half-space elastic theory (Mansinha and Smylie, 1971; Okada, 1985) is briefly introduced in section 2.2.

The analytical solution (Kânoğlu, 2004; Aydın and Kânoğlu, 2017) has been used to compute the runup complementary to the numerical modelling results in Wronna et al. (2020). Using those runup results, the relation of the runup to classical waveform parameters has been presented for an extensive database of initial wave profiles. For Wronna et al. (2019a) in section 3.2 and Wronna et al. (2021) in section 3.3, the concept of the Paleo Digital Elevation Model (PDEM) reconstruction presented by Wronna et al. (2017) has been applied. Moreover, for the reevaluation of the 1858 earthquake parameters based on the macroseismic analysis, laws determined by Casado et al. (2000), Gasperini et al. (2010), and Sbarra et al. (2019) have been used. Those methods are more briefly introduced in section 3.3.

2.1. Tsunami modelling

Tsunamis are surface gravity waves. Gravity waves form when water is disturbed, and gravity acts to reestablish equilibrium. Considering tsunamis, a sudden displacement (sudden ocean bottom deformation, mass movements, volcanic activity) disturbs the free water surface over a large area producing waves with long wavelengths. Then gravity initiates propagation by reestablishing equilibrium, and inertia pulls the displaced mass of the entire water column back towards the initial state. Thus, bordering water columns are affected by this oscillating movement that effectively transports energy over long distances.

Hence, investigation of tsunamis considers the following three main stages: (1) Generation, (2) Propagation, and (3) Inundation.

1.) Generation: Sudden displacements of the entire water column generate tsunamis. The most common causes are earthquakes, volcanic activity, and landslides.

2.) Propagation: Gravity acts to restore equilibrium in the dislocated water body. Closer to the shore, where bathymetry is shallower, shoaling causes deformation of inbound tsunamis, resulting in short wavelengths but larger amplitudes.

3.) Inundation: Tsunami wavelengths are getting shorter closer to the shore, but the wave period is conserved. Thus, water cannot escape back to the ocean, causing overland flow and inundation.

The motion of any fluid can be fully described by the equations of motion. Any motion of viscous fluids and gases can be described with Navier-Stokes's equations based on the conservation of mass and Newton's second law (Vallis, 2017). The rate of change of momentum $\vec{a}$ of a body with mass m, is directly proportional to the sum of the forces applied to the body, $m\vec{a} = \sum \vec{F}$. A brief introduction to the equations of motion, the Navier-Stokes equation and the equation of momentum is given in the Appendix 2.1.

For tsunami simulations, depth-integrated nonlinear long-wave models and computational fluid dynamic models can be applied (Flow Science Inc., 2018; Qu et al., 2019; Sogut and Yalciner, 2019; Franco et al., 2020). For the sake of computational costs most commonly, non-linear shallow water (Imamura, 1995; Titov and Synolakis, 1995; Liu et al., 1998; Tinti and Tonini, 2013; Titov et al., 2016) or dispersive Boussinesq-type (Madsen and Sørensen, 1992; Chen and

Liu, 1995; Kirby et al., 1998; Fuhrman and Madsen, 2009) models are used. Those models are mostly validated through a series of benchmark tests described in Synolakis et al. (2008).

The shallow water equations (SWE) are derived by depth average integration from the ocean bottom to the free surface, eliminating viscous stresses and flow gradients between the vertical coordinates (Synolakis and Bernard, 2006). The assumption that the water body is incompressible allows introducing the free surface elevation η through the hydrostatic approximation for the pressure, $p = \rho g(d + \eta)$. Thus, shallow water models calculate the evolution of the free surface elevation, and the water particle velocity integrated in-depth. Linear SWEs neglect non-linear convective inertia forces and bottom friction terms; they are a good approximation for open ocean propagation. However, primarily the non-linear SWE are used, since nearshore, and coastal impact is of interest. For most tsunami models, it is convenient to consider spherical coordinates, including Coriolis parameters. The non-linear SWE in their Cartesian and spherical form are given in Appendix A2.3.

Numerical tsunami models based on the non-linear SWEs are widely used and have reproduced results for past events with sufficient accuracy. The non-dispersive nature of the non-linear shallow water models tends to overestimate wave amplitudes but within an acceptable range previously argued to serve as a safety buffer. However, the non-linear SWEs are considered suitable for warning purposes (Glimsdal et al., 2013).

For a more accurate tsunami computation, one should include energy dissipation. However, many authors discard energy dissipation in tsunami simulations for the sake of estimating the worst-case scenarios. Dutykh and Dias (2007) name three sources of dissipation for water waves, surface dissipation, body dissipation and bottom friction. For tsunamis, the most important cause of energy dissipation is bottom friction, especially near shore and land propagation. Most numerical models now allow including Bottom friction terms employing the empirical Manning's coefficients (Burwell et al., 2007; Dyakonova and Khoperskov, 2018).

Numerical models based on the SWE remain the most used codes for tsunami simulation. Some examples are the TUNAMI-N2 code (Imamura, 1995), COMCOT (Cornell Multi-grid Coupled Tsunami model) (Liu et al., 1995, 1998), MOST (Method of splitting Tsunami) (Titov and Synolakis, 1995; Titov and González, 1997; Titov et al., 2016) or more recently UNIBO-TSUFD (Tonini et al., 2011; Tinti and Tonini, 2013). The non-linear SWEs are solved using numerical discretization methods such as the finite element or finite differences methods. Discretization using a finite element method can be used to simplify large mesh systems dividing

into smaller finite elements. Widely used codes, such as the TUNAMI-N2 code and COMCOT, apply the commonly used finite differences where each solution domain is divided into a grid of discrete points (e.g., finite grid cells). According to the grid's cell size, the partial differential equations are discretized and form an algebraic system of equations. These equations are solved in a specific point-wise scheme for each cell at each time instant t based on the previous time step. For studies within the framework of this thesis, the numerical model NSWING (Numerical model nonlinear Shallow Water model wIth Nested Grids) has been used (Section 2.2).

2.2.   Setup, description, and application of the numerical model

Non-linear shallow water codes are state-of-the-art tsunami modelling tools. They are easily adaptable for applications where it is necessary to include small- and large-scale grids in one domain. The numerical model NSWING (Miranda et al., 2014) has been used herein. The following chapter describes tsunami generation modelling based on the half-spaced elastic theory and explains the preparation of the bathymetric and topographic data. This section also gives a brief introduction of the numerical model NSWING based on Wang (2009) and Omira (2010).

The setup of the numerical model and input data is a procedure that is not always straightforward and requires precautions. The most important points are, the tsunami source, the compilation of multiple datasets to one DEM, and different input parameters for the numerical model to obtain reliable results. This section exemplifies three main steps to set up a numerical model.

2.2.1.   Tsunami generation: Definition and computation of the tsunami source - The use of the half-space elastic theory for tsunami generation

Here, earthquake-generated tsunamis have been considered. Tsunami sources generated by earthquakes have a unique rupture pattern even for the same geological structure resulting in varying slip values across the rupture area. Post-event seismic and tsunami waveform inversion may reveal the complexity of the source. However, these models are only available after an event, and thus the source complexities may be used to model a past event. Some examples of nonuniform slip distribution for the earthquakes and tsunamis in Chile, Maule, 2010 are Delouis et al. (2010) and Hayes (2010) and in Japan, Tohoku-Oki, 2011 are Ammon et al. (2011); Wei et al. (2012) and Yue and Lay (2013). The most used earthquake-generated tsunamis models employ the half-space elastic theory (Mansinha and Smylie, 1971; Okada, 1985) to compute the vertical deformation of the ocean bottom. Here, a brief introduction to relevant earthquake parameters to apply the half-space elastic theory for tsunami generation is given.

The focus in this thesis is on earthquake-generated tsunami waves. Commonly earthquakes occur close to tectonic faults, for example, along plate boundaries (interplate events), and sometimes also intraplate events may trigger tsunamis. Fortunately, not all submarine earthquakes generate tsunamis. Most submarine earthquakes do not produce sufficient vertical sea surface displacement to generate tsunamis. The dimension and magnitude of vertical sea surface deformation depend mainly on the earthquake's magnitude, rupture mechanism and depth. The magnitude of the earthquake is related to the size of the dislocated area, the dislocation (slip) amount

of the rupture plane and material's rigidity of the rupture area. The seismic moment equation (Aki, 1972) describes this relation as,

$$M_0 = \mu A D, \tag{2.1}$$

where μ is the rigidity of the rupturing area, also defined as shear modulus, A is the area of the rupture fault plane ($L \times W$), where L is the fault length, W is the fault width, and D is the average displacement of the fault plane.

Kanamori and Anderson (1977) presents the seismic moment and moment magnitude relation as

$$M_w = \frac{2}{3} \log M_0 - 6.03 \; . \tag{2.2}$$

It is important to note that rigidity is a material property. Stich et al. (2007) propose a shear modulus of $\mu = 4 \times 10^{10}$ Pa for crustal events and $\mu = 7 \times 10^{10}$ Pa for ocean lithosphere. Matias et al. (2013) suggest the shear modulus of $\mu = 6.5 \times 10^{10}$ Pa for most of tsunamigenic faults in the SWIM except for the Gulf of Cadiz, where the authors consider a rigidity of $\mu = 4 \times 10^{10}$ Pa to be adequate. Thus, considering Aki (1972) and Kanamori and Anderson (1977), an increase in μ means an increase in moment magnitude M_w but the free surface deformation and thus the generated tsunami may remain in the same order of magnitude. Also, an increase in rupture area signifies an increase in moment magnitude M_w. A greater rupture area may also lead to an increase in vertical surface deformation area, which is especially significant if the rupture plane is not perpendicular to the surface and the dislocation along the fault plane is not parallel to the surface. The fault plane orientation and dislocation geometry define the type of the fault and the rupture mechanism. Three main types of faults are distinguished and exemplified in figure 2.1:

- Transform or strike-slip faults: dislocation occurs along the strike in a transform ambient.
- Normal fault: dip-slip rupture mechanism where slip occurs in the direction of the dip angle in an environment that is in extension.
- Inverse fault: dip-slip rupture mechanism where slip occurs in the direction of the dip angle in a compressive environment.
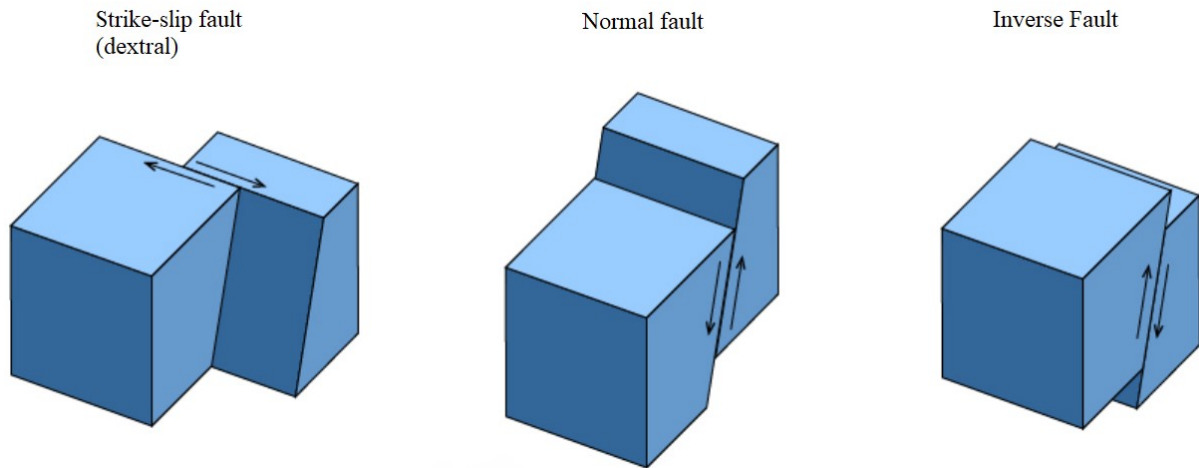
Figure 2.1 Exemplified faults and rupture mechanisms.

The fault type and rupture mechanism can be defined using the fault and dislocation geometry given by the following quantities: the fault's width, length, depth, strike, dip, rake, slip. The fault and dislocation geometry plane are defined as shown in figure 2.2.
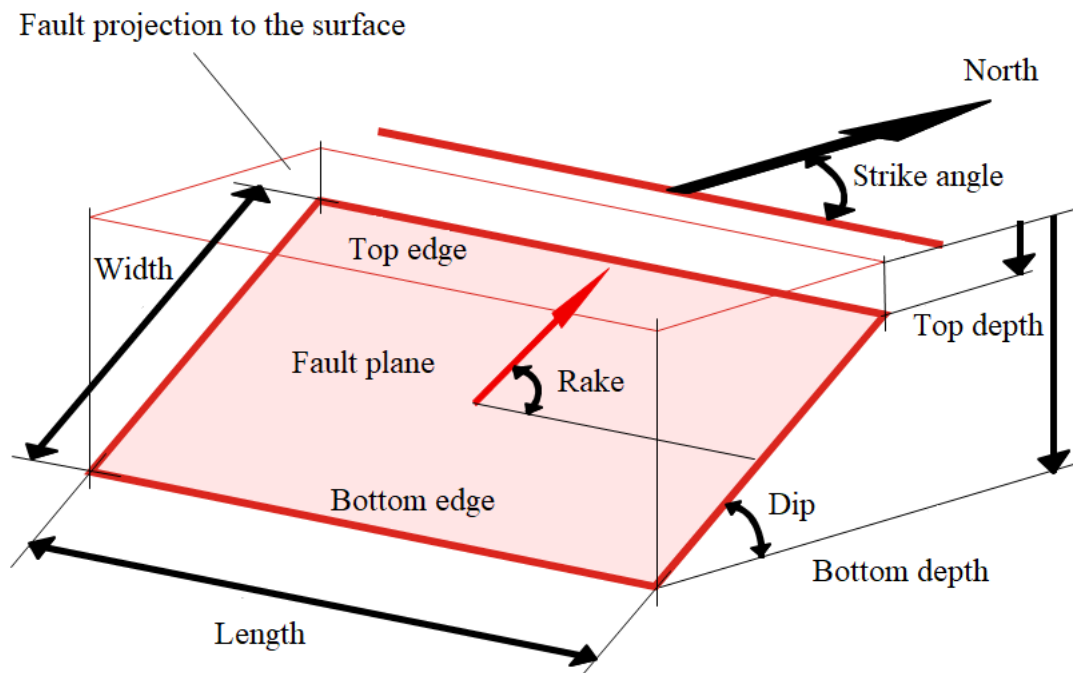
Figure 2.2 Fault plane and dislocation plane parameters adapted after INGV (2015).

The fault's strike is the angle the upper faults edge surface projection to the North. The dip angle measures the inclination of the fault plane from a planar horizontal surface. The rake angle is orientated to the fault strike and defines the direction in which the dislocation occurs. The rake angle also defines the rupture mechanism: 0° and 180° rake angle constitute a pure strike-slip rupture mechanism with no vertical displacement involved, 90° rake angle defines a

pure inverse, and 270° is pure normal rupture mechanism. Most earthquakes involve both strike-slip and dip-slip components, but generally, one mechanism is predominant.

Strike-slip faults are generally not associated with large vertical displacement. Often strike-slip earthquakes include rupture mechanisms with some normal or inverse component; however, only those with considerable vertical displacements may be tsunamigenic (Synolakis, 2003; Kaabouben et al., 2008; Baptista et al., 2016). On the other hand, the recent earthquake and tsunami in Palu, Sulawesi, Indonesia (Gusman et al., 2019; Omira et al., 2019) have demonstrated that strike-slip events may have great tsunamigenic potential in specific environments.

Normal dip-slip faults occasionally cause tsunamis; recent examples are the September 7, 2017, Mexico, Chiapas earthquake and tsunami (Gusman et al., 2018; Ramírez-Herrera et al., 2018) or the July 20, 2017, Bodrum-Kos earthquake (Dogan et al., 2019; Papadopoulos et al., 2019).

However, most of the tsunamigenic earthquakes occur at inverse faults in subduction zones. Some of the major earthquakes and tsunamis at subduction zones due to inverse faulting are the December 26, 2004, Mw 9.1-9.3 Indian ocean earthquake and tsunami (Geist et al., 2007; Grilli et al., 2007), the February 27, 2010, Mw 8.8 Maule, Chile earthquake and tsunami (Delouis et al., 2010; Hayes, 2010), and the March 11, 2011, 9.1 Mw Tohoku-oki earthquake and tsunami (Ammon et al., 2011; Yue and Lay, 2013).

To accurately model the permanent vertical ocean bottom deformation, fault plane size, position and dislocation geometries are needed. Posterior to an earthquake and tsunami event, waveform inversion models reveal fault plane and dislocation parameters. The composition of these parameters may express heterogeneities of fault slip across the fault plane. Methods to obtain these data apply individual or joint inversion of seismic, tsunami, and geodetic data (Duputel et al., 2011; An et al., 2014; Yue et al., 2014; Melgar and Bock, 2015; Ho et al., 2020). Alternatively, if the source is not well constrained, if inversion models are not available or for early warning, simpler models of deformation need to be adopted. Most models for tsunami generation compute the ocean bottom's static deformation based on the half-space elastic theory. For slip on a rectangular fault plane in a homogeneous half-space elastic medium, the analytical formulae of Mansinha and Smylie (1971) or equivalently Okada (1985) allows computing the permanent static deformation of the half-space elastic medium. The analytical formulae's solutions assume that the fault plane and dislocation geometries (c.f. Figure 2.2) determine the medium's general deformation. The main difference between the two models is that Okada's expressions allow for non-double-couple solutions. It is common practice to assume the sea

surface displacement mimics the co-seismic deformation (Kajiura, 1970). Thus, the deformation of the free surface can be considered equal to the vertical ocean bottom deformation. This procedure is valid for most earthquakes since rupture occurs quasi-instantaneous. Dutykh and Dias (2007) suggest that seabed deformation dynamics may positively influence tsunami amplitudes for slow rupture mechanism. Slow ruptures occur, for example, for tsunami earthquakes (Kanamori, 1972; Ide et al., 1993; Satake, 1994; Ratnasari et al., 2020). However, Tanioka et al. (2017) use W-phase inversion models and depth-dependent rigidity (c.f. Eq. 2.1) to use instantaneous deformation based on Okada (1985). Then the authors use the instantaneous surface deformation as the initial condition for tsunami simulation of past events, among them, the 1992 Nicaragua tsunami earthquake, and they yield good agreement with the field observations.

2.2.2. Preparation of topography and bathymetry data for numerical modelling

The source-to-coast propagation requires bathymetry and topography data of large areas, and thus tsunami modelling is computationally intensive. One method to decrease computational time is the implementation of nested grids. Nested grids consider the tsunami source, open ocean propagation and the target size on physically proper different spatial scales. Besides, bathymetry data in the open ocean is often only available on spatial scales of hundreds of metres. For the target areas, on the other hand, small scale bathymetric and topographic features are relevant for tsunami propagation and inundation. Consequently, bathymetry and topography data need to be assembled in a high-resolution DEM with a small grid cell size, in the order of tens of meters or less. The nested grid configuration then allows to couple the grid with different cell sizes for the modelling process. The most important considerations regarding DEM construction and setup of the nested grids are described here.

Tsunami propagations nearshore and on land depend on the composition of small-scale morphological features. Thus, the setup and implementation of appropriate topography and bathymetry data are essential when preparing a numerical tsunami simulation. The DEM of the target site needs to represent the most relevant coastal features and the shoreline accurately. A system of coupled nested grids allows for accurate modelling in a target area where inundation mapping on a local scale is the objective. Important considerations are:

- Bathymetry and topography need to cover the entire area from source to coast, including a detailed DEM of the target area.

- Continuity offshore-onshore: Consideration of the data sets' reference systems, with particular attention to the vertical datum.

- The horizontal resolution in the DEMs for the target area needs to ensure that local effects are modeled accurately.

- For the coupled nested grids, the cell size in the DEM of the target area defines the grid's cell size that covers the source area.

- When defining the source area's grid, it is essential to consider that the surface deformation's dimension is greater than the fault plane according to the half-space elastic theory.

For the source area and open ocean propagation, the General Bathymetric Chart of the Ocean (GEBCO, 2014) is a commonly used data source. Currently, it is available for 15 arc-seconds intervals in different formats with the mean sea level as a vertical reference. Another valuable data source is EMODnet, which offers a general DEM with approximately 1/16th arc-minutes resolution and a collection of high-resolution datasets. Data from GEBCO covers the areas where no high-resolution data are available to avoid gaps in higher resolution datasets. Whatever dataset used must be treated with care since global grids make use of multiple heterogeneous assimilated datasets. However, for inundation modelling on regional or local scales, the above-named global grids' resolutions are too coarse, and a DEM implementing both high-resolution bathymetry and topography is required.

The digital elevation model (DEM) of the target area is necessary to represent the study area with sufficient quality. If not previously built, many data sets comprise just topography or just bathymetry depending on their purpose. Numerical tsunami modelling, including inundation mapping, requires a DEM comprising both detailed bathymetry and topography. These data may be available in vector or grid format. Vector data may contain point, line, or polygon shapes with attributed height or depth information. Point clouds, individual point measurements or topographic and bathymetric contours are some common examples of vector data.

On the other hand, gridded datasets contain mainly already assimilated and processed raw data in equal-sized cells where each cell has one height or depth value. The implementation of bathymetry data from marine surveys, nautical charts, topographic maps, and LIDAR may help refine the study area's resolution. Scanned and vectorized charts and maps can improve a DEM in case of poor digital data quality. Each data set has an attributed horizontal and vertical spatial reference system, depending on its location, spatial extent, and usage. For example, nautical

bathymetric charts for navigational purposes commonly have hydrographic zero (HZ) as a vertical datum.

Contrary to topographic data that has the mean sea level (MSL) as a vertical reference system. Thus, all implemented data must be set to the same spatial and vertical reference system before the DEM reference is defined. Then the DEM reference is chosen according to the sea level at the time of the studied event. In case two data sets cover identical areas, it is crucial to avoid ambiguities and give preference to the more accurate one. For control purposes, GPS measurements at chosen control points may evaluate the quality of a DEM. If the DEM contains many different data sources, a three-dimensional visualization may help to identify errors.

For the target area, the chosen resolution of the DEM determines the quality of the entire tsunami model (Tinti et al., 2011). However, the grid cell size of the resulting DEM may be defined arbitrarily but depends crucially on the implemented composite data sets. For example, LIDAR data may have a resolution in the order of a few meters, but the areas not covered by LIDAR may be only available on the scale of tens of meters or less. Hence, a resolution to represent well the parts outside LIDAR coverage means a trade-off for the LIDAR areas. Vice versa, the choice of a high resolution may represent LIDAR data well, but the zones outside LIDAR coverage require some interpolation to obtain the higher resolution. Interpolating to a higher resolution does not increase the data quality. On the other hand, downscaling from higher to lower resolution also means a loss in quality, but features are not lost; they are present on a coarser scale. Thus, the choice for the final resolution of the DEM, having in mind the quality of data implemented, requires a well-balanced trade-off between quality and computational resources.

The chosen resolution of the most refined grid defines the resolutions in all other nested grids. For the studies within this thesis, a refinement factor of four has been used in all nested grids for numerical modelling. For instance, in Wronna et al. (2019a), where a 4-layer nesting has been used, the DEM in the target area has the highest resolution of 25 m, the corresponding nested layers have 100, 400 and 1600 m resolution.

For a smooth propagation from one layer to the next level layer, the TINTOL tool embedded in the program Mirone suite (Luis, 2007) has been used. This tool enables extracting the required nesting information (correct corner coordinates) for the chosen refinement factor. This process is repeated until the layer with the second-highest resolution. Here, the DEM of the target area is embedded and the nesting information along the DEM borders is retrieved to obtain the layer

with the finest resolution. Finally, all nested layers are stored together with the initial condition to prepare the batch file for execution.

2.2.3. Propagation and inundation - The use of the numerical model NSWING

Once the DEM, the nested grid and the initial condition are ready, the numerical code uses this data to compute tsunami propagation and inundation. The numerical model initiates propagation on the nested grid with the implemented DEM considering the initial conditions. The initial conditions are comprised by the initial displacement of the sea surface and velocity field. If an instantaneous rupture is considered, which is mostly the case the velocity field is set to zero initially.

In Wronna et al. (2019a, 2020 and 2021) the numerical finite-difference model NSWING (Nonlinear Shallow Water Model wIth Nested Grids) (Miranda et al., 2014) has been used. NSWING allows to implement generation area, transoceanic propagation and compute the entire from source-to-coast process including inundation and provides tsunami metrics such as flow depth, flow velocity and runup in high-resolution target areas. NSWING runs on MS Windows operating system, includes core parallelization for increased computational performance and compares closely to the COMCOT (Liu et al., 1998; Wang, 2009; Omira, 2010; Miranda et al., 2014). Thus, NSWING allows for computing more resource-intensive problems. An easy-to-use interface in the application Mirone suite (Luis, 2007) enables an easy setup of the model and input parameterization. The code was validated with the classical benchmark tests (Synolakis et al., 2007) and applied in several studies (e.g., Wronna et al., 2015; Omira et al., 2016, Baptista et al., 2020).

NSWING solves the SWEs applying a second-order discretization and explicit staggered leapfrog finite differences scheme following Liu et al. (1998). The discretization employing the leap-frog finite difference scheme excluding friction terms and Coriolis parameter (linear SWE) is given in Appendix A 2.5. The discretization of the nonlinear SWEs applies the finite staggered leap-frog scheme, but a second-order upwind scheme evaluates the momentum equation's nonlinear convective terms (Appendix 2.6).

NSWING evaluates the friction terms with Manning's formula (Appendix 2.4 and 2.7) that utilizes the empirical Manning coefficient to simulate different bottom roughness conditions. As an example, Linsley and Franzini (1979) evaluated the Manning coefficient empirically using different bottom conditions for a channel flow. However, Bricker et al. (2015) present a synthesis of studies on the Manning coefficient, concluding that most tsunami models

underestimate energy dissipation due to friction. However, NSWING includes the friction terms uniformly. Thus, the friction coefficient should be chosen according to the target site properties. Moreover, for worst-case studies, the friction terms are commonly ignored. The discretization of the bottom friction terms is presented in the Appendix 2.7.
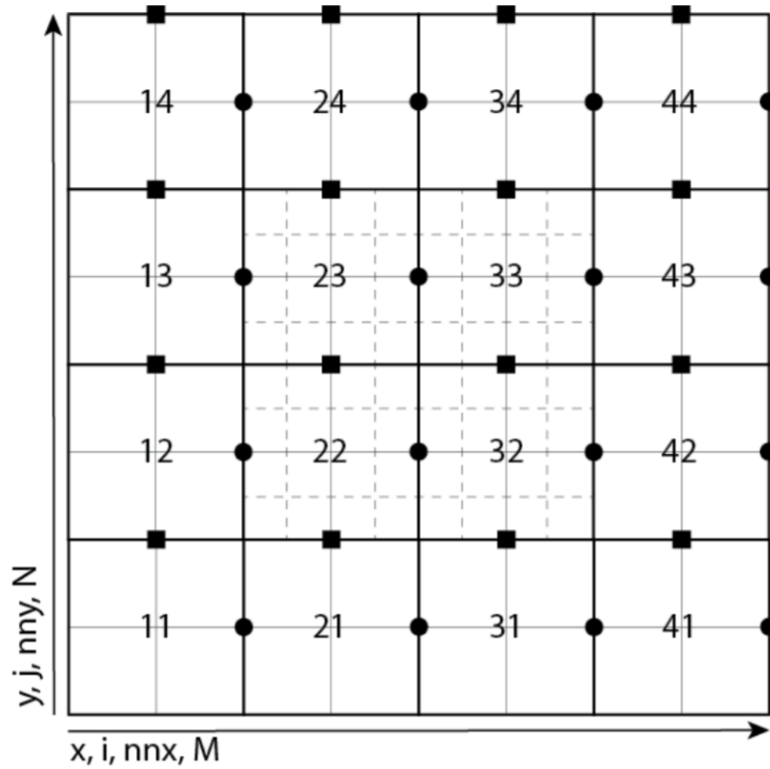
Figure 2.3 Exemplary coordinate system and visualized nested grid. The nesting geometry represents two levels of grids and shown and the ratio of four between grid steps.

NSWING allows the implementation of coupled nested grids to model the complete from Source-to-Coast propagation and inundation. Tsunamis waves change considerably along their propagation path, especially when approaching shallower waters where wave characteristics are strongly affected by near-shore bathymetry. Besides, runup and inundation height and distance depend crucially on the onshore topography. Thus, in coastal areas, a refined DEM, including high resolution bathymetric and topographic data, needs to be implemented. A set of coupled nested grids enables different cell sizes in the nesting, allowing for a ratio-wise reduction of the grid cell size from the source towards a refined resolution at the coast. NSWING requires a refinement factor of 4 within the nested grids. Figure 2.3 depicts the nesting scheme. Higher levels of nesting are equally organized.

To ensure numerical stability and continuity of the numerical computations across different grid sizes in the nested grid setup, the Courant-Friedrichs-Lewy (CFL) condition (Eq. 2.3) must be satisfied. The CFL condition depends on the chosen grid size, maximum still water depth and

time step. NSWING requires $C_{max} \leq 0.5$, and the time step may be adjusted to satisfy the CFL condition.

$$C = u \times \frac{\Delta t}{\Delta x} \tag{2.3}$$

NSWING employs an open boundary condition allowing the waves to propagate outside the grid whenever the domain boundary does not correspond to a coastline or is defined contrarily. NSWING employs an open boundary condition allowing the waves to propagate outside the grid whenever the domain boundary does not correspond to a coastline or is defined contrarily. At the shore, a moving boundary algorithm computes inundation, like Cho (1995), Liu et al. (1995), Cho and Kim (2009) and described in Wang (2009) and Omira (2010). Throughout the inundation process, the moving boundary algorithm tracks the moving shoreline. The shoreline is updated each time step based on classes established by water height level comparison in the neighbouring cells along the shoreline. The moving boundary scheme is designed as a two-dimensional problem and tracks the shoreline in x- and y-direction. Figure (2.4) presents a simplified one-dimensional approach omitting the time step for simplicity.

For a grid point on dry land, the water depth d has a negative value describing the elevation above Mean Water Level (MWL). D_f describes the flooding depth. For a cell on dry land the total water depth $D = d + \eta$ is negative contrary to wet cells with positive D values. As described above, the code uses the continuity equation to evaluate the free surface displacement in the entire domain, including dry cells. The free surface displacement η at dry land cells continues zero because the volume fluxes are zero bordering grid cells. Along the coastline, the total water depth D is evaluated for each instant of time. Here, the moving boundary algorithm determines if the total water depth D is high enough to inundate the adjacent dry land cells and update the shoreline position. The momentum equations determine the volume fluxes only in the wet cells. As exemplified along a one-dimensional profile in figure (2.4), the total depth D is evaluated at grid cell $i - 1$, i, and $i + 1$ and the volume flux is calculated at the borders $i - 1/2$, $i + 1/2$ and $i + 3/2$. Cell $i - 1$ and i are wet cells (c.f. figure 2.4) with total positive water depth and cell $i + 1$ has a total negative water depth value. The shoreline is located between cells i and $i + 1$ where the volume flux is zero, and the dry-wet boundary remains between cells i and $i + 1$. When the total water depth is rising (c.f. figure 2.4), the volume flux at the boundary $i + 1/2$ is no longer zero; the boundary propagates one grid cell in an onshore direction, and the total depth is computed for cell $i + 1$.
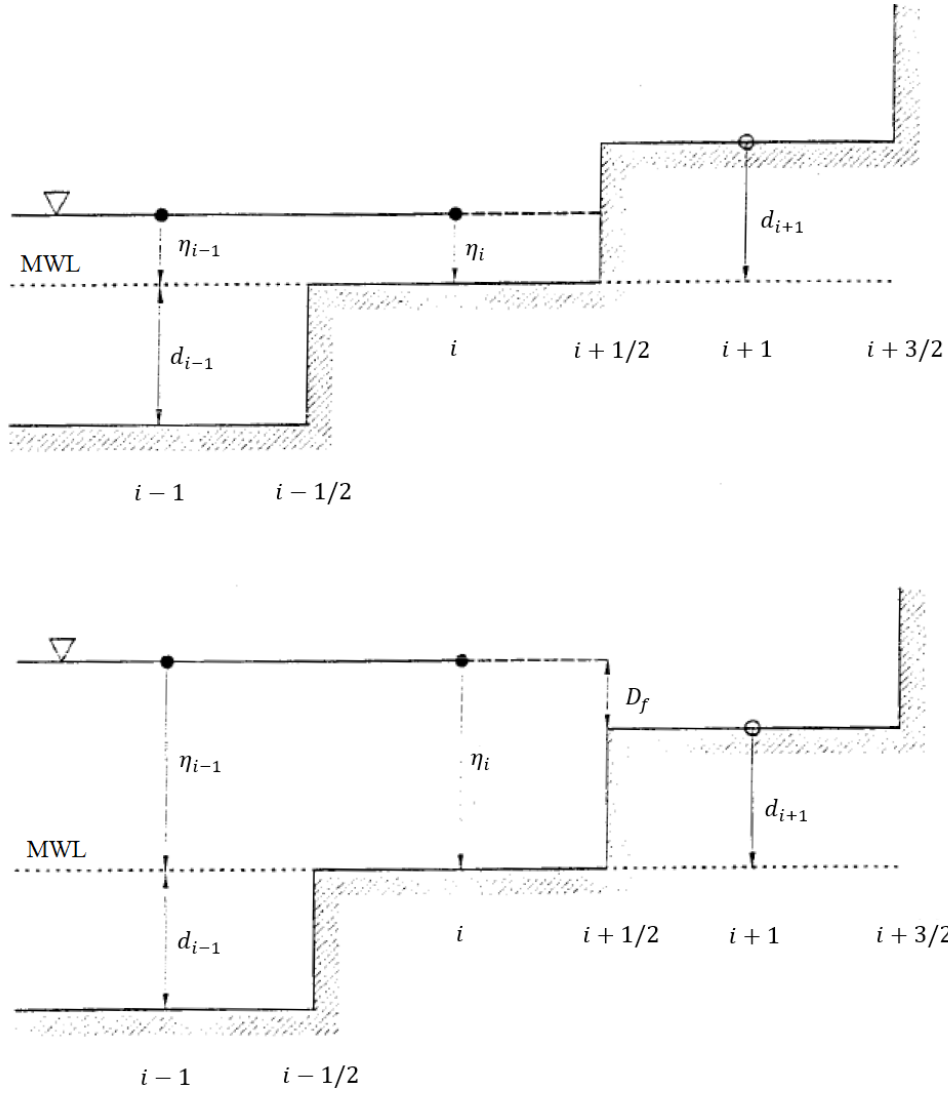
Figure 2.4 Sketch of the moving boundary scheme in one dimension (adapted from Wang 2009).

All possible cases for D_i can be described as:

(i)   For the case $D_{i+1} \leq 0$ and $d_{i+1} + \eta_i \leq 0$, the shoreline stays between cells i and $i + 1$ and the volume flux $P_{i+1/2} = 0$.

(ii)   For the case $D_{i+1} \leq 0$ and $d_{i+1} + \eta_i \geq 0$ the shoreline moves to between the grid cells $i + 1$ and $i + 2$, the volume flux $P_{i+1/2}$ can be non-zero. The volume flux $P_{i+3/2}$ is defined to be zero. The flooding depth is given by $D_f = d_{i+1} + \eta_i$.

(iii)   For the case $D_{i+1} \geq 0$, the shoreline moves to in between grid cells $i + 1$ and $i + 2$. The volume flux $P_{i+1/2}$ can be non-zero, while the volume flux $P_{i+3/2}$ has a zero-value. The flooding depth is given by $D_f = max(d_{i+1} + \eta_i ; d_{i+1} + \eta_{i+1})$.

2.3. Analytical solution

Numerical models based on nonlinear shallow water wave equations (NLSW-equations) (Titov and Synolakis, 1998; Liu et al., 1998; Yalciner et al., 2007; Wang, 2009; Miranda et al., 2014) allow assessing the tsunami runup in 2D. Those models mainly adopt a moving boundary algorithm (Cho, 1995; Liu et al., 1995) to track shoreline motion because of inundation.

However, these models may be inadequate for rapid early warning since the implementation of high-resolution bathymetry and topography in the DEMs and the computation are time-consuming.

Alternatively, to numerical models, analytical solutions of the linear and nonlinear SWEs, are relatively well developed and allow to calculate the runup of different wave types for under certain boundary conditions (Carrier and Greenspan, 1958; Pedersen and Gjevik, 1983; Synolakis, 1987; Pelinovsky and Mazova, 1992; Tadepalli and Synolakis, 1994; Carrier et al., 2003; Kânoğlu, 2004, Tinti and Tonini, 2005; Madsen and Fuhrman, 2008; Madsen and Schäffers, 2010; Didenkulova and Pelinovsky, 2011a; Fuentes et al., 2015; Aydın and Kânoğlu, 2017; Anderson et al., 2017).

A significant improvement for the analytical solutions of the evolution of a wave over a constant sloping plane beach was presented by Carrier and Greenspan (1958), introducing the hodograph transformation for two specific initial wave profiles. Synolakis (1987) extended the approach by Carrier and Greenspan (1958) and solved the nonlinear propagation and runup of a solitary wave for the canonical problem constituting a constant depth region that connects to a sloping beach. They take the waveform at the toe of the beach as the boundary condition for the solution of the linear shallow water equations. However, to introduce geophysical more appropriate wave profiles Tadepalli and Synolakis (1994, 1996) proposed solutions for the linear shallow water equations considering Leading Depression N-waves (LDNs). Tadepalli and Synolakis (1996) introduced a horizontal length scale and a steepness parameter and showed that the LDNs cause higher runup compared to Leading Elevation N-waves (LENs). Carrier et al. (2003) expanded Carrier and Greenspans's (1958) approach and presented a Green function solution, obtaining a complete elliptic integral of the first kind. Experimental data and numerical modelling showed that analytical solution preserves the nonlinear effects, although linearization is used to obtain the boundary condition (Synolakis, 1987; Titov and Synolakis, 1995). Taking advantage of that, Kânoğlu (2004) uses the linearized form of the hodograph transformation for the spatial variable to overcome the difficulties of defining the initial condition. This method results in integrals that are easier to solve and allows the implementation of geophysical

meaningful initial waveforms. That is important since the analysis of long transient periodic waves by Madsen et al. (2008) led them to conclude that the solitary wave paradigm incompletely describes the runup on sloping beach causing order of magnitude errors and propose to overcome the solitary wave-tie to describe N-waves. These authors also conclude that these waves are effectively non-dispersive. Madsen and Schäffer (2010) extended the earlier studies by Synolakis (1987) and Tadepalli and Synolakis (1994). They avoid the solitary wave tie between wavenumber and wave height to depth ratio and present analytical solutions of the shoreline motion and runup for sinusoidal, single, N-, and transient waves. Like Tadepalli and Synolakis (1994, 1996), Madsen and Schäffers (2010) conclude that a greater amplitude ratio between negative-positive amplitude positively influences the runup. Chan and Liu (2012) showed that tsunamis are small-amplitude long waves based on sea surface profiles from the 2011 Tohoku-Oki event. They extended Synolakis' (1987) and Madsen and Schäffer's (2010) work with analytical solutions for cnoidal and multiple solitary waves. They concluded that the accelerating phase of the wave mainly drives the maximum runup for single waves.

Sepúlveda and Liu (2016) used the half-space elastic theory (Okada, 1985) to express the maximum runup in terms of initial source parameters based on earthquake fault plane parameters. These authors find a relationship between the maximum runup and the earthquake source parameters implementing the IVP and BVP solutions of the nonlinear SWEs based on Kânoğlu (2004) and Madsen and Schäffer (2010), respectively.

Other authors focused on different bathymetry settings, for instance, parabolic beach Choi et al. (2008), inclined channels (Didenkulova and Pelinovsky, 2011a) and U- or V-shaped bays (Harris et al., 2016; Didenkulova and Pelinovsky, 2011b; Rybkin et al., 2014; Anderson et al., 2017).

2.3.1. Adaption of the analytical solution

The analytical solution presented in Aydın and Kânoğlu (2017) which is based on the earlier work of Kânoğlu (2004) has been used for Wronna et al. (2020) (section 4.2), and some conference proceedings (c.f. Appendix 1). This method computes the shoreline evolution for a one-dimensional waveform profile. Hence, it requires non-dimensional input parameters for the waveform. In this thesis Aydın and Kânoğlu's (2017) work has been adapted, while their methodology is briefly described in Appendix 2.8.

Aydın and Kânoğlu's (2017) computational framework in MatLab is used to compute the maximum runup for a set of waveforms (Wronna et al., 2020). A subroutine that applies a waveform fitting to the initial conditions obtained using the half-space elastic theory (Mansinha and Smylie, 1971; Okada, 1985) is included. The fitting minimizes the differences of dimensional parameters $\tilde{h}_1$, $\tilde{h}_2$, $\tilde{x}_1$, $\tilde{x}_2$, $\tilde{c}_1$, and $\tilde{c}_2$ to the initial waveform parameters and uses an expression that allows considering both, LENs and LDNs. The expression is,

$$\tilde{\eta}_N(x,0) = \tilde{h}_1 \exp(-\tilde{c}_1(x - \tilde{x}_1)^2) - \tilde{h}_2 \exp(-\tilde{c}_2(x - \tilde{x}_2)^2), \tag{2.4}$$

here $\tilde{\eta}$ is the free surface elevation, $\tilde{h}_1$ and $\tilde{h}_2$ are the amplitudes of the wave profile, $\tilde{c}_1$ and $\tilde{c}_2$ are measures related to each amplitude's wavelength. $\tilde{x}_1$ and $\tilde{x}_2$ are the distances of $\tilde{h}_1$ and $\tilde{h}_2$ to the shore, respectively.

Since Aydın and Kânoğlu's (2017) solution requires dimensionless values, a procedure is implemented that obtains the dimensionless version of the fitted parameters for the maximum runup computation. After the subsequent runup computation, the dimensional runup following the dimensionless quantities proposed in Kânoğlu (2004) is obtained.

In Wronna et al. (2020) (section 4.2), the adapted code, including the subroutine, to compute the runup for a set of 210 initial waveforms has been used.

3. The sources of the 1761 and 1858 tsunamis - Contribution to characterization of the tsunami hazard in SW-Iberia

Complex geological systems and related natural hazards are challenging tasks in natural sciences. The tsunami hazard in Southwest Iberia is mainly characterized by events associated with the plate boundary between Africa and Eurasia. However, source zones with fault systems related to the stable continental regime may partially contribute to the local tsunami hazard.

One primary source of tsunami hazard is the segment of the plate boundary between Africa and Eurasia in the Northeast Atlantic. In the Southwest Iberian Margin (SWIM) the plate boundary is not clearly defined and hosted some of the historic transatlantic tsunami events. In the SWIM, large magnitude events are scarce thus making the tsunami hazard assessment a challenging task. On the other hand, historical events in the stable continental regime (SCR) associated with the Lower Tagus Valley (LTV) are also possibly tsunamigenic. Like the events in the SWIM, most of the stronger events in the LTV are of the pre-instrumental era.

Contrary to instrumental events, the exact location and rupture mechanism of the historical events are poorly understood. Especially in the SWIM, where deformation occurs slowly and stretches over large areas and, in the LTV, a source zone close to urban regions, a better understanding of the tsunami hazard is needed. Since recurrence rates of large magnitude events are low, a better understanding of each event ultimately leads to a better characterization of the seismic and tsunami hazard in the region.

3.1. Introduction to the geologic setting and past tsunamis in the NE Atlantic Ocean offshore Iberia

The plate boundary in the Northeast Atlantic Ocean between Africa and Eurasia extends from the Azores Triple Junction (ATJ) to the Gibraltar Arc. Here, the plate boundary can be subdivided into the ATJ, the Gloria Fault (GF) and the SWIM (c.f. Fig 3.1). Mid-oceanic rifting and active interplate deformation are the predominant geologic processes at the ATJ (Fernandes et al., 2006). The GF extends approximately 800 km from the Azores plateau and is an active transform fault between Eurasia and Africa (Laughton and Whitmarsh, 1974).

Two strong magnitude earthquakes with strike-slip rupture mechanism occurred in the last century in the area. The 8.3 magnitude event on November 25, 1941, located on the Gloria fault (Gutenberg and Richter, 1949; Baptista et al., 2016) and a 7.9 magnitude event on May 25, 1975 located 200 km south of the Gloria Fault (Lynnes and Ruff, 1985; Grimson and Chen, 1986; Buforn et al., 1988) (c.f. Fig. 3.2). Both events had predominant strike-slip rupture mechanisms. The rupture of the 1941 event is associated with the GF, (Baptista et al., 2016). However, the epicentre of the 1975 event has a perpendicular offset to the strike of the GF and locates about 200 km further south. Both events generated tsunamis registered at the tide gauges in Portugal, Spain, Morocco and UK (Debrach, 1946; Moreira, 1984; Baptista et al., 1992; Baptista and Miranda, 2009; Baptista, 2019). The Mw = 7.9, 1975 tsunami was reanalysed by Kaabouben et al. (2008) using tide gauge recordings suggesting the best fit the focal parameters presented by (Lynnes and Ruff, 1985).

In the SWIM, the diversity in focal mechanisms increases, the seismicity distributes over a large area, and the plate boundary is not clearly defined (Sartori et al., 1994; Torelli et al., 1997; Zitellini et al., 2009). Here, the collision between African and European continents at convergence rates of ~ 4 mm/yr (Argus et al., 1989; DeMets et al., 1994) and the westward propagation of the Gibraltar Arc at velocities of ~2 mm/yr according to Gutscher et al. (2012) and Duarte et al. (2013) define the predominant tectonic regime.

The most prominent and most devastating event for Europe with an estimated death toll of about 50000 (National Geophysical Data Center / World Data Service NGDC/WDS, 2019) the November 1, 1755, Lisbon earthquake and tsunami originated in the SWIM area. The magnitude of this event was estimated to be in the range of 8.5 ± 0.3 (Martínez Solares and Arroyo, 2004). People in large parts of Europe and Africa felt the shaking with the strongest intensities on the Iberian Peninsula. This event was studied and discussed extensively, and for the first time, Mitchell (1760) paced the way for modern seismology. Most recent studies locate the event

southwest offshore Iberia in the SWIM, but the geologic structure that caused an event of such magnitude is still under debate (Johnston, 1996; Baptista et al., 1998b; Zitellini et al., 1999; Gràcia et al., 2003; Terrinha et al., 2003). Nevertheless, many studies in the last decades (c.f. Baptista et al., 1998a, b; Gutscher et al., 2006; Barkan et al., 2009; Baptista et al., 2011; Udías, 2019) contributed to constrain the source relatively well for a historical event. In fact, the dimensions of most known faults in the SWIM are not sufficient to cause an 8.5 ± 0.3 magnitude earthquake and generate a tsunami of such size. Consequently, some studies proposed the rupture of multiple sources for the 1755 event (Zitellini et al., 2001; Gràcia et al., 2003; Ribeiro et al., 2006; Terrinha et al., 2009).

In addition to the great Lisbon earthquake, historical reports of tsunamigenic events date back to 60 BC (Mendonça, 1758), and geological evidence was found back to 7000 BP (Lario et al., 2011). Luque et al. (2001, 2002) identified three tsunamigenic deposits and suggested an average recurrence rate of about 2000 years for consecutive events of this order of magnitude. Other prominent events in the area are the December 27, 1722, Tavira tsunami and the March 31, 1761, North Atlantic tsunami. The only instrumental tsunami event in the SWIM was the February 28, 1969 Horseshoe tsunami generated by a magnitude 7.9 earthquake in the Horseshoe abyssal plane (Fukao, 1973) (see Baptista, 2019 for details on these events). The tsunami reached the coast in Portugal about 30 minutes after the earthquake at low tide and had the maximum amplitude recorded at the tide station in Casablanca with 0.6 m (Baptista and Miranda, 2009).

According to the Portuguese tsunami catalogue (Baptista and Miranda, 2009) seven events had an estimated magnitude larger than 7.5, and four had an estimated magnitude larger than 8. Regarding the events with a magnitude > 7.5, three had their generating source in the SWIM, one originated at the GF. Some tsunamigenic events occurred in the Azores archipelago, however they were registered only locally. On the other hand, the tsunamis generated in the SWIM and the GF were registered in large parts of the NE Atlantic. Four tsunami events close to the continent are of local character, three of them caused tsunamis in Tagus estuary. In summary, the strongest earthquakes occurred in the SWIM and GF domain. with the most powerful tsunamis generated in the SWIM because of the dominant compressive structures. Numerous geophysical campaigns identified subsurface geological features that are possibly the sources for some of the events (e.g. ARRIFANO 1992, BIGSETS 1998, SISMAR 2001, SWIM 2009, NEAREST 2010). The most prominent tectonic structures are discussed in chapter 3.2.

Matias et al. (2013) presented a fault and recurrence model for tsunamigenic earthquakes in the SWIM based on earlier computed fault slip rates (Cunha et al., 2012) and showed that their

model is consistent with kinematic plate models. They assess recurrence rates of about 3.6 and 10 kyr for single fault rupture events for events of Mw = 8.0 and Mw ~ 8.7, respectively. For multiple source ruptures due to the proximity of the single structures, the recurrence periods reduce to 0.7 and 3.5 kyr or less. Omira et al. (2015), in the subsequent PTHA for the North-East Atlantic, conclude for a probability of 60% that the maximum tsunami wave height exceeds 1m considering a 100-year return period in some coastal locations and a probability of 50% that the maximum tsunami wave height exceeds 5m considering a 500-year return period, especially in the Gulf of Cadiz. Omira et al. (2015) point out that the coastal areas in the South of Portugal, Southwest of Spain and Northwest of Morocco are the most prone areas to tsunami hazard in the North-East Atlantic. The historical events and the numerous geophysical campaigns underline the structural and seismic complexity in SW-Iberia and alert for future strong magnitude events, albeit the proposed long recurrence rates.

However, as stated earlier recurrence models, DTHA and PTHA, depend crucially on the completeness and quality of earthquake and tsunami catalogues. Considering the Portuguese tsunami catalogue (Baptista and Miranda, 2009) in the SWIM, the important strong magnitude event, the March 31, 1761, transatlantic tsunami remains poorly understood, and the overall seismic and tsunami hazard may be underestimated. Earlier studies assessed the source area for the event (Baptista et al., 2006) but did not present a fault location and associated rupture mechanism. In section 3.2 (Wronna et al., 2019a) a candidate geological source of the 1761 earthquake and transatlantic tsunami is investigated.

Nevertheless, it is crucial to understand the local events because of their proximity to the shore, urban areas and little time for coastal communities to seek shelter. The November 11, 1858 earthquake is another poorly understood earthquake that was possibly tsunamigenic. It ruined large parts of the city and was felt all over Portugal and large parts of the Iberian Peninsula. This earthquake was the most significant event in the 19th century in Portugal (Pereira de Sousa, 1916, 1928). Quintas (1993) provides a description of the river Sado invading Setúbal after the earthquake, causing some boats to sink and leaving some on dry land. This event is not included in the Portuguese tsunami catalogue (Baptista and Miranda, 2009). In section 3.3 (Wronna et al., 2021), macro-seismic analysis is used to reanalyze the earthquake and present possible rupture sources. Subsequently numerical tsunami modelling is applied to evaluate the tsunamigenic potential of an 1858 like event.

3.2. Reanalysis of the 1761 transatlantic tsunami

3.2.1. Abstract

The segment of the Africa–Eurasia plate boundary between the Gloria Fault and the Strait of Gibraltar has been the setting of significant tsunamigenic earthquakes. However, their precise location and rupture mechanism remain poorly understood. The investigation of each event contributes to a better understanding of the structure of this diffuse plate boundary and ultimately leads to a better evaluation of the seismic and tsunami hazard. The 31 March 1761 event is one of the few known transatlantic tsunamis. Macroseismic data and tsunami travel times were used in previous studies to assess its source area. However, no one discussed the geological source of this event. In this study, we present a reappraisal of tsunami data to show that the observations data set is compatible with a geological source close to Coral Patch and Ampere seamounts. We constrain the rupture mechanism with plate kinematics and the tectonic setting of the area. This study favours the hypothesis that the 1761 event occurred in the southwest of the likely location of the 1 November 1755 earthquake in a slow deforming compressive regime driven by the dextral transpressive collision between Africa and Eurasia.

3.2.2. Introduction

The coast along the southwest Iberian margin is prone to earthquakes and tsunamis. The earthquake and tsunami catalogues for the Iberian Peninsula and Morocco report three tsunamigenic earthquakes in the 18th century: 1722, 1755 and 1761 (Mezcua and Martínez Solares, 1983; Oliveira, 1986; Baptista and Miranda, 2009). While the 1722 event is believed to be a local event (Baptista et al., 2007), the 1 November 1755 and the 31 March 1761 earthquakes generated transatlantic tsunamis (Baptista et al., 1998a, b, 2003, 2006; Barkan et al., 2009). The source of the 1755 event has been extensively studied in recent years, e.g. by Baptista et al. (1998a, b), Zitellini et al. (2001), Gutscher et al. (2006) and Barkan et al. (2009).

On the contrary, the tectonic source of 31 March 1761 remains poorly understood. The seismic catalogues present different earthquake locations: 10.00 W, 37.00 N (Mezcua and Martínez Solares, 1983) or 10.50 W, 36.00 N (Oliveira, 1986) (Figs. 3.1 and 3.2). Baptista et al. (2006), used macroseismic intensity data and tsunami travel time observations to locate the source circa

13.00 W, 34.50 N and estimated the magnitude in 8.5. The source location obtained by Baptista et al. (2006) places the 1761 event southwest of the Southwest Iberian Margin (SWIM) in the outer part of the Gulf of Cadiz (Fig. 3.1). The plate boundary between Eurasia and Africa is not well defined in the SWIM area, as the deformation is distributed over a large area. Here, a complex system of faults accommodates the stress driven by the present-day tectonic regime that is constrained by NW–SE plate convergence between Africa and Eurasia at ~ 4 mm year^{-1} (Argus et al., 1989; DeMets et al., 1994) and by the westward migration of the Cadiz Subduction slab ~ 2 mm year^{-1} (Gutscher et al., 2012; Duarte et al., 2013).

The SWIM is dominated by large NE–SW-trending structures limiting the Horseshoe Abyssal Plain (HAP) (Fig. 3.1). The NE–SW-striking structures are the Coral Patch Fault (CPF) (Martínez-Loriente et al., 2013), the Gorringe Bank Fault (GBF) (Zitellini et al., 2009; Jiménez-Munt et al., 2010; Sallarès et al., 2013; Martínez-Loriente et al., 2014), the Horseshoe Fault (HSF) (Gràcia et al., 2003; Zitellini et al., 2004; Martínez-Loriente et al., 2018) and the Marques de Pombal Fault (MPF) (Gràcia et al., 2003; Terrinha et al., 2003; Zitellini et al., 2004) (Fig. 3.1). Other identified NE–SW trending structures are the São Vicente Fault (SVF) (Gràcia et al., 2003; Zitellini et al., 2004), the Horseshoe Abyssal Plain Thrust (HAT) (Martínez-Loriente et al., 2014) and to the south of the CPF, the Seine Hills (SH) (Martínez-Loriente et al., 2013) (Fig. 3.1).

Large WNW–ESE-trending dextral strike-slip faults (the northern WNW–ESE-trending lineament, LN, and the southern WNW–ESE-trending lineament, LS) further characterize the SWIM cutting through the Gulf of Cadiz to the HAP (Zitellini et al., 2009; Terrinha et al., 2009; Rosas et al., 2009) (Fig. 3.1). To the south, the igneous Ampere and Coral Patch seamounts limit the HAP.

In this study, we investigate the geological source of the 1761 transatlantic tsunami. To do this, we start with a reappraisal of previous research, we analyse the tectonic setting of the area and propose a source compatible with plate kinematics. From this source, we compute the initial sea surface displacement. To propagate the tsunami, we build a bathymetric data set based on GEBCO (2014) data to compute wave heights offshore of the observation points presented in Table 3.1. We also compute inundation using high resolution digital elevations models comprising topography and bathymetry in Lisbon and Cadiz to compare the results with the observations. Finally, we use Cadiz and Lisbon observations in 1755 and 1761 to compare the sizes of the events.

3.2.3. Geodynamic context

The plate boundary between Africa and Eurasia in the NE Atlantic Ocean, the Azores – Gibraltar fracture zone (AGFZ), extends from the Azores Triple Junction (ATJ) to the Gibraltar Arc. The main features of the AGFZ are the ATJ; the Gloria Fault (GF) and the SWIM (Fig. 3.1). At the ATJ, active interplate deformation defines the plate boundary (Fernandes et al., 2006). The GF is a large W–E-striking strike-slip fault with scarce seismicity (Laughton and Whitmarsh, 1974) with a strong Mw D 8.3 event on 25 November 1941 (Gutenberg and Richter, 1949; Moreira, 1984; Baptista et al., 2016) (Fig. 3.2). The Gloria Fault defines a sharp boundary between Eurasia and Africa (Laughton and Whitmarsh, 1974). Further east, towards the Gulf of Cadiz, in the plate boundary is not clearly defined (Torelli et al., 1997; Zitellini et al., 2009). Largescale dynamics are imposed by convergence between Africa and Eurasia and by the westward propagation of the Gibraltar Arc. Most recent studies agree that the source of the 1755 Lisbon earthquake with a magnitude of about 8.5±0.3 is in the SWIM (Johnston, 1996; Baptista et al., 1998b; Zitellini et al., 1999; Gutscher et al., 2002; Martínez Solares and Arroyo, 2004; Ribeiro et al., 2006).

In the SWIM, two main sets of faults have been identified: large NE-SW trending thrust faults and WNW-ESE trending dextral strike-slip faults.

Thrust faults include large NE–SW-trending structures, namely the Horseshoe Fault (HSF) (Gràcia et al., 2003; Zitellini et al., 2004; Terrinha et al., 2009; Martínez-Loriente et al., 2018), the Marquês de Pombal Fault (MPF) (Gràcia et al., 2003; Terrinha et al., 2003; Zitellini et al., 2004), the Gorringe Bank Fault (GBF) (Zitellini et al., 2009; Jiménez-Munt et al., 2010; Sallarès et al., 2013; Martínez-Loriente et al., 2014) and the Coral Patch Fault (CPF) (Martínez-Loriente et al., 2013) (Fig. 3.1). The GBF and the CPF bound the Horseshoe Abyssal Plain (HAP). The NE–SW-striking thrusts are deep-rooted faults accompanied by morphological seafloor signatures. Moderate- and low-magnitude events (M<5) characterise the seismicity of the area. These faults lie between the Gorringe Bank and the Strait of Gibraltar (Custódio et al., 2015). South of the HAP the Coral Patch ridge was identified to have a northern and a southern segment (Martínez-Loriente et al., 2013).
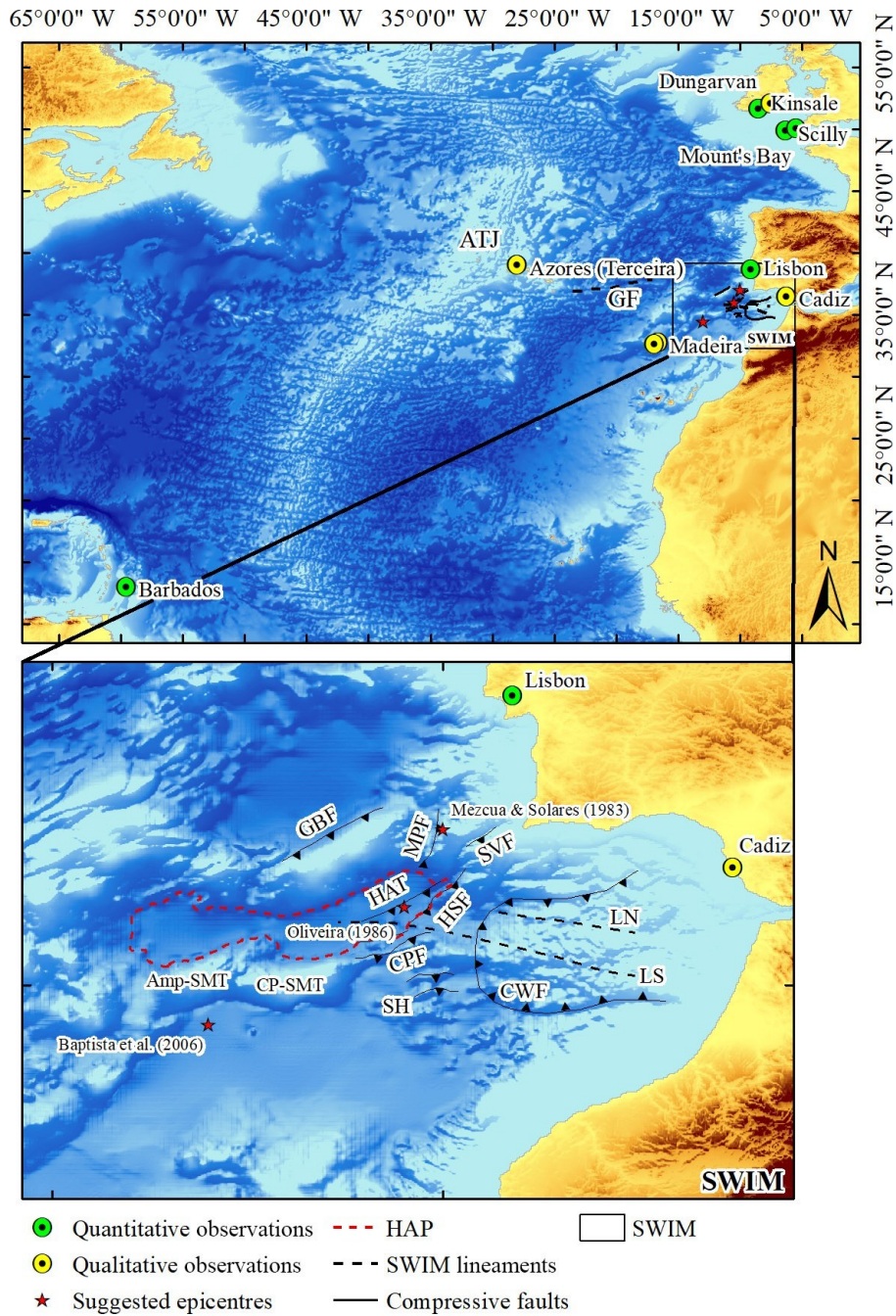
Figure 3.1 The red stars plot the source location by Oliveira (1986), Mezcua and Martínez Solares (1983) and Baptista et al. (2006). The green circles depict the quantitative tsunami observation points, and the yellow circles show the locations of the qualitative descriptions of the tsunami in 1761. The main features of the Azores Gibraltar fracture zone are the Azores Triple Junction (ATJ), the Gloria Fault (GF) and the Southwest Iberian Margin (SWIM). The inset shows the position of the Ampere seamount (Amp-SMT), the Coral Patch Seamount (CP-SMT) and the locations of the known faults. The black lines mark the faults, and the triangles indicate the direction of dip. The dashed black lines trace the main strike-slip faults. The known thrust faults are the Coral Patch Fault (CPF), the Cadiz Wedge Fault (CWF), the Gorringe Bank Fault (GBF), the Horseshoe Fault (HSF), the Marques de Pombal Fault (MPF), the Seine Hills (SH) and the São Vicente Fault (SVF). The shown strike-slip faults are the SWIM lineaments (LN) and (LS) and the Gloria Fault (GF). The dashed red line limits the Horseshoe Abyssal Plain (HAP).

32

Table 3.1 Summary of the available data of the 1761 tsunami at the time. The column TTT lists the observed tsunami travel times. The column polarity indicates the first movement of the sea upward (U) or downward (D).

Location	Long. (°)	Lat. (°)	Local time	TTT (h)	Wave height (m)	Polarity	Period (min)	Duration	Source
Lisbon	−9.13	38.72	13:15	1.25	1.2–1.8	–	6	Lasted until night	Unknown (1761) Molloy (1761); Borlase (1762)
Cadiz	−6.29	36.52	–	–	–	D	– –		Journal des Matieres du Temps (1773)
Kinsale	−8.51	51.67	18:00	6	0.6	U	4	Repeated several times	Annual Register (1761); Borlase (1762)
Isles of Scilly	−6.38	49.92	17:00	5	0.6–1.2	U	–	>2h	Borlase (1762)
Mount's Bay	−5.48	50.08	17:00	5	1.2–1.8	U	12	1h	Borlase (1762)
Dungarvan	−7.48	51.95	16:00	4	–	–	–	5h	Borlase (1762)
Barbados	−59.57	13.03	16:00	7–8	0.45–0.6	–	8	4h but lasted until 6 in the morning.	Mason (1761); Annual Register (1761)
	−59.57	13.03			0.6	–	3–6	Increased again at 10 for short time then de-creased.	Borlase (1762)
Madeira	−16.91	32.62	–	–	~ 1; higher in the east	–	–	Lasted longer in the east than in the south.	Heberden (1761)
Azores	−27.22	38.65	–	–	Large	U	Some min.	3h	Fearns (1761)

Other smaller NE–SW-trending structures are the São Vicente Fault (SVF) (Gràcia et al., 2003; Zitellini et al., 2004), the Horseshoe Abyssal Plain Thrust (HAT) (Martínez-Loriente et al., 2014) and to the south of the CPF, the Seine Hills (SH) (Martínez-Loriente et al., 2013) (Fig. 3.1).

The SWIM lineaments (LN and LS) (Fig. 3.1) have been interpreted as the present-day boundary between the Eurasian and African plates (Zitellini et al., 2009). They are large WNW–ESE trending dextral strike-slip faults with lengths of ~ 130 and 180 km for the LN and LS respectively. OBS monitoring captured numerous moderate-magnitude seismic events (Mw 3–5) at the intersection of the SWIM faults and NE–SW-striking thrusts (Geissler et al., 2010; Silva et al., 2017). Ocean floor morphological signatures like en echelon folds and sets of undulations suggest the quaternary reactivation of the deep-rooted basement faults (Terrinha et al., 2009; Rosas et al., 2009). Terrinha et al. (2009) propose that the present-day deformation in the SWIM

is accommodated by strain partitioning of dextral wrenching along the SWIM lineaments and thrusting along the NE–SW faults in the Gulf of Cadiz and the HAP. Bartolome et al. (2012) attributes the SWIM faults with the capacity to trigger Mw > 8.0 earthquakes.
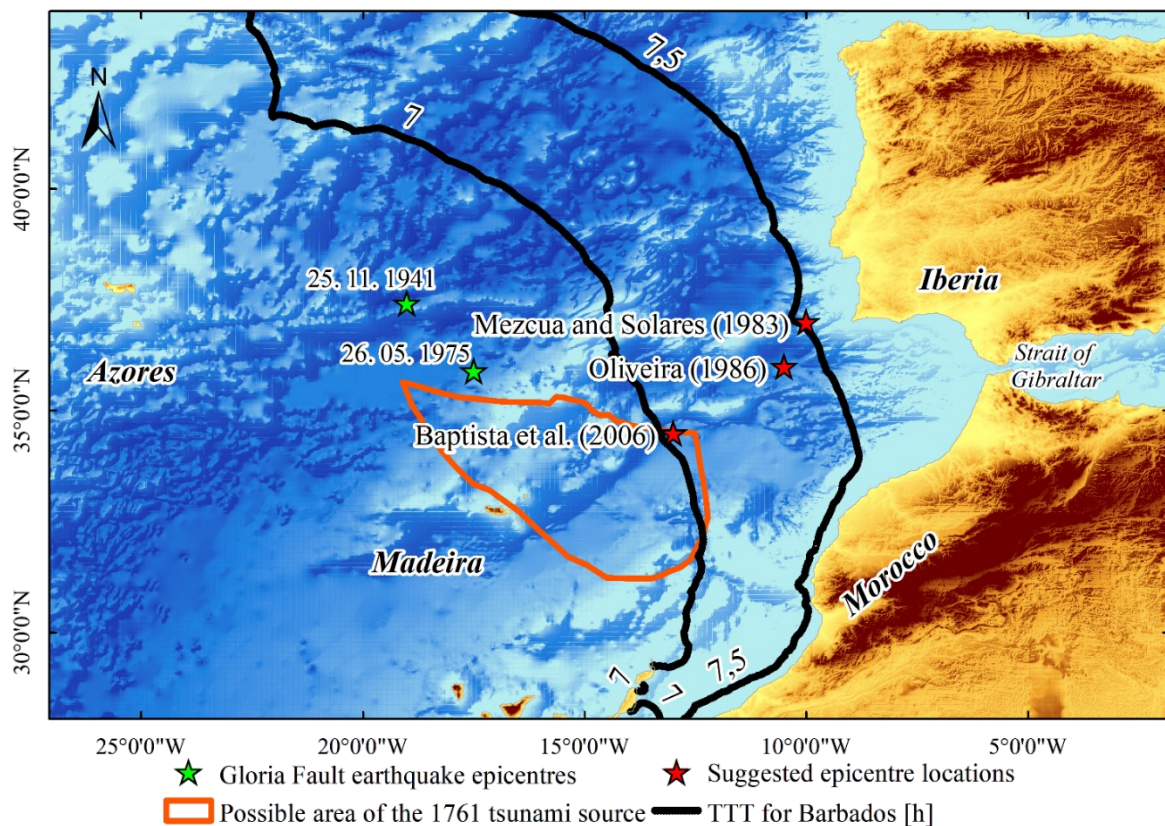
Figure 3.2 The red stars show the proposed source locations for the 1761 earthquake. The green stars present the epicentres of the two high magnitude events in the Gloria Fault zone, and the black lines show the backward ray-tracing contours for the tsunami travel time (TTT) of 7–7.5h to Barbados. The limited orange area defines the results obtained using macroseismic analysis combined with backward ray tracing but discarding the TTT for Barbados by Baptista et al. (2006).

Considering the tectonic structures known today, the CPF is a large-scale fault located closest to the source area of the 1761 event suggested by Baptista et al. (2006). This area, located southwest of the SWIM faults, is in a slow deforming compressive regime driven by the dextral transpressive collision between Africa and Eurasia. Hayward et al. (1999) showed the existence of widespread compressive structures in this region (Coral Patch and Ampere seamounts) based on shallow seismic reflection and side scan sonar data (Figs. 3.1 and 3.3). The tectonic deformation uplifted the oceanic crust, showing the pervasive original NE–SW-striking oceanic fabric formed during oceanic rifting (Hayward et al., 1999; Zitellini et al., 2009). The IGN seismic catalogues list a 6.2 magnitude around the Coral Patch on 11 July 1915 (Instituto Geográfico Nacional, 2018).
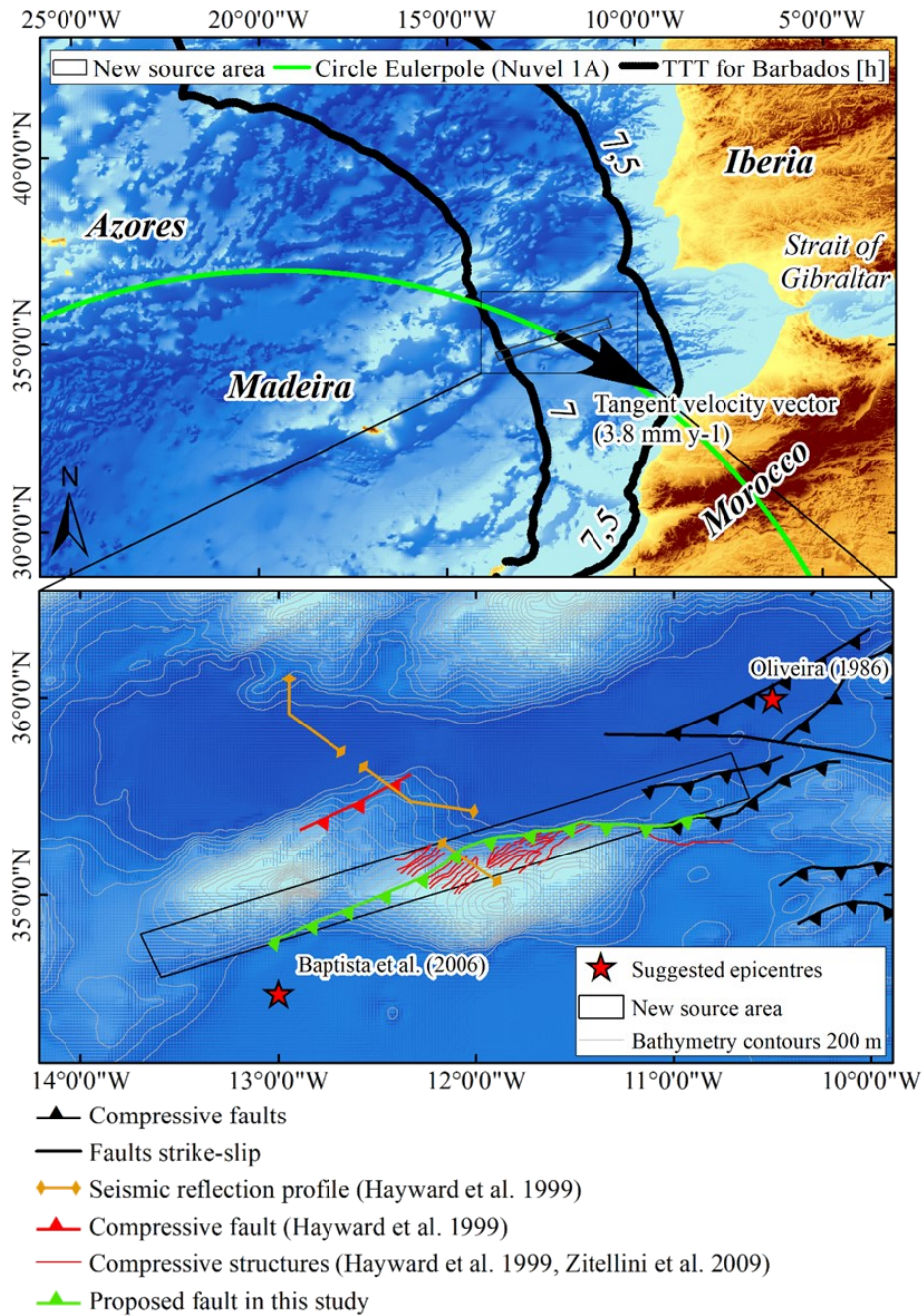
Figure 3.3 A circle around the Euler pole at the proposed possible source location. The model Nuvel 1A (DeMets et al., 1994 and DeMets and Dixon 1999) computes a 3.8 mm year-1 convergence. We plot the tangent velocity vector close to the candidate source. The black lines depict the backward ray-tracing contours in hours, for a tsunami travel time (TTT) of 7–7.5 h to Barbados. In the inset, the black lines plot the thrust and strike-slip faults. The red lines depict the faults and structures proposed in Hayward et al. (1999). The orange lines show the location of the seismic profiles for the areas of the Coral Patch and Ampere seamounts (Hayward et al., 1999). The green line identifies the proposed tectonic structure used in this study. The red stars are the locations of the closest proposed epicentres (Baptista et al., 2006; Oliveira, 1986).

Kinematic plate models (Argus et al., 1989; DeMets and Dixon, 1999; Nocquet and Calais, 2004; Fernandes et al., 2007) predict low convergence rates 3–5 mm year^{-1} between African plates and Eurasia. We used the global kinematic plate model Nuvel-1A. This model is a recalibrated version of the precursor model Nuvel-1 that implements rigid plates and data from plate boundaries such as spreading rates, transform fault azimuths and earthquake slip vectors

35

(DeMets et al., 1990). The NUVEL 1A model predicts a relatively conservative convergence rate of 3.8 mm year^{-1} in the area close to the source area determined by Baptista et al. (2006) for the 1761 tsunami (Fig. 3.2).

Consequently, we propose a fault extending from the western segment of the CPF towards the epicentre proposed by Baptista et al. (2006). We draw the circle around the Euler pole at -20.61° W, 21.03° N according to the plate kinematic model Nuvel 1-A using Mirone suite (Luis, 2007). To do this, we choose Africa as the fixed plate and Eurasia as the moving plate and draw the circle at the centre of the fault in Fig. 3.3. We compute the convergence rate (3.8 mm year^{-1}) and plot the tangent velocity vector along the circle (Fig. 3.3). For this fault, we test different earthquake fault parameters (Table 3.2) and compute the coseismic deformation using the Mansinha and Smylie equations (Mansinha and Smylie, 1971) implemented in the Mirone suite (Luis, 2007). We assume that the initial sea surface elevation mimics the sea bottom deformation and we use it to initiate the tsunami propagation model.

Table 3.2 The fault dimensions and parameters used herein investigate candidate sources of the 1761 event. We describe hypotheses (Hyp.) A-MS, A and B by the fault parameters length (L), width (W), strike, dip, rake, slip and depth. The slip values for hypothesis A-MS are listed for each segment from west to east. Additionally, we present the moment magnitude (Mag.), the assumed shear modulus (μ) and the focal mechanism.

Scenario	L (km)	W (km)	Strike (°)	Dip (°)	Rake (°)	Slip (m)	Depth (km)	Mag.	μ (Pa)	Focal mechanism
Hyp. A-MS	4×50	50	76	40	135	7/15/15/8	10	8.4	4×10^{10}	
Hyp. A	200	50	76	40	135	11	10	8.4	4×10^{10}	
Hyp. B	280	50	254.5	70	45	15	10	8.5	4×10^{10}	

3.2.4. Reassessment of historical data on the 1761 tsunami

Baptista et al. (2006) and Baptista and Miranda (2009) present most of the tsunami observations used herein. Here, we focus on the observations of wave heights, periods, inundation and duration of the sea disturbance that we summarise in Table 3.1. We only reassess the observations in Barbados and Cadiz.

3.2.4.1. *Barbados*

Baptista et al. (2006) discarded the arrival time observation in Barbados. However, we find that this is compatible with the source location. The observations report the tsunami arrival at 16:00 local time (Mason, 1761; Annual Register, 1761; Borlase, 1762). If we use a solar time difference between Lisbon and Barbados of 3.5 h, as in Baptista et al. (1998a, b), we conclude a

tsunami travel time of 7–7.5 h. To validate this TTT (tsunami travel time), we did a backward ray-tracing simulation with a point source in Barbados (see Figs. 3.2 and 3.3) and we find that the TTT is compatible with the source area.

3.2.4.2. *Cadiz*

The Journal des Matiéres du Temps (Journal Historique, 1773) describes the occurrence of an earthquake in April 1773 and compares it with the 31 March 1761 event. The report concludes that no tsunami was observed in 1773 and suggests a withdraw of the sea after the 31 March 1761 earthquake in the city; however, there are no accounts of inundation, neither for the city nor for the causeway. We include this observation to constrain the proposed source better. Table 3.1 presents a summary of all historical data relevant to the tsunami simulation. Figure 3.1 shows the locations of the tsunami observations. Wave heights always refer to the maximum positive amplitude above the still water level.

3.2.5. Tsunami simulations

3.2.5.1. *The numerical model*

We used the code NSWING (Non-linear Shallow Water model wIth Nested Grids) for numerical tsunami modelling. The code solves linear and non-linear shallow water equations (SWEs) in a Cartesian or spherical reference frame using a system of nested grids and a moving boundary condition to track the shoreline motion based on COMCOT (Cornell Multi-grid Coupled Tsunami Model; Liu et al., 1995, 1998). The code was benchmarked with the analytical tests presented by Synolakis et al. (2008) and tested in Miranda et al. (2014) and Baptista et al. (2016), Wronna et al. (2015) and Omira et al. (2015).

For Cadiz and Lisbon only, where high-resolution bathymetric data were available, we employed a set of coupled nested grids with a final resolution of 25m to compute inundation. We compute a new bathymetric data set using the nautical charts close to the coast or lidar data to build a digital elevation model to compute inundation in Lisbon and Cadiz. Close to the tsunami source we interpolate bathymetry data (GEBCO, 2014) to obtain a 1600m grid cell size. We apply a refinement factor of 4 for the four nested grids. Consequently, the intermediate grids have a resolution of 100m and 400m respectively. In Cadiz, we use the soundings and coastline of historical nautical charts from the 18th century (Bellin, 1762; Rocque, 1762) to compute a palaeo digital elevation model (PDEM) (Wronna et al., 2017). To do this, we georeferenced the

old nautical charts and used the modern-day DEM (UG-ICN, 2009) to implement the information from the historical charts. According to Wronna et al. (2017), we systematically remodelled bathymetry and the coastline. To initiate the tsunami propagation model, we compute the coseismic deformation according to the half-space elastic theory (Mansinha and Smylie, 1971) implemented in the Mirone suite (Luis, 2007). Assuming that water is an incompressible fluid, we translate the sea bottom deformation to the initial sea surface deformation and set the velocity field to zero for the time instant t = 0 s. We run the model for 10 h propagation time to ensure that the tsunami reaches all observation points, with the bathymetric model referenced to mean sea level. We compute the offshore wave heights for points located close to the observation points (Fig. 3.1) using virtual tide gauges (VTGs). We include the coordinates and depths of the VTGs in Tables 3.3 and 3.4 in Sect. 3.2.6. For transatlantic propagation, we consider the Coriolis effect in the tsunami simulation. We checked all tsunami simulations against historical data.

For the locations in Ireland, the United Kingdom, the Azores, Madeira and Barbados, we estimate the wave heights near the shore using Green's law (Green, 1838), following Hébert and Schindelé (2015) and Davies et al. (2018). Hébert and Schindelé (2015) concluded that the extrapolation for depths between 10 and 1m generally allowed for a good fit with the observations for the 2004 Indian Ocean tsunami. Green's law is based on the linear shallow water wave equations and allows us to quickly approximate the amplification of wave heights at a shallower depth close to the shore when considering a plane beach. The wave height increases to the fourth root of the ratio between the depth at the shore and the water depth at the VTG. We extrapolate the maximum wave height values between the depths of the VTGs (Tables 3.3 and 3.4) to points located at 5m depth.

$$h_s = \sqrt[4]{\frac{d_s}{d_d}} * h_d \qquad\qquad \text{Eq. (3.1)}$$

where hs and hd are the wave heights at the shore and the VTGs, and ds and dd are the depths at the shore and the VTGs. We use a constant value of 5 m, which is sufficiently close to the shore to be observed by eyewitnesses. The results of the approximation according to Green's law are presented in Tables 3.3 and 3.4.

3.2.5.2.   *Testing the hypothesis*

In the 20th century, two high-magnitude earthquakes occurred in the Gloria Fault (GF) area. Because of this, we tested the compatibility of the tsunami observations in 1761 with the tsunamis produced by the earthquakes of the 25 November 1941 (Lynnes and Ruff, 1985; Baptista

et al., 2016) and 26 May 1975 (Kaabouben et al., 2009, Fig. 3.2). We use the fault plane parameters and rupture mechanism presented in Baptista et al. (2016) and Kaabouben et al. (2008) for the 1941 and 1975 events respectively. The fault dimensions and slip were made compatible with an 8.5 magnitude event using the scaling laws proposed by Wells and Coppersmith (1994), Manighetti et al. (2007), Blaser et al. (2010) and Matias et al. (2013).

These two events produce less than a 1m wave height in the north-east Atlantic and a barely observed wave in the Caribbean islands (Baptista et al., 2016, 2017). Moreover, the epicentres of the 25 November 1941 and 26 May 1975 events are located outside the area determined by Baptista et al. (2006). As expected, the TTTs do not agree with those reported in 1761; therefore, we excluded the GF as a candidate source for the 1761 event and do not consider their results for discussion.

The candidate fault area is centred at 12.00 W, 35.00 N to the west of the large NE–SW-striking compressive structures (Martínez-Loriente et al., 2013) and 85 km northeast of the epicentre suggested by Baptista et al. (2006) (Fig. 3.3). We considered the fact that the historical accounts indicate an earthquake and tsunami less violent than in 1755. To account for this, we used the fault dimensions presented in Table 3.2 corresponding to a magnitude 8.4–8.5 earthquake (Baptista et al., 2006); consequently, the wave heights in Lisbon and Cadiz are smaller than those observed in the 1755 tsunami (Baptista et al., 1998a). The fault dimensions (length and width) presented in Table 3.2 are compatible with the scaling laws of Wells and Coppersmith (1994), Manighetti et al. (2007), Blaser et al. (2010) and Matias et al. (2013).

3.2.5.1.1. Hypotheses A and A-MS

Here we use a strike angle compatible with the study by Martínez-Loriente et al. (2013), which follows the morphology of the Coral Patch scarp and seamount (Figs. 3.1 and 3.3). To take into account the tectonic regime of the source area we choose fault plane parameters compatible with a structure of compressive nature. The velocity vector predicted by NUVEL 1A (Fig. 3.3), together with the short tsunami wave periods (4–12 min) reported in 1761 (Table 3.1), are in line with the chosen dip angle of 40° (Table 3.2). On the other hand, Martínez-Loriente et al. (2013) suggest for the Coral Patch Fault dip angles of 30±5° and a rake angle of 90°. These authors also conclude that the fault root is between 7 and 13 km depth. We approximate the rake angle according to the difference between the convergence arrow given by the circle around the Euler Pole and the fault plane (Fig. 3.3).

The wave period in Lisbon produced by this candidate source is 30 min. This value is not compatible with the observations (Table 3.1). By trying to solve this problem, we implemented a

multi-segment fault here called A-MS. This multi-segment solution consists of four segments, each of which are 50 km. The four segments are placed adjacent to each other, and the rupture mechanism is equal for each segment as in hypothesis A with a mean slip of 11m (Table 2). To investigate the slip distribution, we tested three setups: (1) maximum slip towards the SW, (2) maximum slip towards the NE and (3) maximum slip close to the centre of the fault. In the first setup, the observed withdrawal of the sea in Cadiz is less evident and produces little inundation in Lisbon; in the second setup there is inundation at Cadiz, which is not supported by historical data. All these results led us to select the maximum slip at the centre of the fault. The slip of each segment is presented in Table 3.2. The synthetic waveforms are presented in Fig. 3.5 and discussed in Sects. 3.2.6 and 3.2.7.

3.2.5.1.2.   Hypothesis B

Finally, we test an alternative hypothesis here, called B, which has a larger strike-slip component compared to hypothesis A. This also results in a larger fault length and a steeper dip angle. Here, we consider a rupture along a fault plane rotated about 180 when compared to hypothesis A. To do this, we selected compatible strike and rake angles that result in a sinistral inverse lateral rupture (Table 3.2). The implementation of the different setups of slip distribution in solution B does not improve the quality of the results; therefore, we only consider a single segment fault for this hypothesis. The synthetic waveforms are presented in Fig. 3.7 and discussed in Sects. 3.2.6 and 3.2.7.

3.2.6.   Results

We present the results of hypotheses A-MS and B. Hypothesis A-MS has a more significant inverse component compared to hypothesis B. Once the results of hypotheses A and A-MS produce same wave height values, but the latter produces shorter periods, we opt to present the results for hypothesis A-MS. Figures 3.4–3.7 show the maximum wave height and the synthetic tsunami at the virtual tide gauges (VTGs) computed offshore of each observation point of hypothesis A-MS and B. Tables 3.3 and 3.4 summarise these results. The wave height, as mentioned in Sect. 3.2.4, represents the maximum positive amplitude above the still water level, which is set to mean sea level in the tsunami simulation. Tables 3.3 and 3.4 present the geographical coordinates and depths of the VTGs. To compare the synthetic wave heights with the observations for the locations in Mount's Bay, Isles of Scilly, Kinsale, Dungarvan, Azores, Madeira and Barbados, we used Green's law (Green, 1838) to extrapolate the wave height values for the maximum wave between the depths of the VTGs to points located at 5m depth. For

Lisbon and Cadiz, where high-resolution bathymetry is available, we used two sets of nested grids and computed the tsunami inundation. Here the VTGs are located close to the shore, and the application of Green's law is not necessary.

3.2.6.1. Hypothesis A-MS

Figures 3.4 and 3.5 show the distribution of the maximum wave height and the respective synthetic tsunami records for hypothesis A-MS.
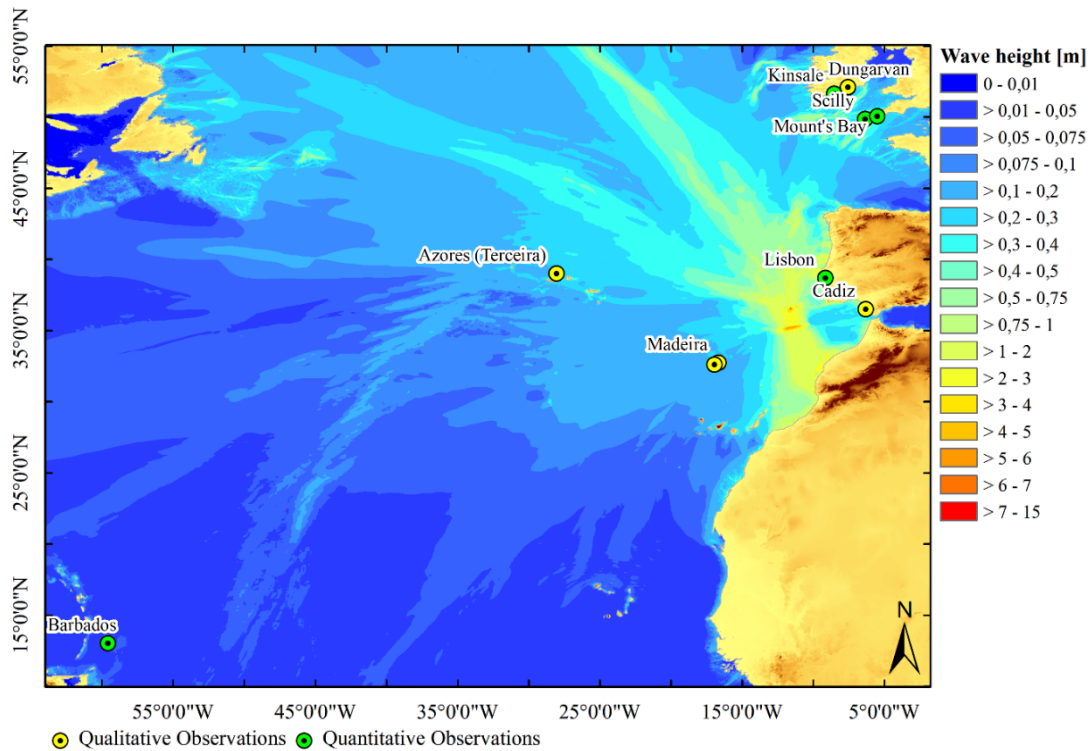
Figure 3.4 Maximum wave height distribution (colour scale in metres) in the Atlantic basin produced by the source of hypothesis A-MS.

The analysis of Fig. 3.4 shows wave heights exceeding 4 m in the Gulf of Cadiz. At some points along the coast of Morocco maximum wave heights are about 5 m. In Great Britain, at the Isles of Scilly and Mount's Bay, maximum wave heights vary between 1.7 and 1.9 m. Along the south coast of Ireland, in Kinsale and Dungarvan, the tsunami simulation predicts a 1m maximum wave height. At the eastern coast of the island of Madeira, the wave heights reach 1 m, whereas on the southern part of the island the wave heights are smaller. At the Azores, close to Terceira, wave heights are slightly higher than 2.5 m along the south coast of the island. The wave heights in the south of Barbados reach 0.5 m.

In Lisbon, the synthetic waveform shows a first peak of 1.4 m with a maximum value close to 1.8 m for the third wave, after 2 h and 20 min of tsunami propagation. The TTT to Lisbon is 1 h and 10 min and the first wave has a period of 20–25 min (Table 3.3 and Fig. 3.5a). In Cadiz,

the synthetic tsunami waveform shows a drawdown 1 h after the earthquake with a negative amplitude of 0.6m and a maximum wave height of 2.4 m (Table 3.3 and Fig. 3.5a).

The Isles of Scilly synthetic tsunami waveform shows a TTT of 4 h and a maximum peak exceeding 0.4 m with 15 min period. In Mount's Bay, TTT is 4 h and 30 min and the maximum wave height is 0.5 m with a 15 min period. In Kinsale, the tsunami model computes a TTT of 4 h and 15 min. The maximum wave height there is about 0.5 m with a period shorter than 15 min. In Dungarvan, the tsunami arrives 5 h after the earthquake. All VTGs in northern Europe recorded the first wave as the leading elevation wave (Fig. 3.5b, c).
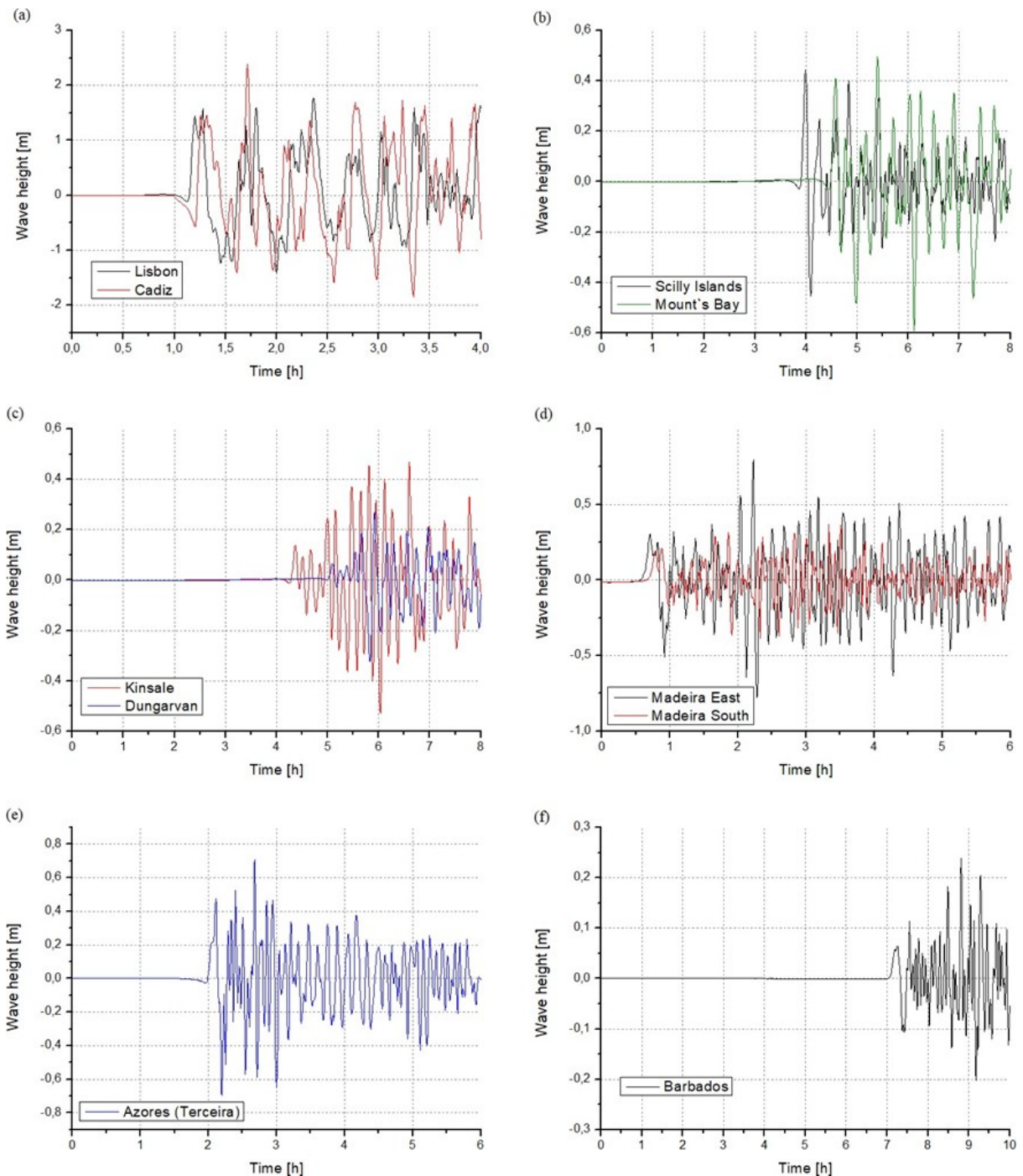
Figure 3.5 VTG records for hypothesis A-MS at the coordinates of the locations presented in table 3.3.

In Madeira, hypothesis A-MS produces maximum wave heights at the VTG of 0.8 m in the eastern part of the island and about 0.4 m in the southern part; the TTT to the east and southern coast of the island is half an hour and 40 min respectively (Fig. 3.5d). In the Azores, close to the island of Terceira, the wave heights reach approximately 0.7 m (Fig. 3.5e).

In Barbados, hypothesis A-MS produces the first wave of about 0.1m after about 7 h with about a 30 min period. Only after 9 h and 30 min does the wave height exceed 0.2m (Fig. 3.5f).

We applied Green's law in all locations except Lisbon and Cadiz to extrapolate the maximum wave height values to a depth of 5 m close to the shore to compare the values with the observations in Sect. 3. We present the maximum wave height values after the application of Green's law in Table 3.3.

Table 3.3 Results of the VTGs for hypothesis A-MS. The column TTT lists the observed tsunami travel times. The column polarity indicates the first movement of the sea upward (U) or downward (D).

Local		VTG coordinates and depth			TTT	Wave height				Polarity	Period
		Lon.	Lat.	d		First	max.	Green's	Obs.		
		[°]	[°]	[m]		[m]	[m]	Law	[m]		[min]
Lisbon		-9.136	38.706	3	~ 1 h 10 min	1.6	1.8	nesting	1.2 – 1.8	D	< 30
Cadiz		-6.291	36.524	4	~ 1 h	-0.6	2.4	nesting	-	D	~ 30
Scilly Islands		-06.383	49.85	50	~ 4 h	0.4	0.4	0.7 m	0.6 – 1.2	U	~ 15
Mount´s Bay		-05.48	50.08	26	~ 4 h 30 min	0.4	0.5	0.8 m	1.2 – 1.8	U	~ 15
Kinsale		-08.500	51.653	28	~ 4 h 15 min	0.1	0.5	0.8 m	0.6	U	< 15
Dungarvan		-07.479	51.949	50	~ 5 h	0.1	0.3	0.5 m	-	U	< 15
Madeira	E	-16.666	32.750	51	~ 30 min	0.3	0.8	1.4 m	-	U	~ 30
	S	-16.926	32.619	51	~ 40 min	0.2	0.4	0.7 m	-	U	~ 30
Azores		-27.150	38.800	53	~ 2 h	0.5	0.7	1.3 m	-	U	~ 15
Barbados		-59.566	13.033	50	~ 7 h	0.1	0.2	0.4 m	0.45 – 0.6	U	~ 30

3.2.6.2. Hypothesis B

In hypothesis B, the dip angle was increased relative to hypothesis A, resulting in the dominant strike-slip mechanism. In Fig. 3.6, we depict the maximum wave height for option B.

By analysing Fig. 3.6 we find maximum wave heights of 15 m along the coast of Morocco. In the Gulf of Cadiz, the wave heights do not exceed 2 m. In Great Britain, at the Isles of Scilly the maximum wave height is close to 2.3 m, and in Mount's Bay, the maximum wave height values reach 1.8 m. For the locations in Ireland, Kinsale and Dungarvan, the maximum wave heights exceed 1.4 m. The eastern part of Madeira experiences wave heights greater than 2.5 m, decreasing towards the southern parts of the island (Fig. 3.6). The maximum wave height exceeds 5.5 m on the eastern side of the island of Terceira in the Azores. For Barbados, this source computes maximum wave heights exceeding 0.7 m.
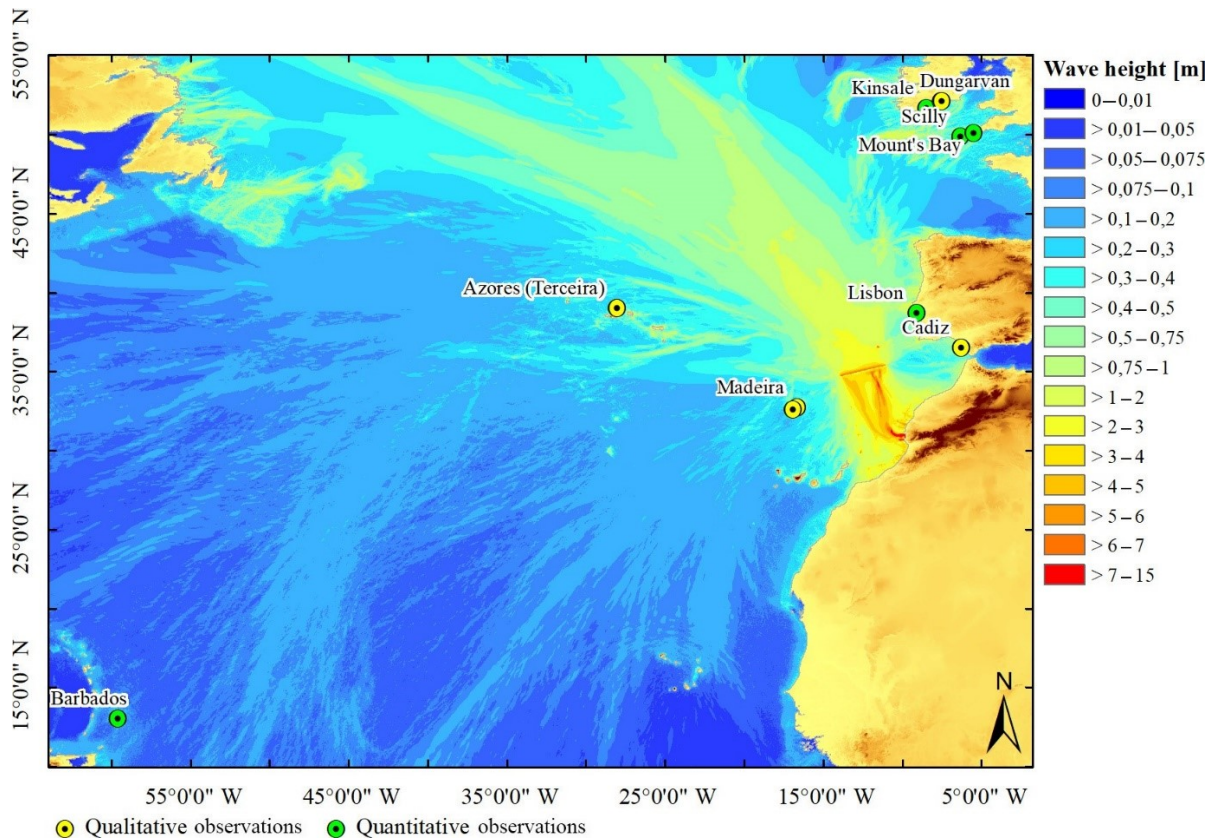
Figure 3.6 Maximum wave height distribution (colour scale in m) in the Atlantic basin produced by the source of hypothesis B.

Figure 3.7 presents the corresponding synthetic tsunami waveforms at the VTGs. Table 3.4 gives a summary of the results. The analysis of the synthetic waveforms shows that a small withdraw of about 0.2 m arrives in Lisbon after 1 h and 15 min followed by a water surface elevation of 0.9 m. The third wave has a maximum positive amplitude of 2.2m (Fig. 3.7a).

The maximum wave height at the Isles of Scilly is 0.5 m (Fig. 3.7b). The first wave reaches 0.4 m, arriving close to 4 h after the earthquake. The synthetic tsunami waveform shows around a 15 min wave period. In Mount's Bay, the first wave of 0.4 m arrives after 4 h and 30 min with a 15 min wave period (Fig. 3.7b). Here, the maximum wave height, 0.7 m, comes more than 6 h after the earthquake. In Kinsale, hypothesis B produces a maximum wave height of 0.6 m. The first wave of 0.2 m wave height in the VTG arrives after 4 h and 15 min of tsunami propagation; here, the period is shorter than 15 min (Fig. 3.7c).

In Madeira, the first and the maximum wave heights are greater in the eastern part of the island compared to the southern part. Maximum wave heights values reach 1.4 m in the eastern part of Madeira and 1.1 m in the southern part of Madeira (Fig. 3.7d). In the Azores, the wave height for Terceira reaches up to 2.4 m (Fig. 3.7e).
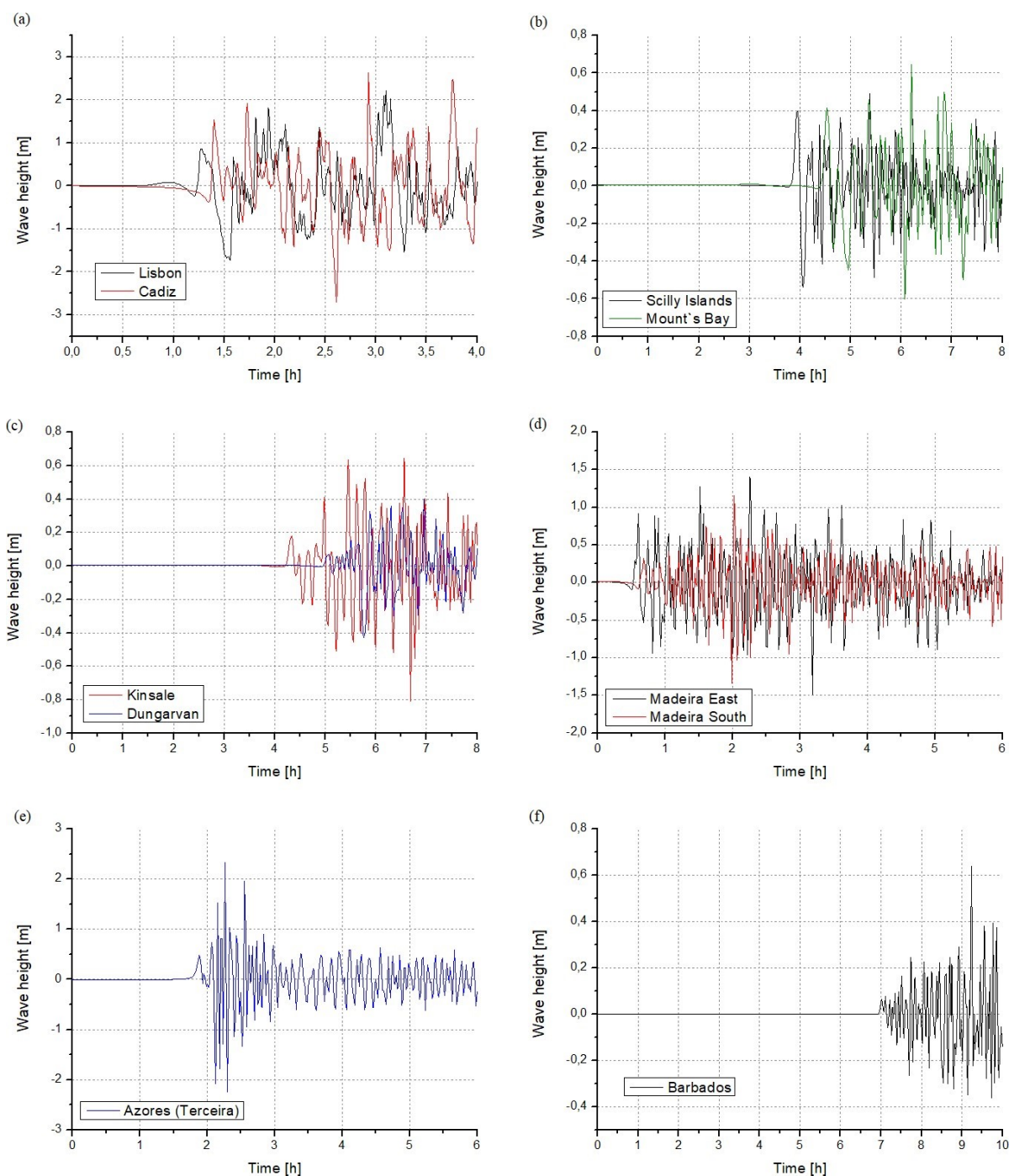
Figure 3.7 VTG records for hypothesis B at the coordinates of the locations presented in Table 3.4.

Hypothesis B predicts a tsunami travel time of 7 h to Barbados with the first peak of less than 0.1 m and a maximum peak of 0.6 m after 9 h and 15 min (Fig. 3.7f). The first wave has a period slightly below 15 min. Table 3.4 gives a summary of the results for hypothesis B.

We also applied Green's law for this solution. We present the maximum wave height values after the application of Green's law in Table 3.4.

Table 3.4 Results of the VTGs for hypothesis B. The column TTT lists the observed tsunami travel times. The column polarity indicates the first movement of the sea upward (U) or downward (D).

Local		VTG coordinates and depth			TTT	Wave height [m]				Polarity	Period
		Lon.	Lat.	D		First	max.	Green's	Obs.		
		[°]	[°]	[m]		[m]	[m]	Law	[m]		[min]
Lisbon		-9.136	38.706	3	~ 1 h 15 min	0.9	2.2	nesting	1.2 – 1.8	D	> 30
Cadiz		-6.291	36.524	4	~ 1 h	-0.4	2.6	nesting	-	D	~ 30
Scilly Islands		-06.383	49.85	50	< 4 h min	0.4	0.5	0.9 m	0.6 – 1.2	U	~ 15
Mount´s Bay		-05.48	50.08	26	~ 4 h 30 min	0.4	0.7	1 m	1.2 – 1.8	U	~ 15
Kinsale		-08.500	51.653	28	~ 4 h 15 min	0.2	0.6	1 m	0.6	U	< 15
Dungarvan		-07.479	51.949	50	~ 5 h	0.1	0.4	0.7 m	-	U	< 15
Madeira	E	-16.666	32.750	51	~ 30 min	0.9	1.4	2.5 m	-	U	~ 30
	S	-16.926	32.619	51	~ 40 min	0.3	1.1	2.1 m	-	U	~ 30
Azores		-27.150	38.800	53	~ 1 h 45 min	0.5	2.4	4.2 m	-	U	~ 15
Barbados		-59.566	13.033	50	~ 7 h	0.1	0.6	1.1 m	0.45 – 0.6	U	~ 30

3.2.7. Discussion

We investigated possible sources of the earthquake and tsunami on the 31 March 1761 earthquake in the Atlantic.

Firstly, we excluded the locations similar to the instrumental events of the 20th century: 25 November 1941 (Baptista et al., 2016) and 26 May 1975 (Kaabouben et al., 2009) because of the incompatibility of tsunami travel times (Fig. 3.2).

Secondly, we placed a source about 85 km to the east of the location proposed by Baptista et al. (2006) (Fig. 3.2).

After setting the source position, we investigated focal mechanisms for the parent earthquake. We selected two focal mechanisms for testing: A and B. Solution A-MS corresponds to focal mechanism A with a multi-segment fault plane as described in Sect. 3.2.3 (Table 3.2).

Our tests produce a set of TTTs compatible with the observations: maximum differences between observed and predicted travel times are 15 min in the near-field and 30 min in the far-field. These differences are acceptable considering that the exact location of the observation points is unknown. Travel time results are valid for A, B and A-MS, as the locations are the same. Tables 3.3 and 3.4 show that the predicted travel times are compatible with a source located in the area west of the Coral Patch.

Any source located in the northeastern Atlantic, south of the Isles of Scilly, produces a shorter tsunami travel time to Scilly than Mount's Bay. This fact shows that the 6 h TTT reported in Kinsale contradicts the 4 h TTT reported for Dungarvan (Fig. 3.1). On the other hand, the tsunami travel times predicted by our numerical simulation are consistent with their position related to the source area. The proposed source A produces wave heights applying Green's law

to the values recorded at the VTGs, which are compatible with the observations in Lisbon, Kinsale, Scilly and Barbados (Fig. 3.5 and Table 3.3). The results of the synthetic wave records of Dungarvan, Madeira and the Azores are compatible with the observations. In Mount's Bay, the wave height computed using Green's law of the VTG value is smaller than the one reported. However, the analysis of Fig. 3.4 shows that the computed maximum wave heights are greater than 1.6 m for Mount's Bay. This value agrees with the observation.

The proposed source B produces wave heights compatible with the observation in Lisbon, Scilly and Mount's Bay. We apply Green's law (Eq. 3.1) using the wave heights recorded at the VTG in Kinsale and Barbados and obtain larger wave heights than reported (Table 3.4). Also, the computed maximum wave heights in Fig. 3.6 are higher than 1.4, 2.2 and 0.7 m for Kinsale, Scilly and Barbados respectively. These values are higher than the ones observed.

At the Azores, the wave height reaches 4.2 m (Table 3.4); however, the descriptions do not report an inundation. Also, at the coast of Morocco, source B predicts wave heights close to 14 m. To our knowledge, the historical documents do not report any abnormal movement of the sea in Morocco.

The observations do not account for inundation in Lisbon. To investigate this fact, we estimated the tide condition in Lisbon for 31 March 1761. To do this, we used a Moon phase table (USNO, 2017) and concluded that the tide was 2.6 m above hydrographic zero (HZ) (in dropping tide conditions) at 13:00 on 31 March 1761 (Table 3.5).

Table 3.5 Tide levels at the time of the earthquake and tsunami arrival.

	Time	Tide condition	Estimated height relative to hydrographic zero
Earthquake	Noon	Full tide	2.9m
Tsunami arrival time	13:15	Dropping tide	2.6m
Max wave height hypothesis AMS	14:15	Dropping tide	2.3m
Max wave height hypothesis B	15:00	Dropping tide	2.1m

The maximum of the synthetic wave record for source AMS is 1.8 m about 2 h and 15 min when the tide dropped below 2.3 m above HZ. Adding 1.8 to 2.3 m, we obtain 4.1 m; this value is less than the tide amplitude in the springtide condition. Considering that the centre of Lisbon was rebuilt 3 m above sea level after the 1755 event (Baptista et al., 2011), the predicted wave heights are compatible, with no flooding.

The proposed source B generates 0.9 m for the first wave height but a maximum wave height of 2.2 m. The maximum wave height occurs at 15:00 UTC and the estimated tide is approximately 2.1 m above HZ. Adding 2.2 to 2.1 we reach spring tide condition of 4.3 m.

Given the considerations above the tide, the analysis favours solution A.

The tidal range in Barbados is about 1 m. This small range might favour the observability of small first waves at tsunami arrival. For source A, the first wave in Barbados is about 0.1 m, which raises the question of whether people might have noticed the advance of the sea. Close to 09:00, 2 h after tsunami arrival, the positive peak in the VTG is higher than 0.2 m, which results in 0.4 m when estimating the wave height when applying Green's law for 5m depth close to the shore. The coeval sources report similar wave height values.

Also, for source B, the wave height is smaller than 0.1m at the VTG at the time of tsunami arrival. About 45 min later the waves are large than 0.2 m. The maximum peak occurs ca. 2 h after tsunami arrival at 09:00. Because of the small amplitude of the tide in Barbados, this location does not contribute to selection from the two candidate sources.

The summary (Annual Register, 1761) states that the waves seemed to abate but at 10:00 they started again with a higher intensity and lasted until the next morning – this observation of greater amplitudes some hours after tsunami arrival fits for both sources. However, the timings of increasing wave heights do not match.

In Cadiz, both sources produce the observed withdrawal. Sources A and B predict a drawdown of 0.6 and 0.4 m respectively. High tide in Cadiz is about 1 h earlier than in Lisbon. Once the tide is in dropping conditions at the time of the tsunami arrival, a larger drawdown is more likely to be observed.

Considering the points discussed above, we conclude our preferred solution is A-MS. The following facts justify our choice:

– The candidate source in hypothesis A-MS is compatible with the geodynamic setting predicted by the NUVEL 1A model (DeMets and Dixon, 1999). NE–SW compressive structures with comparable fault plane parameters have been identified close to the Coral Patch seamount (Figs. 3.1 and 3.3). The proposed structure is possibly propagating and reactivating the NE–SW striking oceanic rifting fabric towards the epicentre suggested by Baptista et al. (2006). Nevertheless, we must stress that Martínez-Loriente et al. (2013) do not suggest an extension of the seismogenic structure at the CPF, although no detailed multi-channel seismic survey has been carried out to the west of the CPF in the proposed source area.

– The wave heights produced by the numerical models are in better agreement with proposed source A-MS.

– Wave heights greater than 14 m produced by hypothesis B would result in a catastrophic scenario, which is rather unlikely and not observed nor reported. Also, the 4.2 m wave height produced by hypothesis B in the Azores would have caused inundation, which has not been reported.

– Although both solutions follow our considerations for Lisbon, the wave heights generated by source A-MS seem to be more comparable to the observed fluctuation of 2.4 m than the wave heights produced by source B.

– The larger drawdown in Cadiz favours solution A-MS.

The reassessment of the reports of Barbados and Cadiz support the choice selected here. While the tsunami travel time for Barbados supports the source location, the fact that there were no inundation reports in Cadiz supports the magnitude and rupture mechanism proposed here.

3.2.8. Conclusion

– The source proposed here for the 1761 event is compatible with the tsunami observation data set, the macroseismic intensity data (Baptista et al., 2006) and with the geodynamic context of the area predicted by the kinematic plate model NUVEL 1-A.

– The source proposed here is located in the SWIM, an area of widespread compressive structures (Hayward et al., 1999), corresponding to a fault that extends from the western segment of the CPF towards the epicentre proposed by Baptista et al. (2006).

The investigation of each historical event in the area contributes to a better understanding of the structure of this diffuse plate boundary and ultimately leads to a better evaluation of the seismic and tsunami hazard. This study, together with the study by Baptista et al. (2006), underlines the need to include the 1761 event in all seismic and tsunami hazard assessments in the northeastern Atlantic basin.

3.3. Reevaluation of the 11 November 1858 Earthquake and Tsunami in Setúbal: A Contribution to the Seismic and Tsunami Hazard Assessment in Southwest Iberia

3.3.1. Abstract

The southwest Iberian Margin (SWIM) hosted a series of tsunamigenic earthquakes. However, strong magnitude earthquakes M > 7.0 are scarce and geological and geophysical evidence suggest that slow deformation occurs on a large area without a discrete plate boundary. The reanalysis of this event is crucial because of its location in a possible transition zone between the diffuse plate boundary and the stable continent regime. The 11 November 1858 earthquake in Setúbal, Portugal, with an estimated M ~ 7, ruined a large part of the city and was felt all over Portugal and large parts of the Iberian Peninsula. Earlier studies suggest an epicentre close to the shore, less than 50 km away, and there exists a description of a tsunami in Setúbal. We use macroseismic intensities and present a reevaluation of the event parameters: depth, epicentre, magnitude, and fault orientation. We select the candidate faults according to the epicentral area and plate kinematics and use scaling laws for the magnitude range. We use tsunami numerical modelling to check the tsunamigenic potential of the event. Finally, we compute the tsunami propagation and inundation for Setúbal for seven candidate scenarios and analyze waveform data obtained at virtual tide gauges. Our results favour an offshore inverse fault compatible with the tsunami observation corresponding to a reverse fault with a 40° strike angle at 13 km depth and a magnitude range of 6.8 ± 0.3.

3.3.2. Introduction

The 11 November 1858 earthquake in Setúbal was the strongest event in the nineteenth century in Portugal (Moreira, 1984, 1991; Pereira de Sousa, 1916, 1928; Rodríguez de la Torre, 1990). The earthquake devastated large parts of Setúbal and its surroundings and caused considerable damage in Lisbon and the Lower Tagus Valley (LTV), although propagation of the seismic shocks to the south was reportedly stronger (Rodríguez de la Torre, 1990) (Fig. 3.8). All over

continental Portugal and large parts of the Iberian Peninsula, people felt the shakings (Martínez Solares and Mezcua, 2002; Martins and Mendes-Victor, 1990). Following Diário do Governo (1858) and Martins and Mendes-Victor (1990), foreshocks occurred around 6 a.m. local time, but the mainshock took place at around 7:15 a.m. local time. Quintas (1993) reproduced in A Roda (2010) commented on the river Sado invading Setúbal (Fig. 3.8) after the earthquake, causing some boats to sink and leaving some on dry land. The coeval source of this information is unclear, but it suggests a tsunami after the earthquake.

The seismicity of this area comprises distant (≥ 300 km) very strong magnitude ($M \geq 7.5$) events associated with the diffuse Eurasia-Nubia plate boundary area and local intraplate strong magnitude ($M \geq 6.0$) events in the stable continental crust (Cabral et al., 2003; Johnston and Kanter, 1990). Large and destructive historic earthquakes occurred in southwest Iberia and mainland Portugal. Offshore events in the oceanic domain such as the great 1755 Mw 8.7 ± 0.25 Lisbon earthquake (Baptista and Miranda, 2009; Mezcua and Martínez Solares, 1983; Oliveira, 1986) and the 1761 Mw $8.4-8.5$ earthquake (Baptista et al., 2006; Wronna et al., 2019) were large enough to generate transatlantic tsunamis.

Within the instrumental period, the 1969 Mw 7.9 Horseshoe earthquake (Baptista, 2019; Fukao, 1973) occurred, generating a tsunami registered at the tide gauges in Portugal, Spain, Morocco. Those events are associated with the diffuse Eurasia-Nubia plate boundary in the southwest of Iberia and the Gulf of Cadiz (Duarte et al., 2011; Sartori et al., 1994; Zitellini et al., 2009). Other destructive events occurred within the continental domain in the LTV. Examples are an event in 1344 (Martínez Solares and Mezcua, 2002) that destroyed parts of Lisbon or the 1531 Mw 6.9 earthquake (Justo and Salwa, 1998). Baptista et al. (2014) conclude for Mw 6.6 for the 1531 earthquake and propose the Vila Franca de Xira Fault (VXF) as a source for the resulting tsunami in the Tagus estuary (Fig. 3.8). The only early instrumental event in the LTV and, therefore, relatively well-understood is the 1909 Mw $6.0-6.2$ Benavente earthquake (Cabral et al., 2013; Fonseca and Vilanova, 2010; Stich et al., 2005; Teves-Costa and Batlló, 2011). Nevertheless, the structure and geometry of the source 1909 are unknown and under debate (Fonseca et al., 2001; Matias et al., 2005). It is worth to mention that the epicenter estimates for the 1344 and 1909 earthquake nearly coincide. We show epicentre estimates for the events in 1344 (Martínez Solares and Mezcua, 2002), 1531 (Martins and Mendes-Victor, 1990) and 1909 (Carrilho et al., 2004) in Fig. 3.8. Since then, within the instrumental period, the seismic activity in the LTV has been low.

Epicentre estimates locate the 1858 Setúbal earthquake offshore and further south than the events associated with the LTV at 9.00 W 38.20 N (Martins and Mendes-Victor, 1990; Vilanova

and Fonseca, 2007), 8.92 W 38.29 N (Martínez Solares and Mezcua, 2002) and more recently 8.802 W 38.244 N, Stucchi et al. (2013) and Gomez-Capera et al. (2015) (Fig. 3.8). Most references indicate an epicentral intensity IX (Moreira, 1991; Pereira de Sousa, 1916, 1928; Rodríguez de la Torre, 1990) except for Galbis Rodríguez (1932) who propose the intensity IX or X the scale of Rossi-Ferrel. Modern-day magnitude estimates for this event vary between 6.5 and 7.2 (Custódio et al., 2015; Gomez-Capera et al., 2015; Martins and Mendes- Victor, 1990; Vilanova and Fonseca, 2007; Stucchi et al., 2013). Ribeiro et al. (2009) propose the east dipping blind thrust of the Príncipe de Avis seamount (Fig. 3.8) as a candidate source for the 1858 earthquake. These authors argue that the proximity to the Horseshoe−Marquês de Pombal fault system (Fig. 3.8) possibly allows the migration of seismic activity towards the north, eventually generating the 1858 Setúbal and the 1909 Benavente earthquakes. Contrary, Moniz and Cabral (2014) suggested that the event could be associated with a hypothetical extension of the Pinhal Novo−Alcochete fault (PNAF) (Fig. 3.8), based on isoseismal lines (Oliveira, 1986) and an instrumental event that occurred on February 20, 2014, M 3.6 event, with Instrumental Intensity III−IV. The PNAF is an N−S trending left-lateral strike-slip fault extending for approximately 25 km to the north of Setúbal. Furthermore, some authors suggest that the area of the 1858 event is structurally related to the LTV (Carvalho et al., 2011; Vilanova and Fonseca, 2004). Gomez-Capera et al. (2015) employ an algorithm called Boxer (Gasperini et al., 1999, 2010) to analyze macroseismic data of the 1858 event. They mainly refer to a limited number of 16 Macroseismic Data Points (MDPs) in Portugal presented in Moreira (1991). However, most modern-day studies rely only on those 16 MDPs which are distributed along the N–S and thus also do not represent a good azimuthal coverage.

The 1858 Setúbal earthquake is of particular interest since the source could locate within the transition zone from a diffuse plate boundary (SWIM) to a stable continental crust (Johnston and Kanter, 1990). The epicentre location offshore and the reported inundation in Setúbal raises the following questions: How does this event fit into the structural tectonic regime of the area? What are possible rupture mechanisms to reproduce the observation in Setúbal? How do this event and the associated structures contribute to the tsunami hazard in the region? Besides, the source mechanism and relating fault have not yet been studied in detail. Moreover, a better understanding of this event will ultimately contribute to a better regional characterization of seismic and tsunami hazard in Iberia.

In this study, we represent a reassessment of the 1858 Setúbal earthquake and possible tsunami. First, we collect and find a total number of 71 MDPs in literature. Then we analyze the available MDPs and present a reassessment of the event. We estimate the depth, the epicentre, the

magnitude, and the fault orientation. After that, we use scaling relationships (Blaser et al., 2010; Wells and Coppersmith, 1994) to estimate the length, width and slip of the fault to compute the tsunami simulations.
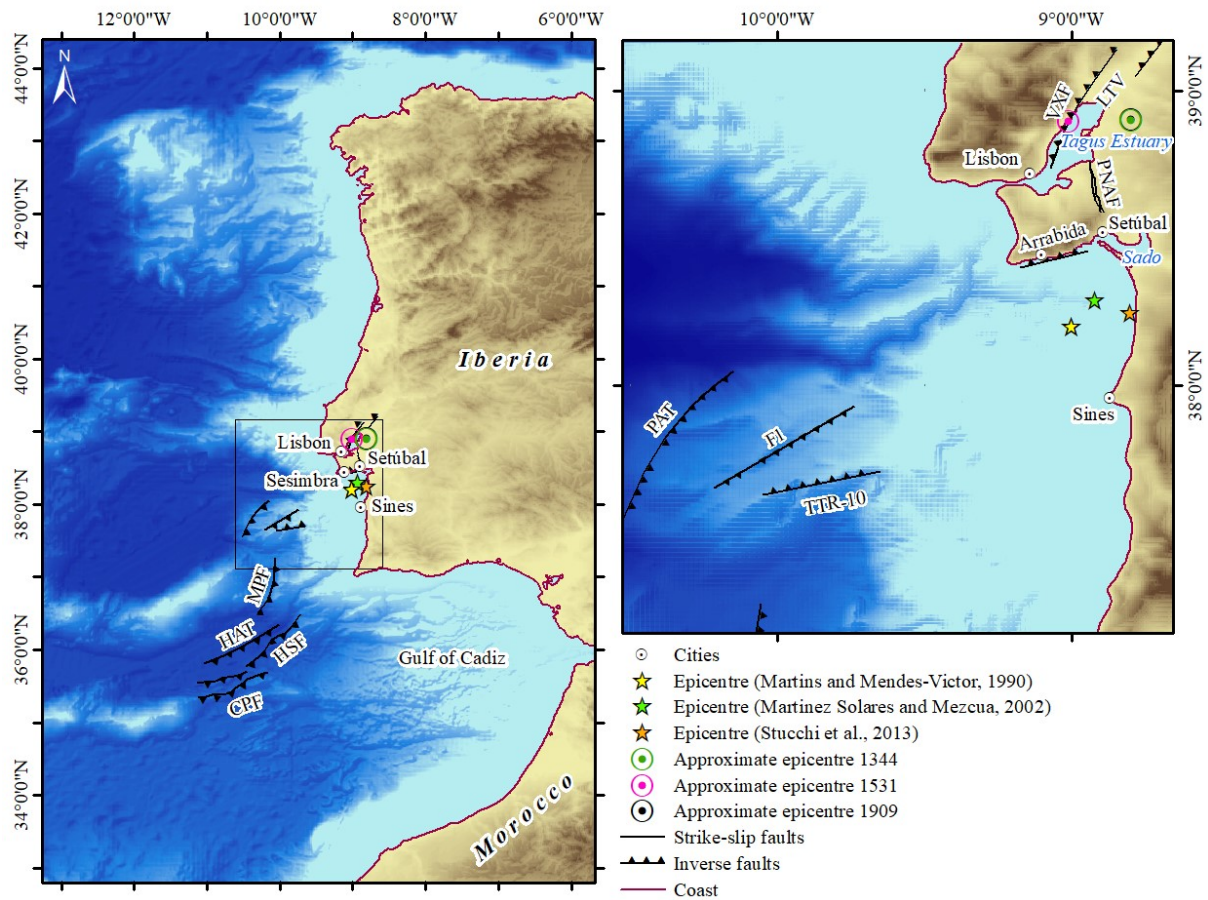
Figure 3.8 The white points depict the main cities, and the colour stars show proposed epicentres for the 1858 earthquake (Martins and Mendes-Victor, 1990; Martínez Solares and Mezcua, 2002; Stucchi et al., 2013). The points with the circles show the approximate epicenter locations of the 1344, 1531 and the 1909 earthquakes. The simple black line shows the Pinhal Novo—Alcochete Fault (PNAF) (Cabral et al., 2003; Moniz and Cabral, 2014) and the black lines with triangles illustrate mapped inverse faults, and the triangles indicate the dipping direction. The inverse faults represented are the southern and northern Coral Patch Fault (CPF) (Martínez-Loriente et al., 2013), the Horseshoe Fault (HSF) (Gràcia et al., 2003; Terrinha et al., 2009; Zitellini et al., 2004), the Horse-shoe Abyssal plain Thrust (HAT) (Martínez-Loriente et al., 2014), the Marques Pombal Fault (MPF) (Gràcia et al., 2003; Terrinha et al., 2003), the Principe the Avis Thrust (PAT) (Ribeiro et al., 2009), the F1 and TTR-10 faults (Terrinha et al., 2003), a thrust fault associated with the Arrabida chain (Cabral et al., 2003; Kullberg et al., 2000; Ribeiro et al., 1990) and in the Lower Tagus Valley (LTV) the Vila Franca de Xira Fault (VXF) (Bap-tista et al., 2014; Cabral et al., 2003; Ribeiro et al., 2009)

3.3.3. Methods

Macroseismic data from the 1858 event was already analyzed by Mezcua (1982), suggesting that the epicentre should be located close to shore at approximately 8.92 W, 38.29 N (Martínez Solares and Mezcua, 2002) (Fig. 3.8). First, we compile and analyze the data to systematically estimate the focal depth, epicentre magnitude and associated errors. Subsequently, we determine the faults orientation, dimensions and rupture mechanism considering the geodynamics of the source region. Based on these parameters, we compute the input for the tsunami

simulations. The port construction transformed the riverfront substantially in the target area Setúbal since 1858. To consider these modifications we build a Paleo Digital Elevation Model (Paleo-DEM) (Wronna et al., 2017) implementing data from a historic hydrographic chart with soundings from 1852 (Vincendon-Dumoulin, 1876) to represent the bathymetric and coastal morphological features more adequately. Finally, we use the Paleo-DEM and seven different fault scenarios for the numerical tsunami simulation.

3.3.3.1. Data

We use the macroseismic intensity data from the studies of Pereira de Sousa (1916, 1928), Galbis Rodríguez (1932), Rodríguez de la Torre (1990), Moreira (1991), and Martínez Solares and Mezcua (2002) (Fig. 3.9). Galbis Rodríguez (1932) presents observations in 38 locations and macroseismic intensities in the Rossi-Ferrel scale (RF). Martínez Solares and Mezcua (2002) present the macroseismic intensities for 16 locations in Spain. We combine these two sets of data because of their complementary character, and they do not contradict each other, except in one location (Fig. 3.10). The two datasets together contain 45 MDPs. Pereira de Sousa (1916, 1928) uses the Mercalli intensity scale of 1909, Rodríguez de la Torre (1990) uses the MSK intensity scale and Moreira (1991) uses the Modified-Mercalli intensity scale 1956 (MMI-56) to present MDPs in 56 and 16 locations, respectively. We converted all datasets in the European macro seismic scale (EMS-98) following Musson et al. (2010). However, the authors of the datasets attributed different macroseismic intensities in 29 locations (Table 3.6). On the other hand, the combination of the three data sets results in 71 MDPs (Table 3.6 and Fig. 3.9). In 15 locations, the interpretation of the macroseismic intensity only varies to one degree, but in ten cases, the interpretation of the macroseismic intensity varies two degrees or more. The most remarkable differences appear for the locations, Santiago do Cacém, Sevilla and Sines. Galbis Rodríguez (1932) attributes VII on the RF scale. According to Musson et al. (2010), this value converts into VI on the EMS-98 scale. Nevertheless, Moreira (1991) attributes an intensity of VIII and Rodríguez de la Torre (1990) even IX for Santiago de Cacém. According to Galbis Rodríguez (1932) the intensity in Sines is VI whereas Moreira (1991) attributed VIII-IX and Rodríguez de la Torre (1990) even IX. Santiago do Cacém and Sines are located close to each other and relatively close to the epicentral area (Fig. 3.11). After analyzing the data set of Galbis Rodríguez (1932), we find that the author presents first the locations where the earthquake was felt with the maximum intensity of IX–X (R.F.) and then switches directly to the intensity VII (R.F.) listing several Portuguese sites. On the next page, the author

continues the listing and then repeats the intensity VII (R.F.) with another set of locations in Portugal. We are uncertain if the first listing of the intensity VII is not possibly mistaken since it includes locations such as Sines, Santiago do Cacém, Almada, Lisbon and Sacavém, which reportedly have had greater intensities when comparing to the other data sets (Moreira, 1991; Pereira de Sousa, 1916, 1928) (Fig. 3.9). On the other hand, Galbis Rodríguez' (1932) list with intensity VII also includes some distant locations, for example, Borba, where VII (R.F.) would agree with Pereira de Sousa (1916) after conversion.

For Sevilla Galbis Rodríguez (1932) assigned the degree IV whereas Martínez Solares and Mezcua (2002) attribute the intensity VI (Fig. 3.10). Rodríguez de la Torre (1990) attributes the degree VII defending his choice with the following evidence: the entire population felt it, and people gather in the streets in panic; descriptions of the moving objects and ringing bells; and collapsed roofs and damaged buildings. Pereira de Sousa (1916, 1928) even attributes VII–VIII confirming Rodríguez de la Torre's (1990) choice. Pereira de Sousa (1916, 1928) considers an intensity of VIII for Sacavém, but he mentions doubts that it might have had the intensity IX considering the damages (Fig. 3.10).

Some minor differences may result from the conversion since the degrees are descriptive scales rather than numeric values. Musson et al. (2010) do not present the Mercalli intensity scale of 1909 for conversion purposes. However, they explain that Mercalli believed that the intensity scales should have 12 degrees around 1902 and Cancani (1904) proposed modifying the scale to consider very strong earthquakes. For that reason, we consider the Mercalli–Cancani–Sieberg scale (MCS) to be representative for the Mercalli intensity scale of 1909 mentioned in Pereira de Sousa (1916, 1928) and Rodríguez de la Torre (1990).

To treat the uncertainties discussed above, we proceed systematically applying a schematic approach to assess the earthquake metrics (a) for each data set individually and (b) for the average value at each site of the observations and (c) for locations comprising unique MDPs values by ignoring diverging observations. First, we compiled the data and cross-checked it with available coeval and other more recent references (Bravo Monge et al., 1990; Choffat and Bensaude, 1912; Diário do Governo, 1858; Miranda, 1935; Navarro-Neumann, 1917, 1921; Perrey, 1860; Prado, 1863; Rey Pastor, 1927). Then we decided on four different independent data sets (Table 3.6):
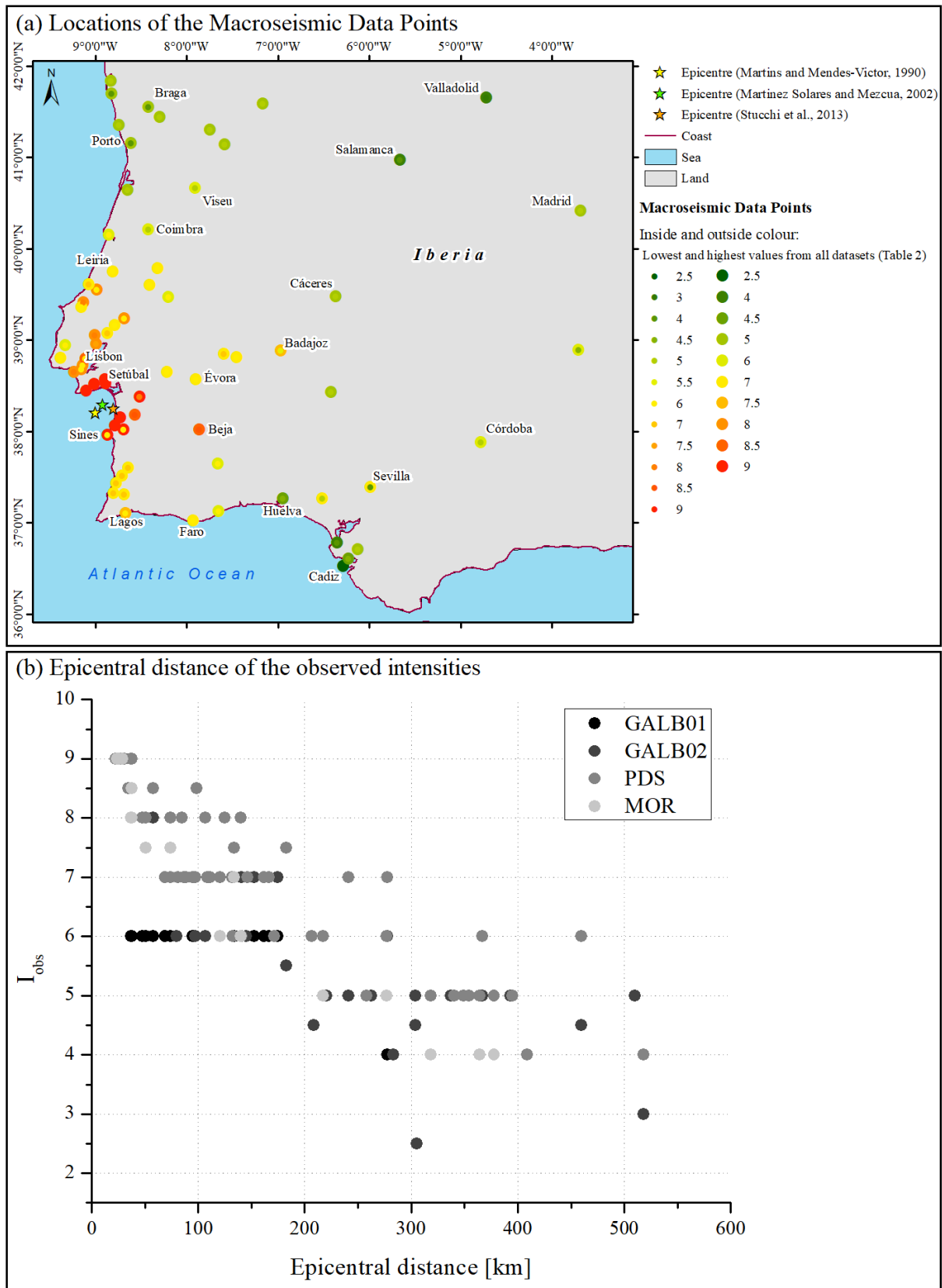
Figure 3.9 (a) Locations of the combined Macroseismic Data Points (MDPs) considering the observations from Pereira de Sousa (1916, 1928), Galbis Rodríguez (1932), Rodríguez de la Torre (1990), Moreira (1991) and Martínez Solares and Mezcua (2002). The color scale of the individual points depicts the lowest and the highest observed intensities. **(b)** shows the observed intensities of the data sets GALB01, GALB02, PDS, MOR converted to EMS-98 relative to the epicentral distance (km) considering the epicentre presented by Martínez Solares and Mezcua (2002) (c.f. Table 3.6)
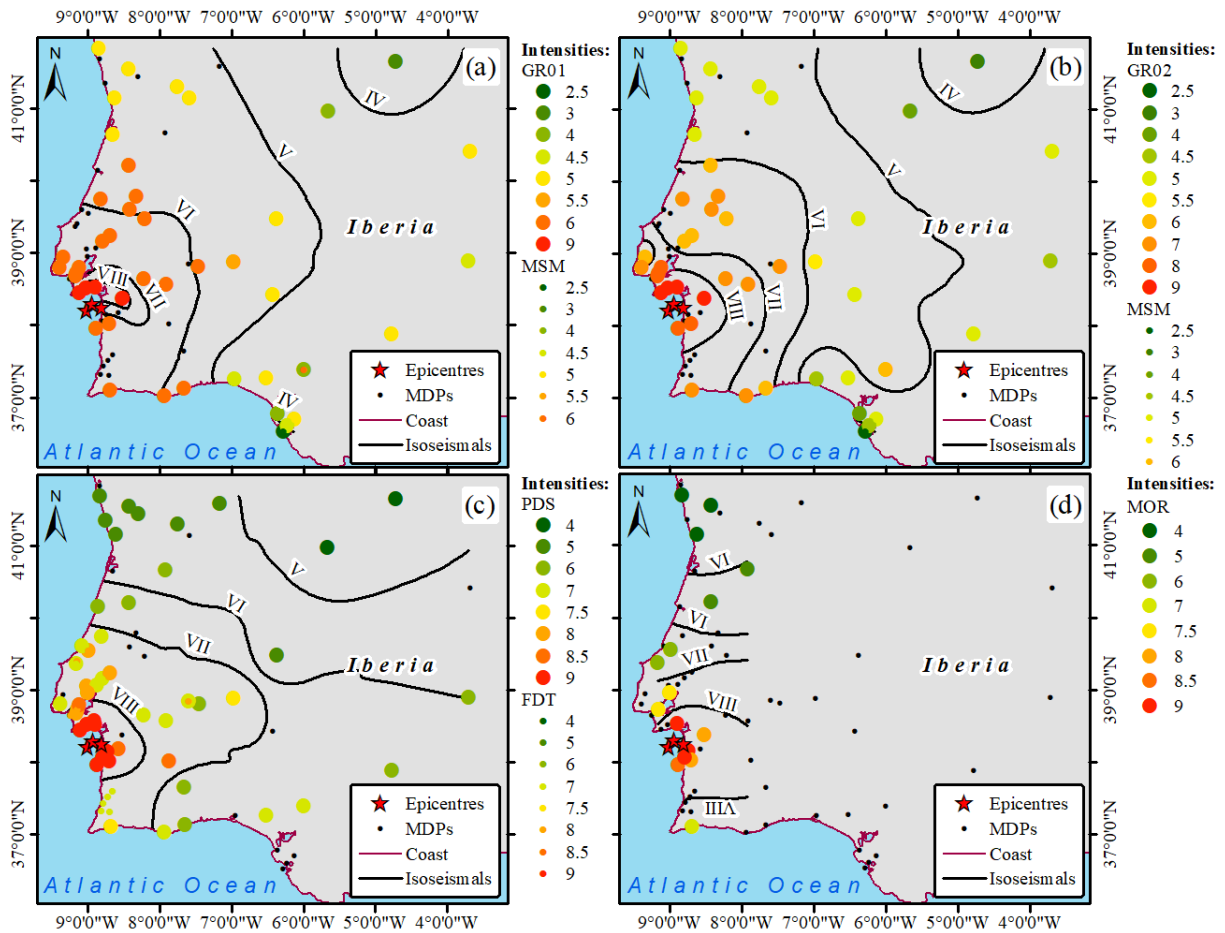
Figure 3.10 Intensities for each dataset and the resulting isoseismal lines for **(a)** the original dataset GALB01 consisting of GR01 and MSM (Galbis Rodríguez, 1932; Martínez Solares and Mezcua, 2002), **(b)** the interpreted dataset GALB02 consisting of GR02 and MSM (Galbis Rodríguez, 1932; Martínez Solares and Mezcua, 2002), **(c)** the dataset PDS consisting of PS and FDT (Pereira de Sousa, 1916, 1928; Rodríguez de la Torre, 1990), and **(d)** the dataset MOR (Moreira 1991) (c.f. Table 3.6)

(1) A combination of of the original data set GR01 (Galbis Rodríguez, 1932) and MSM (Martínez Solares and Mezcua, 2002), hereafter referenced as GALB01;

(2) the corrected data set GR02 (Galbis Rodríguez, 1932) assuming the listing error as stated above and thus considering the intensity VIII (R.F.) for the corresponding sites in combination with MSM (Martínez Solares and Mezcua, 2002), hereafter referenced as GALB02;

(3) The data sets PS (Pereira de Sousa, 1916, 1928) and FDT (Rodríguez de la Torre, 1990) hereafter referenced as PDS;

(4) Moreira (1991), hereafter referenced as MOR. We present the original data GR01, GR02, MSM, PS and FDT and the data compilation GALB01, GALB02, PDS and MOR in Table 3.6 and depict the intensities for each dataset and the resulting isoseismal lines in Figs. 3.9, 3.10

Our goal is to effectively determine the epicentral area rather than the reevaluation of MDPs. To include the uncertain intensities, we use three different approaches.

58

1. We consider the lowest, average, and highest numerical values of all observations considering semi-integers (Gasperini, 2001). Considering GALB01 and GALB02, that procedure results in different average numerical values, AV01 and AV02, respectively (c.f. Table 3.6). For the lowest and highest, we do not differentiate since it includes the entire range of uncertainties.

2. We only consider the location with unique value or where all data sources agree (Albarello and D'Amico, 2004). We also differentiate for GALB01 and GALB02, resulting in two sets of MDPs of identical values, ID01 and ID02, respectively. Here, we do not consider semi-integer values (c.f. Table 1).

3. Since this may introduce substantial uncertainty (Gasperini et al., 2010), we consider each observation dataset separately.

Table 3.6 MDPs per location, and author and intensity level

Location	Easting	Northing	GALB01			GALB02		PDS			MOR		Intensity level					
			GR01	MSM	I_{obs}	GR02	I_{obs}	PS	FDT	I_{obs}	MOR	I_{obs}	Low	AV01	AV02	High	ID01	ID02
Abrantes	568816.1606	4368907.544	VI	-	6	VI	6	-		-			6	6	6	6	6	6
Alcacer do Sal	542452.5912	4247313.234	IX	-	9	IX	9	-		-	VIII	8	8	8.5	8.5	9	-	-
Alcobaca	501546.5350	4377702.737	-	-	-	-	-	VIII	VIII	8	VI	6	6	7	7	8	-	-
Alenquer	499221.2560	4322658.116	-	-	-	-	-	VIII	VIII	8	-	-	8	8	8	8	8	8
Aljezur	517454.7974	4130279.224	-	-	-	-	-	-	VII	7	-	-	7	7	7	7	7	7
Almada	486343.8778	4281167.543	VI	-	6	VIII	8	VIII	VIII	8	-	-	6	7	8	8	-	8
Almargo	958911.2577	4318002.854	-	IV-V	4.5	IV-V	4.5	VI	VI	6	-	-	4.5	5.25	5.25	6	-	-
Almonte	720268.6659	4127051.501	-	V	5	V	5	VII	VII	7	-	-	5	6	6	7	-	-
Alqueidao de St. Amaro	558567.2955	4404340.458	VI		6	VII	7	-			-	-	6	6	7	6	6	7
Aveiro	529931.5822	4499299.137	V		5	V	5	-			-	-	5	5	5	5	5	5
Azambuja	511418.8426	4324552.896	-		-	-	-	VII	VII	7	-	-	7	7	7	7	7	7
Azeitao	498779.5505	4263401.793	IX		9	IX	9	IX	IX	9	-	-	9	9	9	9	9	9
Badajoz	676085.6856	4305418.652	-	V-VI	5.5	V-VI	5.5	VII-VIII	VII-VIII	7.5	-	-	5.5	6.5	6.5	7.5	-	-
Beja	599806.8234	4208089.244	-		-	-	-	VIII-IX	VIII-IX	8.5	-	-	8.5	8.5	8.5	8.5	-	-
Borba	634152.3483	4296382.213	VI	-	6	VII	7	VI	VI	6	-	-	6	6	6.5	6	6	-
Braga	548371.2553	4599977.596	V	-	5	V	5	V	V	5	IV	4	4	4.67	4.67	5	-	-
Caceres	726224.4293	4372681.059	V	F	5	V	5	V	V	5	-	-	5	5	5	5	5	5
Cadiz	743007.8160	4045386.134	-	II-III	2.5	II-III	2.5	-			-	-	2.5	2.5	2.5	2.5	-	-
Caldas de Rainha	488084.8843	4361537.465	-		-	-	-	-	VIII	8	-	-	8	8	8	8	8	8
Caminha	513866.6482	4631248.155	V	-	5	V	5	-			-	-	5	5	5	5	5	5
Caparica	479500.7808	4277362.763	-		-	-	-	-	VIII	8	-	-	8	8	8	8	8	8
Cartaxo	518402.4408	4334553.800	VI	-	6	VI	6	VII	VII	7	-	-	6	6.5	6.5	7	-	-
Coimbra	549359.6737	4450782.890	VI	-	6	VI	6	VI	VI	6	V	5	5	5.67	5.67	6	-	-
Cordoba	871273.8277	4201017.812	-	V	5	V	5	VI	VI	6	-	-	5	5.5	5.5	6	-	-

Location																		
Estremoz	622187.6884	4300629.051	-		-	-	-	VII	VII	7	-	-	7	7	7	7	7	7
Evora	595830.0681	4269301.428	VI	-	6	VII	7	VII	VII	7	-	-	6	6.5	7	7	-	7
Faro	595004.3178	4097513.250	VI	-	6	VII	7	VII	VII	7	-	-	6	6.5	7	7	-	7
Figueira da Foz	512690.5382	4444527.601	-					VI	VI	6	-	-	6	6	6	6	6	6
Grandola	537837.7053	4225431.046	-					VIII-IX	VIII-IX	8.5	-	-	8.5	8.5	8.5	8.5	-	-
Guimaraes	558810.3716	4588064.284	-					V	V	5	-	-	5	5	5	5	5	5
Huelva	681874.7349	4125797.954	-	IV-V	4.5	IV-V	4.5	-					4.5	4.5	4.5	4.5	-	-
Jerez de la Frontera	756650.0230	4065773.652	-	V	5	V	5	-					5	5	5	5	5	5
Lagos	528967.4494	4106237.372	VI	-	6	VII	7	VII-VIII	VII-VIII	7.5	VII	7	6	6.83	7.17	7.5	-	-
Leiria	516535.7839	4399362.158	VI	-	6	VII	7	VII	VII	7	-	-	6	6.5	7	7	-	7
Lisbon	487829.5175	4285714.730	VI	-	6	VIII	8	VIII	VIII	8	VII-VIII	7.5	6	7.17	7.83	8	-	-
Madrid	950980.7680	4486843.243	-	V	5	V	5	-					5	5	5	5	5	-
Mafra	471573.1016	4309947.551	VI	-	6	VI	6	-					6	6	6	6	6	6
Marmelete	527737.5472	4128864.742	-		-	-	-	-	VII	7	-	-	7	7	7	7	7	7
Melides	523833.1463	4222160.123	-					IX	IX	9	IX	9	9	9	9	9	9	9
Mertola	618130.9943	4167049.459	-					VI	VI	6	-	-	6	6	6	6	6	6
Montemor o Novo	568397.5322	4278008.955	VI	-	6	VII	7	VII	VII	7	-	-	6	6.5	7	7	-	7
Obidos	486474.6368	4356961.116	-					VII	VII	7	VI	6	6	6.5	6.5	7	-	-
Odeceixe	520259.6824	4142821.895	-					-	VII	7	-	-	7	7	7	7	7	7
Odemira	531778.8475	4161274.723	-					-	VII	7	-	-	7	7	7	7	7	7
Palmela	508601.6965	4268956.660	-					IX	IX	9	-	-	9	9	9	9	9	9
Pederneira	493904.7728	4384030.970	-					VII	VII	7	-	-	7	7	7	7	7	7
Porto	532641.2483	4555481.617	V	-	5	V	5	V	V	5	IV	4	4	4.67	4.67	5	-	-
Puerto de Santa Maria	747952.5983	4054189.368	-	IV-V	4.5	IV-V	4.5	-					4.5	4.5	4.5	4.5	-	-
Sacavem	490620.7706	4293700.550	VI	-	6	VIII	8	VIII-IX	VIII-IX	8.5	-	-	6	7.25	8.25	8.5	-	-
Salamanca	780716.6370	4540677.182	-	IV	4	IV	4	IV	IV	4	-	-	4	4	4	4	4	4
Sanlucar de Barrameda	736318.9224	4073405.511	-	IV	4	IV	4	-					4	4	4	4	4	4

Site	X	Y																
Santarem	527359.3592	4342681.231	VI	-	6	VI	6	VIII	VIII	8	-	-	6	7	7	8	-	-
Santiago de Cacem	526798.3663	4207745.182	VI	-	6	VIII	8	IX	IX	9	VIII	8	6	7.67	8.33	9	-	-
Sao Teotonio	525893.8306	4151823.915	-	-	-	-	-	-	VII	7	-	-	7	7	7	7	7	7
Sesimbra	491186.3208	4255195.400	IX	-	9	IX	9	IX	IX	9	-	-	9	9	9	9	9	9
Setubal	509589.1145	4263518.395	IX	-	9	IX	9	IX	IX	9	IX	9	9	9	9	9	9	9
Sevilla	766398.4594	4142054.638	IV	VI	4	VI	6	VII-VIII	VII-VIII	7.5	-	-	4	5.5	6.5	7.5	-	-
Sines	511420.4712	4200941.116	VI	-	6	VIII	8	IX	IX	9	VIII-IX	8.5	6	7.83	8.5	9	-	-
Sintra	467176.7777	4294761.563	VI	-	6	VII	7	VII	VII	7	-	-	6	6.5	7	7	-	7
St. Andre	518861.3030	4212383.041	-	-	-	-	-	IX	IX	9	IX	9	9	9	9	9	9	9
Tavira	620009.4957	4109815.131	VI	-	6	VI	6	VI	VI	6	-	-	6	6	6	6	6	6
Tomar	550739.4153	4383751.447	VI	-	6	VII	7	-		-	-	-	6	6	7	6	6	7
Tras os montes	652794.9141	4605101.333	-	-	-	-	-	V	V	5	-	-	5	5	5	5	5	5
Valenca de Douro	618917.3913	4555488.187	V	-	5	V	5	-		-	-	-	5	5	5	5	5	5
Valladolid	856251.1036	4620098.409	-	III	3	III	3	IV	IV	4	-	-	3	3.5	3.5	4	-	-
Viana do Castelo	514396.1106	4615705.737	-	-	-	-	-	V	V	5	IV	4	4	4.5	4.5	5	-	-
Vila do Conde	521497.7176	4578198.504	-	-	-	-	-	V	V	5	-	-	5	5	5	5	5	5
Villa Franca de Xira	500866.4658	4311782.952	-	-	-	-	-	VIII	VIII	8	VII-VIII	7.5	7.5	7.75	7.75	8	-	-
Villa Real	605150.6147	4572932.539	V	-	5	V	5	V	V	5	-	-	5	5	5	5	5	5
Viseu	592057.8059	4501474.004	-	-	-	-	-	VI	VI	6	V	5	5	5.5	5.5	6	-	-
Zafra	725389.4864	4256350.871	-	V	5	V	5	-		-	-	-	5	5	5	5	5	5

3.3.3.2. Focal Depth, Epicenter, and Magnitude Estimation

First, we estimate the expected depth range of the 1858 event using the method by Sbarra et al. (2019). They used a learning data set of instrumental events to derive an empirical formula that relates the slope of the attenuation curve within the first 50 km with the depth of the earthquake. Then they applied their approach to a couple of instrumental and historical events and found good agreement suggesting that their approach is independent of magnitude. We compute the slopes of the attenuation curves and use their formula to compute the expected depth range for the MDPs GALB01, GALB02, PDS, MOR, AV01 and AV02.

Plotting the intensity versus the distance by considering the epicentre by Martínez Solares and Mezcua (2002), we find that the data agrees well with the attenuation law presented by Casado et al. (2000). Their work on seismic attenuation in the Iberian Peninsula incorporates this event, considering as mean radius of the isoseismal: 44 km (IX), 70 km (VIII), 115 km (VII), 180 km (VI), 270 km (V), 370 km (IV), 500 km (III), meaning that it is close to their 'low attenuation law' described by:

$$I_{est} = 5.557 + 0.902 I_0 + 0.014 I_0^2 - 1.762 \ln(d) - 0.00207 d \qquad (3.2)$$

where I_{est} is the estimated intensity, I_0 is the intensity at the epicentral area and d is the distance to the fault in km.

Proposed estimates locate the epicentre of the 1858 event close to the shore; thus, the azimuthal coverage of the isoseismal is limited mainly to the eastern areas. If we consider the MDPs in an above-described manner and use the attenuation relationship in Eq. (1) to estimate the epicentre, there will be a trade-off between the value we chose as epicentral intensity I_0 and the epicentre location. The misfit of the value of the mean square error given by,

$$\epsilon = \frac{\sum_{k=1}^{N_{MDP}} \sqrt{\left(I_{obs}^k - I_{est}^k\right)^2}}{N_{MDP}} \qquad (3.3)$$

where N_{MDPs} is the number of MDPs, we consider a point source and a hypocentral depth of 10 km for the low-intensity attenuation model of Casado et al. (2000), and the epicentre is located where the error is the minimum. For each set of MDPs, we use a range of I_0 to identify the minimum of all minima. The minimum of all minima is the epicentre for each data set, and we use the corresponding error grids to compute the average error grid for all data sets.

$$\bar{\epsilon}_{i,j} = \frac{\sum_{k=1}^{N_g} \epsilon_{i,j}}{N_g} \tag{3.4}$$

where $\epsilon_{i,j}$ is the error at each i,j-coordinate for each grid point and N_g is the number of error grids. We depict average error grid and the corresponding average error contours considering the ten data sets (c.f. Table 3.6) in Fig. 3.11.
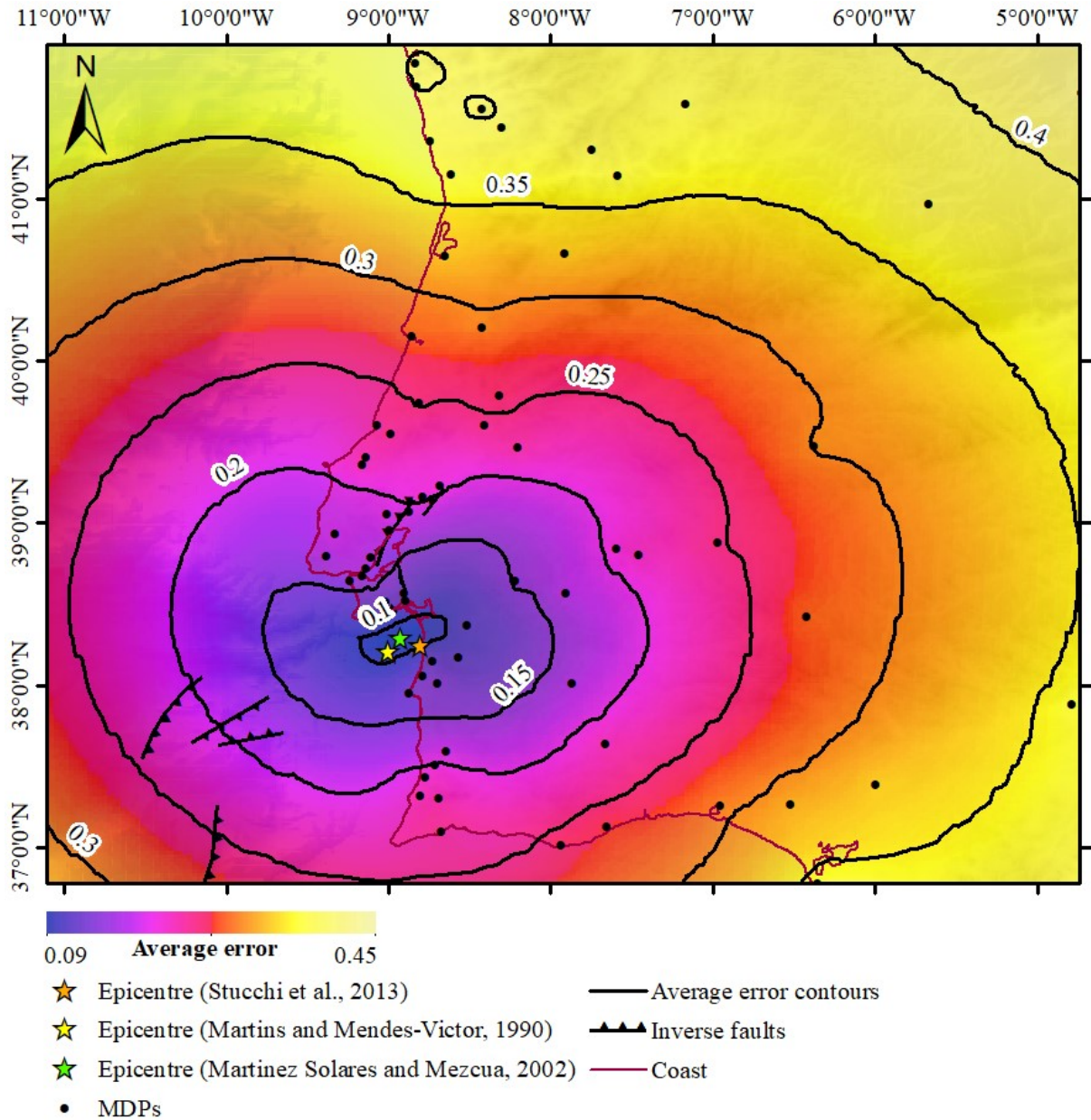
Figure 3.11 The average error field and corresponding error contours computed using Eq. 3 considering the data sets GALB01, GALB02, PDS, MOR, Low, AV01, AV02, High, ID01, ID02

The magnitude estimates for the 1858 event vary from 6.5 to 7.1. Vilanova and Fonseca (2007) found Mw 7.1 ± 0.3 using regression of the isoseismal areas according to Johnston and Kanter (1990). On the other hand, the most recent estimate is Mw 6.5 ± 0.76 proposed by Gomez-

Capera et al. (2015). They adapt the Boxer methodology (Gasperini et al., 1999, 2010). This estimate is based on the MDPs by Moreira (1991) (c.f. Table 3.6 column MOR) and the calibration dataset for the Boxer coefficients in stable continent regions (SCR). The calibration does not include events of this magnitude nor events on the Iberian Peninsula, mainly due to lack of data. To compensate for this, Gomez-Capera et al. (2015) apply the method, including the SCR-coefficients to the 1909 Benavente earthquake and obtain good agreement with previous moment magnitude estimates (Stich et al., 2005; Teves-Costa and Batlló, 2011). However, the 1909 Benavente earthquake data contains 454 MDPs and has a lower estimated magnitude than the 1858 Setúbal event, resulting in considerable smaller uncertainty. Gomez-Capera et al. (2015) adopt the Boxer method computing a magnitude M_I for each intensity class according to a function by Sibol et al. (1987),

$$M_I = a_I + b_I * log^2(A_I) + c_I * I_0^2 \tag{3.5}$$

where M_I is the magnitude for the i-th intensity, A_I is the area of the i-th isoseismal intensity, I_0 is the epicentral intensity, and a_I, b_I, and c_I are the coefficients for the SCR. Since the calibration data set contains events with a maximum moment magnitude of 5.5 the coefficients a_I, b_I, and c_I are for the SCR for a maximum isoseismal intensity of $I = 6$, and thus missing the intensities 7, 8 and 9 observed during the 1858 Setubal event. This fact and the limited amount of MDPs in Moreira (1991) dataset may underestimate the event's magnitude.

Gasperini et al. (2010) present an alternative method to estimate the macroseismic magnitude.

$$M_j = \frac{1}{d}\{I_j + \hat{a}(D_j - \hat{h}) + \hat{b}[\ln(D_j) - \ln(\hat{h})] - c \tag{3.6}$$

Where M_j is the macroseismic magnitude at each observation point, I_j is the observed intensity, D_j is the distance of the observation point to the epicenter, $\hat{h}$ is an average depth and $\hat{a}$ and $\hat{b}$ are the coefficients for the extended and c and d are the standard attenuation law fitted to Italian data (table 3.7).

Table 3.7 The coefficients $\hat{a}$, $\hat{b}$, $\hat{h}$ c, d used for magnitude estimation following Gasperini et al. (2010) in equation 3.6. σ_{M_w} is the standard deviation for the estimated moment magnitude M_w.

$\hat{a}$	$\hat{b}$	$\hat{h}$	c	d	σ_{M_w}
0.0009±0.0002	1.172±0.014	4.49±0.20	-4.446±0.645	2.210±0.122	0.31

The average depth $\hat{h}$ was used by Gasperini et al. (2010) to obtain best fits for the empirical I_0-M_w relationships and not the actual depth value for the given earthquake, thus $\hat{h}$ does not represent the depth of the event. The final magnitude of the earthquake is then computed as the mean of all M_j.

Alternatively, we use the empirical I_0-M_w relation for the SCR region presented in Stucchi et al. (2013).

$$M_w = 0.528 + 0.655I_0 \tag{3.7}$$

3.3.3.3. Fault Plane Orientation and Rupture Mechanism (Checking Geodynamics)

Here, we adopt the Boxer methodology (Gasperini et al., 2010). This method determines the axial orientation of the rupture source in the range of $0°-180°$, given as the weighted axial mean of the azimuthal distribution of MDPs above a chosen threshold I_{min}. Accordingly, we chose the threshold using the estimated subsurface rupture length (Wells and Coppersmith, 1994) to be closest to the mean distance of I_{min} varying according to the datasets used (c.f. Table 3.8). The ratio between the effective epicentral distance to the site and the predicted according to the attenuation law (Casado et al., 2000) defines the weights. We apply the Rayleigh and Kuiper test to check the circular distribution of data and evaluate the statistical significance of the computed fault orientation. Then we take Eurasia as the fixed plate and draw circles around the Euler pole at -20.61 W, 21.03 N according to the kinematic plate model Nuvel 1-A (DeMets et al., 1994; DeMets and Dixon 1999) to decide on a rupture mechanism for each fault according to its orientation with respect to the circle.

3.3.3.4. Numerical Tsunami Modelling

For the subsequent tsunami simulations, we use the code NSWING (Non-linear Shallow Water model wIth Nested Grids) (Miranda et al., 2014, Miranda and Luis, 2019). NSWING solves linear and nonlinear shallow water equations in Cartesian or spherical coordinates and allows implementing a system of coupled nested grids and computes inundation following a moving boundary scheme to track the moving shoreline (Liu et al., 1995, 1998). The code was benchmarked according to Synolakis et al. (2008) and used in Wronna et al., (2015, 2020), Omira et al. (2016). Baptista et al., (2016, 2020) use NSWING to compare modelling results with real event tide gauge recordings.
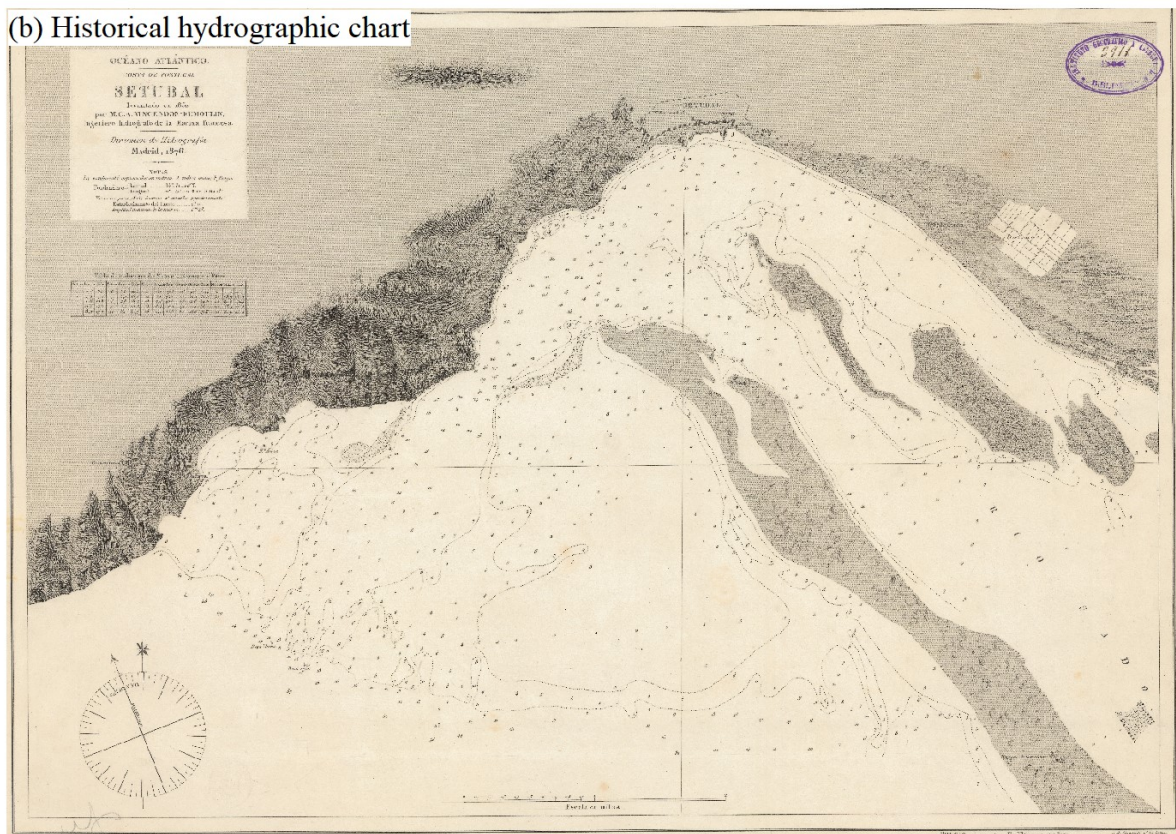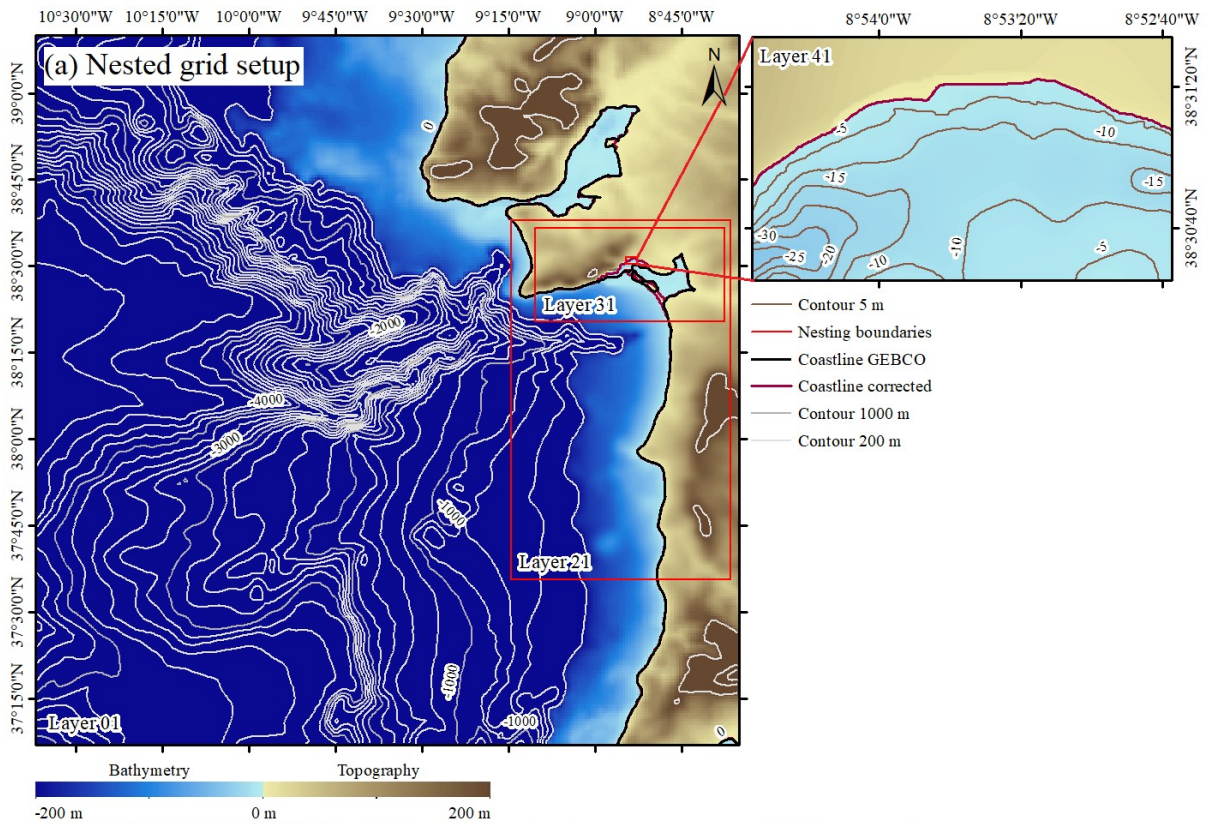
Figure 3.12 (a) depicts the nested grid setup. **(b)** shows the hydrographic chart by Vincendon-Dumoulin (1876)

We built a set of coupled nested grids to compute tsunami propagation from the source to the

shore (Fig. 3.12). The largest grid contains data from General Bathymetric Chart of the Ocean

(GEBCO, 2014), but interpolation of the original GEBCO data results in a false representation of the shoreline close to Setúbal, and since this is the source area of the earthquake, we impl mented a higher resolute LIDAR-data (Direção-Geral do Território, 2011) to compensate for this (Fig. 3.12). This layer has an approximate resolution of 0.008 degrees. We are using a total of four nested grids, and a refinement factor of 4 results in a resolution of 0.000125 degrees in the target area. The chosen timestep of 2 s satisfies the Courant-Friedrichs-Lewy condition to ensure numerical stability for the grids and we ran the numerical model for 3 h propagation time. For the target area, Setúbal, we built a Paleo-DEM applying a method presented in Wronna et al. (2017) that uses historical nautical charts and topographic maps. We implemented bathymetric data from the hydrographic chart by Vincendon-Dumoulin (1876) and re-traced the shoreline to reassemble the morphological conditions in 1858 (Fig. 3.12). It is worth to mention the data sounding of the historical chart was carried out already in 1852 and thus before the earthquake.

We use the half-space elastic theory (Mansinha and Smylie, 1971) embedded in the Mirone suite program (Luis, 2007) to compute the coseismic deformation according to the fault param-eters obtained from the analysis of the MDPs. It is common practice to assume that water is an incompressible fluid and thus that the sea surface displacement mimics the vertical coseismic deformation. Therefore, we transfer the vertical coseismic deformation to the sea surface and use it to launch the tsunami simulations. In the simulation, we use the mean sea-level as a ver-tical reference and compute offshore wave heights at chosen Virtual Tide Gauges (VTGs) in the Digital Elevation Model (DEM) (Fig. 3.14).

3.3.4. Results

We present the results and the error for each I_0 at each intensity level in Table 3.8 and Fig. 3.13. The obtained epicentres are in line with the previously suggested ones (Gomez-Capera et al., 2015; Martins and Mendes-Victor, 1990; Martínez Solares and Mezcua, 2002). The western-most epicentre results when considering the dataset PDS. We obtain the easternmost and inland located epicentre at 8.702 W, 38.343 N using the dataset GALB01 (Table 3.8, Fig. 3.13). The epicentres obtained using all the other data sets lay within a 20 km E–W trending stretch with relatively well-defined latitude at 38.313 ± 0.06 N and longitude 8.879 ± 0.12 W, which is confirmed by the average error contours when considering all epicentre estimates (Figs. 3.11 and 3.13). The epicentres for the datasets AV02 and ID01 and the datasets AV01 and GALB02 are identical. For the GALB01 and the PDS dataset,we obtain the lowest and largest epicentral

intensity $I_0 = 8.6$ and $I_0 = 9.7$, respectively. The magnitude estimates for all datasets are within a range of 6.5–7.1 ± 0.31 when considering Eq. (3.6). The more conservative approach Eq. (3.7) results in a magnitude range of 6.2–6.9 ± 0.25. The best fits for the depth estimates vary between 1 and 29.6 km; the uncertainty increases with depth following the approach by Sbarra et al. (2019). The mean fault orientation has a strike of approximately 40 ± 7 degrees. Here, we discard the fault orientation for the datasets PDS, MOR, AV02 and ID01 because the Rayleigh-test resulted in probability values of 0.96, 0.38, 0.2, and 0.12 and thus exceed the 0.1 significance level which was similarly used by Gasperini et al. (2010). We obtain mean fault dimensions of 13.83 ± 2.14 km width 29.5 ± 5.5 km length. We plot the corresponding fault planes and orientations in Fig. 3.13.

Table 3.8 The coordinates for the epicentres, the maximum epicentral intensities, the minimum error of the epicentre estimation defined in Eq. 3.3, the estimated moment magnitude according to Eqs. 3.6 and 3.7, the hypocentral depth, the strike of the fault and the resulting fault plane dimensions according to Wells and Coppersmith (1994) for the datasets GALB01, GALB02, PDS, MOR, LOW, AV01, AV02, HIGH, ID01, ID02. Below we present the average value considering all results of this study and the associated standard deviation abbreviated as StDv. We discarded the fault orientations marked with an asterisk

MDP dataset	Epicenter coordinates		I_0	ϵ	M_w		Depth (km)	Strike (°)	Fault plane	
	Lon. (°)	Lat. (°)			Eq. 3.6 ±0.31	Eq. 3.75 ±0.25			W (km)	L (km)
GALB01	-8.702	38.434	8.6	0.12	6.5	6.2	10.2 ± 3.6	47.8	11	22
GALB02	-8.840	38.326	9.1	0.10	6.7	6.5	8.6 ± 2.7	30.4	14	29
PDS	-9.183	38.182	9.7	0.09	7.1	6.9	28.1 ± 14.7	38.5*	20	50
MOR	-8.954	38.254	8.9	0.09	6.7	6.4	4.0 ± 0.8	27.6*	14	29
LOW	-8.794	38.362	8.8	0.10	6.6	6.3	1.0 ± 0.0	41.8	12	26
AV01	-8.840	38.326	9.1	0.08	6.7	6.5	5.0 ± 1.2	44.1	14	29
AV02	-8.931	38.290	9.3	0.08	6.8	6.6	11.5 ± 4.2	40.7*	15	33
HIGH	-8.817	38.326	9.4	0.09	6.9	6.7	29.6 ± 15.1	32.2	17	38
ID01	-8.931	38.290	9.2	0.06	6.8	6.6	12.4 ± 4.7	41.4*	15	33
ID02	-8.794	38.344	9.2	0.09	6.8	6.6	17.5 ± 7.7	41.6	15	33
Average	-8.879	38.313	9.13	0.09	6.76	6.53	12.8	39.6	13.8	29.5
StDv	±0.12	±0.06	±0.3	0.02	±0.16	±0.19	±9.2	±7	±2.1	±5.5

The fault planes are close to perpendicular to the Eulerpole circle with a plate velocity of 4.7 mm/year concerning Africa location as fixed. Moreover, the strike of the compressive structures F1, TTR-10 and Arrabida chain are similar. So, we can conclude that we must consider a compressive regime for the fault planes orientation according to the MDP datasets. We consider the minimum, average and maximum fault dimension, the mean depth, and mean strike of the obtained fault orientations for the tsunami simulation. The applied method does not determine the

dip direction; thus, we consider both northwest and southeast dipping cases. We assume a dip angle of 40 degrees for all thrust faults and rigidity of 3×10^{10} Pa for all cases. Additionally, we tested the proposed extension of the PNAF considering a strike-slip source according to Moniz and Cabral (2014), testing it with the most considerable magnitude of 7.1. We summarize the parameters for the numerical tsunami modelling in Table 3.9.
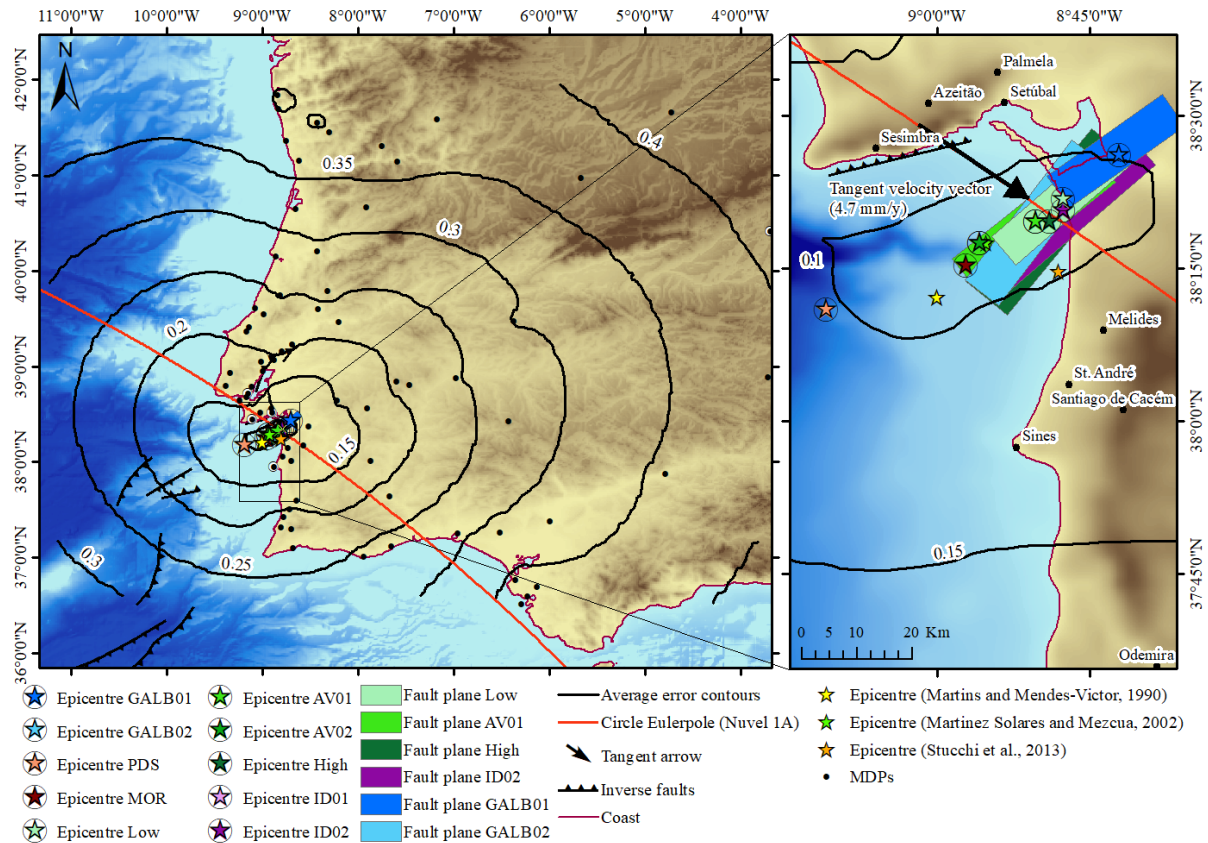
Figure 3.13 The coloured stars represent the determined epicentres for the defined datasets. The contours represent the average error considering all datasets. The red circle illustrates the circle around the Eulerpole at - 20.61 W, 21.03 N and the arrow plots the tangent velocity vector and gives a relative plate velocity of 4.7 mm per year computed by the kinematic plate model Nuvel 1-A (DeMets et al., 1994). The black points show the location of all Macroseismic Data Points (MDPs). The rectangles depict the fault planes considering the strike, width, and length (c.f. Table 3.8)

The initial sea level deformation for the strike-slip fault scenario SS71 has a maximum of 0.16 m (Fig. 3.14) and the simulation predicts that the maximum wave height in the Sado estuary is less than 0.2 m. Close to the shore in Setúbal, the maximum water level reaches 0.18 m (Fig. 3.14). The recordings at the VTGs a maximum sea elevation of 0.08 m at the VTG located at the Estuary (VTG Est.) entrance of the Sado river (Fig. 3.14).

We plot the VTG recording for the thrust scenarios R65s, R65n, R67s, R67n, R71s and R71n in Fig. 3.15 and present the results of the numerical tsunami simulations in Figs. 3.16, 3.17, 3.18.

Table 3.9 Rupture parameters and focal mechanisms used for tsunami modelling

Fault	M_w	L (km)	W (km)	Strike (°)	Dip (°)	Rake (°)	Slip (m)	Depth (km)	Focal mechanism
R65s	6.5	22	11	40	40	90	1	12.8	
R65n	6.5	22	11	220	40	90	1	12.8	
R67n	6.7	29.5	14	40	40	90	1.3	12.8	
R67n	6.7	29.5	14	220	40	90	1.3	12.8	
R71s	7.1	50	20	40	40	90	2.2	12.8	
R71n	7.1	50	20	220	40	90	2.2	12.8	
SS71	7.1	68	14.3	160	85	10	1.7	5	
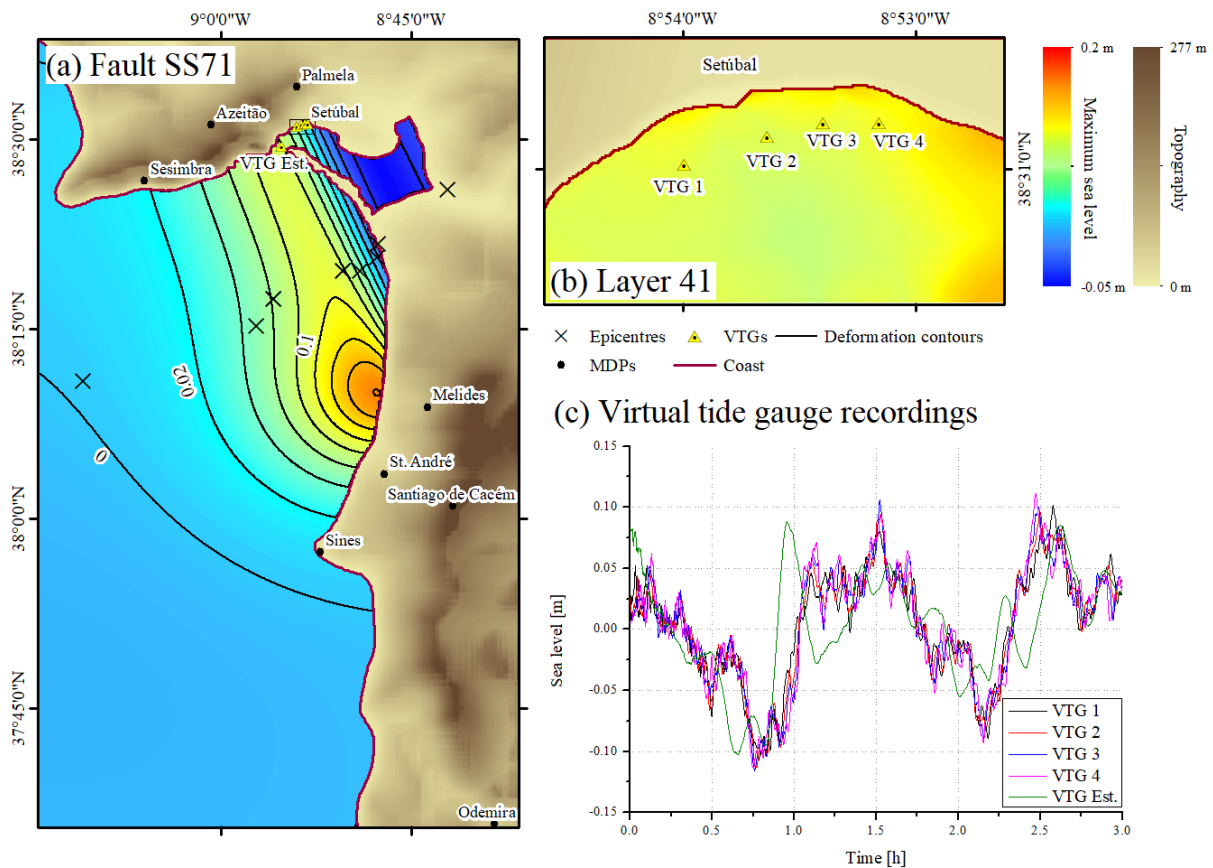
Figure 3.14 Results for the strike-slip scenario SS71. **(a)** shows the deformation field and contours (m) of the tsunami generated by the co-seismic deformation of the SS71 fault scenario, **(b)** shows the Virtual Tide Gauge (VTG) locations and the maximum sea level (m) due to the tsunami caused by the SS71 fault scenario at the target site in Setúbal and c shows the recordings of the sea elevation (m) at the Virtual Tide Gauges
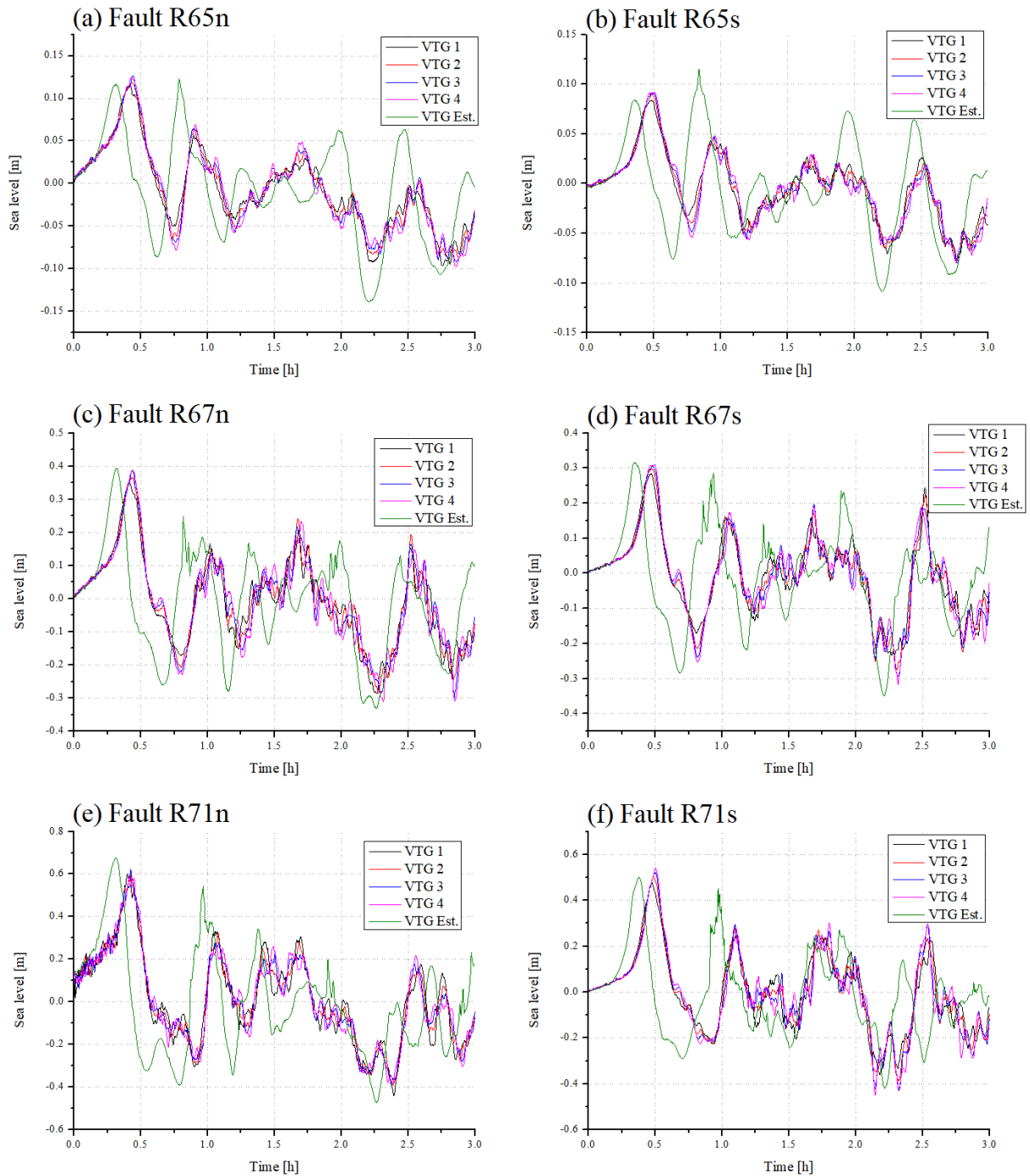
Figure 3.15 The Virtual Tide Gauge (VTG) records for **(a)** the R65n fault scenario, **(b)** the R65s fault scenario, **(c)** the R67n fault scenario, **(d)** the R67s fault scenario, **(e)** the R71n fault scenario, **(f)** the R71s fault scenario (c.f. Table 3.9)

The two cases, the north- and the south-dipping thrust fault considering a $M_w = 6.5$, R65n and R65s generate wave heights at the VTGs of about 0.1 m (Fig. 3.15). The south-dipping thrust fault R65s producing a maximum sea level of less than 0.08 m is less effective in terms of tsunami genesis compared to the north-dipping thrust fault R65n. We observe the same effect for the thrust faults with greater magnitude. The south-dipping thrust faults are less effective than their northern counterparts. The north dipping thrust fault R67n with a $M_w = 6.7$ generates

a maximum sea level elevation at the VTGs of about 0.1 m greater than the south-dipping thrust fault R67s. Furthermore, the north-dipping thrust fault R71n with $M_w = 7.1$ produces a maximum water level of about 0.05 m larger than its southern dipping counterpart.
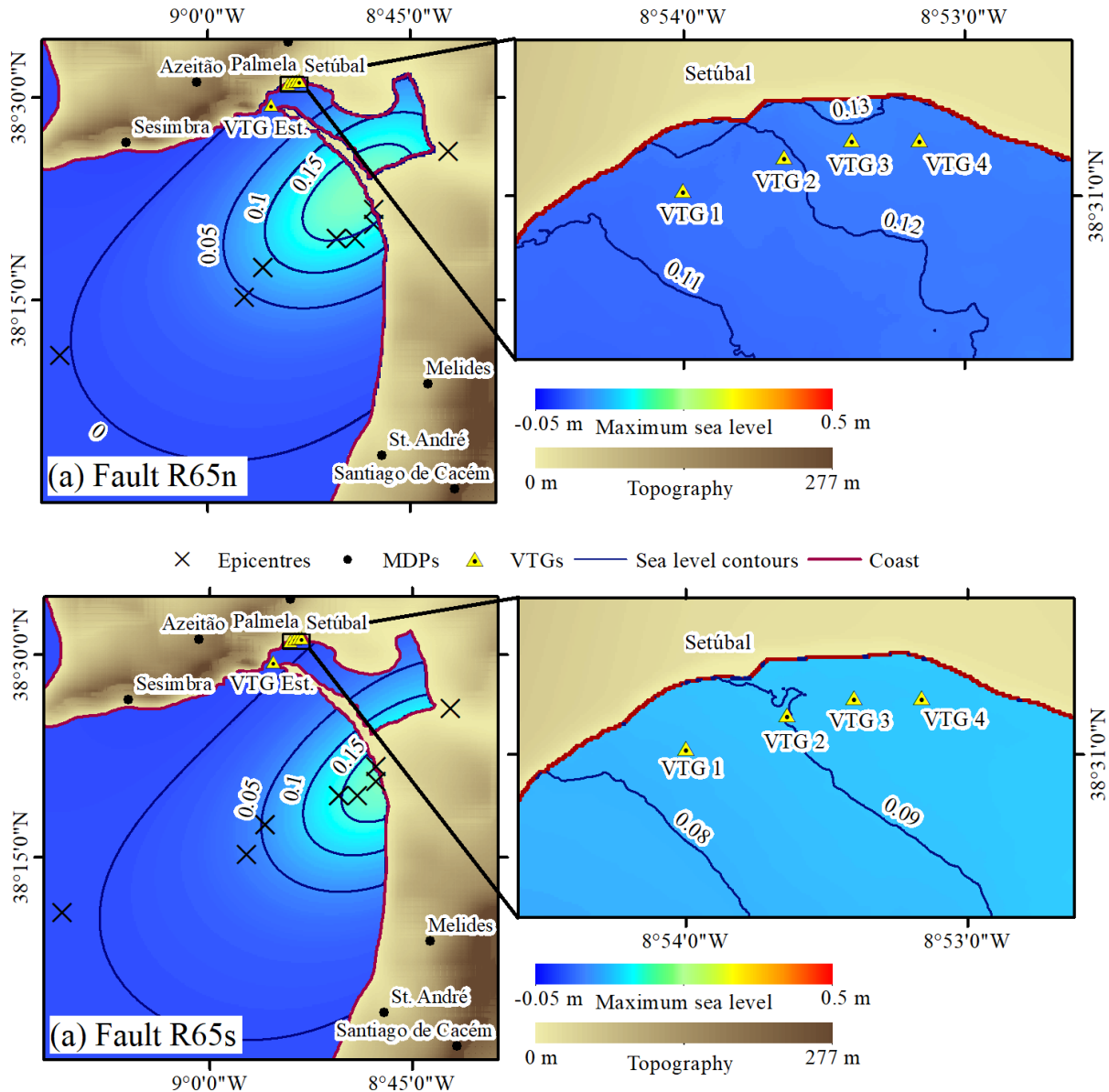
Figure 3.16 Results for the reverse fault scenario R65n **(a)** and R65s **(b)**. The left panel shows the deformation field and contours (m) of the tsunami generated by the co-seismic deformation of the R65n and R65s fault scenario, and the right panel shows the Virtual Tide Gauge (VTG) locations and the maximum sea level and the corresponding contours (m) due to the tsunami caused by the R65n and R65s fault scenario at the target site in Setúbal

The maximum uplift generated by both thrust faults with $M_w = 6.5$ is less than 0.2 m, and the resulting maximum water elevation in the Sado estuary for the north- and south-dipping thrust is about 0.13 m and 0.09 m, respectively (Figs. 3.15 and 3.16). Both thrust faults cause only minor inundation in some adjacent cells to the Sado river.
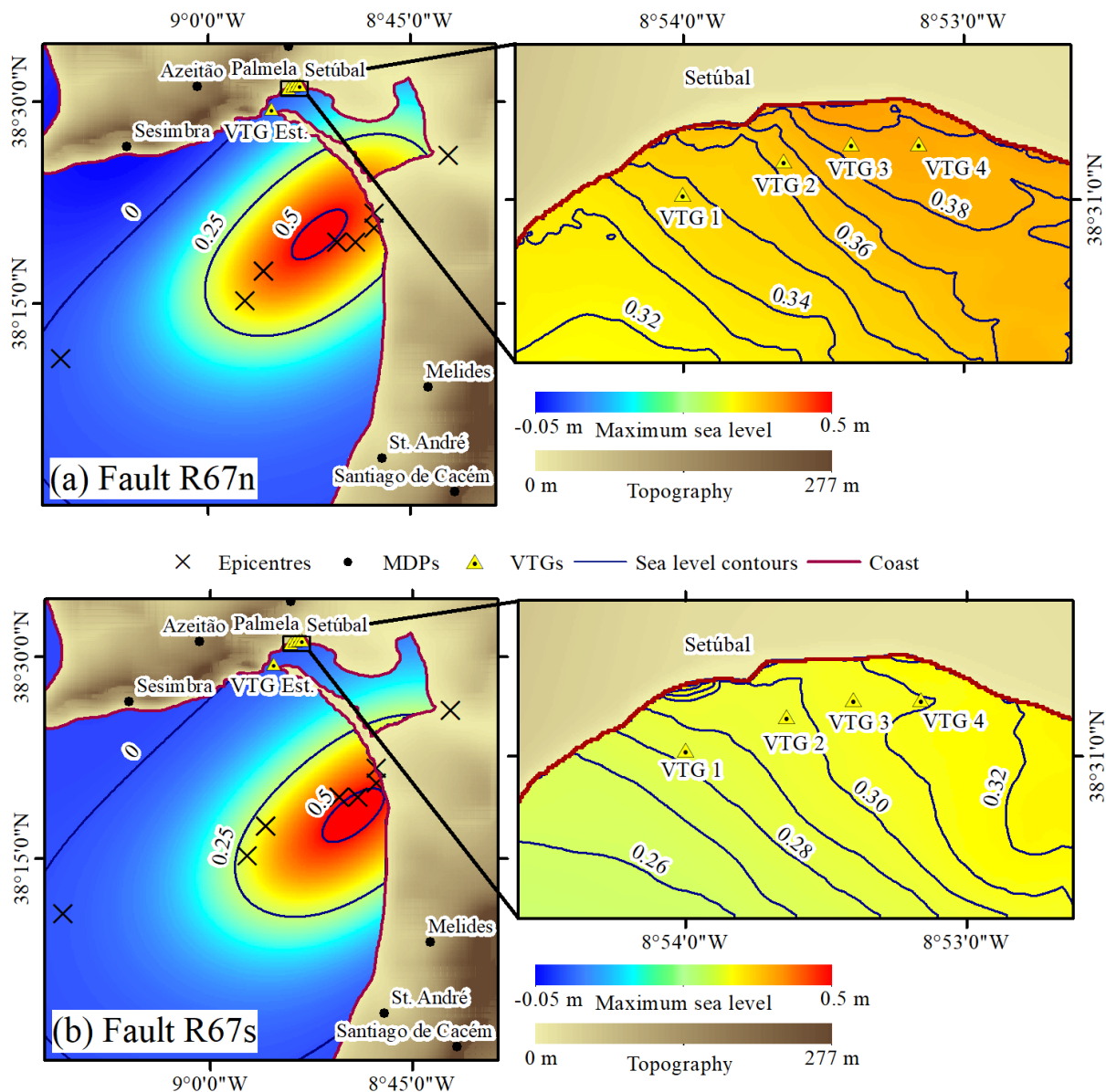
Figure 3.17 Results for the reverse fault scenario R67n **(a)** and R67s **(b)**. The left panel shows the deformation field and contours (m) of the tsunami generated by the co-seismic deformation of the R67n and R67s fault scenario, and the right panel shows the Virtual Tide Gauge (VTG) locations and the maximum sea level and the corresponding contours (m) due to the tsunami caused by the R67n and R67s fault scenario at the target site in Setúbal

Both thrust faults with $M_w = 6.7$ generate a tsunami with a maximum water level of about 0.5 m close to shore near Melides (Fig. 3.17). The VTG register a maximum water elevation of 0.4 and 0.3 m by the north- and south-dipping faults R67n and R67s, respectively (Fig. 3.15). Close to the shore in Setúbal, the corresponding wave heights are 0.4 and 0.3 m (Fig. 3.15). Like the $M_w = 6.5$ thrust faults, the tsunamis generated by the $M_w = 6.7$, inundate bordering cells of the river Sado, although a more significant number.

The most effective fault considering tsunami genesis is fault R71n with maximum water elevations of 0.6 m at the VTG recordings. The offshore tsunami at the maximum of the initial tsunami waveform has a water elevation of about 0.75 m (Fig. 3.18). This fault causes a maximum

water level of about 1 m at the shore and produces some considerable inundation along the beaches in the city Setúbal of 1858 with a maximum inundation distance of ca. 40 m. Contrary, the south-dipping thrust fault R71s produces 0.5 m water elevation at the VTGs along the riverbanks in Setúbal. The maximum wave height close to the shore is 0.55 m, and the resulting inundation is less than the one produced by the north-dipping fault.
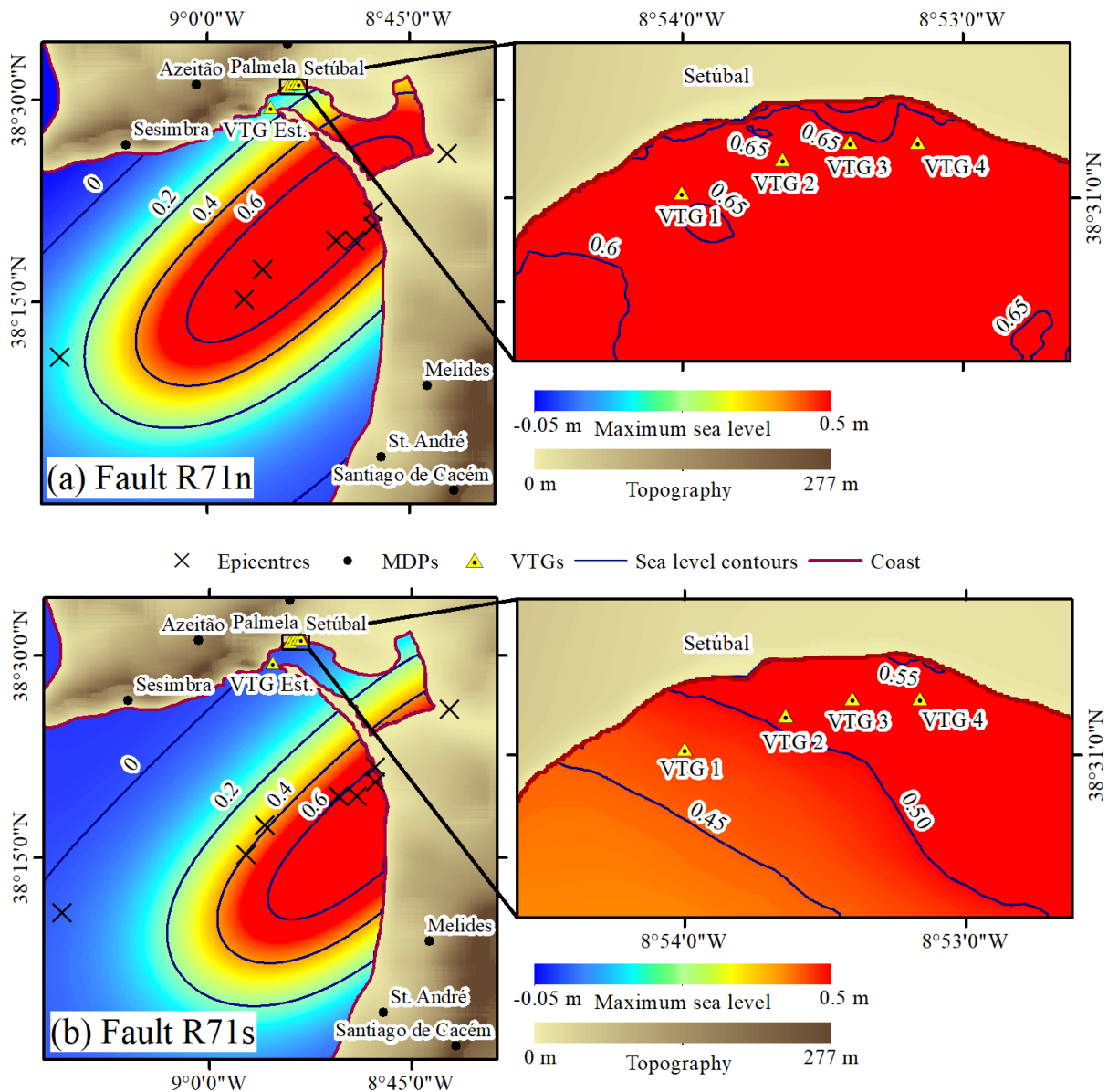
Figure 3.18 Results for the reverse fault scenario R71n **(a)** and R71s **(b)**. The left panel shows the deformation field and contours (m) of the tsunami generated by the co-seismic deformation of the R71n and R71s fault scenario, and the right panel shows the Virtual Tide Gauge (VTG) locations and the maximum sea level and the corresponding contours (m) due to the tsunami caused by the R71n and R71s fault scenario at the target site in Setúbal

3.3.5. Discussion

We use MDPs to reassess the depth, epicentre, magnitude, and fault orientation of the 11 November 1858 earthquake in Setúbal.

75

The most recent works and the SHARE European Earthquake Catalogue (SHEEC) (Stucchi et al., 2013; Gomez-Capera et al., 2015) use a total number of 16 MDPs in Portugal (Moreira, 1984). Consequently, their estimates rely on this limited number of MDPs. Thus, the combination of other datasets may help reveal more details, especially considering historical events. Here we compile the data in the references and those non-present in the SHEEC and use 71 MDPs.

Being aware that historic macroseismic data contains inherent uncertainties we find the magnitude and epicentre estimates range in line with previous results supporting the schematic approach. Moreover, the larger number of MDPs allows estimating the fault orientation, where we find an average of 40 ± 7 degrees. That is about 50 degrees different to the earlier proposed extension of the PNAF with a strike-slip mechanism (Moniz and Cabral, 2014). Besides, the average error contours and the distribution of the epicentres along the computed strike support the proposed fault orientation. The kinematic plate model NUVEL 1A (DeMets and Dixon, 1999) predicts a tangent velocity of 4.7 mm/years, suggesting a thrust mechanism for the determined fault orientation which agrees with the areas stress pattern (Borges et al., 2001; Ribeiro et al., 1996). The new fault's strike and the kinematic plate model suggest a compressive regime and a thrust rupture mechanism for the 1858 event. This result contradicts the PNAF-hypothesis; nevertheless, we consider it for the tsunami simulation and find that this strike-slip fault has insignificant tsunamigenic potential. Moreover, according to scaling relationships (Blaser et al., 2010; Wells and Coppersmith, 1994), a strike-slip rupture with Mw ~ 7 should be approximately 60 km long. That is about twice the length of the known PNAF. On the other hand, the simple source model used for tsunami modelling does not consider eventual fault geometry complexities that might result in more effective tsunami genesis, even for strike-slip rupture mechanisms.

A geological structure of the dimensions for Mw ~ 7 is not known in the epicentral area but is close to parallel to the inferred fault system related to the Arrabida chain (Cabral et al., 2003; Kullberg et al., 2000; Ribeiro et al., 1990) and could eventually be an extension of the active thrust faults F1 or TTR10 (Ribeiro et al., 2000; Terrinha et al., 2003). However, those faults are approximately 80 km southwest of the epicentral area. Alves et al. (2003, 2009) mapped some NW–SE normal faults between the Arrabida chain and Sines but no connection to thrust faults offshore. Those faults are approximately perpendicular to the faults proposed in this study and most likely related to Mesozoic rifting. Thus, they are not necessarily contradictory to the results of our analysis especially when considering the world stress data (Heidbach et al., 2016; Stich et al., 2020) and GNSS data (Matos et al., 2018; Palano et al., 2015) in the proposed

source area. Our findings, the missing geological evidence, and the ambiguities in the proposed source zone require further field investigation.

Considering the tsunami simulations, we observe that the northern dipping faults independent of the magnitude have more significant tsunamigenic potential than their southern counterparts. Commonly, and according to the half-space elastic (Mansinha and Smylie, 1971; Okada, 1985), tsunamis are Leading Depression N-waves (LDN). Tsunamis with larger leading depressions may positively influence the runup (Madsen and Schäffers, 2010; Wronna et al., 2020). The co-seismic deformations in this study produce a leading depression of less than 0.1 m and thus, have only subordinate importance. Another reason for more effective tsunami genesis of the north-dipping faults may be that they disturb a more extensive area of water as a larger fraction of their co-seismic deformation is submarine compared to the south-dipping faults. Moreover, the north dipping faults also cause uplift to a larger area in the Sado Estuary. We also speculate that this may cause the smaller ripples on VTG recordings for the north dipping faults (c.f. Figure 8a, c and e).

The only description of the tsunami in 1858, to our knowledge, is reproduced in Quintas (1993). Further, no other tsunami observations elsewhere are known. The day of the earthquake was a stormy day with heavy rainfalls (Miranda, 1935); thus, we may speculate that a weak tsunami was eventually less likely to be observed in the agitated water of the Atlantic than in the relatively calm waters of the Sado estuary. Therefore, if we consider the description in Quintas (1993) trustworthy, the only source capable of producing some inundation and leaving boats on dry land is the northern dipping Mw 7.1 fault. We also investigated the tide at the time of the earthquake using a moon phase table and concluded that the tide was full at around 6 a.m., and at 7 a.m., the tide was 3.08 m above hydrographic zero. This tide condition could favour a more significant inundation when considering a lower magnitude event.

Considering the results of the macroseismic analyses, a magnitude of 7.1 is the upper bound of the magnitude range. However, under certain circumstances, a shallower fault or larger and localized slip values may also result in significant sea level perturbation and inundation even with a smaller moment magnitude (see Baptista et al., 2014).

3.3.6. Conclusions

Our study shows that the macroseismic analysis considering a larger or composite datasets is crucial for a better understanding of historical events.

The determination of the epicentral area using a range of epicentre intensity values (I_0) allows computing the average error field considering multiple datasets. For the 1858 event our analysis suggests an epicentral area south of Setúbal (Fig. 3.13).

Concerning the possible fault mechanism, our results favour a compressive rupture. Our preferred solution is a north dipping thrust fault with a 40 ± 7degree strike probably subparallel to the Arrabida Chain centred at the coordinates at 8.879 W, 38.313 N, located at a mean depth of 12.8 km. The thrust fault and rupture mechanism suggested is compatible with the kinematic plate model NUVEL-1A.

Tsunami numerical modelling suggests that an earthquake of magnitude close to 7 with revers fault mechanism may generate a tsunami that reproduces the observation. On the other hand, the Mw 7.1 strike-slip scenario does not support the tsunami observation. It is worth noting that we could not verify the tsunami observation because most coeval sources were not available for consultation. The proposed fault may generate tsunamis of low to moderate intensity with short travel times that may impact harbour infrastructure, previously affected by seismic shaking.

In summary, the 1858 event should be considered in future tsunami hazard assessments in the SWIM area.

4. Tsunami propagation and runup - A new tsunami runup predictor

Tsunami impact parameters can be summarized as the tsunami runup, inundation height, and flow depth. These parameters are also the most common ones to be measured during post-event field surveys (c.f. Chapter 5). The tsunami runup height is the elevation the seawater reached relative to the sea level at the time of the tsunami. Thus, a quick estimate of tsunami runup may be helpful to delimit an evacuation area, i.e., establish safe zones along an exposed coast. Practically, the tsunami runup height might vary significantly along the affected coast depending on source orientation, coastal bathymetry, and topography, etc. Hence, the runup estimate is challenging since it depends on many nonlinear factors such as accurate nearshore bathymetry and topography, bottom roughness, wave breaking, and other sources of energy dissipation. Most numerical models do not include wave breaking, but some of them may produce better results if they consider a source of energy dissipation, primarily including bottom friction (c.f. Chapter 2.1). Nevertheless, numerical models compute the tsunami impact relatively well but require a certain amount of time which is limited for early warning. Moreover, high resolution bathymetric and topographic data, which is required by numerical models to have accurate estimates, is often not available over large coastal stretches.

The ultimate goal of any tsunami warning system is to estimate the parameters of the tsunami impact before the tsunami hits the target coast is. There might be enough time to evacuate the target coast for far-field events. For instance, Hawaii's civil defence lasts about three hours to evacuate the entire coastline (National Research Council, 2011), which is possible for far-field events. A couple of operating forecasting systems are in place, for example, at the National Oceanic and Atmospheric Administration (NOAA) (Titov et al., 2016), the Indonesian Meteorology, Climatology, and Geophysical Agency (BKGM) (Rudloff et al., 2009), the Japan Meteorological Agency (JMA, 2013), and the Australia Tsunami Warning Systems (Greenslade et al., 2019). However, this is challenging for nearshore events and since most tsunamis travel at fast speeds in the deep ocean. In addition, it is hard to anticipate their generating mechanism. Hence, for events closer to the shore tsunami, rapid early warning systems must be developed. For such systems, the estimation of the tsunami impact must occur within a short time or nearly instantly. Thus, the development of methods for quick runup estimation is needed.

In this thesis, a new method is developed to evaluate the runup quickly, based on a source-to-coast approach. The formulation calculates the expected runup height based on estimated waveform parameters. Early warning systems that currently only estimate expected wave heights

close to the shore could implement this method, presenting additional information on tsunami runup height for emergency managers.

4.1.   A new tsunami runup predictor

4.1.1. Abstract

We introduce a new parameter, tsunami runup predictor (TRP), relating the accelerating phase of the wave to the length of the beach slope over which the wave is travelling. We show the existence of a relationship between the TRP and the runup for different initial waveforms, i.e. leading elevation *N*-waves (LENs) and leading depression *N*-waves (LDNs). Then, we use the TRP to estimate tsunami runup for past tsunami events. The comparison of the runup estimates against field data gives promising results. Thus, the TRP provides first-order estimates of tsunami runup once the offshore waveform is known or estimated and, therefore, it could be beneficial to be implemented in tsunami early warning systems.

4.1.2. Introduction

Tsunamis have been causing enormous loss of lives and assets repeatedly (Synolakis and Bernard, 2006; Kânoğlu et al., 2015). Preparedness and timely early warning could mitigate losses for future events. There are a limited number of operational forecasting methodologies such as the ones used at the National Oceanic and Atmospheric Administration (NOAA) (Titov et al., 2016), the Indonesian Meteorology, Climatology, and Geophysical Agency (BKGM) (Rudloff et al., 2009), the Japan Meteorological Agency (JMA) (2013), and the Australia Tsunami Warning Systems (Greenslade et al., 2019).

One significant guiding parameter in tsunami warning is the maximum runup, defined as the difference in elevation between the maximum tsunami penetration and the still water line at the time of an event (Fig. 4.1).
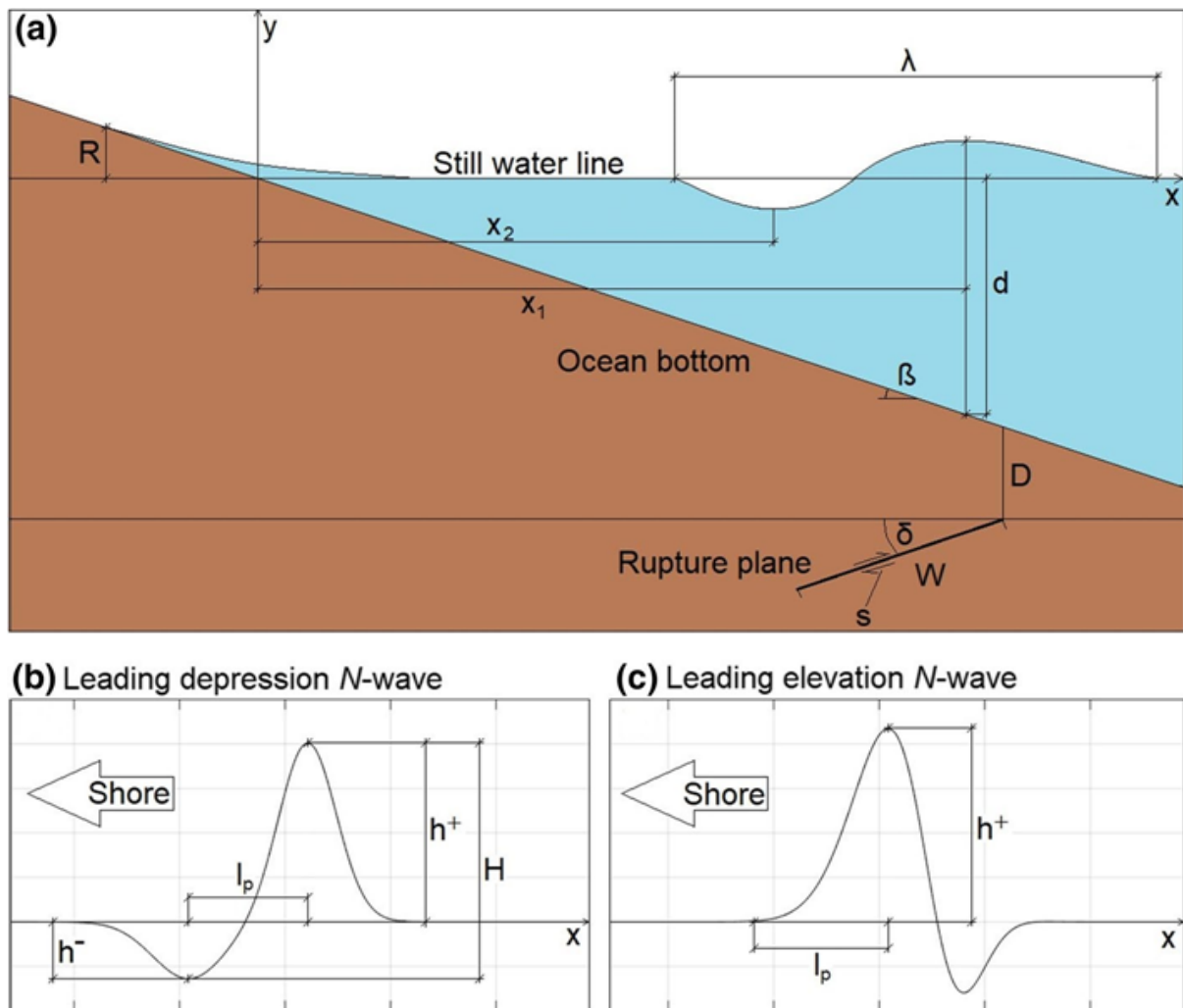
Figure 4.1 Definition sketch. a The shoreline is located at the origin of the coordinate system. R shows the maximum runup. β is the beach slope angle, and d is the ocean depth at maximum amplitude. Wave parameters: x_1 and x_2 are the distances of the maximum amplitude of the crest h^+ and the minimum amplitude of the through h^- to the shore, respectively. λ shows the wavelength. Fault plane parameters: D, W, δ and s are the depth of the fault top to the ocean bottom, the width of the fault, the dip of the fault, and the fault slip amount, respectively; b definition parameters for LDNs; l_p is the horizontal length of the wave face, and h^+ and h^- are the positive and negative amplitudes, respectively; c definition parameters for LENs; l_p is the horizontal length of the wave face, and h^+ is the positive amplitude.

Numerous studies have addressed the long wave runup on a beach through numerical and analytical methods. Numerical models compute tsunami runup solving the nonlinear shallow water-wave (NSW) equations (Imamura, 1995; Titov and Synolakis, 1995, 1998; Liu et al., 1998; Tinti and Tonini, 2013; Miranda et al., 2014; Titov et al., 2016; Miranda and Luis, 2019) or Boussinesq-type equations (Madsen and Sørensen, 1992; Chen and Liu, 1995; Kirby et al., 1998; Fuhrman and Madsen, 2009), mostly validated and verified through Synolakis et al., (2008). Application of these models to field cases employs the half-space elastic theory (Okada, 1985; Mansinha and Smylie, 1971) to produce the initial waveforms for earthquake-generated tsunamis. These models compute wave propagation and runup using appropriate digital elevation models (DEMs). Numerical models may predict inundation parameters with high accuracy since they solve tsunami propagation on a real bathymetry using waveforms compatible with

earthquake parameters. However, at least currently, these models may be unsuitable to be used in real time implementing high-resolution bathymetry and topography in the DEMs since the computation with high-resolution is time-consuming. Besides, such bathymetry and topography data could be proprietary. Runup may be computed using a moving boundary algorithm (Liu et al., 1995, 1998). However, accurate runup computation depends on many factors such as accurate near shore bathymetry and topography, bottom roughness, wave breaking, and energy dissipation. Most numerical tsunami models do not solve wave breaking, but they produce better inundation results if they include some numerical dissipation or using bottom friction including the Manning-coefficient (Burwell et al., 2007; Bricker et al., 2015). However, numerical models allow computation of tsunami impact reasonably well.

On the other hand, analytical methods estimate the runup in the correct order of magnitude (e.g. Synolakis, 1987; Pelinovsky and Mazova, 1992; Kânoğlu and Synolakis, 1998; Kânoğlu, 2004; Tinti and Tonini, 2005; Didenkulova et al., 2006, 2007a, b; Aydın and Kânoğlu, 2017). Indeed, the analytical solutions have some limitations, such as using the shallow water-wave theory and idealized bathymetric profiles. Synolakis (1987) presented a solution to the linear shallow water-wave equation for the canonical problem -a constant depth region connected to a sloping beach- and extended the linear solution to the nonlinear solution using Carrier and Greenspan's (1958) hodograph transformation. Tadepalli and Synolakis (1994, 1996) proposed leading depression *N*-waves (LDNs) to be more appropriate to describe a realistic initial tsunami waveform. Tadepalli and Synolakis (1996) include a horizontal length scale and a steepness parameter. They demonstrated that LDNs produce higher runup than solitary and leading elevation *N*-waves (LENs) with the same amplitude. Later, Madsen et al. (2008) concluded that the solitary wave tie to describe *N*-waves as proposed by Tadepalli and Synolakis (1994, 1996) does not appropriately represent spatial and temporal scales of realistic geophysical tsunamis. Madsen and Schäffer (2010) presented analytical runup solutions for sinusoidal, single, N, and transient waves to overcome this problem. As also implied in Tadepalli and Synolakis (1994, 1996), they demonstrated that a larger amplitude ratio negative–positive amplitude positively influences the runup. Chan and Liu (2012) studied the runup numerically and analytically, adapting and extending the earlier solutions of Synolakis (1987) and Madsen and Schäffer (2010) for cnoidal and multiple solitary waves. Using profiles from the 2011 Tohoku-Oki, Japan tsunami, they find that the triggered tsunami waveform was different from a solitary wave in near- and farfields. Moreover, they concluded that the accelerating phase of the incident wave controls the maximum runup.

Further, Kânoğlu (2004) proposed that Carrier and Greenspan's (1958) hodograph transformation can be linearized for the spatial variable to define the initial condition, a vexing issue. Aydın and Kânoğlu (2017) provided an efficient computational framework using Kânoğlu's (2004) approach and solved the NSW equations employing eigenfunction expansion on a sloping beach as a classical initial value problem.

Sepúlveda and Liu (2016) expressed maximum runup in terms of earthquake fault plane parameters. They use Okada (1985) to estimate initial source parameters. Further, they identified a general relationship between the maximum runup and earthquake source parameters adopting the boundary and initial value problem solutions of the nonlinear shallow water-wave equations through Madsen and Schäffer (2010) and Kânoğlu (2004), respectively.

Further, McGovern et al. (2018) studied runup using a pneumatic long wave generator. They observed a relationship between the relative slope length and the dimensionless runup and suggested the relative slope length as the explanatory variable for the runup. The relative slope length relates the wavelength with the beach's wetted length, over which the wave travels. Moreover, they recommended the use of expanded datasets with varying slopes and depths to validate their solution. However, McGovern et al. (2018) do not include the amplitude ratio, as in Madsen and Schäffer (2010), which directly influences the runup. Further, they do not consider Chan and Liu's (2012) conclusion that the wave's accelerating phase mainly controls the runup.

In this study, we compute runup numerically and analytically over a constant sloping beach having different slopes for earthquake-generated initial waveforms with different source parameters. We then introduce a new parameter, tsunami runup predictor (TRP), and its relation to the runup. The TRP combines the wave's accelerating phase that we define as the horizontal length of the wave face, the wetted length of the slope, and the amplitude ratio to a single parameter, thus including the findings of the studies summarized previously. Finally, we use the TRP to estimate the runup for past events. We discuss the results compared to the field measurements and observe that the mean- and extreme-field maximum runup measurements are related to the TRP.

4.1.3. Runup computation

We produced a database of initial tsunami waveforms (ITWs) of LENs and LDNs, using the half-space elastic theory (Mansinha and Smylie, 1971) embedded in MIRONE suite (Luis, 2007). It is common practice to assume that the sea surface elevation over the epicentral area

mimics the ocean bottom's co-seismic deformation for earthquake-induced tsunamis. We varied the fault plane parameters -dip, width, depth, and slip, and the distance of the fault to the shore,- and the beach slope (Fig. 4.1, Table 4.1) and computed 210 ITWs. We assumed a rake angle of 90° for all cases.

We first used the numerical model nonlinear shallow water model with nested grids (NSWING) (Miranda and Luis, 2019) to evaluate the maximum runup. NSWING solves the NSW equations in a Cartesian or spherical reference system, allows for nested grids, and employs a moving boundary algorithm to track the shoreline motion during the inundation like Cornell multi-grid coupled tsunami model (COMCOT) (Liu et al., 1995, 1998). The code was benchmarked according to the analytical tests presented by Synolakis et al. (2008) and applied in Miranda et al. (2014), Omira et al. (2015), Wronna et al. (2015), Baptista et al. (2017) and Wronna et al. (2017, 2019a). We used a synthetic bathymetry with the dimensions of 80 × 520 km2 with a constant slope (Fig. 4.2). We used a coupled nested grids system from 320 m at offshore up to 5 m resolution at near and onshore.

Moreover, we applied the analytical solution of Aydın and Kânoğlu (2017). Their method computes the shoreline elevation and velocity for a given initial waveform with or without initial velocities. We fitted N-waves in exponential waveforms as used in Kânoğlu (2004) and Aydın and Kânoğlu (2017) to each of the ITWs from the database to obtain the profiles as input to the analytical solution.

Table 4.1 Fault plane parameters and slopes used in modelling. Here, D, W, δ and s represent the fault depth, the width, the dip angle, and the slip amount, respectively; x1 is the distance of the initial wave to the shore and β is the nearshore beach slope

Faultplane parameters					Beach slope
Depth	Width	Dip	Slip	Distance to the shore	ß
[km]	[km]	[°]	[m]	[km]	[°]
10 - 40	20 - 150	10 - 60	1 - 10	100 - 360	1 - 5
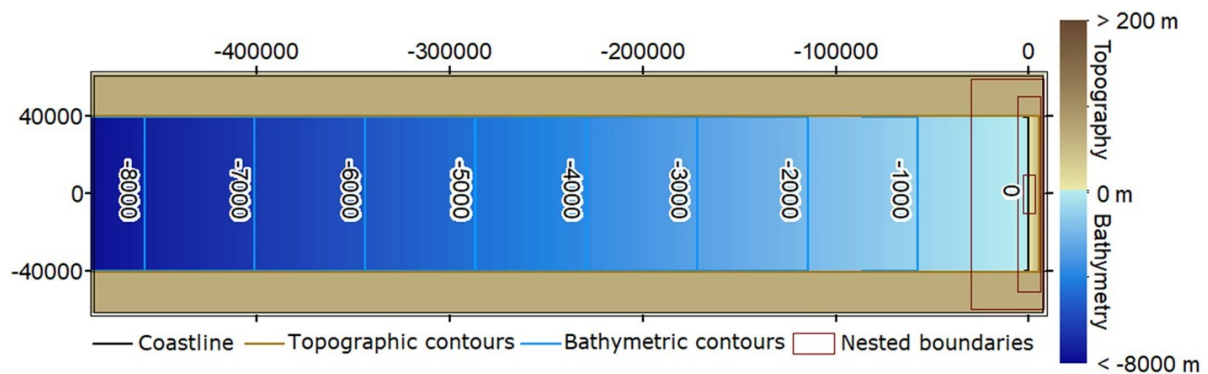
Figure 4.2 Definition sketch for the bathymetry used in the numerical model. Quantities are in meters.

4.1.4. The tsunami runup predictor

McGovern et al. (2018) suggested the relative slope length sl as the primary parameter controlling the maximum runup. They defined sl as

$$sl = \frac{\sin \beta}{d} \lambda, \qquad (4.1)$$

where β is the beach slope, d is the water depth, and λ is the wavelength. This relationship describes the length of the wetted slope with respect to the wavelength. Besides, Chan and Liu (2012) suggested that the maximum runup also crucially depends on the wave's accelerating phase. We also observed the strong influence of the wave steepness on the maximum runup as McGovern et al. (2018). Hence, we propose to use the horizontal length of the wave face l_p (Fig. 4.1) to describe the accelerating phase of the wave since we reach a similar conclusion from the runup results. We define l_p as the distance between the maximum and the minimum amplitudes for LDNs and the distance from the maximum height to the 5% tail of the positive amplitude for LENs (Fig. 4.1b and c). We also include the amplitude ratio $\tilde{\mu} = h^-/h^+$, where h^- is the minimum amplitude of the trough and h^+ is the maximum amplitude of the crest, to distinguish between LENs and LDNs (Madsen and Schäffer, 2010). Since the accelerating phases for LENs do not include negative amplitude, using the amplitude ratio for LEN becomes irrelevant. Hence, we present the TRP, $\tilde{\phi}$, as,

$$\tilde{\phi}_{LEN} = \frac{1}{l_p} \frac{d}{\sin \beta} \text{ and } \tilde{\phi}_{LDN} = \frac{\tilde{\mu}}{l_p} \frac{d}{\sin \beta}, \qquad (4.2)$$

for LENs and LDNs, respectively. Here, d is the water depth at the maximum wave height. We also define the dimensionless maximum runup as,

$$\tilde{R}_{LEN} = \frac{R}{h^+} \text{ and } \tilde{R}_{LDN} = \frac{R}{H/\tilde{\mu}}, \qquad (4.3)$$

where R is the maximum runup and $H = h^+ + |h^-|$. Further, we search for a relationship between the maximum runup and TRP in the form of $\tilde{R} = a\tilde{\phi}^b$ to fit our numerical and analytical data set. We approximately identify maximum runup as,

$$\tilde{R}_{LEN} = 2.15 \, \tilde{\phi}_{LEN}^{0.5} \text{ and } \tilde{R}_{LDN} = 1.1 \, \tilde{\phi}_{LDN}^{0.7}, \qquad (4.4)$$

for LEN and LDN, and present the results in Figs. 4.3 and 4.4, respectively.
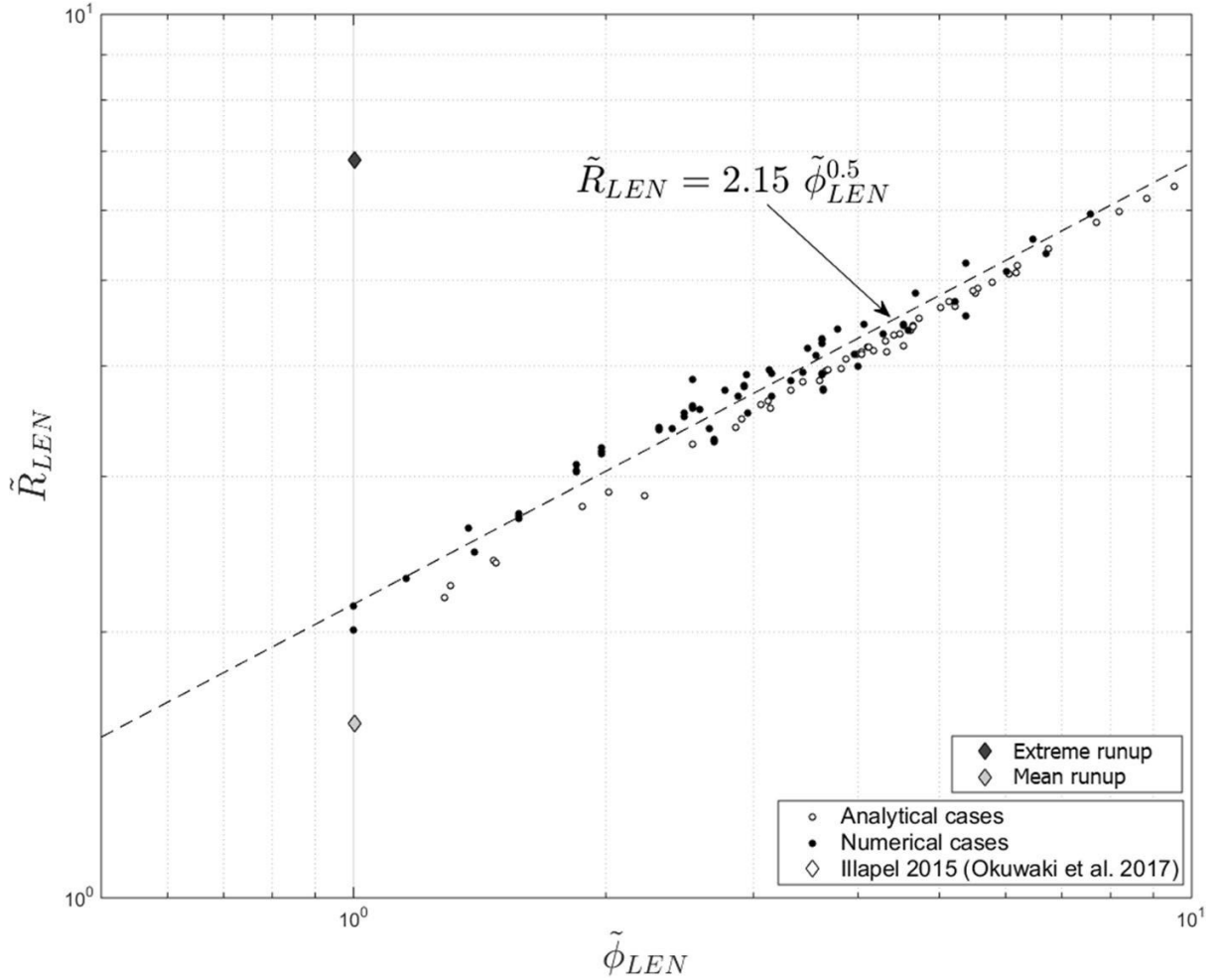
Figure 4.3 The maximum runup in respect to the TRP for LENs. The circles and dots show analytical and numerical maximum runup results, respectively. The dashed line shows Eq. 4.4. The initial waveform for the Illapel tsunami is a LEN. The dark and the light diamonds show the mean- and extreme-field maximum runup measurements along the target coastline for the Illapel tsunami, respectively.

4.1.5. The application of the TRP to the field observations

We set down to use field data to test the new runup formulation based on TRP. We use Nicaragua 1992 (Dziewonski et al., 1995; Piatanesi et al., 1996; Okal and Synolakis, 2004); Indonesia, Java 1994 (Dziewonski et al., 1995; Abercrombie et al., 2001; Okal and Synolakis, 2004); Mexico, Colima 1995 (Dziewonski et al., 1997; Mendoza and Hartzell, 1999; Okal and Synolakis, 2004); Chile, Maule 2010 (Delouis et al., 2010; Hayes, 2010; Sepúlveda and Liu, 2016); Japan, Tohoku-Oki, 2011 (Ammon et al., 2011; Wei et al., 2012; Yue and Lay, 2013); Chile, Iquique 2014 (Wei, 2014) and Chile, Illapel 2015 (Okuwaki et al., 2017) events to test our empirical solutions. Table 4.2 lists the source models we have used for these events. We use the centroid moment tensor (CMT) and inversion models to compute the ITW through Mansinha and Smylie (1971). We then trace a profile along the maximum sea level elevation orthogonal to the ITW to identify the parameters h^+, h^-, and l_p. We approximate the target beach slope angle β and

the water depth d at the maximum h^+ using the GEBCO (2014) bathymetry. We then use these parameters to compute dimensionless runup $\tilde{R}$, using Eqs. 4.2, 4.3 and 4.4, depending on initial wave polarity, i.e., LDN or LEN, for all the cases listed in Table 4.2, and present the results in Figs. 4.3 and 4.4, and Table 4.3. Then, we compare the estimates to the mean- and extreme-field maximum runup measurements for each event (National Geophysical Data Center / World Data Service NGDC/WDS, 2019) in Figs. 4.3 and 4.4. Analysing Fig. 4.4, reluctant to have a conclusion from a few data points, we observe that the dimensionless extreme maximum runup heights, $\tilde{R}_{LDN,\ Ext}$, for the cases Java, Mexico, Maule, Tohoku-Oki, and Iquique, follow

$$\tilde{R}_{LDN,\ Ext} = 2.8\,\tilde{\phi}_{LDN}^{0.7}. \tag{4.5}$$

This result indicates that even extreme runup might follow a similar law to Eq. 4.4, with a factor of about 2.5. Our results are compatible with the mean- and extreme-field maximum runup measurements.
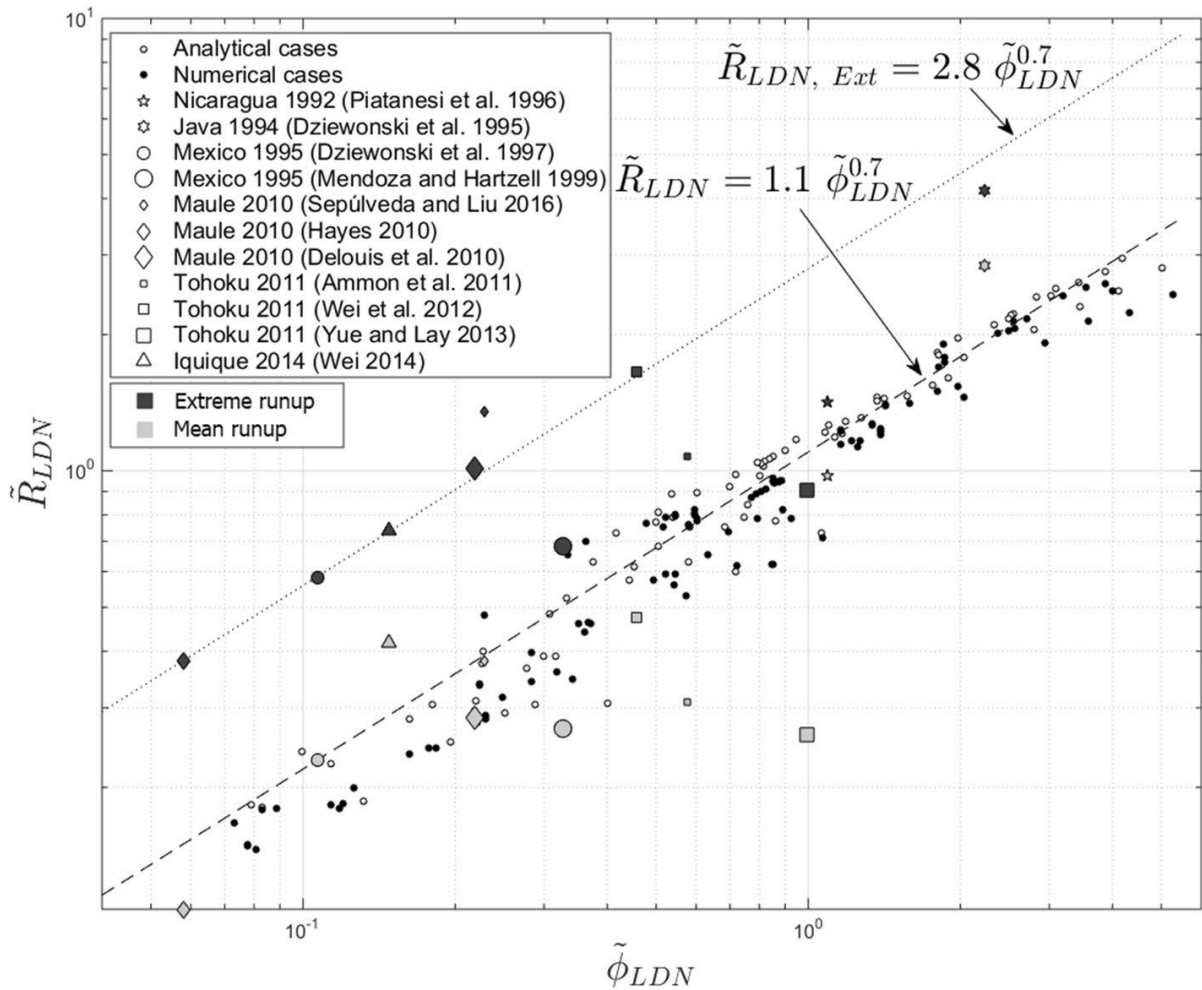
Figure 4.4 The maximum dimensionless runup in respect to the TRP for LDNs. The circles and dots show the analytical and numerical maximum runup results, respectively. The dashed line shows a fit to the numerical and analytical runup results (Eq. 4.4). The dotted line depicts the fitted law (Eq. 4.5) for the extreme runup $\tilde{R}_{LDN,\ Ext}$ values from the field measurements. Each symbol depicts runup values for one event; the mean- and extreme-field maximum runup measurements are presented in dark and light, respectively.

Table 4.2 The source parameters and beach slopes used for the field cases. Here, M_w represents the moment magnitude δ, W, D, and s represent the fault dip angle, the width, the depth, and the slip amount, respectively; and β is the nearshore beach slope.

Event	References	Source type	M_w	δ [°]	W [km]	D [km]	s [m]	β [°]
Nicaragua 1992	Dziewonski et al. (1995) Piatanesi et al. (1996) Okal and Synolakis (2004)	Inversion	7.7	12 – 16	40 – 100	15	5	2
Java, Indonesia 1994	Dziewonski et al. (1995) Abercrombie et al. (2001) Okal and Synolakis (2004)	CMT	7.8	7 – 12	80 (max slip: 40 km)	16	3.4	1
Colima, Mexico 1995	Dziewonski et al. (1997) Okal and Synolakis (2004)	CMT	8.0	9	100	15	4.3	3.2
	Mendoza and Hartzell (1999)	Inversion	8.0	14	100	15	4.3	3.2
Maule, Chile 2010	Sepúlveda and Liu (2016)	CMT	8.8	20	100	30	10	1.8
	Hayes (2010)	Inversion	8.8	18	200	0.2	14	1.8
	Delouis et al. (2010)	Inversion	8.8	18	280	0.7	20	1.8
Tohoku-Oki, Japan 2011	Ammon et al. (2011)	Inversion	9.1	12	210	1	40	1.7
	Wei et al. (2012)	Inversion	9.1	10	210	1	45	1.7
	Yue and Lay (2013)	Inversion	9.1	10	210	1	70	1.7
Iquique, Chile 2014	Wei (2014)	Inversion	8.2	15	130	5.6	10	1.4
Illapel, Chile 2015	Okuwaki et al. (2017)	Inversion	8.3	19	100	6	8	3.6

Specifically, we have the following observations regarding the field application of the TRP.

The TRP estimate using the waveform based on the inversion by Piatanesi et al. (1996) is within the field observation range for the 1992 Nicaragua event (Table 4.3).

In the 1994 Java, post-event field surveys report the measured tsunami runup in only four locations (Maramai and Tinti, 1997, NGDC/WDS, 2019). The TRP model underestimates the mean- and extreme-field maximum runup measurements for this event. A possible explanation is that the rupture originated at a locked subducting seamount (Abercrombie et al., 2001), resulting in the concentration of maximum slip distribution along a small area. Hence, this produces a relatively short length of the accelerating phase of the wave l_p that is not well reproduced when using CMT parameters to compute the ITW.

The co-seismic deformation occurs partially onshore, resulting in shoreline subsidence or uplift for the 2010 Maule, 2014 Iquique, and 2015 Illapel, Chile events (Omira et al., 2016). Fritz et al., (2011) measured a maximum runup height of 29 m decaying fast from this maximum value to values between 5 and 10 m for the Maule event. Both of our predictions are in line with their observations. For the Iquique event, the post-event field survey reported runup heights ranging 2–3 m with a maximum value of 4.6 m (Catalán et al., 2015). The prediction of the runup is 1.8

m for the Iquique event. For the Illapel event, our prediction lies within the range of most of the measurements between 2 and 6 m (Aránguiz et al., 2016). However, it underestimates the extreme runup of 13.6 m (Contreras-López et al., 2016). Aránguiz et al. (2016) found an extreme runup of 10.8 m for the Illapel event and used numerical modelling to explain the runup distribution. Their modelled values represent well the tide gauge recordings and mostly the measured runup values between 2 and 6 m. However, they do not reproduce their maximum measured runup; the authors attribute this extreme value to the deep offshore bathymetry and the pocket beach morphology.

We considered 3 different inversion models and obtained very different results ranging between 15.1 and 47.4 m (Table 4.3) for the Japan, Tohoku-Oki, 2011 event. The differences in the inversion models and their corresponding wave height profiles may explain the diversity of different results obtained. We overestimate the maximum runup about 20% for an ITW produced for the Tohoku-Oki case based on Yue and Lay (2013) inversion model (Fig. 4.4, Tables 4.2 and 4.3). Ammon et al. (2011) and Wei et al. (2012) inversion models of the Tohoku-Oki event results in an underestimation of the maximum runup of about 28 and 60%, respectively (Table 4.3). However, we overestimate the mean runup values for the Tohoku-Oki event independently from the inversion models used here. The overestimation of the runup for the Tohoku-Oki inversion through Yue and Lay (2013) possibly results because of the extreme values of the ITW where we calculate a wave height H of more than 25 m in the open ocean and a relatively large amplitude ratio $\tilde{\mu}$ close to 0.6, i.e. larger values of $\tilde{\mu}$ result in higher runup (Madsen and Schäffer, 2010).

Considering the 1995 Colima, Mexico event, different solutions for the tsunami source in the empirical model produced considerable discrepancies. The model using the CMT solution profile produces a 4 m runup. In comparison the inversion model profile produces a runup of 8 m, which is much closer to the maximum measured runup (Fig. 4.4, Tables 4.2 and 4.3).

Table 4.3 The waveform parameters, TRP and dimensionless runup values for the field cases. The observed mean and extreme runup values are also tabulated. Here, h^- is the minimum amplitude of the trough, h^+ is the maximum amplitude of the crest, $H = h^+ + |h^-|$ and $\tilde{\mu} = h^-/h^+$. l_p is the horizontal length of the wave face, β is the target beach slope angle and d is the water depth at the maximum wave height. $\tilde{\phi}$ is calculated from Eq. 4.2, $\tilde{R}$ and corresponding R from Eqs. 4.4 and 4.3, respectively, depending on the polarity of the initial wave, i.e. LEN or LDN. The mean ($\tilde{R}_{mean}$) and extreme ($\tilde{R}_{Ext}$) runup values are calculated based on field data using Eq. 4.3. Refer to Table 4.2 for the references of the source models.

Event	References	Source	Profile type	h^+ [m]	h^- [m]	H [m]	l_p [m]	β [°]	d [m]	$\tilde{\mu}$	$\tilde{\phi}$	$\tilde{R}$	R_{TRP} [m]	Observed R_{mean} [m]	R_{max} [m]
Nicaragua 1992	Dziewonski et al. (1995) Piatanesi et al. (1996) Okal and Synolakis (2004)	Inversion	LDN	2.05	-0.85	2.90	52483	2	4816	0.4152	1.0918	1.28	8.2	6.8	9.9
Indonesia Java 1994	Dziewonski et al. (1995) Maramai and Tinti (1997) Abercrombie et al. (2001) Okal and Synolakis (2004)	CMT	LDN	1.14	-0.59	1.73	43838	1	3295	0.5193	2.2370	2.11	6.5	9.5	13.9
Mexico Colima 1995	Dziewonski et al. (1997) Okal and Synolakis (2004)	CMT	LDN	1.80	-0.19	1.99	68798	3.2	3846	0.1067	0.1069	0.25	4.3	4.3	10.9
	Mendoza and Hartzell (1999)	Inversion	LDN	1.88	-0.25	2.13	31475	3.2	4310	0.1336	0.3277	0.55	8.0	4.3	10.9
Chile Maule 2010	Sepúlveda and Liu (2016)	CMT	LDN	4.00	-0.92	4.92	92477	1.8	2906	0.2287	0.2288	0.43	8.4	8.2	29
	Hayes (2010)	Inversion	LDN	4.18	-0.24	4.43	82597	1.8	2595	0.0580	0.0581	0.16	11.4	8.2	29
	Delouis et al. (2010)	Inversion	LDN	5.16	-1.13	6.29	42499	1.8	1336	0.2191	0.2192	0.41	10.9	8.2	29
Japan Tohoku-Oki 2011	Ammon et al. (2011)	Inversion	LDN	9.59	-3.40	12.99	100380	1.7	4823	0.3549	0.5749	0.81	27.3	11.3	39.3
	Wei et al. (2012)	Inversion	LDN	6.37	-2.33	8.70	175990	1.7	6513	0.3660	0.4566	0.69	15.1	11.3	39.3
	Yue and Lay (2013)	Inversion	LDN	16.15	-9.60	25.76	152090	1.7	7532	0.5946	0.9925	1.19	47.4	11.3	39.3
Chile Iquique 2014	Wei (2014)	Inversion	LDN	0.80	-0.12	0.93	42998	1.4	1051	0.1480	0.1481	0.32	1.8	2.6	4.6
Chile Illapel 2015	Okuwaki et al. (2017)	Inversion	LEN	2.03	0	2.03	50411	3.6	3172	-	1.0021	2.15	4.4	3.2	13.9

4.1.6. Final remarks

We used numerical and analytical methods to compute the runup on constant sloping beaches. We generated the ITW dataset, including the maximum runup using different earthquake fault parameters and constant sloping bathymetries with different beach slopes. We introduced a new dimensionless parameter TRP and further, we present relation to the maximum runup for LEN and LDN initial waveforms separately. Our results suggest a strong correlation between these parameters (Figs. 4.3 and 4.4).

Further, we applied the empirical model for past tsunamis and compare the runup predictions to the field measurements. We hypothesize that underestimating the maximum runup in the real events may result from the fact that the empirical model considers simplified 1-D bathymetric profiles. We speculate that the fact that our model does not account for changes in coastal bathymetry and topography may explain some of the discrepancies of the runup predictions (Tang et al., 2009; Aránguiz et al., 2016) and needs some further investigation. However, the local bathymetric effects on the runup are beyond the scope of this study.

We also developed a formulation (Eq. 4.5) for the extreme-field measured maximum runup that produces reliable results for all events tested here (Fig. 4.4). The multiplication factor is about 2.5 compared to the mean runup, even though this needs further validation with more cases. However, we speculate that heterogeneous slip distribution may account for some of the differences in the runup estimates. Distribution of slip along the faults may lead to a larger runup. Concentrated areas of slip influence the length of the wave's accelerating phase, thus may lead to a higher runup. Consequently, runup estimates depend crucially on the quality of the estimated/measured wave shape. Interestingly, Geist and Dmowska (1999) and Geist (2002) found that heterogeneous slip distribution may greatly influence tsunami wave steepness and runup. Geist (2002) found that the nearshore tsunami amplitude can vary a factor of 3 when considering variable heterogeneous slip distribution patterns. Recent studies (Baglione et al., 2017; Melgar et al., 2019) discuss the importance of the heterogeneous slip distribution to nearshore tsunami runup. Rapidly available earthquake parameters based on CMT solutions do not contain information on heterogeneous slip distribution along the fault. The conclusion for the cases 2011 Tohoku-Oki, Japan, and 1995 Colima, Mexico events, where we tested more than one ITW, confirm that the sources used for the field observations are approximate solutions and may include uncertainties. This fact highlights the need for an efficient sea level observation

system to measure the waveform offshore; thus, the runup can be estimated in real-time, independently from the generation mechanism.

We conclude that the empirical method presented here allows for a quick estimate of the runup in coastal stretches where no high-resolution terrain models are available. Once the waveform is estimated, the empirical runup estimation method based on the TRP could be a powerful tool for a tsunami early warning system.

5. Assessment of tsunami impact: The September 28, 2018, Palu-Sulawesi post-tsunami field survey

It is necessary to understand the impact of each past tsunami event. To better understand natural disasters like tsunamis, it is essential to assess their impact metrics. Especially since the 1992 Nicaragua tsunami (Baptista et al., 1993, Satake et al., 1993), the scientific community gathered efforts to assess each event's impact systematically. The assessment of the impact then serves scientists of many fields to verify modelling results, better constrain the tsunami sources, test new approaches, or detect especially exposed areas, among other applications.

5.1.   The September 28, 2018 Palu-Sulawesi earthquake and tsunami

At 18:02:45 local time (UTC+8) on September 28, 2018, a powerful Mw 7.5 earthquake occurred on the island of Sulawesi. It affected mainly the bay of Palu and its surroundings. The USGS located the earthquake's epicentre at 0.256 S and 119.846 E (Fig. 5.1) and determined a shallow strike-slip rupture mechanism. Only minutes after the earthquake, a surprisingly powerful tsunami struck the bay of Palu, causing widespread destruction of property and more than 4,000 casualties (Sangadji, 2019).
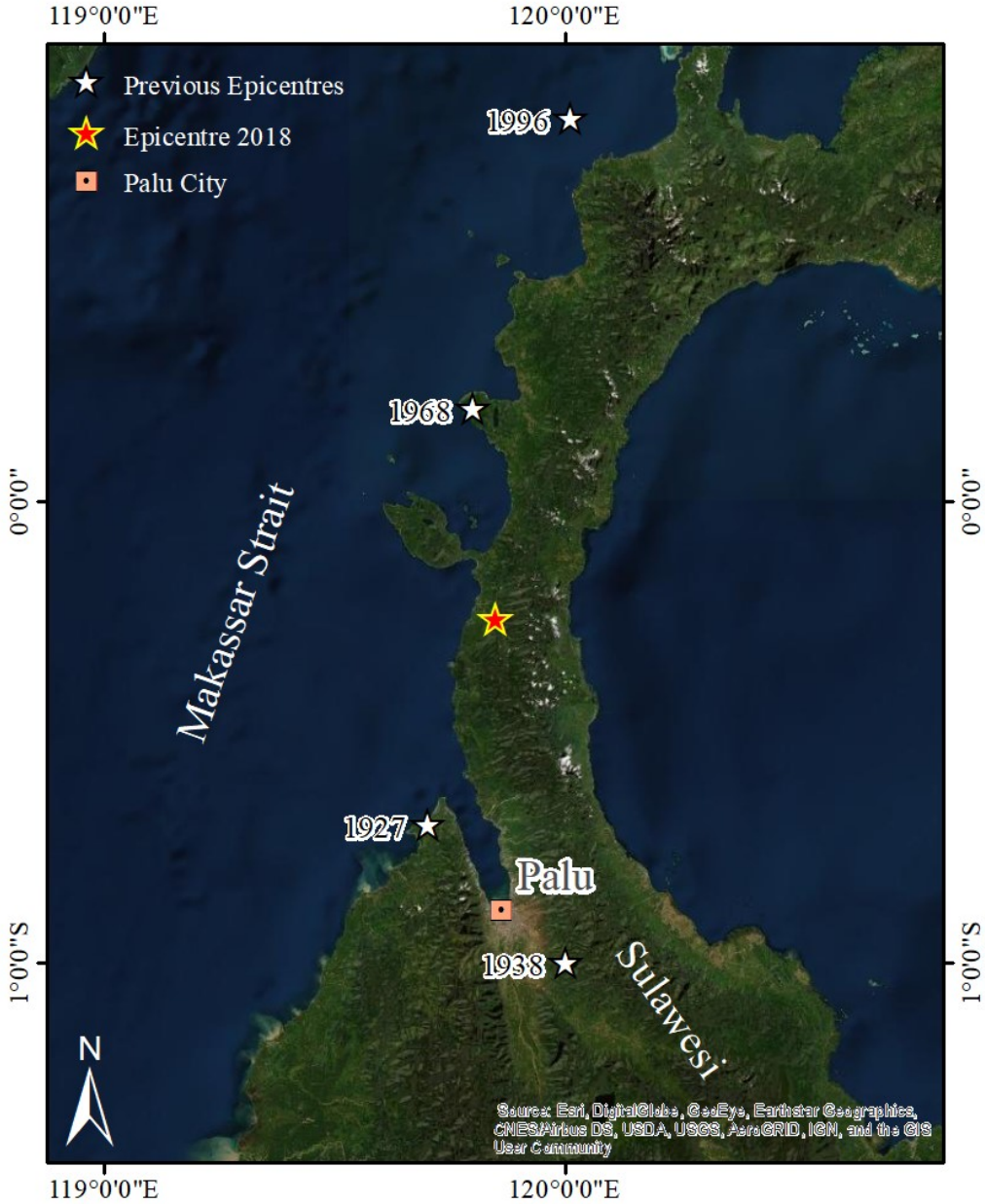
Figure 5.1 The epicentre locations of the earthquakes of the last century (Pelinovsky et al. 1997) in the Donggala-Palu region. The red star shows the epicentre of the most recent September 28, 2018, Palu earthquake.

Indonesia is one of the most vulnerable countries against tsunami disasters. Especially in the eastern part of Indonesia (Prasetya et al., 2001), where microplates accommodate the stress exerted by the triple junction setting; the Pacific-Philippine and the India Australia plate subduct below the Sunda Plate at rates of 75 and 90 mm/yr (Walpersdorf et al., 1998; Socquet et al., 2006; Spencer, 2011). Within this fragmented microplate setting, relatively high seismicity, results in thrust, rift and transform rupture mechanisms. The rupture of the September 2018 earthquake occurred along a 200 km long sub-segment of the Palu-Koro fault, a left-lateral strike-slip fault crossing Sulawesi and connects with the Minahassa Trench in the north (Bellier et al., 2001; Socquet et al., 2006).

Sulawesi has a long history of tsunamigenic earthquakes. From 1820 to 1982, fourteen tsunamis occurred in Sulawesi Island (Prasetya et al., 2001). Just in the Donggala - Palu region, five tsunamigenic earthquakes occurred in the last century, in 1927, 1938, 1968, 1996 and 2018 (Pelinovsky et al., 1997; Prasetya et al., 2001) (Fig. 5.1). Thus, on average, every 23 years, a tsunami occurs in that region. However, these events had presumed associated vertical thrusting or standard faulting mechanisms and generated local tsunamis of up to 10 m wave height or larger (Soloviev and Go, 1974; Pelinovsky et al., 1997; Prasetya et al., 2001).

However, the 2018 Palu earthquakes rupture mechanism had a predominant horizontal dislocation (USGS, 2018; Socquet et al., 2019). That rupture mechanism resulted in a co-seismic deformation of the earthquake that seemed unable to justify the tsunami observations, surprising authorities, and the scientific community. Nevertheless, Indonesia's Meteorology, Climatology and Geophysics council (Badan Meteorologi, Klimatologi, dan Geofisika, BMKG) issued an initial warning 5 minutes after the earthquake alerting for wave heights 0.5 – 3m but lifted the warning after about 30 minutes (Thandlam et al., 2019). However, the earthquake had damaged power and communication systems, preventing the warning from being timely disseminated. Besides, the size of the tsunami for Palu Bay was underestimated in the warning message (European Commission, 2018) due to lack of sea level data.

Several institutions (JRC, IPMA, METU, GFZ Potsdam) launched initial tsunami models based on the first available fault estimates (USGS, 2018). The first early modelling efforts vastly underestimated the tsunami observations in the bay of Palu. Moreover, some amateur videos indicate a large landslide on the western side of the bay.

The objectives of the subsequent UNESCO International Tsunami Survey Team (ITST) field survey were to measure the tsunami impact on shore (runup and inundation height, inland penetration) and to identify possible sources, especially coastal landslides. This chapter exemplifies

the work presented in Yalciner et al. (2018a), Wronna et al. (2019b) and published in Omira et al. (2019) (Appendix 4).

5.2. Field assessment of the tsunami impact in the Palu – Donggala region

In the aftermath of the September 28, 2018, Palu earthquake, a team of international scientists from different disciplines and agencies formed the International Tsunami Survey Team (ITST) supported by UNESCO and initiated by the Joint Research Centre (JRC) of the European Commission. The objectives of the ITST survey were to assess the coastal impact of the tsunami and measure corresponding runup heights and flow depths. The field survey was planned and conducted in close collaboration with Indonesian authorities with the objective to fill the gaps and complement previous surveys (c.f. the Indonesian National Tsunami Survey Teams, NTST-Palu). The presurvey meeting took place on November 5, 2018, at BMKG (Badan Meteorologi, Klimatologi, dan Geofisika) office. The UNESCO-IOC ITST survey took place from November 7 – 11, 2018 and covered mainly the lateral areas of the bay from Tanjung Karang cape on the western side of the bay to Balaesang north of the epicentre location on the eastern side of the bay (Fig. 5.2).

The team collected the data according to the guidelines and conventional methods published in UNESCO-IOC ITST Post-Tsunami Survey Field Guide 2nd Edition (UNESCO, 2014). This section presents the results of the field survey and exemplifies the data collection process at selected sites. Figure 5.3 presents the definition of the tsunami metrics.
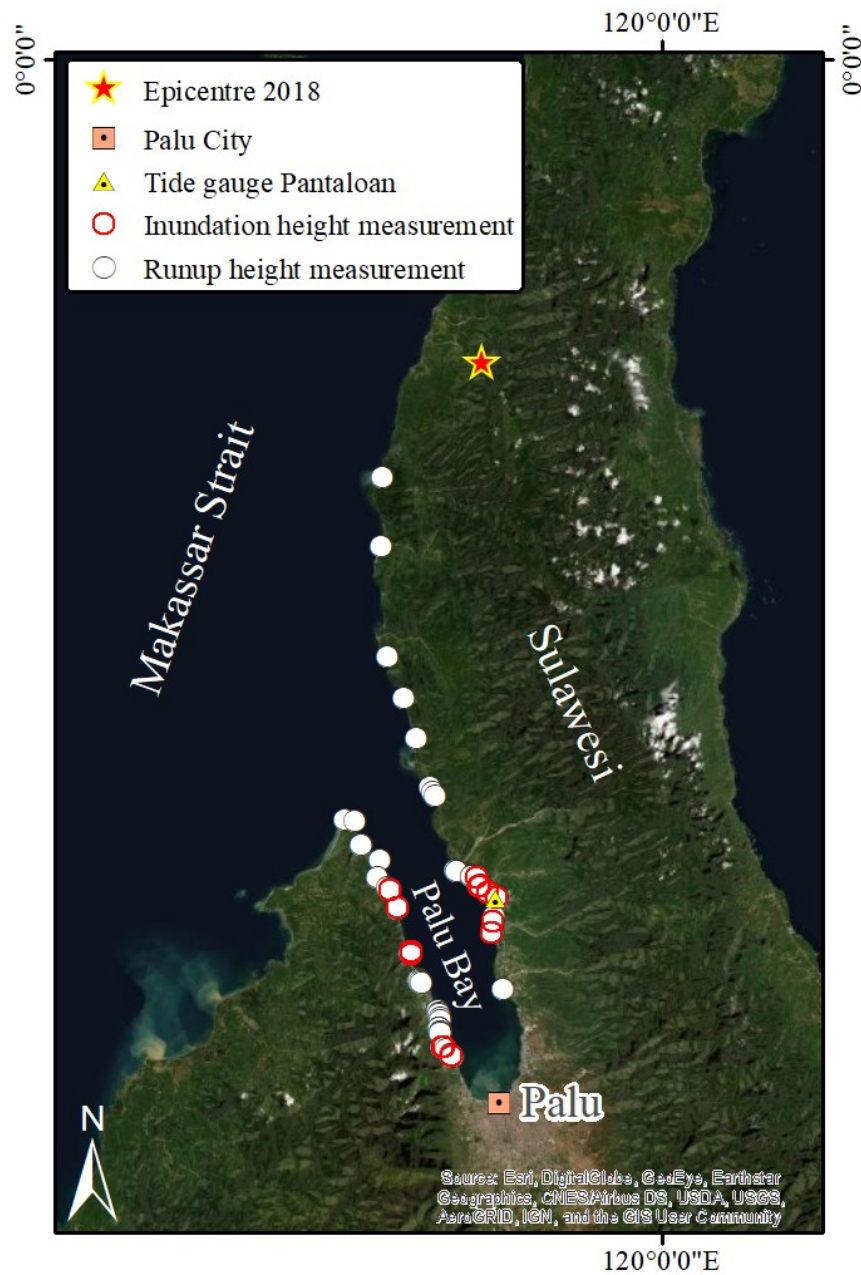
Figure 5.2 shows the surveyed points around Palu bay, the white points depict the locations with runup height measurements, and the red circles show the complementary inundation height measurements.
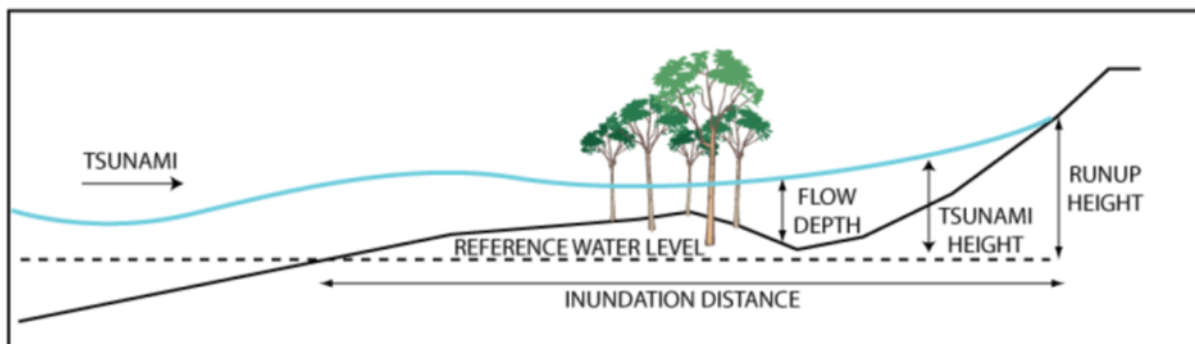
Figure 5.3 Definition of the tsunami metrics; inundation distance, flow depth, tsunami height, runup height and inundation distance (UNESCO, 2014).

99

Pre-survey data collection:

The pre-survey data selection consists of maps, charts, pictures, videos, tidal records, pre- and post-event satellite images, and data from previous surveys. The only tide gauge in Palu bay located in Pantoloan recorded the tsunami signal with about 2m positive amplitude around 6 minutes after the earthquake (c.f. Fig. 5.2 for location and Fig. 5.4 for the tsunami signal). The water level shortly before the tsunami is considered as the reference water level for the time of the event. The data is available at the Agency for Geospatial Information Indonesia (Badan Informasi Geospasial - BIG) (http://tides.big.go.id). The tsunami signal is shown in figure 5.4 (Valkaniotis et al., 2018). Carvajal et al. (2019) analyzed CCTV and amateur video recordings from social networks and inferred the tsunami waveform at that location. They suggest that the 1 min sampling rate of the tide gauge recording in Pantoloan is too low to capture the hazardous short period tsunami (1 – 2 mins) that struck almost instantly after the earthquake (Carvajal et al., 2019, Sepúlveda et al., 2020, Schambach et al., 2021).
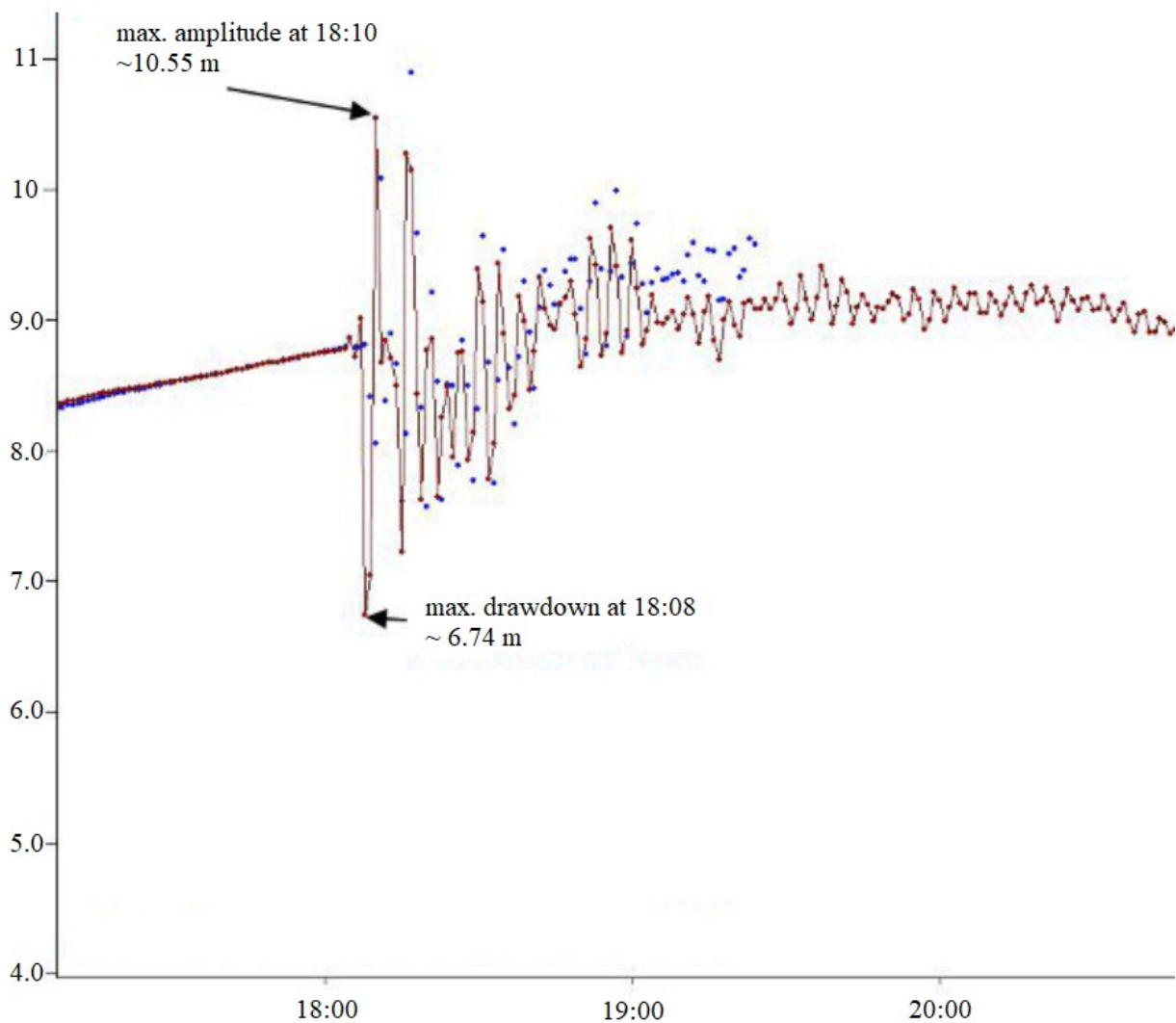
Figure 5.4 The tide gauge recording in Pantoloan port adapted after Valkaniotis et al. (2018) (Fig. 5.2). The tide at the time of the event was ~ 1 m above MSL.

Field survey equipment: The equipment for the measurements consisted of optical level (handheld and tripod; GPS station; laser ruler; tripods and surveying rods. Additionally, cameras have been used to take photographs of the tsunami impact at the surveyed locations in Palu bay.

Field survey measurements: Runup and inundation depth was measured using the equipment listed above. The locations of the runup and inundation measurements are depicted in Fig. 5.1. The tsunami runup and inundation height has been inferred using deposited debris, water marks and impact marks and from the extent of destruction of construction and vegetation (Fig. 5.6, 5.7, 5.8 and 5.10). A total number of 16 tsunami inundation height and 62 runup height data points has been collected. At 10 locations coastal landslides have been identified and the rim of the head scarp has been tracked and its height has been measured. The data has been collected with reference to the sea level at the time of each measurement and was later corrected concerning the reference water level according to the Palu tide at the time of the event (Fig. 5.4). The corrected runup and inundation height values are listed in table 5.1 and figure 5.2. Complementarily, the team interviewed eyewitnesses for a better understanding. Some interviewees commented that they heard an explosion-like noise, and they could specify the direction, which helped to identify the locations of some of the coastal landslides. Those observations were especially advantageous in locations where the occurrence of coastal landslides was unclear. The location and measurements of the identified coastal landslides are given in table 5.2.

Omira et al. (2019) presented the results of the UNESCO-IOC ITST field survey. The article is in Appendix 4.

Table 5.1 Locations and measurements around Palu Bay during the UNESCO-IOC International Tsunami Field Survey. The letters E and W indicate if the location is located on the eastern or western side of the bay. All measurements have been corrected to the reference tide level at the time of the event. The type indicates the type of measurement.

Location	E/W	Latitude (°)	Longitude (°)	Measurement (m)	Type R = Runup ID = Inundation height
Alindau	E	- 0.35395	119.76194	–	–
Bulu Salugoo	E	- 0.41283	119.76123	–	–
Kaliburu	E	- 0.50688	119.76654	–	–
Bulu Sigalari	E	- 0.54152	119.77979	0.9	R
Enu	E	- 0.576	119.79038	–	–
Bulu Kadia	E	- 0.61711	119.80202	1.9	R
Bulu Kadia	E	- 0.62206	119.80442	1.8	R
Bulu Kadia	E	- 0.62508	119.80626	1.2	R
Labuan	E	- 0.68803	119.82413	1.5	R
Labuan	E	- 0.68846	119.82472	2.4	R
Labuan	E	- 0.68888	119.82536	3.7	R
North Ngapa	E	- 0.69341	119.83815	1.8	R
North Ngapa	E	- 0.69341	119.83815	1.9	R
Ngapa	E	- 0.69345	119.84258	4.7	R
Ngapa	E	- 0.69345	119.84258	4.8	R

Ngapa	E	- 0.69396	119.84213	4.0	IH
Ngapa	E	- 0.69400	119.84205	4.8	IH
Tongge	E	- 0.70052	119.84512	3.6	R
Tongge	E	- 0.70131	119.84492	3.7	IH
Tongge	E	- 0.70137	119.84438	3.9	R
Tongge	E	- 0.70140	119.84438	4.0	IH
Tongge	E	- 0.701933	119.845994	4.0	R
Panda	E	- 0.70707	119.85292	3.9	R
Panda	E	- 0.7072	119.85204	4.3	R
Panda	E	- 0.70724	119.85160	4.9	IH
Pantoloan	E	- 0.71065	119.85852	2.4	R
Pantoloan	E	- 0.71069	119.85892	4.0	IH
Pantoloan	E	- 0.710718	119.858905	2.7	R
Pantoloan	E	- 0.71101	119.85819	2.4	R
Pantoloan South	E	- 0.7275	119.85716	4.0	R
Pantoloan South	E	- 0.73141	119.85616	4.2	R
Pantoloan South	E	- 0.73141	119.85616	6.7	IH
Bamba	E	- 0.7406	119.85586	2.9	R
Bamba	E	- 0.74087	119.8548	3.1	IH
Sambugan	E	- 0.78863	119.86406	2.7	R
Tanjungkarang	W	- 0.644865	119.73036	–	–
Tanjungkarang	W	- 0.64576	119.73892	0.2	R
Donggala	W	- 0.66646	119.74395	1.6	R
Donggala	W	- 0.66648	119.74395	1.7	R
Ujung	W	- 0.67972	119.75997	2.0	R
Nambo	W	- 0.69457	119.75741	1.5	R
Kabonga Besar	W	- 0.70263	119.76599	0.4	R
Kabonga Besar	W	- 0.70400	119.76805	1.4	R
Kabonga Besar	W	- 0.70450	119.76836	1.9	IH
Kabonga Besar	W	- 0.70491	119.76864	1.2	R
Parigga	W	- 0.71933	119.77466	1.2	IH
Parigga	W	- 0.72029	119.77517	2.1	R
Parigga	W	- 0.72056	119.77511	2.4	R
Loli-Pesua	W	- 0.75721	119.78611	2.7	IH
Loli-Pesua	W	- 0.75774	119.78524	3.9	R
Loli-Pesua	W	- 0.75837	119.78547	4.7	R
Loli-Pesua	W	- 0.75883	119.78643	3.9	IH
Lolisaluran	W	- 0.78036	119.79317	5.1	R
Lolisaluran	W	- 0.78113	119.79318	6.4	R
Lolisaluran	W	- 0.78303	119.79373	3.0	R
Lolisaluran	W	- 0.78408	119.79532	3.5	R
Tamunggu	W	- 0.80727	119.80934	6.2	R
Tamunggu	W	- 0.809486	119.80981	5.9	R
Tamunggu	W	- 0.80987	119.80996	5.3	R
Tamunggu	W	- 0.81330	119.81055	5.4	R
Tamunggu	W	- 0.81558	119.81068	3.9	R
Watusampu	W	- 0.8216	119.8099	6.3	R
Watusampu	W	- 0.82207	119.81024	5.7	R
Watusampu	W	- 0.8222	119.81013	5.4	R
Watusampu	W	- 0.82511	119.81090	1.5	R
Watusampu	W	- 0.82513	119.81087	2.0	R
Watusampu	W	- 0.82648	119.81115	0.3	R
North Benteng	W	- 0.83772	119.81371	7.9	IH
North Benteng	W	- 0.83782	119.81317	4.7	IH
North Benteng	W	- 0.83784	119.8125	8.3	R
North Benteng	W	- 0.83997	119.81594	1.8	R
Benteng	W	- 0.84491	119.81947	4.2	R
Benteng	W	- 0.84514	119.82011	5.2	IH
Benteng	W	- 0.84562	119.82067	8.7	IH
Benteng	W	- 0.84591	119.82061	3.8	R
Benteng	W	- 0.84642	119.82117	9.1	R

Here, the data collection process and two locations where the UNESCO-IOC ITST took measurements are exemplified. The two sites are Ngapa on the east coast of Palu Bay close to the tide gauge in Pantoloan and Benteng on the west coast of Palu Bay where a large coastal landslide was recorded.

(Fig. 5.5). First, the runup limit or inundation height indicator have been identified. Then the GPS coordinates of the point have been collected and the exact time has been recorded to correct the data afterwards concerning the reference water level at the time of the event. The handheld device works well for short inundation distances. For the measurement, the optical level on the tripod projects a horizontal line pointing towards the surveying rod. The intersection of the projected line with the rod gives the height difference. If the height to measure is greater than the rod, we took stepwise measurements and summed the measured differences. A stepwise measurement may introduce some uncertainties. Typical uncertainties for tsunami inundation and runup height measurements are in the range of ±0.3 m (Heidarzadeh et al., 2018).

For the coastal landslides, we measured the length of the rim of the head scarp, tracking it with GPS. For the height of the head scarp, we used the surveying rod.

Table 5.2 Landslides identified in Palu Bay during the UNESCO-IOC International Tsunami Field Survey

Location	E/W	Latitude (°)	Longitude (°)	Length of the rim of the head-scarp (m)	Max. height of the main scarp (m)
Donggala	W	- 0.666	119.744	~ 500	8.0
Ujung	W	- 0.680	119.760	~ 300	-
Loli-Pesua	W	- 0.758	119.785	~ 250	3.5
Tamunggu	W	- 0.809	119.809	~ 400	1.5
Tamunggu	W	- 0.815	119.810	~ 300	2.0
North Benteng	W	- 0.837	119.813	~ 700	-
Benteng	W	- 0.846	119.821	~ 1000	3.0
Pantoloan South	E	- 0.731	119.856	~ 800	2.0
Tongge	E	- 0.701	119.844	~ 500	2.0
Labuan	E	- 0.688	119.825	~ 800	2.0

Figure 5.5 (a) shows the teammates measuring the height difference using the tripod optical level and the surveying rod; (b) The colleagues from JRC measuring the height difference with the handheld optical level.

Observations in Ngapa:

In Ngapa (Wani) on the eastern side of Palu bay, the tsunami impact caused heavy destruction close to the shore, leaving behind remaining foundations of destroyed buildings and deposited boats inland (up to 100 m from the shore). In a private house a CCTV video captured the tsunami's impact, washing away the brick fence and inundating the area. The CCTV video of the earthquake and the impact of the tsunami is online (Source:

https://www.youtube.com/watch?v=8qaP7BCN87Mandab_channel=XPLAYTVXPLAYTV).

At that location measurements have been taken at the watermarks of the building. In the back of the building where the CCTV cameras were installed, we observe a 0.7 m flow depth corresponding to a 4.0 m tsunami inundation height at that location. Further inland, the maximum runup height was measured at the street, corresponding to 4.7 m. Figure 5.6 shows some of the observations. Ngapa is located between Tongge and Labuan (Fig. 5.2), where the UNESCO-IOC ITST identified coastal landslides and measured rims of the head scarp with 500 m and 800 m length respectively and with 2 m height (Fig 5.6 c and 5.7) (c.f. table 5.2).

Figure 5.6 (a) shows the destruction in Ngapa; there are remaining foundations from buildings in the front and boats deposited inland in the back. (b) shows the approximately 500 × 2 m rim of the head scarp of the coastal landslide in Tongge. (c) a colleague is indicating the watermark at the building with the CCTV camera.
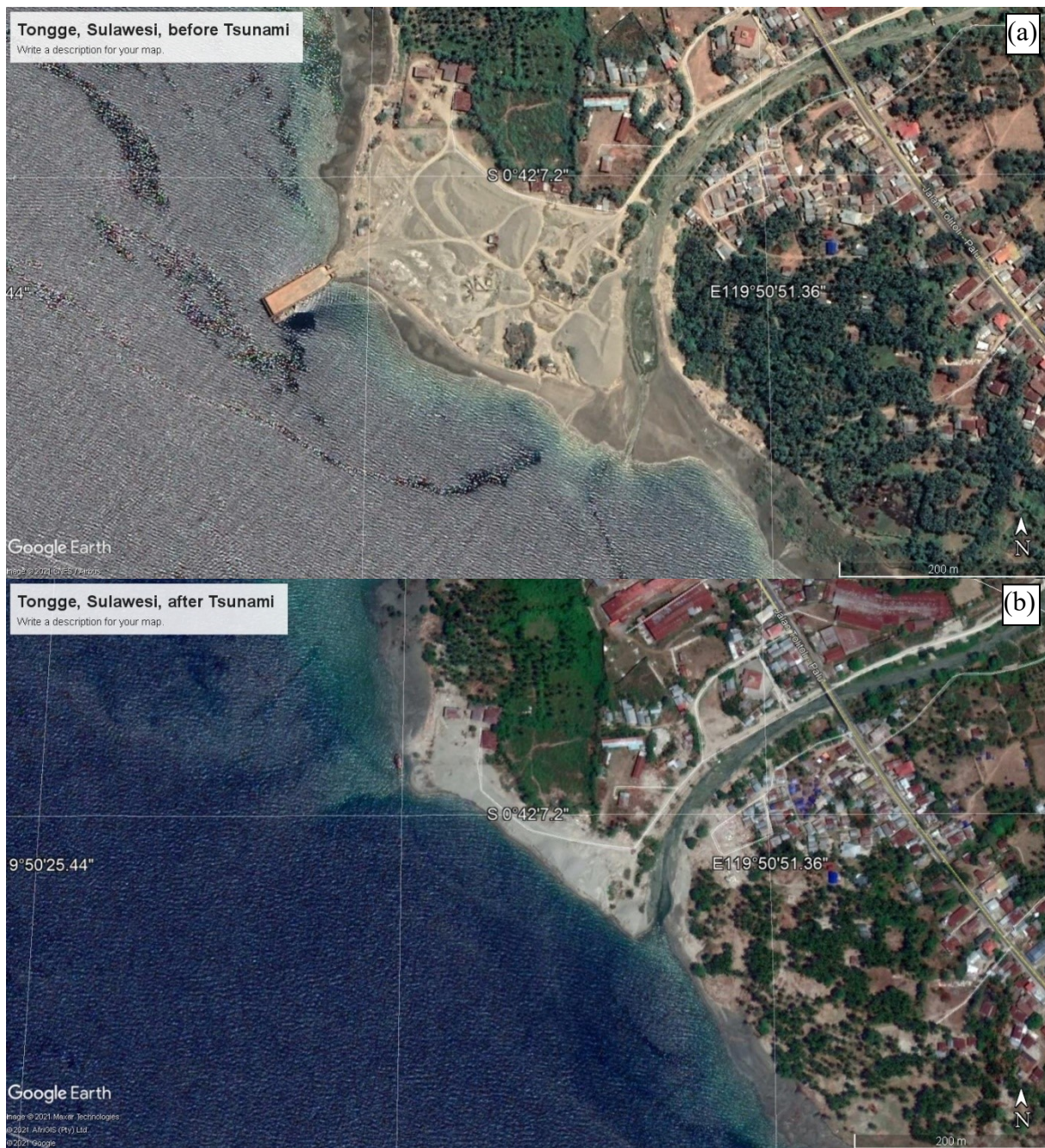
Figure 5.7 (a) shows the pre-tsunami satellite image of the observation site in Tongge confirming the intact gravel deposit at a river mouth (b) shows the post-tsunami satellite image of the observation site in Tongge with the remaining part of the gravel deposit.

106

Figure 5.8 shows deposited debris indicates the inundation extent and runup height in Labuan. Here, the maximum runup height measurement is 3.7 m.

Observations in Benteng:

Two amateur videos indicate a large landslide on the western side of the bay. One was recorded by Captain Ricoseta Mafella from the cockpit at around 1500 feet after departing from Palu airport. (Source: https://www.instagram.com/p/BoRttnsn5po/?taken-by=icoze_ricochet).

Another amateur video filmed on a boat located to the north captured the formation of a giant wave in the distance and a couple of minor landslide-generated tsunamis closer. A frame of this video is shown in figure 5.9 d.

(Source: https://www.youtube.com/watch?v=61ItBglP-YMandt=2sandab_channel=errorTV).

Both videos indicate approximate locations of the mass failures along the western shore of Palu bay. The UNESCO-IOC ITST identifies the large 1000 m extended rim of the head scarp with 3 m height in Benteng (Fig. 5.9 c). The eyewitnesses first observed a wave retreat and after that a massive wave 'as tall as the coconut trees' falling on the land. Indeed, the UNESCO-IOC ITST observes heavy tsunami impact close to the shore, such as heavily damaged houses, broken trees and branches, brown leaves of vegetation (after being submerged in saltwater) (Fig. 5.9). A maximum tsunami inundation height of 8.7 m and a maximum runup height of 9.1 m has been measured at that location. The inundation distance here is relatively and the slope of the coast is steeper with about 20° compared to the eastern side.
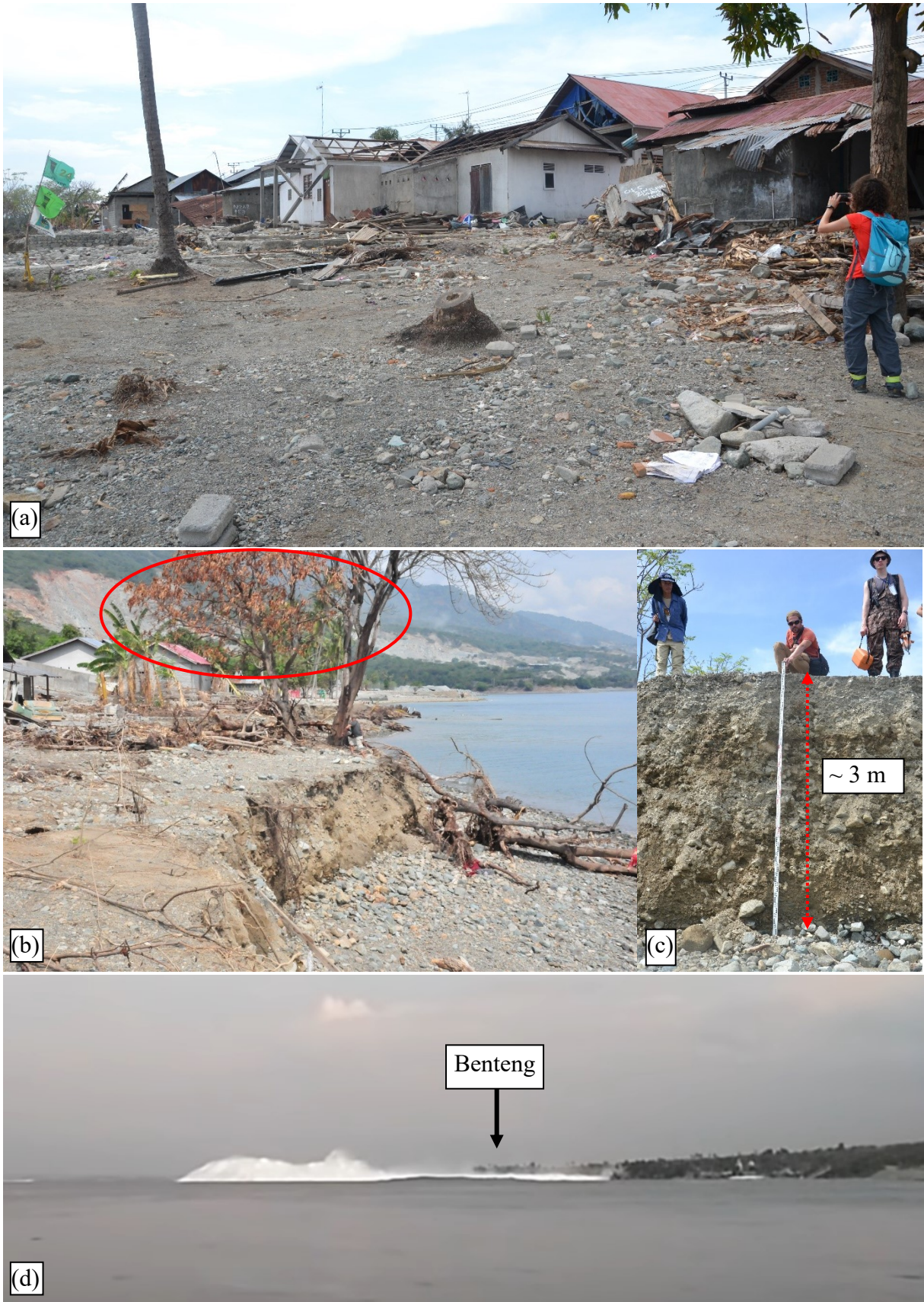
Figure 5.9 (a) The observed tsunami damage in Benteng; (b) Brown leaves, impact marks and broken branches of trees; (c) Measur-ing the height of the head scarp; (d) Frame of the video shot on the boat to the north of Benteng showing the massive wavefront.

5.3. Final remarks

The main conclusions of the field survey are:

1. A heavily impacted coast has been observed by the UNESCO-IOC ITST with massive damage to property and the environment. The measurements included 62 runup and 16 inundation height values along about 125 km coastline, mainly around Palu bay. The maximum runup and inundation height value were found in the village Benteng with 9.1 and 8.7 m, respectively. Additionally, the survey discovered ten coastal landslides indicated by amateur videos or eyewitness accounts.

2. The collected tsunami inundation and runup height data confirms the massive tsunami impact in Palu Bay. The values of the runup data have a high variability within the bay, and in some locations, severe localized tsunami impact has been observed. The distribution of collected measurements in the proximity of identified coastal landslides confirms that local landslides contributed locally to the tsunami impact. Nevertheless, a co-seismic contribution to the inundation height and runup values could not be ruled out. More recent modelling results confirm that assumption (Schambach et al., 2021).

3. Many eyewitnesses were willing to share their observations with the ITST team. In some locations, these observations have been crucial for identifying wave direction and additional coastal landslides. Moreover, concerning the sites where eyewitnesses were interviewed, their accounts agree with tsunami inundation and runup height measurements. It is essential to mention the local guides that led the interviews with the eyewitnesses with the necessary sensibility after such a catastrophic event. With the local support and knowledge of the general conditions, it was possible to identify more locations to take measurements.

The assessment of the tsunami impact through field surveys is an indispensable tool to understand each tsunami event better. Especially for the 2018 Palu-Sulawesi tsunami, many particularities could be identified within the field reconnaissance. Although many of the studies point towards the equal contribution of co-seismic deformation plus landslide sources (Gusman et al., 2019; Ulrich et al., 2019; Aránguiz et al. 2020; Schambach et al., 2021) still the main contributor could not be doubtlessly identified (Sepúlveda et al., 2020; Higuera et al., 2021; Han et al., 2021). However, Schambach et al. (2021) point out that it was crucial using the mapped landslides to achieve the result that agrees with the runup measurements.

Besides the scientific value of the field survey and the data collected to understand this event better, a personal conclusion is that the experience in the field allows one to relate the dimension

of measurements to oneself. A surveyor can set oneself in relation to 10 m runup height, a 3 m head scarp, or 488 m of inundation distance in the field. Assessing the tsunami impact in the field enables one to project oneself in an eyewitness's position and look up to an impact mark or the rim of the head scarp. Literal descriptions, photographs or even videos sometimes do not transmit that direct comparison. That direct comparison transmits the subjective feeling of the own vulnerability and provides a better understanding of the actual dimensions in the field. Finally, the author would like to thank all ITST colleagues, local guides, and other supporters for their valuable contribution to the UNESCO-IOC ITST survey (some of them are shown in Fig 5.10).

Figure 5.10 From left to right in the back row Dr Andrey Zaytsev, Pavel Pronin, Dr Ahmet C. Yalciner, Adel Giniyatullin, Dr Purna S. Putra. In the middle, from left to right, Dr Rachid Omira and Martin Wronna. Front row, from left to right Dr. Semeidi Husrin, Pamela Probst, Dr. Chiara Proietti, Gözde Güney Doğan, Dr. Maria Ausilia Paparo, Dr. Rahman Hidayat and a local guide.

6. Conclusion and final remarks

Previous studies investigate the source of most historical tsunamis included in the Portuguese catalog (Rabinovich et al., 1998; Baptista et al., 2003; Baptista et al., 2007; Kaabouben et al., 2008; Baptista and Miranda, 2009; Baptista et al., 2014; Baptista et al., 2016; Reis et al.; 2017; Baptista, 2019). Exceptions are the March 31, 1761, earthquake that generated a transatlantic tsunami and the November 11, 1858, earthquake that eventually generated a local tsunami.

For the March 31, 1761, earthquake, and transatlantic tsunami, a candidate-source is proposed by simulating the source-to-coast envelope of the tsunami enabling the comparison of the modelling results with observation data. Wronna et al. (2019a) proposes a source, located in the SWIM, corresponding to a fault that extends from the western segment of the CPF in the northeast towards the epicentre suggested by Baptista et al. (2006) in the southwest.

For the November 11, 1858, Setúbal earthquake, the macroseismic analyses considering 71 MDPs revealed new knowledge on the source of the event. The data analyses performed here, using a range of I_0 to identify the minimum of all minima, allowed to identify the epicentral area suggesting an alternative fault plane orientation and a compressive rupture mechanism. The proposed source is a north dipping NE-SW extending thrust fault centred at the coordinates at 8.879W, 38.313N, with a mean depth of 12.8 km (Wronna et al., 2021). Subsequent source-to-coast tsunami simulation revealed that low to moderate intensity tsunamis could impact the shore with short travel time to the coast.

The studies on the sources of the March 31, 1761, transatlantic tsunami and the November 11, 1858, earthquake and tsunami show the need to include these events in future hazard assessments.

Forecasting tsunami impact in real time is crucial to save lives. For near-shore sources, rapid impact estimation is required. In this thesis, the tsunami impact parameter runup has been proposed employing numerical and analytical methods following a source-to-coast approach to relate the initial tsunami waveform with the runup onshore. The new Tsunami Runup Predictor (TRP) is an empirical formulation that allows estimating the runup instantly for LENs and LDNs once the waveform is known. The TRP-formulation requires the waveform parameters, maximum amplitude, minimum amplitude, the distance between wave crest and trough, the beach's slope angle, and the water depth at the site of maximum amplitude observation.

The TRP method is also applied for a set of past tsunamis. The results agree well with field measurements of past tsunami events. We also observe that for the extreme runup values, the same relation is valid applying a multiplication factor of about 2.5.

Despite the tragic occurrence of the September 28, 2018, Palu-Sulawesi event it was an opportunity to assess the tsunami impact in the field within the framework of this thesis. The preliminary determination of the earthquake focal mechanism which co-seismic deformation was not capable to generate a tsunami of such size, caused a debate in the scientific community on the source of this event. The post-event field reconnaissance aimed to observe and survey tsunami impact to contribute to the understanding of the sources of the tsunami. The author of this thesis contributed as a member of the UNESCO-IOC ITST field survey (Omira et al., 2019).

The Palu-Sulawesi UNESCO-ITST Post-Tsunami Field Survey confirmed massive tsunami impact on coastal population, infrastructure, and environment. Tens of runup and inundation height measurements revealed a high variability of the tsunami impact in the bay with maximum values larger than 9 m. Moreover, the field survey revealed ten coastal sectors with landslide scarps as additional sources confirming that the Palu tsunami was a multiple source event. In summary, this thesis contributes to a better understanding of the **source to coast** tsunami phenomenon:

- two candidate sources for historic tsunamigenic earthquakes contributing to a better characterization of the tsunami hazard in the SWIM
- a new method for quick source-to-coast runup estimation contributing to a better understanding of the relation between waveform and tsunami runup
- the assessment of tsunami impact parameters in the Palu-Donggala region after the September 28, 2018, Palu-Sulawesi Mw 7.5 earthquake and tsunami.

6.1. Future research and final considerations

Detection, monitoring, and early warning of tsunamis need to be improved to better protect populations at risk.

For countries prone to the tsunami hazard, mostly national agencies are responsible for tsunami warning centres. Tsunami warning includes monitoring for earthquakes and tsunamis. If an earthquake occurs, warning centers use seismic networks to evaluate the location, depth, and magnitude of an event. In case the earthquake meets certain criteria, that are often defined in a decision matrix a warning message is issued. However, appropriate computation of these parameters lasts at least 5 minutes before a warning can be issued or not. The evaluation of the seismic parameters does not allow for tsunami detection, but it allows evaluating if an earthquake had tsunamigenic potential. Consequently, an initially issued warning does not necessarily mean that a tsunami has been detected. Thus, if an event had tsunamigenic potential, the

eventually generated tsunami requires confirmation through detection. Then warning centers use in-situ sea-level data (DART buoys, tide gauges) to determine whether a tsunami was generated and if the warning message needs to be refined or cancelled.

Together with coastal sea level stations, the DART buoy network has significantly improved TWS, especially for mid to far-field events. However, the deployment and maintenance of DART buoys are expensive, and their lifetime is limited. Moreover, Piratary and vandalism have reportedly damaged many buoys (National Research Council, 2011; Thandlam et al., 2019).

Still there are limitations in tsunami detection capabilities and the determination of the offshore tsunami metrics is challenging. Some of the previously mentioned recent tsunami events have not been detected before landfall. In extreme cases the evaluation of tsunamis based on seismic networks may bare the risk that first threat messages are issued before earthquake stopped rupturing (c.f. Tohoku-Oki 2011). This fact highlights the need for an efficient sea level observation system to measure the waveform offshore. For non-seismic tsunamis a warning through seismic networks is not possible. Because of that a non-seismic tsunami especially on the local and regional scale may remain undetected until they strike the shore (c.f. Anak Krakatoa, Indonesia, 2018, Nuugaatsiaq, Greenland, 2017).

For those cases tsunami detection and warning methods need to be reviewed and adapted. For non-seismic sources a feasible tsunami warning system has not yet been developed. Considering local or regional non-seismic tsunamis a much denser network of sea-level monitoring systems or alternative technologies for tsunami detection are required. Future technologies for TWS could include, for example, earthquake and tsunami detection through fibre optic cables such as Science Monitoring and Reliable Telecommunications (SMART) Cables (Matias et al., 2021) or advanced space-based near to real-time systems to detect ocean surface altimetric anomalies (Silva et al., 2021).

Within the period of the PhD-investigation, the catastrophic September 28, 2018, Sulawesi, Palu earthquake happened. This event generated a multiple-source tsunami with runup values greater than 9 m inside the bay of Palu. The contributing generation mechanism included coastal landslides, most likely co-seismic deformation, and eventually submarine mass failures. The UNESCO-ITST observed massive coastal tsunami impact in Palu bay within the post-tsunami field survey and contributed with 62 runup and 16 inundation heights measurements. Further, the authors identified ten coastal landslides as contributing tsunami sources. The collected data within the UNESCO-ITST field survey contributed significantly to a better understanding of the particularities of the Palu disaster. Nevertheless, the extent of the contributing mechanisms

is still a matter of debate (Ulrich et al., 2019; Sepúlveda et al., 2020; Higuera et al., 2021; Schambach et al., 2021; Han et al., 2021).

Thandlam et al. (2019) stress that there is an urgent need in improving early warning systems and present a thorough review of what went wrong during the Palu event. These authors analyzed what they called 'failure' in the early warning system. While they discussed important political, financial, and societal issues regarding early warning preparedness and mitigation measures, possibly the early warning system was not fully functional due to earlier mentioned problems (expensive maintenance, vandalism, communication breakdown after the earthquake, among others). Certainly, all the shortcomings within the early warning process chain require a critical review and analysis and subsequent correction and improvement. However, it should be mentioned that even a fully functional operational warning system could not have provided a timely tsunami warning for most of the locations in Palu Bay.

What could we have learnt from this tragic earthquake and tsunami?

1. It was a reminder that even modern tsunami warning systems are not designed to detect and warn of a local event in complex geological settings. There are not enough sensors to detect small initial conditions such as local landslides. Depending on the landslides' sizes, those sources may dissipate quickly over increasing distances, but they may be highly devastating locally. Thus, we have reminded the future efforts should invest in systems that allow to warn population exposed to local and regional seismic and non-seismic sources.

2. Sea-level detection sensors are essential tools for tsunami warning systems and post-event analysis. If a tsunami is not detected, no appropriate warning can be issued. The analysis of the seismic data is an essential tool for tsunami warning, nevertheless they do not cover non-seismic sources. Thus, we have learnt that we need to overcome those limitations, testing future alternatives to extend existing warning systems, especially in complex tectonic and near-shore domains.

   Tragically only a couple of months later, the Sunda Strait tsunami struck Indonesia again, causing another 400 casualties. The volcanic activity of Anak Krakatoa caused a flank collapse generating this tsunami. A set of sensors with a high sampling rate in the near field around Anak Krakatoa could have detected the tsunami and enabled authorities to issue a warning.

3. It is vital to ensure that communication systems continue to work correctly, even after an earthquake of that magnitude. For many locations in the bay of Palu, it may have

been difficult to issue a timely warning. Nevertheless, for future events appropriate warnings may save some lives. Earthquake resilient communication systems should be implemented, especially for sensors that could record relevant information for warning purposes.

4. Specifically, in Sulawesi and Palu-Donggala, a region where tsunamis occur frequently, authorities and communities were surprised by the magnitude of the tsunami. Indeed, it is surprising that a strike-slip rupture mechanism generates a tsunami that produces runup heights up to 10 m. However, the information on the type of rupture is available only some minutes after the event. For communities at risk, it is not relevant if a strike-slip, inverse earthquake or another source generated the tsunami. Regardless of the generation mechanism and contributing sources, considering the Palu event, many livelihoods could have been saved if people were prepared to react appropriately. For events like in Sulawesi Island, especially concerning the earthquake and tsunami of Palu Bay, applies 'the earthquake is the earliest warning possible', and communities must be prepared to respond adequately. The Palu tsunami demonstrated the need for effective preparedness and mitigation measures for communities at risk. These programs are crucial for locations with complex geologic and tectonic settings and locations where sources are located close to shore and communities. In Ngapa and many other locations, the tsunami struck in less than 5 minutes (Omira et al., 2019). No warning system will be operational in the short- and mid-term to issue alerts in less than 5 minutes. Signposting evacuation routes alone is not enough. Exposed communities need preparedness programs to respond correctly with or without warning. Thus, we have learnt that the only possibility to protect people from tsunamis generated close to shore is through preparedness, training, and mitigation.

Besides, there is an urgent need in fostering awareness and preparedness among other coastal communities worldwide. Also, the recent European tsunami events triggered by a Mw 6.9 earthquake in Kos-Bodrum on July 20, 2017, and by a Mw 7.0 earthquake between the Aegean Island Samos and Turkey south of Izmir on October 30, 2020, highlighted the need for increasing the awareness of coastal communities and authorities through preparedness and mitigation programs (e.g., Tsunami Ready, Last Mile) (UNESCO, 2020). Thus, disaster risk management is a priority for many communities, especially for the most exposed ones.

Finally, it should be stressed that besides improving tsunami detection, forecast and warning systems, there is a need to focus on education. Educational efforts like the Tsunami Ready

programs improve the coastal community's preparedness and ultimately minimize loss of lives and assets. Once the communities are prepared, they are ready to respond appropriately and in time before the next tsunami strikes. These measures could start immediately if the societal and political and will is there.

References

Abercrombie, R.E., Antolik M, Felzer K, Ekström G (2001) The 1994 Java tsunami earthquake: Slip over a subducting seamount. J Geophys Res Solid Earth 106(B4):6595–6607, https://doi.org/10.1029/2000JB900403

Aki, K. (1972) Earthquake mechanism. Tectonophysics 13(1-4), 423-446

Albini, P., Musson, R.M., Rovida, A., Locati, M., Gomez Capera, A.A., Viganò, D. (2014) The global earthquake history. Earthq. Spectra 30(2), 607-624

Alves, T.M., Gawthorpe, R.L., Hunt, D.W., Monteiro, J.H. (2003) Cenozoic tectono-sedimentary evolution of the western Iberian margin. Mar. Geol. 195(1-4), 75-108, https://doi.org/10.1016/S0025-3227(02)00683-7

Alves, T.M., Moita, C., Cunha, T., Ullnaess, M., Myklebust, R., Monteiro, J.H., Manuppella, G. (2009) Diachronous evolution of Late Jurassic–Cretaceous continental rifting in the northeast Atlantic (west Iberian margin). Tectonics, 28(4), https://doi.org/10.1029/2008TC002337

Ambraseys, N.N. (1985) Intensity Attenuation and Magnitude Intensity Relationships for Northwest European Earthquakes. Earthq. Eng. Struct. D. 13, 733–778

Ammon, C.J., Lay, T., Kanamori, H., Cleveland, M. (2011) A rupture model of the 2011 off the Pacific coast of Tohoku earthquake. Earth Planets Space 63(7):33, https://doi.org/10.5047/eps.2011.05.015

An, C., Sepúlveda, I., Liu, P.L.-F. (2014) Tsunami source and its validation of the 2014 Iquique, Chile, earthquake. Geophys. Res. Lett. 41(11), 3988-3994

Anderson, D., Harris, M., Hartle, H., Nicolsky, D., Pelinovsky, E.N., Raz, A., Rybkin, A., (2017) Runup of long waves in piecewise sloping U-shaped bays. Pure Appl. Geophys. 174, 3185–3207 (2017). https://doi.org/10.1007/s00024-017-1476-3

Annual Register, Volume 4, 92–95, 1761. available at: https://babel.hathitrust.org/cgi/pt?id=uva.x001119514;view=1up;seq=104 (last access: January 31, 2019).

Albarello, D., D'Amico, V. (2004) Attenuation relationship of macroseismic intensity in Italy for probabilistic seismic hazard assessment. Boll. di Geofis. Teor. ed Appl. 45(4), 271-284

Aránguiz, R., González, G., González, J., Catalán, P.A., Cienfuegos, R., Yagi, Y., Okuwaki, R., Urra, L., Contreras, K., Del Rio, I., Rojas, C. (2016) The 16 September 2015 Chile tsunami from the post-tsunami survey and numerical modeling perspectives. Pure Appl Geophys 173(2):333–348

Aránguiz, R., Esteban, M., Takagi, H., Mikami, T., Takabatake, T., Gómez, M., González, J., Shibayama, T., Okuwaki, R., Yagi Y., Shimizu, K., Achiari H., Stolle, J., Robertson, I., Ohira, K., Nakamura, R., Nishida, Y., Krautwald, C., Goseberg, N., Nistor, I. (2020) The

2018 Sulawesi tsunami in Palu city as a result of several landslides and coseismic tsunamis. Coast. Eng. J. 62(4), 445-459

Argus, D.F., Gordon, R.G., DeMets, C., Stein, S. (1989) Closure of the Africa-Eurasia-North America plate motion circuit and tectonics of the Gloria fault. J. Geophys. Res.-Sol. Ea. 94, 5585– 5602, https://doi.org/10.1029/JB094iB05p05585

Aydın, B., Kânoğlu, U. (2017) New analytical solution for nonlinear shallow water-wave equations. Pure Appl. Geophys. 174(8):3209-3218, https://doi.org/10.1007/s00024-017-1508-z

Baglione, E., Armigliato, A., Pagnoni, G., Tinti, S. (2017) Heterogeneous slip distribution on faults responsible for large earthquakes: characterization and implications for tsunami modelling. EGU General Assembly Conference Abstracts (p. 7929)

Baptista, A.M., Priest, G.R., Murty, T.S. (1993) Field survey of the 1992 Nicaragua tsunami. Mar. Geodesy, 16(2), 169-203

Baptista, M.A., Miranda, P., Victor, L.M. (1992) Maximum entropy analysis of Portuguese tsunami data; the tsunamis of 28.02. 1969 and 26.05. 1975. Sci. Tsunami Hazards, 10(1), 9-20

Baptista, M.A., Miranda, P.M.A., Miranda, J.M., Victor, L.M. (1998a) Constrains on the source of the 1755 Lisbon tsunami inferred from numerical modelling of historical data on the source of the 1755 Lisbon tsunami. J. Geodyn., 25, 159–174, https://doi.org/10.1016/S0264-3707(97)00020-3

Baptista, M.A., Heitor, S., Miranda, J.M., Miranda, P., Victor, L.M. (1998b) The 1755 Lisbon tsunami; evaluation of the tsunami parameters. J. Geodyn., 25, 143–157

Baptista, M.A., Miranda, J.M., Chierici, F., Zitellini, N. (2003) New study of the 1755 earthquake source based on multi-channel seismic survey data and tsunami modeling. Nat. Hazards Earth Syst. Sci. 3(5), 333-340

Baptista, M.A., Miranda, J.M., Luis, J.F. (2006) In search of the 31 March 1761 earthquake and tsunami source. Bull. Seismol. Soc. Am. 96(2), 713-7211, doi:10.1785/0120050111

Baptista, M.A., Miranda, J.M., Lopes, F.C., Luis, J.F. (2007) The source of the 1722 Algarve earthquake: evidence from MCS and Tsunami data. J. Seismol. 11(4), 371-380

Baptista, M.A., Miranda, J.M. (2009) Revision of the Portuguese catalog of tsunamis. Nat. Hazards Earth Syst. Sci. 9, 25–42, https://doi.org/10.5194/nhess-9-25-2009

Baptista, M.A., Miranda, J.M., Omira, R., Antunes, C. (2011) Potential inundation of Lisbon downtown by a 1755-like tsunami. Nat. Hazards Earth Syst. Sci., 11(12), 3319-3326

Baptista, M.A., Miranda, J.M., Batlló, J. (2014) The 1531 Lisbon earthquake: A tsunami in the Tagus estuary?. Bull. Seismol. Soc. Am. 104(5), 2149-2161

Baptista, M.A., Miranda, J.M., Batlló, J., Lisboa, F., Luis, J., Maciá, R. (2016) New study on the 1941 Gloria Fault earthquake and tsunami. Nat. Hazards Earth Syst. Sci., 16, 1967–1977, https://doi.org/10.5194/nhess-16-1967-2016

Baptista, M.A., Miranda, J.M., Matias, L., Omira, R. (2017) Synthetic tsunami waveform catalogs with kinematic constraints. Nat. Hazards Earth Syst. Sci. 17(7):1253–1265, https ://doi.org/10.5194/nhess -17-1253-2017

Baptista, M.A. (2019) Tsunamis along the azores gibraltar plate boundary. Pure Appl. Geophys. 1-12

Baptista, M.A., Miranda, J.M., Omira, R., El-Hussain, I. (2020) Study of the 24 September 2013 Oman Sea tsunami using linear shallow water inversion. Arab. J. Geosci. 13(14), 1-12

Barkan, R., Uri, S., Lin, J. (2009) Far field tsunami simulations of the 1755 Lisbon earthquake: Implications for tsunami hazard to the US East Coast and the Caribbean. Mar. Geol. 264(1-2), 109-122

Bartolome, R., Gràcia, E., Stich, D., Martínez-Loriente, S., Klaeschen, D., de Lis Mancilla, F., Lo Iacono, C., Dañobeitia, J.J., Zitellini, N. (2012) Evidence for active strike-slip faulting along the Eurasia-Africa convergence zone: Implications for seismic hazard in the southwest Iberian margin. Geology, 40, 495–498

Behrens, J., Løvholt, F., Jalayer, F., Lorito, S., Salgado-Gálvez, M.A., Sørensen, M., Abadie, S., Aguirre-Ayerbe, I., Aniel-Quiroga, I., Babeyko, A., Baiguera, M., Basili, R., Belliazzi, S., Grezio, A., Johnson, K., Murphy, S., Paris, R., Rafliana, I., De Risi, R., Rossetto, T., Selva, J., Taroni, M., Del Zoppo, M., Armigliato, A., Bureš, V., Cech, P., Cecioni, C., Christodoulides, P., Davies, G., Dias, F., Bayraktar, H.B., González, M., Gritsevich, M., Guillas, S., Harbitz, C.B., Kânoğlu, U., Macías, J., Papadopoulos, G.A., Polet, J., Romano, F., Salamon, A., Scala, A., Stepinac, M., Tappin, D.R., Thio, H.K., Tonini, R., Triantafyllou, I., Ulrich, T., Varini, E., Volpe, M., Vyhmeister, E. (2021) Probabilistic Tsunami Hazard and Risk Analysis: A Review of Research Gaps. Front. Earth Sci. 9:628772, doi: 10.3389/feart.2021.628772

Bellier, O., Sébrier, M., Beaudouin, T., Villeneuve, M., Braucher, R., Bourles, D., Siame, L., Putranto, E., Pratomo, I. (2001) High slip rate for a low seismicity along the Palu-Koro active fault in central Sulawesi (Indonesia). Terra Nova, 13(6), 463-470

Bellin, J.N. (1762) Carte hydrographique de La Baye De Cadix. Versailles

Bernard, E., Titov, V. (2015) Evolution of tsunami warning systems and products. Phil. Trans. R. Soc. A, 373(2053), 20140371

Bevacqua, E., Maraun, D., Vousdoukas, M.I., Voukouvalas, E., Vrac, M., Mentaschi, L., Widmann, M. (2019) Higher probability of compound flooding from precipitation and storm surge in Europe under anthropogenic climate change. Sci. Adv. 5(9), p.eaaw5531

Blaser, L., Krüger, F., Ohrnberger, M., Scherbaum, F. (2010) Scaling relations of earthquake source parameter estimates with special focus on subduction environment. Bull. Seismol. Soc. Am., 100(6), 2914-2926

Bommer, J.J., Stafford, P.J. (2016) Seismic hazard and earthquake actions. In Seismic design of buildings to Eurocode 8 (pp. 21-54), CRC Press

Borges, J.F., Fitas, A.J., Bezzeghoud, M., Teves-Costa, P. (2001) Seismotectonics of Portugal and its adjacent Atlantic area. Tectonophysics, 331(4), 373-387

Borlase, W. (1762) Some Account of the extraordinary Agitation of the Waters in Mount's-bay, and other Places, on the 31st of March 1761, in a Letter for the Reverend C. Lyttelton. Philos. T. Roy. Soc., 52, 418–431

Borrero, J.C., Solihuddin, T., Fritz, H.M., Lynett, P.J., Prasetya, G.S., Skanavis, V., Semeidi Husrin, S., Kushendratno, Kongko, W., Istiyanto, D.C., Daulat, A., Purbani, D., Salim, H.L., Hidayat, R., Asvaliantina, V., Usman, M., Kodijat, A., Son, S., Synolakis, C.E. (2020) Field survey and numerical modelling of the December 22, 2018 Anak Krakatau Tsunami. Pure Appl. Geophys. 177, 2457-2475

Bravo Monge, J.B., López Arroyo, A., Rodríguez de la Torre, F. (1990) Terremoto de Setubal de 1858. Programa de investigación de sismicidad histórica. Instituto Geográfico Nacional, Informe interno, p. 17

Bricker, J.D., Gibson, S., Takagi, H., Imamura, F. (2015) On the need for larger manning's roughness coefficients in depth-integrated tsunami inundation models. Coast. Eng. J. https://doi.org/10.1142/S0578563415500059

Brito, F.B. (1597) Monarquia Lusitana, Lisboa Imprensa Nacional – Casa da Moeda, Facsimile. 1973–88

Buforn, E., Udías, A., Colombas, M. (1988) Seismicity, source mechanisms and tectonics of the Azores – Gibraltar plate-boundary. Tectonophysics, 152, 89–118

Burwell, D., Tolkova, E., Chawla, A. (2007) Diffusion and dispersion characterization of a numerical tsunami model. Ocean Model. 19(1–2):10–30

Butler, R. (2019) Seismic precursors to a 2017 Nuugaatsiaq, Greenland, earthquake–landslide–tsunami event. Nat. Hazards 96(2), 961-973

Cabral, J., Moniz, C., Ribeiro, P., Terrinha, P., Matias, L. (2003) Analysis of seismic reflection data as a tool for the seismotectonic assessment of a low activity intraplate basin–the Lower Tagus Valley (Portugal). J. Seismol. 7(4), 431-447

Cabral, J., Moniz, C., Batlló, J., Figueiredo, P., Carvalho, J., Matias, L., Teves-Costa, P., Dias, R., Simão, N. (2013) The 1909 Benavente (Portugal) earthquake: search for the source. Nat. Hazards 69(2), 1211-1227

Cabral, N. (2020) Revision of the Azorean catalogue of tsunamis. Geol. Soc. Lond. spec. publ. 501

Cancani, A. (1904) Sur l'emploi d'une double echelle sismique des intensitès, empirique et absolue. Gerlands Beitr Geophys 2:281–283

Carrier, G.F., Greenspan, H.P. (1958) Water waves of finite amplitude on a sloping beach. J. Fluid Mech. 4(1):97–109. https://doi.org/10.1017/S0022112058000331

Carrier, G.F., Wu, T.T., Yeh, H. (2003) Tsunami runup and drawdown on a plane beach. J. Fluid Mech. 475, 449–461

Carrilho, F., Nunes, J.C., Pena J.A. (2004) Catálogo Sísmicode Portugal Continental e Região Adjacente 1970–2000. In: Senos LM (coord) Instituto de Meteorologia. Lisbon, p 227

Carvalho, J., Rabeh, T., Bielik, M., Szalaiová, E., Torres, L., Silva, M., Carrilho, F., Matias, L., Miranda, J.M. (2011) Geophysical study of the Ota–VF Xira–Lisbon–Sesimbra fault zone and the lower Tagus Cenozoic basin. J. Geophys. Eng. 8(3), 395-411

Carvalho, A., Costa, A.C., Oliveira, C.S. (2009) A finite–fault modeling of the 1755 Lisbon earthquake sources. In The 1755 lisbon earthquake: revisited (pp. 433-454). Springer, Dordrecht

Carvajal, M., Araya-Cornejo, C., Sepúlveda, I., Melnick, D., Haase, J.S. (2019) Nearly instantaneous tsunamis following the Mw 7.5 2018 Palu earthquake. Geophys. Res. Lett. 46(10), 5117-5126

Casado, C.L., Palacios, S.M., Delgado, J., Peláez, J.A. (2000) Attenuation of intensity with epicentral distance in the Iberian Peninsula. Bull. Seismol. Soc. Am. 90(1), 34-47

Catalán, P.A., Aránguiz, R., González, G., Tomita, T., Cienfuegos, R., González, J., Shrivastava, M.N., Kumagai, K., Mokrani, C., Cortés, P., Gubler, A. (2015) The 1 April 2014 Pisagua tsunami: observations and modeling. Geophys. Res. Lett. 42(8):2918–2925, https ://doi.org/10.1002/2015G L0633 33

Chakrabarti, P.D. (2018) Tsunami Aid and Its Effectiveness. In The Asian Tsunami and Post-Disaster Aid (pp. 305-330). Springer, Singapore.

Chan, I.C., Liu, P.L.-F. (2012) On the runup of long waves on a plane beach. J. Geophys. Res. Oceans 117:C08006, https://doi.org/10.1029/2012JC007994

Chen, Y., Liu, P.L.-F. (1995) Modified boussinesq equations and associated parabolic models for water wave propagation. J. Fluid Mech. 288:351–381, https://doi.org/10.1017/S0022112095001170

Cho, Y.S. (1995) Numerical simulations of tsunami propagation and run-up (Doctoral dissertation, Cornell University)

Cho, Y.S., Kim, J.M. (2009) Moving boundary treatment in run-up process of tsunami. J. Coast. Res. 482-486

Choffat, P., Bensaude, A. (1912) Estudos sobre o sismo do Ribatejo de 23 de abril de 1909. Com. Serv. Geol. de Portugal, p. 145

Choi, B.H., Pelinovsky, E., Kim, D.C., Didenkulova, I., Woo, S.-B. (2008) Two- and three-dimensional computation of solitary wave runup on non-plane beach. Nonlinear Process Geophys. 15, 489–502. doi:10.5194/npg-15-489-2008

Contreras-López, M., Winckler, P., Sepúlveda, I., Andaur-Álvarez, A., Cortés-Molina, F., Guerrero, C.J., Mizobe, C.E., Igualt, F., Breuer, W., Beyá, J.F., Vergara, H. (2016) Field survey of the 2015 chile tsunami with emphasis on coastal wetland and conservation areas. Pure Appl. Geophys. 173:349–367. https ://doi. org/10.1007/s0002 4-015-1235-2

Cunha, T.A., Matias, L.M., Terrinha, P., Negredo, A.M., Rosas, F., Fernandes, R.M.S., Pinheiro, L.M. (2012) Neotectonics of the SW Iberia margin, Gulf of Cadiz and Alboran Sea: a reassessment including recent structural, seismic and geodetic data. Geophys. J. Int. 188(3), 850-872

Cushman-Roisin, B., Beckers, J.-M. (2005) Introduction to Geophysical Fluid Dynamics - Physical and Numerical Aspects. Academic Press

Custódio, S., Dias, N.A., Carrilho, F., Góngora, E., Rio, I., Marreiros, C., Morais, I., Alves, P., Matias, L. (2015). Earthquakes in western Iberia: Improving the understanding of lithospheric deformation in a slowly deforming region. Geophys. J. Int. 203(1), 127-145

Davies, G., Griffin, J., Løvholt, F., Glimsdal, S., Harbitz, C.B., Thio, H.K., Lorito, S., Basili, R., Selva, J., Geist, E., Baptista, M.A. (2018) A global probabilistic tsunami hazard assessment from earthquake sources. Geol. Soc. Lond. spec. publ. 456, https://doi.org/10.1144/SP456.5

Debrach, J. (1946) Raz de marée d'origine sismique en registrée sur le littoral atlantique du Maroc (in french). Service de Physique du Globe et de Metéorologie, Annales, Maroc

Delouis, B., Nocquet, J.M., Vallée, M. (2010) Slip distribution of the February 27, 2010 Mw=8.8 Maule earthquake, central Chile, from static and high-rate GPS, InSAR, and broadband teleseismic data. Geophys. Res. Lett. https://doi.org/10.1029/2010GL043899

DeMets, C., Gordon, R.G., Argus, D.F., Stein, S. (1990) Current plate motions. Geophys. J. Int., 101, 425–478

DeMets, C., Gordon, R.G., Argus, D.F., Stein, S. (1994) Effect of recent revisions to the geomagnetic reversal time scale on estimates of current plate motions. Geophys. Res. Lett. 21, 2191– 2194, https://doi.org/10.1029/94GL02118

DeMets, C., Dixon, T.H. (1999) New kinematic models for Pacific-North America motion from 3 Ma to present, I: Evidence for steady motion and biases in the NUVEL-1A model. Geophys. Res. Lett., 26, 1921–1924, https://doi.org/10.1029/1999GL900405

Diário de Governo (1858) Numeros, 267, 268, 269 e 272

Didenkulova, I.I., Zahibo, N., Kurkin, A.A., Pelinovsky, E.N. (2006) Steepness and spectrum of a nonlinearly deformed wave on shallow waters. Izv. Atmos. Ocean Phy. 42(6):773–776, https://doi.org/10.1134/S0001433806060119

Didenkulova, I.I., Pelinovsky, E.N., Soomere, T., Zahibo, N. (2007a) Runup of nonlinear asymmetric waves on a plane beach. In: Kundu A (ed) Tsunami and nonlinear waves. Springer, Berlin, pp 175–190, https ://doi.org/10.1007/978-3-540-71256 -5_8

Didenkulova, I.I., Kurkin, A.A., Pelinovsky, E.N. (2007b) Run-up of solitary waves on slopes with different profiles. Izv. Atmos. Ocean Phy. 43(3):384–390, https://doi.org/10.1134/S0001433807030139

Didenkulova, I.I., Pelinovsky, E.N. (2011a) Nonlinear wave evolution and runup in an inclined channel of a parabolic crosssection. Phys. Fluids, 23, 086602, doi:10.1063/1.3623467

Didenkulova, I.I., Pelinovsky, E. N. (2011b) Runup of tsunami waves in U-shaped bays. Pure Appl. Geophys. 168, 1239–1249, doi:10.1007/s00024-010-0232-8

Direção-Geral do Território (2011) Modelo Digital do Terreno das Zonas Costeiras de Portugal Continental com resolução de 2 m (600 m mar, 400 m terra) – LiDAR, Direção de Serviços de Geodesia e Informação Geográfica, Direção-Geral do Território (DGT), Lisboa.

Dogan, G.G., Annunziato, A., Papadopoulos, G.A., Guler, H.G., Yalciner, A.C., Cakir, T.E., Sozdinler, C.O., Ulutas, E., Arikawa, T., Suzen, M.L., Guler I., Probst, P., Kânoğlu, U., Synolakis, C. (2019) The 20th July 2017 Bodrum–Kos Tsunami Field Survey. Pure Appl. Geophys. 176(7), 2925-2949

Duarte, J.C., Rosas, F.M., Terrinha, P., Gutscher, M.A., Malavieille, J., Silva, S., Matias, L. (2011) Thrust–wrench interference tectonics in the Gulf of Cadiz (Africa–Iberia plate boundary in the North-East Atlantic): insights from analog models. Mar. Geol. 289(1-4), 135-149

Duarte, J.C., Rosas, F.M., Terrinha, P., Schellart, W.P., Boutelier, D., Gutscher, M.A., Ribeiro, A. (2013) Are subduction zones invading the Atlantic? Evidence from the southwest Iberia margin. Geology 41, 839–842, https://doi.org/10.1130/G34100.1

Dutykh, D., Dias, F. (2007) Water waves generated by a moving bottom. In Tsunami and Nonlinear waves (pp. 65-95), Springer Berlin Heidelberg

Duputel, Z., Rivera, L., Kanamori, H., Hayes, G.P., Hirshorn, B., Weinstein, S. (2011) Real-time W phase inversion during the 2011 off the Pacific coast of Tohoku Earthquake. Earth Planets Space 63(7), 535-539

Dyakonova, T., Khoperskov, A. (2018) Bottom friction models for shallow water equations: Manning's roughness coefficient and small-scale bottom heterogeneity. J. Phys. Conf. Ser. Vol. 973, No. 1, p. 012032, IOP Publishing

Dziewonski, A.M., Ekström, G., Salganik, M.P. (1995) Centroid-moment tensor solutions for April–June 1994. Phys Earth Planet Inter 88(2):69–78, https ://doi.org/10.1016/0031-9201(94)03006 -5

Dziewonski, A.M., Ekström, G., Salganik, M.P. (1997) Centroid-moment tensor solutions for october–december 1995. Phys Earth Planet Inter 101(1–2):1–12, https://doi.org/10.1016/S0031-9201(96)03199-8

EM-DAT (2017) The Emergency Events Database - Université catholique de Louvain (UCL) - CRED, D. Guha-Sapir - www.emdat.be, Brussels, Belgium

European Commission (2018) Mw 7.5 Earthquake in Indonesia, 28 Sep 2018 GDACS Earthquake RED Alert, GDACS Tsunami ORANGE Alert 01 Oct 2018 - Emergency Report - UPDATE #1. Available at: http://learningfromearthquakes.org/2018-09-28-palu-indonesia/images/2018_09_28_palu_indonesia/pdfs/preliminary_reports/JRC-Emergency-Report.pdf (last access: November 12, 2021)

Fearns, J. (1761) Letter to The London Chronicle, No. 731, p. 214. Available at: https://news-paperarchive.com/uk/middlesex/london/london-chronicle/ (last access: January 31, 2019)

Fernandes, R.M.S., Bastos, L., Miranda, J.M., Lourenço, N., Ambrosius, B.A.C., Noomen, R., Simons, W. (2006) Defining the plate boundaries in the Azores region. J. Volcanol. Geoth. Res. 156, 1–9, https://doi.org/10.1016/j.jvolgeores.2006.03.019

Fernandes, R.M.S., Miranda, J.M., Meijninger, B.M.L., Bos, M.S., Noomen, R., Bastos, L., Ambrosius, B.A.C., Riva, R.E.M. (2007) Surface velocity field of the Ibero-Maghrebian segment of the Eurasia-Nubia plate boundary. Geophys. J. Int. 169, 315–324

Flow Science Inc. (2018) Flow-3D®, Version 12.0, User's Manual. Available at: https://www.flow3d.com (last access: January 31, 2020), Santa Fe, USA

Fonseca, J.F.B.D., Vilanova, S.P., Bosi, V., Meghraoui, M. (2001) Reply [to "Comment on 'Investigations unveil Holocene thrusting for onshore Portugal'"]. EOS Trans. Am. Geophys. Union 82(32), 352-353

Fonseca, J.F.B.D., Vilanova, S.P. (2010) The 23 April 23 1909 Benavente (Portugal) M 6.3 earthquake. Seismol. Res. Lett. 81(3), 534-536

Franco, A., Moernaut, J., Schneider-Muntau, B., Strasser, M., Gems, B. (2020) The 1958 Lituya Bay tsunami–pre-event bathymetry reconstruction and 3D numerical modelling utilising the computational fluid dynamics software Flow-3D. Nat. Hazards Earth Syst. Sci. 20(8), 2255-2279

Fritz, H.M., Petroff, C.M., Catalán, P.A., Cienfuegos, R., Winckler, P., Kalligeris, N., Weiss, R., Barrientos, S.E., Meneses, G., Valderas-Bermejo, C., Ebeling, C., Papadopoulos, A., Contreras, M., Almar, R., Dominguez, J.C., Synolakis, C.E. (2011) Field survey of the 27 february 2010 Chile tsunami. Pure Appl. Geophys. 168(11):1989–2010, https://doi.org/10.1007/s00024-011-0283-5

Fuentes, M.A., Ruiz, J.A., Riquelme, S. (2015) The runup on a multilinear sloping beach model. Geophys. J. Int. 201, 915–928, doi:10.1093/gji/ggv056

Fuhrman, D.R., Madsen, P.A. (2009) Tsunami generation, propagation, and run-up with a high-order Boussinesq model. Coast. Eng. 56(7):747–758, https://doi.org/10.1016/j.coastaleng.2009.02.004

Fukao, Y. (1973) Thrust faulting at a lithospheric plate boundary the Portugal earthquake of 1969. Earth Planet. Sci. Lett. 18(2), 205-216

Galbis Rodríguez, J. (1932) Catálogo sísmico de la zona comprendida entre los meridianos 5° e. y 20° W. de Greenwich y los paralelos 45° y 25° N. Instituto Geográfico y Catastral, t. I, p. 807

Gasperini, P., Bernardini, F., Valensise, G., Boschi, E. (1999) Defining seismogenic sources from historical earthquake felt reports. Bull. Seismol. Soc. Am. 89(1), 94-110

Gasperini, P. (2001) The attenuation of seismic intensity in Italy: A bilinear shape indicates dominance of deep phases at epicentral distances longer than 45 km. Bull. Seismol. Soc. Am. 91, 826–841

Gasperini, P., Vannucci, G., Tripone, D., Boschi, E. (2010) The location and sizing of historical earthquakes using the attenuation of macroseismic intensity with distance. Bull. Seismol. Soc. Am. 100(5A), 2035-2066

GEBCO (2014) The general bathymetric chart of the oceans, GEBCO_2014 grid, version 20150318. Available at: https ://www.gebco.net (last access: November 21, 2019)

Geissler, W.H., Matias, L., Stich, D., Carrilho, F., Jokat, W., Monna, S., IbenBrahim, A. Mancilla, F., Gutscher, M.-A., Sallarès, V., Zitellini, N. (2010) Focal mechanisms for sub–crustal earthquakes in the Gulf of Cadiz from a dense OBS deployment. Geophys. Res. Lett. 37, L18309, doi:10.1029/2010GL044289

Geist, E.L., Dmowska, R. (1999) Local tsunamis and distributed slip at the source. Pure Appl. Geophys. 154:485–512

Geist, E.L. (2002) Complex earthquake rupture and local tsunamis. J. Geophys. Res. Solid Earth 107(B5):ESE 2–1– ESE 2–15, https://doi.org/10.1029/2000JB000139

Geist, E.L., Parsons, T. (2014) Undersampling power-law size distributions: effect on the assessment of extreme natural hazards. Nat. Hazards 72(2), 565-595

Geist, E.L., Titov, V.V., Arcas, D., Pollitz, F.F., Bilek, S.L. (2007) Implications of the 26 December 2004 Sumatra–Andaman earthquake on tsunami forecast and assessment models for great subduction-zone earthquakes. Bull. Seismol. Soc. Am. 97(1A), S249-S270

Gjevik, B., Pedersen, G., Dybesland, E., Harbitz, C.B., Miranda, P.M.A., Baptista, M.A., Mendes-Victor, L., Heinrich, P., Roche R., Guesima, M. (1997) Modeling tsunamis from earthquake sources near Gorringe Bank southwest of Portugal. J. Geophys. Res. 102(C13), 27 931–27 949

Glimsdal, S., Pedersen, G.K., Harbitz, C.B., Løvholt, F. (2013) Dispersion of tsunamis: does it really matter?. Nat. Hazards Earth Syst. Sci. 13(6), 1507-1526

Gomez-Capera, A.A., Rovida, A., Gasperini, P., Stucchi, M., Viganò, D. (2015) The determination of earthquake location and magnitude from macroseismic data in Europe. Bull. Earthq. Eng. 13(5), 1249-1280

González, F.I., Geist, E.L., Jaffe, B., Kânoğlu, U., Mofjeld, H., Synolakis, C.E., Titov, V.V., Arcas, D., Bellomo, D., Carlton, D., Horning, T., Johnson, J., Newman, J., Parsons, T., Peters, R., Peterson, C., Priest, G., Venturato, A., Weber, J., Wong, F., Yalciner, A.C. (2009) Probabilistic tsunami hazard assessment at seaside, Oregon, for near-and far-field seismic sources. J. Geophys. Res. Oceans 114(C11)

Gràcia, E., Dañobeitia, J.J., Vergés, J., and PARSIFAL Team (2003) Mapping active faults offshore Portugal (36∘ N– 38∘ N): Implications for seismic hazard assessment along the southwest Iberian margin. Geology31, 83–86

Green, G. (1838) On the motion of waves in a variable canal of small depth and width. Proc. Camb. Philos. Soc. 6, 457

Greenslade, D.J., Uslu, B., Allen, S.C., Kain, C.L., Wilson, K.M., Power, H.E. (2019) Evaluation of Australian tsunami warning thresholds using inundation modelling Pure Appl. Geophys. 177, 1425–1436 (2020), https://doi.org/10.1007/s00024-019-02377-z

Grezio, A., Babeyko, A., Baptista, M.A., Behrens, J., Costa, A., Davies, G., Geist, E.L., Glimsdal, S., González, F.I., Griffin, J., Harbitz, C.B., LeVeque, R.J., Lorito, S., Løvholt, F., Omira, R., Mueller, C., Paris, R., Parsons, T., Polet, J., Power, W., Selva, J., Sørensen, M.B., Thio, H.K. (2017) Probabilistic tsunami hazard analysis: Multiple sources and global applications. Rev. Geophys. 55(4), 1158–1198, https://doi.org/10.1002/2017RG000579

Grilli, S.T., Ioualalen, M., Asavanant, J., Shi, F., Kirby, J.T., Watts, P. (2007) Source constraints and model simulation of the December 26, 2004, Indian Ocean Tsunami. J. Waterw. Port, Coast. Ocean Eng. 133(6), 414-428

Grilli, S.T., Tappin, D.R., Carey, S., Watt, S.F., Ward, S.N., Grilli, A.R., Engwell, S.L., Zhang, C., Kirby, J.T., Schambach, L., Muin, M. (2019) Modelling of the tsunami from the December 22, 2018 lateral collapse of Anak Krakatau volcano in the Sunda Straits, Indonesia. Sci. Rep. 9(1), 1-13

Grimson, N.L., Chen, W.P. (1986) The Azores-Gibraltar plate boundary: Focal mechanisms, depths of earthquakes, and their tectonic implications. J. Geophys. Res. 91, 2029-2047

Gupta, H.K., Gahalaut, V.K. (2013) Three Great Tsunamis: Lisbon (1755), Sumatra-Andaman (2004) and Japan (2011). Springer.

Gusman, A.R., Mulia, I.E., Satake, K. (2018) Optimum sea surface displacement and fault slip distribution of the 2017 Tehuantepec earthquake (Mw 8.2) in Mexico estimated from tsunami waveforms. Geophys. Res. Lett. 45(2), 646-653

Gusman, A.R., Supendi, P., Nugraha, A.D., Power, W., Latief, H., Sunendar, H., Widiyantoro, S., Daryono, Wiyono, S.H., Hakim, A., Muhari, A., Wang, X., Burbidge, D., Palgunadi, K., Hamling, I., Daryono, M.R. (2019) Source model for the tsunami inside Palu Bay following the 2018 Palu earthquake, Indonesia. Geophys. Res. Lett. 46(15), 8721-8730

Gutenberg, B., Richter, C.F. (1949) Seismicity of the Earth and associated phenomena, Princeton University Press, Princeton, New Jersey

Gutscher, M.A., Malod, J., Rehault, J.P., Contrucci, I., Klingelhoefer, F., Mendes-Victor, L., Spakman, W. (2002) Evidence for active subduction beneath Gibraltar. Geology 30(12), 1071-1074

Gutscher, M.A., Baptista, M.A., Miranda, J.M. (2006) The Gibraltar Arc seismogenic zone (part 2): constraints on a shallow east dipping fault plane source for the 1755 Lisbon earthquake provided by tsunami modeling and seismic intensity. Tectonophysics 426, 153–166, https://doi.org/10.1016/j.tecto.2006.02.025

Gutscher, M.A., Dominguez, S., Westbrook, G.K., Le Roy, P., Rosas, F., Duarte, J.C., Terrinha, P., Miranda, J.M., Graindorge, D., Sallares, V., Bartolome, R. (2012) The Gibraltar subduction: A decade of new geophysical data. Tectonophysics 574, 72–91, https://doi.org/10.1016/j.tecto.2012.08.038

Han, P., Yu, H., Yu, X. (2021) A sloshing induced Tsunami: 2018 Palu Bay event. Appl. Ocean Res. 117, 102915

Harris, M.W., Nicolsky, D.J., Pelinovsky, E.N., Pender, J.M., Rybkin, A.V. (2016) Run-up of nonlinear long waves in U-shaped bays of finite length: Analytical theory and numerical computations. J. Ocean Eng. Mar. Energy 2(2), 113–127, doi:10.1007/s40722-015-0040-4

Hayes G (2010) Updated result of the Feb 27, 2010 Mw 8.8 Maule, chile earthquake. National earthquake information center (NEIC) of United States geological survey. United States, Reston, VA. Available at: from https://earthquake.usgs.gov/earthquakes/eqinthenews/2010/us2010tfan/finite_fault (last access: October 17, 2019)

Hayward, A., Watts, A.B., Westbrook G.K., Collier J.S. (1999) A seismic reflection and GLORIA study of compressional deformation in the Gorringe Bank region, Eastern North Atlantic. Geophys. J. Int. 138, 831–850, https://doi.org/10.1046/j.1365246x.1999.00912.x

Heberden, T. (1761) An Account of the Earthquake felt in the Island of Madeira, 31 March 1761, communicated by Heberden, W., Philos. T. Roy. Soc., 52, p.155

Hébert, H., Schindelé, F. (2015) Tsunami impact computed from offshore modeling and coastal amplification laws: insights from the 2004 Indian Ocean Tsunami. Pure Appl. Geophys., 172, 3385–3407

Heidarzadeh, M., Pirooz, M.D., Zaker, N.H., Yalciner, A.C. (2009) Preliminary estimation of the tsunami hazards associated with the Makran subduction zone at the northwestern Indian Ocean. Nat. Hazards 48(2), 229-243

Heidarzadeh, M., Muhari, A., Wijanarto, A.B. (2018) Insights on the source of the 28 September 2018 Sulawesi tsunami, Indonesia based on spectral analyses and numerical simulations. Pure Appl. Geophys. 176(1), 25-43, https://doi.org/10.1007/s00024-018-2065-9

Heidarzadeh, M., Ishibe, T., Sandanbata, O., Muhari, A., Wijanarto, A.B. (2020). Numerical modeling of the subaerial landslide source of the 22 December 2018 Anak Krakatoa volcanic tsunami, Indonesia. Ocean Eng. 195, 106733

Heidbach, O., Rajabi, M., Reiter, K., Ziegler, M., and Wsm Team. (2016) World stress map database release 2016. GFZ Data Services, 10

Heinrich, P., Baptista, M.A., Miranda, P.M.A. (1994) Numerical Simulations of the 1969 Tsunami along the Portuguese coasts. Sci. Tsunami Hazards 12(1), 3–25

Henriques, M.C., Mouzinho, M.T., Ferrão, N.M. (1988) Sismicidade de Portugal, Osismo de 26 de Janeiro de 1531. Ministério do Planeamento e Administração doe Terriório, Lisbon, Portugal (in Portuguese)

Higuera, P., Sepulveda, I., Liu, P.L.-F. (2021) Filling in the gaps of the tsunamigenic sources in 2018 Palu Bay tsunami. arXiv preprint arXiv:2105.07718

Ho, T.C., Satake, K., Watada, S., Hsieh, M.C., Chuang, R.Y., Aoki, Y., Mulia, I.E., Gusman, A.R., Lu, C.H. (2020) Tsunami Induced by the Strike-Slip Fault of the 2018 Palu Earthquake (Mw= 7.5), Sulawesi Island, Indonesia. Earth Space Sci. 8(6), e2020EA001400

Hoechner, A., Ge, M., Babeyko, A.Y., Sobolev, S.V. (2013) Instant tsunami early warning based on real-time GPS–Tohoku 2011 case study. Nat. Hazards Earth Syst. Sci. 13(5), 1285-1292

ICG/NEAMTWS (2011) Interim Operational Users Guide for the Tsunami Early Warning and Mitigation System in the Northeastern Atlantic, the Mediterranean and Connected Seas (NEAMTWS), Version 2.0. Available at: https://www.ingv.it/cat/images/images/documenti/NEAMTWS-OpUGversion_2_0_Final.pdf (last access: March 17, 2021)

Ide, S., Imamura, F., Yoshida, Y., Abe, K. (1993) Source characteristics of the Nicaraguan tsunami earthquake of September 2, 1992. Geophys. Res. Lett. 20(9), 863-866.

Imamura, F. (1995) Long waves in two-layers: governing equations and numerical model. Sci. Tsunami Hazards 13(1):3–24

INGV Istituto Nazionale di Geofisica e Vulcanologia (2015) Individual Seismogenic Sources. Available at: http://diss.rm.ingv.it/diss/index.php/tutorial/15-individual-seismogenic-sources (last access: September 9, 2021)

Instituto Geográfico Nacional (IGN) (2018) Earthquake catalogue - Earthquakes from 1370 A.D. to present. Available at: http://www.ign.es/web/ign/portal/sis-catalogo-terremotos/ (last access: February 1, 2018)

Japan Meteorological Agency (JMA) (2013) Lessons learned from the tsunami disaster caused by the 2011 Great East Japan earthquake and improvements in JMA's tsunami warning system. Available at: https://www.data.jma.go.jp/svd/eqev/data/en/tsunami/LessonsLearned_Improvements_brochure.pdf (last access: January 24, 2020)

Jiménez-Munt, I., Fernàndez, M., Vergés, J., Afonso, J.C., Garcia-Castellanos, D., Fullea, J. (2010) Lithospheric structure of the Gorringe Bank: Insights into its origin and tectonic evolution. Tectonics, 29, TC5019, https://doi.org/10.1029/2009TC002458

Johnston, A.C., Kanter, L.R. (1990) Earthquakes in stable continental crust. Sci. Am. 262(3), 68-75

Johnston, A.C. (1996) Seismic moment assessment of earthquakes in stable continental regions—III. New Madrid 1811–1812, Charleston 1886 and Lisbon 1755. Geophys. J. Int. 126(2), 314- 344

Journal Historique (1756) Journal Historique sur Les Matières du Tems contenant quelques nouvelles de Litterature, et autres Remarques curieuses, Suite des Tremblements de Terre, p. 462, (in French)

Journal Historique (1773) Suite de La Clef ou Journal Historique sur Les Matieres du Tems, contenant quelques nouvelles de Litterature, et autres Remarques curieuses, Juin 1773, Premiere Partie, Tome CXIII, Paris, 462–464, 1773 (in French)

Justo, J.L., Salwa, C. (1998) The 1531 Lisbon earthquake. Bull. Seismol. Soc. Am. 88(2), 319-328

Kaabouben, F., Brahim, A.I., Toto, E., Baptista, M.A., Miranda, J.M., Soares, P., Luis, J.F. (2008) On the focal mechanism of the 26.05.1975 North Atlantic event contribution from tsunami modeling. J. Seismol. 12, 575–583

Kaabouben, F., Baptista, M.A., Brahim, A.I., Mouraouah, A.E., Toto, A. (2009) On the moroccan tsunami catalogue. Nat. Hazards Earth Syst. Sci. 9(4), 1227-1236

Kajiura, K. (1970) Tsunami source, energy and the directivity of wave radiation. Bull. Earthq. Res. Inst. 48:835–869.

Kanamori, H. (1972) Mechanism of tsunami earthquakes. Phys. Earth Planet. Inter. 6(5), 346-359

Kanamori, H., Anderson, D.L. (1977) Importance of physical dispersion in surface-wave and free oscillation problems – review. Rev. Geophys. 15(1): 105-112

Kânoğlu, U., Synolakis, C.E. (1998) Long wave runup on piecewise linear topographies. J. Fluid Mech. 374:1–28, https://doi.org/10.1017/S0022112098002468

Kânoğlu, U. (2004) Nonlinear evolution and runup–rundown of long waves over a sloping beach. J. Fluid Mech. 513:363–372, https://doi.org/10.1017/S002211200400970X

Kânoğlu, U., Titov, V.V., Bernard, E., Synolakis, C.E. (2015) Tsunamis: bridging science, engineering and society. Philos. Trans. R. Soc. A. Math. Phy. Eng. Sci. 373:20140369, https://doi.org/10.1098/rsta.2014.0369

Kim, V. (2011). Japan damage could reach $235 billion, World Bank estimates. Retrieved March 21, 2011

Kirby, J.T., Wei, G., Chen, Q., Kennedy, A.B., Dalrymple R.A. (1998) Funwave 1.0: fully nonlinear Boussinesq wave model documentation and user's manual. Research Rep. CACR-98–06, Center for Applied coastal research, Univ. of Delaware, Newark. Available at: https://resolver.tudelft.nl/uuid:d79bba08-8d35-47e2-b901-881c86985ce4 (last access: January 24, 2020)

Kullberg, M.C., Kullberg, J.C.R., Terrinha, P. (2000) Tectónica da cadeia da Arrábida. Memórias de Geociências, (2), 35-84

Laughton, A.S., Whitmarsh, R.B. (1974) The Azores-Gibraltar plate boundary, in: Geodynamics of Iceland and the North Atlantic area, edited by: Kristjansson, L., NATO Advanced Study Institute, Reykjavik, Springer, the Netherlands, 63–81, https://doi.org/10.1007/978-94-010-2271-2_5

Lario, J., Zazo, C., Goy, J.L., Silva, P.G., Bardaji, T., Cabero, A., Dabrio, C.J. (2011) Holocene palaeotsunami catalogue of SW Iberia. Quat. Int. 242(1), 196-200

Linsley, R.K., Franzini, J.B. (1979) Water Resources Engineering. 3rd Edition. McGraw-Hill Book Co., New York, pp 125–126

Liu, P.L.-F., Cho, Y.S., Briggs, M.J., Kanoglu, U., Synolakis, C.E. (1995) Runup of solitary waves on a circular island, J. Fluid Mech. 302, 259–285, https://doi.org/10.1017/S0022112095004095

Liu, P.L.-F., Woo, S.B., Cho, Y.S. (1998) Computer programs for tsunami propagation and inundation. Cornell University New York. Available at: https://tsunami-portal.nacse.org/documentation/COMCOT_tech.pdf (last access: January 24, 2020)

LNEC (1986) A Sismicidade Histórica e a Revisão do Catálogo Sísmico. Proc. 36/11/7368. Laboratório Nacional de Engenharia Civil. Ministério do Equipamento Social (in Portuguese)

Luis, J.F. (2007) MIRONE: A multi-purpose tool for exploring grid data. Comput. Geosci. 33(1):31–41, https://doi.org/10.1016/j.cageo.2006.05.005

Luque, L., Lario, J., Zazo, C., Goy, J.L., Dabrio, C.J., Silva, P.G. (2001) Tsunami deposits as paleoseismic indicators: examples from the Spanish coast. Acta geol. hisp. 36(3), 197-211

Luque, L., Lario, J., Civis, J., Silva, P.G., Zazo, C., Goy, J.L., Dabrio, C.J. (2002) Sedimentary record of a tsunami during Roman times, Bay of Cadiz, Spain. J. Quat. Sci. Published for the Quaternary Research Association, 17(5-6), 623-631

Lynnes, C.S., Ruff, L.J. (1985) Source process and tectonic implications of the great 1975 North Atlantic earthquake. Geophys. J. Int. 82, 497–510

Madsen, P.A., Sørensen, O.R. (1992) A new form of the Boussinesq equations with improved linear dispersion characteristics: part 2—a slowly-varying bathymetry. Coast. Eng. 18(3–4):183–204, https://doi.org/10.1016/0378-3839(92)90019-Q

Madsen, P.A., Fuhrman, D.R. (2008) Run-up of tsunamis and long waves in terms of surf-similarity. Coast. Eng. 55(3), 209–223, https://doi.org/10.1016/j.coastaleng.2007.09.007

Madsen, P.A., Fuhrman, D.R., Schäffer, H.A., (2008) On the solitary wave paradigm for tsunamis. J. Geophys. Res. Oceans 113:C12012, https://doi.org/10.1029/2008JC004932

Madsen, P.A., Schäffer, H.A. (2010) Analytical solutions for tsunami runup on a plane beach: single waves, N-waves and transient waves. J. Fluid Mech. 645, 27–57, https://doi.org/10.1017/S00221120099924 85

Manighetti, I., Campillo, M., Bouley, S., Cotton, F. (2007) Earthquake scaling, fault segmentation, and structural maturity. Earth Planet. Sc. Lett. 253, 429–438, https://doi.org/10.1016/j.epsl.2006.11.004

Mansinha, L.A., Smylie, D.E. (1971) The displacement fields of inclined faults. Bull. Seismol. Soc. Am. 61(5):1433–1440

Maramai, A., Tinti, S. (1997) The 3 June 1994 Java tsunami: a post-event survey of the coastal effects. Nat. Hazards 15(1):31–49, https://doi.org/10.1023/A:1007957224367

Mason, A. (1761) Letter to the Reverend Thomas Birch, D. D. Secretary to the Royal Society, relating to an extraordinary agitation of the Sea there, 31st of March 1761. Philos. T. Roy. Soc. 52, 477–478

Marcos, M., Rohmer, J., Vousdoukas, M.I., Mentaschi, L., Le Cozannet, G., Amores, A. (2019) Increased extreme coastal water levels due to the combined action of storm surges and wind waves. Geophys. Res. Lett. 46(8), pp. 4356-4364

Martínez-Loriente, S., Gràcia, E., Bartolome, R., Sallarès, V., Connors, C., Perea, H., Lo Iacono, C., Klaeschen, D., Terrinha P., Dañobeitia J.J., Zitellini, N. (2013) Active deformation in old oceanic lithosphere and significance for earthquake hazard: Seismic imaging of the Coral Patch Ridge area and neighboring abyssal plains (SW Iberian Margin), Geochem. Geophy. Geosy. 14, 2206–2231, https://doi.org/10.1002/ggge.20173

Martínez-Loriente, S., Sallarès, V., Gràcia, E., Bartolome, R., Dañobeitia, J.J., Zitellini, N. (2014) Seismic and gravity constraints on the nature of the basement in the Africa-Eurasia plate boundary: New insights for the geodynamic evolution of the SW Iberian Margin. J. Geophys. Res. 119, 127–149, https://doi.org/10.1002/2013JB010476

Martínez-Loriente, S., Gràcia, E., Bartolome, R., Perea, H., Klaeschen, D., Dañobeitia, J.J., Zitellini, N., Wynn, R.B., Masson, D.G. (2018) Morphostructure, tectono-sedimentary evolution and seismic potential of the Horseshoe Fault, SW Iberian Margin. Basin Res. 30, 382–400, https://doi.org/10.1111/bre.12225

Martínez Solares, J.M., Arroyo, A.L., Mezcua, J. (1979) Isoseismal map of the 1755 Lisbon earthquake obtained from Spanish data. Tectonophysics 53(3-4), 301-313

Martínez Solares, J.M., Lopez-Arroyo, A. (2004) The great historical 1755 earthquake: Effects and damage in Spain. J. Seismol. 8, 275– 294, https://doi.org/10.1023/B:JOSE.0000021365.94606.03

Martínez Solares, J.M., Mezcua, J. (2002) Catálogo sísmico de la Península Ibérica (880 a.C. - 1900). Instituto Geográfico Nacional, available at: http://www.ign.es/web/resources/sismologia/publicaciones//Catalogohasta1900.pdf (last access: September 15, 2021)

Martins, I., Mendes-Victor, L.A. (1990) Contribuição para o estudo da Sismicidade de Portugal Continental. (in Portuguese)

Martins, I., Mendes-Victor, L.A. (2001) Contribution to the Study of Seismicity in the West Margin of Iberia. Univ. Lisboa, IGIDL Pub 25, ISSN 0870-2748

Matias, L., Ribeiro, A., Baptista, M.A., Zitellini, N., Cabral, J., Terrinha, P., Teves-Costa, P., Miranda, J.M. (2005) Comment on "Lisbon 1755: a case of triggered onshore rupture?" by Susana P. Vilanova, Catarina F. Nunes, and Joao FBD Fonseca. Bull. Seismol. Soc. Am. 95(6), 2534-2538

Matias, L.M., Cunha, T., Annunziato, A., Baptista, M.A., Carrilho, F. (2013) Tsunamigenic earthquakes in the Gulf of Cadiz: fault model and recurrence. Nat. Hazards Earth Syst. Sci. 13(1), 1-13

Matias, L., Carrilho, F., Sá, V., Omira, R., Niehus, M., Corela, C., Barros, J., Omar, Y. (2021) The contribution of submarine optical fiber telecom cables to the monitoring of earthquakes and tsunamis in the NE Atlantic. Front. Earth Sci. 9:686296 doi:10.3389/feart.2021.686296

Matos, C., Custódio, S., Batlló, J., Zahradník, J., Arroucau, P., Silveira, G., Heimann, S. (2018). An Active Seismic Zone in Intraplate West Iberia Inferred From High-Resolution Geophysical Data. J. Geophys. Res.: Solid Earth 123(4), 2885-2907, https://doi.org/10.1002/2017JB015114

McGovern, D.J., Robinson, T., Chandler, I.D., Allsop, W., Rossetto, T. (2018) Pneumatic long-wave generation of tsunami-length waveforms and their runup. Coast. Eng. 138:80–97. https://doi.org/10.1016/j.coastaleng.2018.04.006

Melgar, D., Bock, Y. (2015) Kinematic earthquake source inversion and tsunami runup prediction with regional geophysical data. J. Geophys. Res.: Solid Earth 120(5), 3324-3349

Melgar, D., Williamson, A.L., Salazar-Monroy, E.F. (2019) Differences between heterogenous and homogenous slip in regional tsunami hazards modelling. Geophys. J. Int. 219(1):553–562, https://doi.org/10.1093/gji/ggz299

Mendes-Victor, L., Oliveira, C.S., Azevedo, J. Ribeiro, A. (Eds.). (2008) The 1755 Lisbon earthquake: revisited (Vol. 7). Springer Science and Business Media

Mendonça, J.M. (1758) Historia Universal dos Terramotos que tem havido no mundo de que ha noticia desde a sua criação até ao seculo presente. Biblioteca Nacional de Lisboa, Portugal, 272 pp., (in Portuguese)

Mendoza, C., Hartzell, S. (1999) Fault-slip distribution of the 1995 Colima-Jalisco, Mexico, earthquake. Bull. Seismol. Soc. Am. 89(5):1338–1344

Mezcua, J. (1982) Catálogo general de isosistas de la peninsula Iberica. Instituto Geográfico Nacional. Publicacion 202. Available at: http://www.ign.es/web/resources/sismologia/publicaciones//CatalogoGeneralIsosistas.pdf (last access: September 15, 2021)

Mezcua, J., Martínez Solares, J.M. (1983). Seismicity of the Ibero–Maghrebian area. Instituto Geográfico Nacional Report, Madrid

Miranda, R.D. (1935). A terra: revista de sismologia e geofísica.Volume 21-1935

Miranda, J.M., Luis, J.F., Reis, C., Omira, R., Baptista, M.A. (2014) Validation of NSWING, a multi-core finite difference code for tsunami propagation and run-up. Paper Number S21A-4390, Natural hazards, American geophysical union (AGU) fall meeting, San Francisco

Miranda, J.M., Luis, J. (2019) NSWING (Non-linear Shallow Water model With Nested Grids). Instituto Dom Luiz, available at: https://github.com/joa-quim/NSWING (last access: March 31, 2021)

Mitchell, J. (1760) Conjectures concerning the cause, and observations upon the phenomena, of earthquakes. Philos. Trans. R. Soc. Lond. 2, 566-574.

Molloy, M. (1761) XXVII. Another account of the same earthquake: In a letter from Mr. Molloy, dated there 3 April 1761, to Keane Fitzgerald, Esq; F. R. S, Philos. T. Roy. Soc., 52, 142–143, https://doi.org/10.1098/rstl.1761.0028

Moniz, C., Cabral, J. (2014) The Pinhal Novo-Alcochete fault zone in the seismotectonic framework of the Lower Tagus Valley (Lisbon Region). In: Álvarez Gómez JA, Martín González F., Una aproximación multidisciplinar al estudio de las fallas activas, los terremotos y el riesgo sísmico. Volumen de resúmenes. Segunda reunión Ibérica sobre fallas activas y paleosismología, 3-6

Moreira, V.J. De S. (1984) Sismicidade Histórica de Portugal Continental. Revista do Instituto nacional de Meteorologia e Geofísica

Moreira, V.J. De S. (1991) Sismicidade Histórica de Portugal Continental. Revista do Instituto nacional de Meteorologia e Geofísica

Musson, R.M., Grünthal, G., Stucchi, M. (2010) The comparison of macroseismic intensity scales. J. Seismol. 14(2), 413-428

National Geophysical Data Center / World Data Service (NGDC/WDS) (2019) Global historical tsunami database. National Geophysical Data Center NOAA. doi.org/10.7289/V5PN93H7. Accessed 21 November 2019

National Research Council (2011) Tsunami Warning and Preparedness: An Assessment of the U.S. Tsunami Program and the Nation's Preparedness Efforts. Washington, DC: The National Academies Press. doi: 10.17226/12628

Navarro-Neumann, M.S. (1917) Ensayo sobre la sismicidad del suelo español. Bol. R. Soc. Esp. Hist. Natural pp. 83-109

Navarro-Neumann, M.S. (1921) Lista de los terremotos mas notables sentidos en la península Ibérica desde los tiempos mas remotos, hasta 1917, inclusive, con ensayo de agrupación en regiones y períodos sísmicos. La Estación Sismológica y el Observatorio Astronómico y Meteorológico de Cartuja (Granada). Memorias y trabajos de vulgarización científica. pp. 11-65

Nocquet, J.M., Calais, E. (2004) Geodetic measurements of crustal deformation in the Western Mediterranean and Europe. Pure Appl. Geophys., 161, 661–681

Okada, Y. (1985) Surface deformation due to shear and tensile faults in a half-space. Bull. Seismol. Soc. Am. 75(4):1135–1154

Okal, E.A., Synolakis, C.E. (2004) Source discriminants for near-field tsunamis. Geophys. J. Int. 158(3):899–912, https ://doi.org/10.1111/j.1365-246X.2004.02347.x

Okuwaki, R., Yagi, Y, Aránguiz, R., González, J., González, G. (2017) Rupture process during the 2015 Illapel, Chile earthquake: Zigzag-along-dip rupture episodes. In: Braitenberg C, Rabinovich A (eds) The Chile-2015 (Illapel) earthquake and tsunami. Pageoph Topical Volumes, Birkhäuser, pp 23–32, https :// doi.org/10.1007/978-3-319-57822 -4_3

Oliveira, C.S. (1986) A sismicidade Histórica em Portugal Continental e a Revisão do Catálogo sísmico Nacional. Laboratório Nacional de Engenharia Civil, Proc. 36/1177638, 235, Lisboa, Portugal, (in Portuguese)

Omira, R. (2010) Modeling Tsunamis Impact in northwestern Morocco and southwestern Iberia. PhD–Dissertation, Ibn Tofail University, Morocco

Omira, R., Baptista, M.A., Matias, L. (2015) Probabilistic tsunami hazard in the Northeast Atlantic from near-and far-field tectonic sources. Pure Appl. Geophys. 172(3-4), 901-920, https://doi.org/10.1007/s00024-014-0949-x

Omira, R., Baptista, M.A., Lisboa, F. (2016) Tsunami characteristics along the Peru–Chile trench: Analysis of the 2015 Mw8. 3 Illapel, the 2014 Mw8. 2 Iquique and the 2010 Mw8. 8 Maule tsunamis in the near-field. Pure Appl. Geophys. 173(4), 1063-1077, https://doi.org/10.1007/s00024-016-1277-0

Omira, R., Dogan, G.G., Hidayat, R., Husrin S., Prasetya G., Annunziato A., Proietti C., Probst P., Paparo M.A., Wronna M., Zaytsev A., Pronin P., Giniyatullin A., Putra P.S., Hartanto D., Ginanjar G., Kongko W., Pelinovsky E., Yalciner A.C. (2019) The September 28th, 2018, Tsunami In Palu-Sulawesi, Indonesia: A Post-Event Field Survey. Pure Appl. Geophys. 176, 1379–1395 (2019), https://doi.org/10.1007/s00024-019-02145-z

Omira, R., Ramalho, I. (2020) Evidence-Calibrated Numerical Model of December 22, 2018, Anak Krakatau Flank Collapse and Tsunami. Pure Appl. Geophys. 177(7), 3059-3071

Palano, M., González, P.J., Fernández, J. (2015) The Diffuse Plate boundary of Nubia and Iberia in the Western Mediterranean: Crustal deformation evidence for viscous coupling and fragmented lithosphere. Earth Planet. Sci. Lett. 430, 439-447, https://doi.org/10.1016/j.epsl.2015.08.040

Papadopoulos, G., Agalos, A., Charalampakis, M., Kontoes, C., Papoutsis, I., Atzori, S., Svigkas, N., Triantafyllou, I. (2019) Fault models for the Bodrum–Kos tsunamigenic earthquake (Mw6. 6) of 20 July 2017 in the east Aegean Sea. J. Geodyn. 131, 101646

Paris, A., Okal, E.A., Guérin, C., Heinrich, P., Schindelé, F., Hébert, H. (2019) Numerical modeling of the June 17, 2017 landslide and tsunami events in Karrat Fjord, West Greenland. Pure Appl. Geophys. 176(7), 3035-3057

Pedersen, G., Gjevik, B. (1983) Run-up of solitary waves. J. Fluid Mech. 135, 283-299

Pelinovsky, E.N., Mazova, R.K. (1992) Exact analytical solutions of nonlinear problems of tsunami wave run-up on slopes with different profiles. Nat. Hazards, 6(3), 227-249, https://doi.org/10.1007/BF00129510

Pelinovsky, E.N., Yuliadi, D., Prasetya, G., Hidayat, R. (1997) The 1996 Sulawesi tsunami. Nat. Hazards, 16(1), 29-38

Pereira de Sousa, F.L. (1916) O megasismo do 1.o de novembro de 1755 em Portugal. Acompanhado dum estudo demografico e sobre rochas de construçao. Distritos de Beja e Evora. Extracto Rev. Ob. Pub. e Minas, vol. II, p. 216, (in Portuguese)

Pereira de Sousa, F.L. (1919) O terremoto do 1 de Novembro de 1755 em Portugal e um estudo demográfico. Serviços Geológicos, 4 vols., 1–4, 72–73, 403–510, 806–831, (in Portuguese)

Pereira de Sousa, F.L. (1928) O terremoto do 1.o de novembro de 1755 em Portugal e um estudo demografico. Distrito de Lisboa. Servicios Geologicos, vol. III, pp. 479-949, (in Portuguese)

Perrey, A. (1847) Sur les tremblements de terre de la Péninsule Ibérique, Annales des sciences physiques et naturelles, d'agriculture et d'industrie, X. Société Royale d'agriculture, d'histoire naturelle et des arts utiles, Lyon, 463–514, (in French)

Perrey A. (1860) Note sur les tremblements de terre en 1858, avec Suppléments. Mémoires couronnés et autres mémoires puliés par l'Académie Royale des Sciences, Lettres et Beaux-Arts de Belgique, t. 12. Available at: http://eost.u-strasbg.fr/jv/geoarchive/Perrey/Perrey1862_1858B.pdf (last access: September 15, 2021) (in French)

Piatanesi, A., Tinti, S., Gavagni, I. (1996) The slip distribution of the 1992 Nicaragua earthquake from tsunami run-up data. Geophys. Res. Lett. 23(1):37–40

Prado, de C. (1863) Los terremotos de la provincia de Almeria. Revista Minera. Available at: http://www.ign.es/web/resources/sismologia/publicaciones//CasianoPradoAlmeria.pdf (last access: September 15, 2021)

Prasetya, G., De Lange, W., Healy, T. (2001) The Makassar Strait tsunamigenic region, Indonesia. Nat. Hazards 24, 295–307, doi:10.1023/A:1012297413280

Priest, G.R., Witter, R.C., Zhang, Y.J., Goldfinger, C., Wang, K., Allan, J.C. (2017) New constraints on coseismic slip during southern Cascadia subduction zone earthquakes over the past 4600 years implied by tsunami deposits and marine turbidites. Nat. Hazards 88(1), 285-313

Qu, K., Tang, H.S., Agrawal, A. (2019) Integration of fully 3D fluid dynamics and geophysical fluid dynamics models for multiphysics coastal ocean flows: Simulation of local complex free-surface phenomena. Ocean Model. 135, 14-30

Quintas, M.C. (ed.) (1993) Monografia de São Julião. Setúbal Junta de Freguesia de S. Julião

Rabinovich, A.B., Miranda, P., Baptista, M.A. (1998) Analysis of the 1969 and 1975 Tsunamis at the Atlantic Coast of Portugal and Spain. Oceanology 38(4), 463-469

Ramírez-Herrera, M.T., Corona, N., Ruiz-Angulo, A., Melgar, D., Zavala-Hidalgo, J. (2018) The 8 September 2017 tsunami triggered by the M w 8.2 intraplate earthquake, Chiapas, Mexico. Pure Appl. Geophys. 175(1), 25-34

Rangel-Buitrago, N., Neal, W.J., Bonetti, J., Anfuso, G., de Jonge, V.N. (2020) Vulnerability assessments as a tool for the coastal and marine hazards management: An overview. Ocean Coast. Manag. 189, p. 105134

Ratnasari, R.N., Tanioka, Y., Gusman, A.R. (2020) Determination of Source Models Appropriate for Tsunami Forecasting: Application to Tsunami Earthquakes in Central Sumatra, Indonesia. Pure Appl. Geophys. 177(6), 2551-2562

Reis, C., Omira, R., Matias, L., Baptista, M.A. (2017) On the source of the 8 May 1939 Azores earthquake–tsunami observations and numerical modelling. Geomat. Nat. Hazards Risk 8(2), 328-347

Rey Pastor, A. (1927) Traits sismiques de la Peninsule Iberique. Instituto Geográfico y Catastral, 72 pp. y 16 fot.

Ribeiro, A., Kullberg, M.C., Kullberg, J.C., Manuppella, G., Phipps, S. (1990) A review of Alpine tectonics in Portugal: foreland detachment in basement and cover rocks. Tectonophysics 184(3-4), 357-366

Ribeiro, A., Cabral, J., Baptista, R., Matias, L. (1996) Stress pattern in Portugal mainland and the adjacente Atlantic region, West Iberia. Tectonics 15: 641–659, https://doi.org/10.1029/95TC03683

Ribeiro, A., Terrinha, P., Zitellini, N., Víctor, L.M., Dañobeitia, J., Carrilho, F., Matias, L., Pinheiro, L., BIGSETS TEAM (2000) Estrutura e sismotectónica da Margem Sudoeste Portuguesa. 3° Simpósio sobre a Margem Ibérica Atlântica, Faro

Ribeiro, A., Mendes-Victor, L., Cabral, J., Matias, L., Terrinha, P. (2006) The 1755 Lisbon earthquake and the beginning of closure of the Atlantic. European Review 14(2), 193-205, doi:10.1017/S1062798706000196

Ribeiro, A., Mendes-Victor, L.A., Matias, L., Terrinha, P., Cabral, J., Zitellini, N. (2009). The 1755 Lisbon earthquake: a review and the proposal for a tsunami early warning system in the Gulf of Cadiz. In The 1755 Lisbon Earthquake: Revisited (pp. 411-423). Springer, Dordrecht

Rocque, J. (1762) A Plan of the City of Cadiz and the environs with the Harbour, Bay and Soundings at Low Water also a Particular Plan of the Town and Fortifications from the Collection of Capt. Clark and Improved by the late John Rocque, Topographer to his Majesty, Bibliothèque nationale de France, département Cartes et plans, CPL GE DD-2987

Roda, A. (2010). Paços do Concelho/ Câmara Municipal de Setúbal. Available at: https://mfm-a-roda.blogspot.com/2010/01/pacos-do-concelho-camara-municipal-de.html. (last access: October 8, 2021)

Rodríguez de la Torre, F. (1990) Sismología y sismicidad en la península Ibérica durante el siglo XIX. Tesis Doctoral. Fac. de Geografía e Historia, Universidad de Barcelona, cinco tomos

Rodríguez de la Torre, F. (1997) Revisión del Catálogo Sísmico Ibérico (años 1760 a 1800) Estudio realizado para el Instituto Geográfico Nacional, mediante convenio de investigación número 7.070, de 1997, Madrid

Rosas, F.M., Duarte, J.C., Terrinha, P., Valadares, V., Matias, L. (2009) Morphotectonic characterization of major bathymetric lineaments in Gulf of Cadiz (Africa–Iberia plate boundary): insights from analogue modelling experiments. Mar. Geol. 261(1-4), 33-47

Rothé, J.P. (1951) The structure of the bed of the Atlantic Ocean. Eos Trans. Am. Geophys. Un. 32, 457–461, doi:10.1029/TR032i003p00457

Rudloff, A., Lauterjung, J., Münch, U., Tinti, S. (2009) The GITEWS Project (German-Indonesian tsunami early warning system). Nat. Hazards Earth Syst. Sci. 9:1381–1382, https://doi.org/10.5194/nhess-9-1381-2009

Rybkin, A., Pelinovsky, E.N., Didenkulova, I. (2014) Nonlinear wave run-up in bays of arbitrary cross-section: Generalization of the Carrier-Greenspan approach. J. Fluid Mech. 748, 416–432. doi:10.1017/jfm.2014.197

Sallarès, V., Martínez-Loriente, S., Prada, M., Gràcia, E., Ranero, C.R., Gutscher, M.A., Bartolome, R., Gailler, A., Dañobeitia, J.J., Zitellini, N. (2013) Seismic evidence of exhumed mantle rock basement at the Gorringe Bank and the adjacent Horseshoe and Tagus abyssal plains (SW Iberia). Earth Planet. Sc. Lett., 365, 120–131, https://doi.org/10.1016/j.epsl.2013.01.021

Sangadji, R. (2019) Central Sulawesi disasters killed 4340 people, final count reveals. Jakarta Post

Santos, A., Koshimura, S. (2015) The historical review of the 1755 Lisbon Tsunami. J. geod. geomat. eng. 1, 38-52

Sarri, A., Guillas, S., Dias, F. (2012) Statistical emulation of a tsunami model for sensitivity analysis and uncertainty quantification. arXiv preprint arXiv:1203.6297

Sartori, R., Torelli, L., Zitellini, N., Peis, D., Lodolo, E., (1994) Eastern segment of the Azores–Gibraltar line (central-eastern Atlantic): an oceanic plate boundary with diffuse compressional deformation. Geology 22, 555–558

Satake, K., Bourgeois, J., Abe, K., Abe, K., Tsuji, Y., Imamura, F., Iio, Y., Katao, H., Noguera, E., Estrada, F. (1993) Tsunami field survey of the 1992 Nicaragua earthquake. EOS Trans Am Geophys Union 74(13), 145-157

Satake, K. (1994) Mechanism of the 1992 Nicaragua tsunami earthquake. Geophys. Res. Lett. 21(23), 2519-2522

Sbarra, P., Burrato, P., Tosi, P., Vannoli, P., De Rubeis, V., Valensise, G. (2019) Inferring the depth of pre-instrumental earthquakes from macroseismic intensity data: a case-history from Northern Italy. Sci. Rep. 9(1), 1-13

Schambach, L., Grilli, S.T., Tappin, D.R. (2021) New high-resolution modeling of the 2018 Palu tsunami, based on supershear earthquake mechanisms and mapped coastal landslides, supports a dual source. Front. Earth Sci., 8, 627

Sepúlveda, I., Liu, P.L.-F (2016) Estimating tsunami runup with fault plane parameters. Coast Eng 112:57–68, https://doi.org/10.1016/j.coastaleng.2016.03.001

Sepúlveda, I., Haase, J.S., Carvajal, M., Xu, X., Liu, P.L. (2020) Modeling the Sources of the 2018 Palu, Indonesia, Tsunami Using Videos From Social Media. J. Geophys. Res. Solid Earth 125(3), e2019JB018675

Sibol M.S., Bollinger G.A., Birch J.B. (1987) Estimations of magnitudes in central and eastern North America using Intensity and Felt Area. Bull Seismol Soc Am 77:1635–1654

Silva, N., Catarino, N., Ávila, N., Baptista, M.A., Wronna, M. (2021), A Tsunami Space-Based Early Warning System. Tsunami detection from Space – a nearly real-time system to detect ocean surface altimetric anomalies with satellites. Blog EN, Earth Observation,

Satellite Navigation, SpaceBy pyddeimos20 de April de 2021, available at: https://elecnor-deimos.com/tsunami-prevention-gnss-r/ (last access: September 15, 2021)

Silva, S., Terrinha, P., Matias, L., Duarte, J.C., Roque, C., Ranero, C.R., Geissler, W.H., Zitellini, N. (2017) Micro-seismicity in the Gulf of Cadiz: Is there a link between micro-seismicity, high magnitude earthquakes and active faults?. Tectonophysics, 717, 226-241

Socquet, A., Simons, W., Vigny, C., McCaffrey, R., Subarya, C., Sarsito, D., Ambrosius, B., Spakman, W., (2006) Microblock rotations and fault coupling in SE Asia triple junction (Sulawesi, Indonesia) from GPS and earthquake slip vector data. J. Geophys. Res. 111, B08409, doi:10.1029/2005JB003963

Socquet, A., Hollingsworth, J., Pathier, E., Bouchon, M. (2019) Evidence of supershear during the 2018 magnitude 7.5 Palu earthquake from space geodesy. Nat. Geosci. 12(3), 192-199.

Sogut, D.V., Yalciner, A.C. (2019) Performance Comparison of NAMI DANCE and FLOW-3D® Models in Tsunami Propagation, Inundation and Currents using NTHMP Benchmark Problems. Pure Appl. Geophys. 176(7), 3115-3153

Soloviev, S.L., Go, Ch.N. (1974) A catalogue of tsunamis on the western shore of the Pacific Ocean. Moscow, "Nauka" Publishing House, 308p, English translation: Soloviev S.L., Go Ch.N. (1984), A catalogue of tsunamis on the western shore of the Pacific ocean, Translation by Canada Institute for Scientific and Technical Information, National Research Council, Ottawa, Canada KIA OS2

Sørensen, M., Spada, M., Babeyko, A., Wiemer, S., Grunthal, G. (2012) Probabilistic tsunami hazard in the Mediterranean Sea. J. Geophys. Res. Solid Earth 117(B1), https://doi.org/10.1029/2010JB008169

Sousa, M.F. (1678) Europa portuguesa segunda edicion correta, ilustrada y añadida en tantos lugares y con tales ventajas que es labor nueva por su autor Manuel de Faria y Sousa, tomo I [–III], printed by: Craesbeeck de Mello, d'Antonio, 1678–1680, Biblioteca Nacional de Lisboa, Portugal, Tomo I 491 pp., Tomo II 224pp., Tomo III 594 pp., (in Portuguese)

Spencer, J.E. (2011) Gently dipping normal faults identified with Space Shuttle radar topography data in central Sulawesi, Indonesia, and some implications for fault mechanics. Earth Planet. Sci. Lett. 308(3-4), 267-276

Stich, D., Batlló, J., Macià, R., Teves-Costa, P., Morales, J. (2005) Moment tensor inversion with single-component historical seismograms: The 1909 Benavente (Portugal) and Lambesc (France) earthquakes. Geophys. J. Int. 162(3), 850-858

Stich, D., Mancilla, F., Pondrelli, S., Morales, J. (2007) Source analysis of the February 12th 2007, Mw 6.0 Horseshoe earthquake: Implications for the 1755 Lisbon earthquake. Geophys. Res. Lett. 34, L12308, doi:10.1029/2007GL030012

Stich, D., Martínez Solares, J.M., Custódio, S., Batlló, J., Martín, R., Teves-Costa, P., Morales, J. (2020) Seismicity of the iberian Peninsula. In The geology of Iberia: A geodynamic approach (pp. 11-32), Springer, Cham

Stucchi, M., Rovida, A., Capera, A.G., Alexandre, P., Camelbeeck, T., Demircioglu, M.B., Gasperini, P., Kouskouna, V., Musson, R.M.W., Radulian, M., Sesetyan, K., Vilanova, S., Baumont, D., Bungum, H., Fäh, D., Lenhardt, W., Makropoulos, K., Martínez Solares, J.M., Scotti, O., Živčić, M., Albini, P., Batlló, J., Papaioannou, C., Tatevossian, R., Locati, M., Meletti, C., Viganò, D., Giardini, D. (2013). The SHARE European earthquake catalogue (SHEEC) 1000–1899. J. Seismol. 17(2), 523-544, https://doi.org/10.1007/s10950-012-9335-2

Synolakis, C.E. (1987) The runup of solitary waves. J. Fluid Mech. 185, 523-545. https://doi.org/10.1017/S002211208700329X

Synolakis, C.E. (2003) Tsunami and Seiche. In Earthquake Engineering Handbook, edited by Chen, W.-F. and Scawthorn, C., CRC Press, 9–1-9–90

Synolakis, C.E., Bernard, E.N. (2006) Tsunami science before and beyond Boxing Day 2004. Phil. Trans. R. Soc. A.3642231–2265, http://doi.org/10.1098/rsta.2006.1824

Synolakis, C.E., Bernard, E.N., Titov, V.V., Kânoğlu, U., González, F.I. (2007) Standards, criteria, and procedures for NOAA evaluation of tsunami numerical models. NOAA Tech Memo OAR PMEL-135, NTIS: PB2007-109601, NOAA/Pacific Marine Environmental Laboratory, Seattle, WA, pp 55

Synolakis, C.E., Bernard, E.N., Titov, V.V., Kânoğlu, U., González, F.I. (2008) Validation and verification of tsunami numerical models. Pure Appl. Geophys. 165(11–12), 2197–2228. https://doi.org/10.1007/s00024-004-0427-y

Tadepalli, S., Synolakis, C.E. (1994) The run-up of N-waves on sloping beaches. Proc. R. Soc. Lond. A Math. Phys. Sci., 445(1923), 99-112, https://doi.org/10.1098/rspa.1994.005

Tadepalli, S., Synolakis, C.E. (1996) Model for the leading waves of tsunamis. Phys. Rev. Lett. 77(10), 2141– 2144, https://doi.org/10.1103/PhysRevLett.77.2141

Tang, L., Titov, V.V., Chamberlin, C.D. (2009) Development, testing, and applications of site-specific tsunami inundation models for real-time forecasting. J Geophys Res Oceans. https://doi.org/10.1029/2009JC005476

Tanioka, Y., Miranda, G.J.A., Gusman, A.R., Fujii, Y. (2017) Method to determine appropriate source models of large earthquakes including tsunami earthquakes for tsunami early warning in Central America. Pure Appl. Geophys. 174, 3237–3248, https://doi.org/10.1007/s00024-017-1630-y

Terrinha, P., Pinheiro, L.M., Henriet, J.P., Matias, L., Ivanov, M.K., Monteiro, J.H., Akhmetzhanov, A., Volkonskaya, A., Cunha, T., Shaskin, P., Rovere, M. (2003) Tsunamigenic-seismogenic structures, neotectonics, sedimentary processes and slope instability on the southwest Portuguese Margin. Marine Geology, 195(1-4), 55-73, https://doi.org/10.1016/S0025-3227(02)00682-5

Terrinha, P., Matias, L., Vicente, J., Duarte, J., Luís, J., Pinheiro, L., Lourenço, N., Diez, S. Rosas, F., Magalhães, V., Valadares, V., Zitellini, N., Roque, C., Mendes Víctor, L., and MATESPRO Team (2009) Morphotectonics and strain partitioning at the Iberia–Africa

plate boundary from multibeam and seismic reflection data. Mar. Geol., 267, 156–174, https://doi.org/10.1016/j.margeo.2009.09.012

Teves-Costa, P., Batlló, J. (2011) The 23 April 1909 Benavente earthquake (Portugal): macro-seismic field revision. J Seismol 15, 59–70 https://doi.org/10.1007/s10950-010-9207-6

Thandlam, V., Rutgersson, A., Rahaman, H. (2019) Are we in the right path in using early warning systems?. J. extreme events, 6(02), 1950003

Thiebot, E., Gutscher, M.A. (2006) The Gibraltar Arc seismogenic zone (part 1): constraints on a shallow east dipping fault plane source for the 1755 Lisbon earthquake provided by seismic data, gravity and thermal modeling. Tectonophysics, 426(1-2), 135-152

Tinti, S., Tonini, R. (2005) Analytical evolution of tsunamis induced by near-shore earthquakes on a constant-slope ocean. J. Fluid Mech. 535, 33–64. doi:10.1017/ S0022112005004532

Tinti, S., Tonini, R., Bressan, L., Armigliato, A., Gardi, A., Guillande, R., Valencia, N., Scheer, S. (2011) Handbook of tsunami hazard and damage scenarios. SCHEMA (Scenarios for Hazard-induced Emergencies Management). Project n°030963, specific targeted research project, space priority, JRC Scientific and Technical Reports, 1-41

Tinti, S., Tonini, R. (2013) The UBO-TSUFD tsunami inundation model: validation and application to a tsunami case study focused on the city of Catania. Italy. Nat. Hazards Earth Syst. Sci. 13(7):1795–1816. https://doi.org/10.5194/nhess-13-1795-2013

Titov, V.V., Synolakis, C.E. (1995) Modeling of breaking and nonbreaking long-wave evolution and runup using VTCS-2. J. Waterway Port Ocean Coast. Eng. 121(6):308–316, https://doi.org/10.1061/(ASCE)0733-950X(1995)121:6(308)

Titov, V.V., González, F.I. (1997) Implementation and testing of the method of splitting tsunami (MOST) model

Titov, V.V., Synolakis, C.E. (1998) Numerical modeling of tidal wave runup. J. Waterway Port Ocean Coast. Eng. 124: 157–171

Titov, V.V., Kânoğlu, U., Synolakis, C.E. (2016) Development of MOST for real-time tsunami forecasting. J. Waterway Port Ocean Coast. Eng. 142(6):03116004, https ://doi.org/10.1061/(ASCE)WW.1943-5460.00003 57

Tonini, R., Armigliato, A., Pagnoni, G., Zaniboni, F., Tinti, S. (2011) Tsunami hazard for the city of Catania, eastern Sicily, Italy, assessed by means of Worst-case Credible Tsunami Scenario Analysis (WCTSA). Nat. Hazards Earth Syst. Sci. 11(5), 1217-1232

Torelli, L., Sartori, R., Zitellini, N. (1997) The giant chaotic body in the Atlantic Ocean off Gibraltar: new results from a deep seismic reflection survey. Mar. Petrol. Geol. 14, 125–134, https://doi.org/10.1016/S0264-8172(96)00060-8

Udías, A. (2019) Large Earthquakes and Tsunamis at Saint Vincent Cape before the Lisbon 1755 Earthquake: A Historical Review. Pure Appl. Geophys. 177, 1739–1745 (2020), https://doi.org/10.1007/s00024-019-02323-z

UG-ICN (2019) Tsunami inundation maps along the south west Spanish coast, deliverable d7.1 of the 6th European framework programme project TRANSFER, available at: https://cordis.europa. eu/project/rcn/81399/factsheet/en (last access: August 1, 2018)

Ulrich, T., Vater, S., Madden, E.H., Behrens, J., van Dinther, Y., Van Zelst, I., Fielding, E.J., Liang, C., Gabriel, A.-A. (2019) Coupled, physics-based modeling reveals earthquake displacements are critical to the 2018 Palu, Sulawesi tsunami. Pure Appl. Geophys. 176, 4069–4109, doi:10.1007/s00024-019-02290-5

UNESCO (2014) International Tsunami Survey Team (ITST) Post-Tsunami Survey Field Guide, 2nd Edition, IOC Manuals and Guides No.37. Paris: UNESCO 2014 (English)

UNESCO (2020). Serious tsunami hits Greece and Turkey after 7.0 earthquake. Available at: https://ioc.unesco.org/news/serious-tsunami-hits-greece-and-turkey-after-70-earthquake, (last access: April 30, 2021)

Unknown (1761) An Account of the Earthquake at Lisbon, 31 March 1761: In a Letter from thence, dated 2 April 1761, to Joseph Salvador, Esq, F.R.S. Philos. Trans. Letter XXVI, 141–142

USGS (2018) M 7.5 - 70 km N of Palu, Indonesia. Available at: https://earth-quake.usgs.gov/earthquakes/eventpage/us1000h3p4/executive (last access: April 30, 2021)

USNO (United States Naval Observatory) (2017). Available at: http://aa.usno.navy.mil/data/docs/MoonPhase.php, (last access: February 1, 2018)

Valkaniotis, S., Ganas, A., Tsironi V., Barberopoulou, A. (2018) A preliminary report on the M7.5 Palu 2018 earthquake co-seismic ruptures and landslides using image correlation techniques on optical satellite data. Zenodo, https://doi.org/10.5281/zenodo.1467128

Vallis, G.K. (2017) Atmospheric and oceanic fluid dynamics. Cambridge University Press

Vilanova, S.P., Nunes, C.F., Fonseca, J.F.B.D (2003) Lisbon 1755: a case of triggered onshore rupture?. Bull. Seismol. Soc. Am. 93(5), 2056-2068

Vilanova, S.P., Fonseca, J.F.B.D (2004) Seismic hazard impact of the Lower Tagus Valley fault zone (SW Iberia). J. Seismol. 8(3), 331-345

Vilanova, S.P., Fonseca, J.F.B.D. (2007) Probabilistic seismic-hazard assessment for Portugal. Bull. Seismol. Soc. Am. 97(5), 1702-1717

Vincendon-Dumoulin, M.C.A. (1876) Setubal [Material cartográfico] levantado en 1852 por M.C.A. Vincendon-Dumoulin, ingeniero hidrógrafo de la marina francesa ; J. Galván lo grabó ; J. de Gangoiti go. la letra, Escala [ca. 1:27.500], (W 8°59'28"-W 8°46'35"/N 38°32'23"-N 38°25'23") Dirección de Hidrografía, Madrid, available at: https://www.ign.es/web/catalogo-cartoteca/resources/html/000172.html, (last access: March 5, 2021)

Vizcaino, A., Gràcia, E., Pallàs, R., Garcia-Orellana, J., Escutia, C., Casas, D., Willmott, V., Diez, S., Asioli, A., Dañobeitia, J.J. (2006) Sedimentology, physical properties and age

of mass transport deposits associated with the Marques de Pombal Fault, Southwest Portuguese Margin. Nor. J. Geol. 86, 177-186, Trondheim, ISSN 029-196X

Vogt, J., Levret, A. (1985) Révision d'anciens séismes ibéro-maghrébins, rapport: Études de sites de faisabilité d'une première centrale électronucléaire au Maroc. Maroc: Sofratome and Off. Nat. Elec

Walpersdorf, A., Rangin, C., Vigny, C. (1998) GPS compared to long-term geologic motion of the north arm of Sulawesi. Earth Planet. Sci. Lett. 159(1-2), 47-55

Wang, X. (2009) COMCOT user manual-version 1.7. School of Civil and Environmental Engineering, Cornell University Ithaca, NY 14853, USA

Walter, T.R., Haghighi, M.H., Schneider, F.M., Coppola, D., Motagh, M., Saul, J., Babeyko, A., Dahm, T., Troll, V.R., Tilmann, F., Heimann, S., Valade, S., Triyono, R., Khomarudin, R., Kartadinata, N., Laiolo, M., Massimetti, F., Gaebler, P. (2019) Complex hazard cascade culminating in the Anak Krakatau sector collapse. Nat. Commun. 10(1), 1-11

Wei, S., Graves, R., Helmberger, D., Avouac, J.P., Jiang, J. (2012) Sources of shaking and flooding during the Tohoku-Oki earthquake: a mixture of rupture styles. Earth Planet Sci. Lett. 333:91–100, https ://doi. org/10.1016/j.epsl.2012.04.006

Wei, S. (2014) Apr./0.1/2014 (Mw 8.1), Iquique, Chile, Source models of large earthquakes. Available at: https://www.tectonics.caltech.edu/slip_history/2014_chile/index.html, (last access: November 21, 2019)

Wells, D.L., Coppersmith, K.J. (1994) New empirical relationships among magnitude, rupture length, rupture width, rupture area, and surface displacement. Bull. Seismol. Soc. Am. 84(4), 974-1002

Williams, R., Rowley, P., Garthwaite, M.C. (2019) Reconstructing the Anak Krakatau flank collapse that caused the December 2018 Indonesian tsunami. Geology 47(10), 973-976

Wijetunge, J.J. (2014) A deterministic analysis of tsunami hazard and risk for the southwest coast of Sri Lanka. Cont Shelf Res. 79, 23-35

Wronna, M., Omira, R., Baptista, M.A. (2015) Deterministic approach for multiple-source tsunami hazard assessment for Sines, Portugal. Nat. Hazards Earth Syst. Sci. 15(11), 2557-2568

Wronna, M., Baptista, M.A., Götz, J. (2017) On the construction and use of a Paleo-DEM to reproduce tsunami inundation in a historical urban environment–the case of the 1755 Lisbon tsunami in Cascais. Geomatics, Nat. Hazards Risk. 8(2), 841-862

Wronna, M., Baptista, M.A., Miranda, J.M. (2019a) Reanalysis of the 1761 transatlantic tsunami. Nat. Hazards Earth Syst. Sci. 19, 337–352, https://doi.org/10.5194/nhess-19-337-2019

Wronna, M., Hidayat, R., Husrin, S., Prasetya, G., Annunziato, A., Dogan, G.G., Zaytsev, A., Omira, R., Proietti, C., Probst, P., Paparo, M.A., Pronin, P., Giniyatullin, A., Putra, P.S., Hartanto, D., Ginanjar, G., Kongko, W., Pelinovsky, E., Baptista, M.A., Yalciner, A.C.

(2019b) Insights in the UNESCO Post-Event Field Survey of the September 28th, 2018 Palu Tsunami. Geophysical Research Abstracts Vol. 21, EGU2019-11544-2, EGU General Assembly 2019

Wronna, M., Baptista, M.A., Kânoğlu, U. (2020) A new tsunami runup predictor. Nat. Hazards 105, 1571–1585, https://doi.org/10.1007/s11069-020-04366-1

Wronna, M., Baptista, M.A., Miranda, J.M. (2021) Reevaluation of the 11 November 1858 Earthquake and Tsunami in Setúbal: A Contribution to the Seismic and Tsunami Hazard Assessment in Southwest Iberia. Pure Appl. Geophys. https://doi.org/10.1007/s00024-021-02885-x

Yalciner, A.C., Pelinovsky, E., Zaitsev, A., Kurkin, A., Ozer, C., Karakus, H., Ozyurt, G. (2007) Modeling and visualization of tsunamis: Mediterranean examples. In Tsunami and Nonlinear Waves, (pp. 273-283), Springer, Berlin, Heidelberg

Yalciner, A.C., Hidayat, R., Husrin, S., Prasetya, G., Annunziato, A., Doğan, G.G., Zaytsev, A., Omira, R., Proietti, C., Probst, P., Paparo, M.A., Wronna, M., Pronin, P., Giniyatullin, A., Putra, P.S., Hartanto, D., Ginanjar, G., Kongko, W., Pelinovsky, E. (2018a) The 28th September 2018 Palu Earthquake and Tsunami ITST, 07 – 11 November Post Tsunami Field Survey Report, (Short). http://itic.ioc-unesco.org/images/stories/itst_tsunami_survey/itst_palu/ITST-Nov-7-11-Short-Survey-Report-due-on-November-23-2018.pdf

Yalciner, A.C., Hidayat, R., Husrin, S., Prasetya, G., Annunziato, A., Doğan, G.G., Zaytsev, A., Omira, R., Proietti, C., Probst, P., Paparo, M.A., Wronna, M., Pronin, P., Giniyatullin, A., Putra, P.S., Hartanto, D., Ginanjar, G., Kongko, W., Pelinovsky, E. (2018b) Field Survey on the Coastal Impacts of the September 28, 2018 Palu, Indonesia Tsunami. 2018 Fall AGU Abstract

Yue, H., Lay, T. (2013) Source rupture models for the Mw 9.0 2011 Tohoku earthquake from joint inversions of high-rate geodetic and seismic data. Bull. Seismol. Soc. Am. 103(2B):1242–1255, https://doi.org/10.1785/0120120119

Yue, H., Lay, T., Rivera, L., An, C., Vigny, C., Tong, X., Baez Soto, J.C. (2014) Localized fault slip to the trench in the 2010 Maule, Chile Mw= 8.8 earthquake from joint inversion of high-rate GPS, teleseismic body waves, InSAR, campaign GPS, and tsunami observations. J. Geophys. Res. Solid Earth 119(10), 7786-7804

Zhang, B. (2011) Top 5 most expensive natural disasters in history. AccuWeather.com, 30

Zitellini, N., Chierici, F., Sartori, R., Torelli, L. (1999) The tectonic source of the 1755 Lisbon earthquake and tsunami. Ann. Geophys. 42(1)

Zitellini, N., Mendes, L.A., Cordoba, D., Danobeitia, J., Nicolich, R., Pellis, G., Ribeiro, A., Sartori, R., Torelli, L., Bartolome, R., Bortoluzzi, G., Calafato, A., Carrilho, F., Casoni, L., Chierici, E., Corela, C., Correggiari, A., Delia Vedova, B., Gràcia, E., Jornet, P., Landuzzi, M., Ligi, M., Magagnoli, A., Marozzi, G., Matias, L., Penitenti, D., Rodriguez, P., Rovere, M., Terrinha, P., Vigliotti, L., Ruiz, A.Z. (2001) Source of 1755 Lisbon earthquake and tsunami investigated. EOS Trans Am Geophys Union, 82(26), 285-291

Zitellini, N., Rovere, M., Terrinha, P., Chierici, F., Matias, L., BIGSETS Team (2004) Neogene through Quaternary tectonic reactivation of SW Iberian passive margin. Pure Appl. Geophys. 161(3), 565-587

Zitellini, N., Gràcia, E., Matias, L., Terrinha, P., Abreu, M.A., DeAlteriis, G., Henriet, J.P., Dañobeitia, J.J., Masson, D.G., Mulder, T., Ramella, R., Somoza, L., Diez, S. (2009) The quest for the Africa–Eurasia plate boundary west of the Strait of Gibraltar. Earth Planet. Sc. Lett. 280, 13–50, https://doi.org/10.1016/j.epsl.2008.12.005

Appendix

1. Conference proceedings

List of conference proceedings in chronological order:

1.1. 2D+1D Runup estimations compared with field data of the three recent Chilean Events; the 2010 Maule, the 2014 Iquique and the 2015 Illapel tsunamis

Wronna, M., Kanoglu, U., Baptista, M. A. (2017). 2D+1D Runup Estimations compared with field data of the three recent Chilean Events; the 2010 Maule, the 2014 Iquique and the 2015 Illapel Tsunamis. In EGU General Assembly Conference Abstracts (Vol. 19, p. 8299).

In tsunami sciences, it is a desirable goal to forecast the inundation areas quickly after an event. A promising approach is to combine numerical modelling by applying nonlinear shallow water wave equations with one-dimensional (1-D) analytical solution. Here we use synthetic waveforms as input for 1-D analytical runup estimation and compare the results with the measured runup values of the 2010 Mw 8.8 Maule, the 2014 Mw 8.2 Iquique and the 2015 Mw 8.3 Illapel tsunamis. The three earthquakes occurred along the Peru-Chile Trench with the most damaging Maule event on February 27th, 2010 on the southern part between the Nazca and South American plate. After that event, maximum runup values reach 29 m at the city of Constitutiòn. We compute the waveforms of the events using their co-seismic deformations as the initial conditions in the nonlinear shallow water numerical model. We trace profiles orthogonal to the source at the points of runup measurements and extract the synthetic waveform and the slope of the bathymetry. We then use the synthetic waveforms and bathymetric profiles as input for the 1-D long wave runup theory. The comparison reveals that the 2D+1D runup estimations deliver reasonable results compared to measured runup. But in some cases over- and underestimation occurs. Especially underestimation is a critical issue for early warning purposes, and additional fine tuning of the methodology is needed. This study received funding from project ASTARTE-Assessment Strategy and Risk Reduction for Tsunamis in Europe a collaborative project Grant 603839, FP7-ENV2013 6.4-3.

1.2. Inundation and runup caused by two transatlantic tsunamis in the 18th century in Cadiz

Wronna, M., Kanoglu, U., Baptista, M. A. and Miranda J. M. (2017). Inundation and runup caused by two transatlantic tsunamis in the 18th century in Cadiz. International Tsunami Symposion, Bali-Flores, 21-25 August 2017, ID – 024.

The tsunami catalogs for the Northeast Atlantic include two tsunamigenic earthquakes in the 18th century. The first one is the 1st November 1755 Lisbon event and tsunami the less known 31st March 1761. Both earthquakes triggered transatlantic tsunamis. As both events are of pre-instrumental nature, the exact sources are unknown. Analysis of the historical data helped to discriminate the sources of these events better.

In this study, we use a nonlinear shallow water wave numerical model with nested grids to compute propagation and inundation, hence maximum runup for these two events. In the numerical model, we employ the Paleo-DEM for Cadiz (Spain) and use as the initial condition the wave triggered by the co-seismic displacement of the proposed sources for the 1755 and 1761 events. The results confirm historical reports of massive inundation in 1755 and overtopping of the causeway between Cadiz and the mainland. As for the 1761 tsunami our results confirm the smaller inundation occurring mainly at the beaches.

However, detailed inundation mapping applying nested grids is a time-consuming procedure. Cadiz is located close to a diffuse plate boundary between Nubia and Eurasia, with a variety of possible sources. Here, the time for warning and evacuation is uncomfortably short. Recently studies use 2D numerical + 1D analytical longwave runup theory to rapid forecasting of tsunami run up.

Therefore, we further investigated the use of the 2D + 1D maximum runup estimate, by extracting the 1-D waveforms from the 2D propagation results and couple them with an analytical solution deduced for solitary wave and N-waves at the nearshore. Our results show that in the case of the 1755 event the analytical maximum runup estimates are similar to those obtained with the full nonlinear shallow water wave numerical modelling results and with the historical data. However, in the case of the 1761 event, the results are not less satisfactory. The more complex asymmetric waveform may be a possible cause for the discrepancies.

1.3. Comparison of maximum runup through analytical and numerical approaches for different fault parameters estimates

Wronna, M., Kanoglu, U., Baptista, M. A. and Miranda J. M. (2017). Comparison of maximum runup through analytical and numerical approaches for different fault parameters estimates. In AGU Fall Meeting Abstracts.

The one-dimensional analytical runup theory in combination with near shore synthetic wave-forms is a promising tool for tsunami rapid early warning systems. Its application in realistic cases with complex bathymetry and initial wave condition from inverse modelling have shown that maximum runup values can be estimated reasonably well. In this study we generate a sim-plistic bathymetry domains which resemble realistic near-shore features. We investigate the accuracy of the analytical runup formulae to the variation of fault source parameters and near-shore bathymetric features. To do this we systematically vary the fault plane parameters to compute the initial tsunami wave condition. Subsequently, we use the initial conditions to run the numerical tsunami model using coupled system of four nested grids and compare the results to the analytical estimates. Variation of the dip angle of the fault plane showed that analytical estimates have less than 10% difference for angles 5-45 degrees in a simple bathymetric do-main. These results shows that the use of analytical formulae for fast run up estimates consti-tutes a very promising approach in a simple bathymetric domain and might be implemented in Hazard Mapping and Early Warning.

1.4. Field survey on the coastal impacts of the September 28, 2018 Palu, Indonesia tsunami

Yalciner A.C., Hidayat R., Husrin S., Prasetya G., Annunziato A., Doğan G.G., Zaytsev A., Omira R., Proietti C., Probst P., Paparo M.A., Wronna M., Pronin P., Giniyatullin A., Putra P.S., Hartanto D., Ginanjar G., Kongko W., Pelinovsky E. (2018b). Field Survey on the Coastal Impacts of the September 28, 2018 Palu, Indonesia Tsunami. 2018 Fall AGU Abstract.

The September 28, 2018 Palu Mw7.5 Earthquake in Sulawesi Island in Indonesia triggered an unexpected tsunami that caused damage and loss of lives in the region. A field survey by the UNESCO International Survey Team has been performed between November 07 and 11, 2018 covering the entire coast of Western Palu Bay up to Tanjung Karang cape and the Eastern Palu bay coast up to the earthquake epicenter region. The survey aimed at understanding and docu-ment the tsunami effects and also the tsunami generation mechanisms through measuring and

observing the tsunami effects. The survey also attempted to understand the uncertainties of the event from source-to-coast and, therefore, contribute to a better characterization of the tsunami and its impact, and provide information to enable enhancement of tsunami disaster risk management practices.

The survey methodology consists of several steps by following The UNESCO International Tsunami Survey Team (ITST) Post -Tsunami Survey Field Guide 2nd Edition, 2014 (http://itic.iocunesco.org/images/stories/itst_tsunami_survey/survey_documents/field_survey_guide/ITST_FieldSurveyGuide_229456E.pdf during the survey.

The team collected tsunami hydrodynamic data such as arrival time, direction of incoming wave, shape of the first wave, number of waves, runup height, flow depth, inundation height and the inundation limit from tsunami left traces and eyewitness interviews. The survey findings show that the generation mechanism of the tsunami is not only due to the co-seismic deformation but also coastal subsidence and/or subaerial/submarine landslides are possible secondary sources. The main impact of the tsunami is observed along the coasts of the Palu Bay located tens of kilometers away from the earthquake epicenter area (0.1781S 119.8401E, USGS). Several collapses of coastal sectors and/or landslides were observed in the western and eastern coasts especially in the river mouth areas that also present the tsunami highly-impacted locations. The tsunami impact is low after Tanjung Karang location of Donggala tip region on the western side of the bay. Small or no tsunami observations were reported at North after Towaja region on the eastern side of the bay. Most tsunami energy focus was observed inside narrow bays with very localized effects. The tsunami propagated along the rivers inland and on the low-lying zones with high damage on the coastal settlements. The results of measurements and observations on tsunami nearshore amplitude, flow characteristics, flow depth and damage findings are presented and discussed for the further studies on the event.

1.5. Numerical and analytical study on fault plane parameters influencing tsunami runup

Wronna, M., Kanoğlu, U., and Baptista, M. A. (2018). Numerical and analytical study on fault plane parameters influencing tsunami runup. In EGU General Assembly Conference Abstracts (p. 8746).

The application of the one-dimensional analytical runup theory could be a proficient tool for tsunami rapid early warning systems. Runup could be estimated reasonably well through

analytical studies once initial wave profile is identified. However, this raises the need for a better understanding of the impact of the fault plane parameters on the runup. To achieve this, we schematically change the dip, the depth and the width of the fault and compute the initial conditions for the tsunami numerical model and analytical studies. Our synthetic bathymetry domains include a sloping beach of one degree and the same sloping beach connected to 5000 m constant depth to investigate the initial value problem and the boundary value problem. To model tsunami propagation and inundation, we used a nonlinear shallow water numerical model comprising coupled 4-layer coupled nested grids. We compare the results of the simulations and the results of the analytical runup formulae. Our study shows that for dip values between 30 - 50 degrees and fault depths up to 20 km, the analytical formulae and numerical model produce runup heights with a maximum difference of 15%. This work was sponsored by the Fundação para a Ciência e a Tecnologia (FCT) through project UID/GEO/50019/2013/IDL-LA and project ASTARTE- Assessment Strategy and Risk Reduction for Tsunamis in Europe. Project Grant 603839, FP7-ENV2013 6.4-3.

1.6. Insights in the UNESCO Post-Event field survey of the September 28th, 2018 Palu tsunami

Wronna M., Hidayat R., Husrin S., Prasetya G., Annunziato A., Dogan G.G., Zaytsev A., Omira R., Proietti C., Probst P., Paparo M.A., Pronin P., Giniyatullin A., Putra P.S., Hartanto D., Ginanjar G., Kongko W., Pelinovsky E., Baptista M.A., Yalciner A.C. (2019b). Insights in the UNESCO Post-Event Field Survey of the September 28th, 2018 Palu Tsunami. Geophysical Research Abstracts Vol. 21, EGU2019-11544-2, 2019. EGU General Assembly 2019.

A tsunami followed the September 28th, 2018, Palu earthquake (Mw7.5) that caused widespread devastation in the Bay of Palu on the Island of Sulawesi, Indonesia. The automatic source estimation computed a left lateral strike-slip mechanism at a shallow depth with an earthquake epicentre located about 80 km north from the city of Palu. A large part of the strike-slip rupture occurred on land, and this mechanism usually does not produce enough uplift to generate a tsunami of that intensity which surprised authorities and the scientific community. First modelling efforts could also not explain the observed impact of the tsunami when considering only the seismic source. International efforts led to a UNESCO international tsunami survey with the objective to quantify the tsunami impact along the shore of the affected region. The team performed in total 78 measurements composed of runup height and inundation height in 32 locations along the 125 km coastline in the Palu Bay and up to the earthquake epicentre. The

tsunami caused significant destruction inside the bay, and outside only minor effects have been observed. The maximum measured values reach 9.1 m for runup height and 8.7 m for the inundation height close to Benteng in the southwest of Palu Bay. In ten locations inside the bay, the team found coastal sectors that collapsed into the sea after the earthquake. Also, the distribution of the measured runup and inundation height around the collapsed areas suggest their contribution as secondary tsunami sources. Here, we present the findings of the field survey with a particular focus on the areas around Pantoloan and Benteng. In Pantoloan, tide gauge measurements are available and close to Pantoloan security cameras captured the impact of the tsunami. In Benteng, the team identified the biggest coastal collapse in their survey and measured the highest runup.

1.7. A new predictor for tsunami runup

Wronna, M., Kânoğlu, U., and Baptista, M. A. (2020). A new predictor for tsunami runup. In EGU General Assembly Conference Abstracts (p. 557).

We present a new Tsunami Runup Predictor (TRP). The TRP includes the length of the beach slope, the length of the accelerating phase of the wave plus the amplitude ratio for leading depression waves. We use numerical and analytical tools to compute the runup for a dataset of 210 initial tsunami waveforms. In our tests, the slope angle of the beach varies between 1 and 5 degrees and the distance of the initial wave to the coast varies between 50 and 360 km. The results show a high correlation between the TRP and the dimensionless runup, enabling the definition of an empirical formula to predict the runup. We further test the empirical formula

using a set of past events with field data. The comparison of the empirical estimates with the runup measurements of post-tsunami surveys gives promising results. The TRP allows estimating the tsunami runup in real-time once the offshore waveform is known. The capacity to predict the maximum runup along the coast in real-time and include it in routine operations of Tsunami Early Warning Systems will constitute an enormous advance.

2. Methodological concepts

2.1. Equations of motion

The Navier-Stokes equations, the conservation of momentum per unit volume is given by,

$$\rho \frac{D\vec{v}}{Dt} = \rho \left(\frac{\partial \vec{v}}{\partial t} + (\vec{v} \cdot \nabla)\vec{v} \right) = -\nabla p + \mu \Delta \vec{v} + \left(\zeta + \frac{\mu}{3} \right) \nabla(\nabla \cdot \vec{v}) + \vec{f}, \tag{A2.1}$$

where ρ is the density, p is the static pressure, $\vec{v}$ is the velocity of a fluid particle, μ is the dynamic viscosity, ζ is the volume viscosity, $\vec{f}$ denotes body forces such as gravity or Coriolis. ∇ is the Nabla-operator, and Δ is the Laplace-operator. Relevant for this thesis are the Navier-Stokes equations for incompressible fluids. This assumption simplifies the continuity equation to be non-divergent $\nabla \cdot \vec{v} = 0$. The equation of momentum simplifies to

$$\rho \left(\frac{\partial \vec{v}}{\partial t} + (\vec{v} \cdot \nabla)\vec{v} \right) = -\nabla p + \mu \Delta \vec{v} + \vec{f}, \tag{A2.2}$$

That allows describing within a system of partial differential equations with two equations the components speed and pressure in function of time and space.

2.2. Partial differential equations for incompressible fluids

The set of partial differential equations for incompressible fluids (Cushman-Roisin and Beckers 2005):

$$x: \rho \left(\frac{du}{dt} + f_* w - fv \right) = -\frac{\partial p}{\partial x} + \frac{\partial \tau_{xx}}{\partial x} + \frac{\partial \tau_{xy}}{\partial y} + \frac{\partial \tau_{xz}}{\partial z}, \tag{A2.3 a}$$

$$y: \rho \left(\frac{dv}{dt} + fu \right) = -\frac{\partial p}{\partial y} + \frac{\partial \tau_{yx}}{\partial x} + \frac{\partial \tau_{yy}}{\partial y} + \frac{\partial \tau_{yz}}{\partial z}, \tag{A2.3 b}$$

$$z: \rho \left(\frac{dw}{dt} - f_* u \right) = -\frac{\partial p}{\partial z} - \rho g + \frac{\partial \tau_{zx}}{\partial x} + \frac{\partial \tau_{zy}}{\partial y} + \frac{\partial \tau_{zz}}{\partial z}, \tag{A2.3 c}$$

Here ρ is the density, p is the pressure, g is the gravitational acceleration, the τ terms represent normal and shear stresses because of friction, $f = 2\Omega \sin \varphi$ is the Coriolis parameter, and φ is the latitude, $f_* = 2\Omega \cos \varphi$ is the reciprocal Coriolis parameter (which is neglected for the most geophysical approximations), where Ω is the rotation rate of the earth, and $\frac{d\vec{v}}{dt}$ is,

$$\frac{du}{dt} = \frac{\partial u}{\partial t} + \frac{\partial u}{\partial x}\frac{\partial x}{\partial t} + \frac{\partial u}{\partial y}\frac{\partial y}{\partial t} + \frac{\partial u}{\partial z}\frac{\partial z}{\partial t} = \frac{\partial u}{\partial t} + u\frac{\partial u}{\partial x} + v\frac{\partial u}{\partial y} + w\frac{\partial u}{\partial z} \tag{A2.4 a}$$

$$\frac{dv}{dt} = \frac{\partial v}{\partial t} + \frac{\partial v}{\partial x}\frac{\partial x}{\partial t} + \frac{\partial v}{\partial y}\frac{\partial y}{\partial t} + \frac{\partial v}{\partial z}\frac{\partial z}{\partial t} = \frac{\partial v}{\partial t} + u\frac{\partial v}{\partial x} + v\frac{\partial v}{\partial y} + w\frac{\partial v}{\partial z} \qquad \text{(A2.4 b)}$$

$$\frac{dw}{dt} = \frac{\partial w}{\partial t} + \frac{\partial w}{\partial x}\frac{\partial x}{\partial t} + \frac{\partial w}{\partial y}\frac{\partial y}{\partial t} + \frac{\partial w}{\partial z}\frac{\partial z}{\partial t} = \frac{\partial w}{\partial t} + u\frac{\partial w}{\partial x} + v\frac{\partial w}{\partial y} + w\frac{\partial w}{\partial z} \qquad \text{(A2.4 c)}$$

The stress tensor terms τ are given as:

$$\tau_{xy} = \tau_{yx} = \mu\left(\frac{\partial u}{\partial y} + \frac{\partial v}{\partial x}\right) \qquad \text{(A2.5 a)}$$

$$\tau_{xz} = \tau_{zx} = \mu\left(\frac{\partial u}{\partial z} + \frac{\partial w}{\partial x}\right) \qquad \text{(A2.5 b)}$$

$$\tau_{xy} = \tau_{yx} = \mu\left(\frac{\partial u}{\partial y} + \frac{\partial v}{\partial x}\right) \qquad \text{(A2.5 c)}$$

$$\tau_{xx} = 2\mu\left(\frac{\partial u}{\partial x}\right) \qquad \text{(A2.5 d)}$$

$$\tau_{yy} = 2\mu\left(\frac{\partial v}{\partial y}\right) \qquad \text{(A2.5 e)}$$

$$\tau_{zz} = 2\mu\left(\frac{\partial w}{\partial z}\right) \qquad \text{(A2.5 f)}$$

For incompressible fluids, the continuity equation simplifies, stating that the divergence of the velocity vector field is zero. Hence, mass is conserved, and the continuity equation is,

$$\nabla \cdot \vec{v} = \frac{\partial u}{\partial x} + \frac{\partial v}{\partial y} + \frac{\partial w}{\partial z} = 0, \qquad \text{(A2.6)}$$

2.3. The non-linear SWE

The non-linear SWE in Cartesian coordinates are written as,

$$\frac{\partial P}{\partial t} + \frac{\partial}{\partial x}\left(\frac{P^2}{D}\right) + \frac{\partial}{\partial y}\left(\frac{PQ}{D}\right) + gD\frac{\partial \eta}{\partial x} + \tau_x D = 0, \qquad \text{(A2.7 a)}$$

$$\frac{\partial Q}{\partial t} + \frac{\partial}{\partial x}\left(\frac{PQ}{D}\right) + \frac{\partial}{\partial y}\left(\frac{Q^2}{D}\right) + gD\frac{\partial \eta}{\partial y} + \tau_y D = 0, \qquad \text{(A2.7 b)}$$

and conservation of mass,

$$\frac{\partial \eta}{\partial t} + \frac{\partial P}{\partial x} + \frac{\partial Q}{\partial y} = -\frac{\partial d}{\partial t}. \qquad \text{(A2.7 c)}$$

Here η is the free surface elevation, D is the total water depth given as the sum of the still water depth d and the free surface elevation $D = d + \eta$. P and Q represent the horizontal components of the volume flux, and τ_x and τ_y are the bottom friction terms in x- and y- directions, respectively.

The non-linear SWE in spherical coordinates are written as,

$$\frac{\partial P}{\partial t} + \frac{1}{R \cos \varphi} \frac{\partial}{\partial \psi} \left(\frac{P^2}{D}\right) + \frac{1}{R} \frac{\partial}{\partial \varphi} \left(\frac{PQ}{D}\right) + \frac{gD}{R \cos \varphi} \frac{\partial \eta}{\partial \psi} - fQ + \tau_\psi D = 0, \qquad \text{(A2.8 a)}$$

$$\frac{\partial Q}{\partial t} + \frac{1}{R \cos \varphi} \frac{\partial}{\partial \psi} \left(\frac{PQ}{D}\right) + \frac{1}{R} \frac{\partial}{\partial \varphi} \left(\frac{Q^2}{D}\right) + \frac{gD}{R} \frac{\partial \eta}{\partial \psi} + fP + \tau_\varphi D = 0, \qquad \text{(A2.8 b)}$$

with conservation of mass,

$$\frac{\partial \eta}{\partial t} + \frac{1}{R \cos \varphi} \left[\frac{\partial P}{\partial \psi} + \frac{\partial}{\partial \varphi} (\cos \varphi Q)\right] = -\frac{\partial d}{\partial t}. \qquad \text{(A2.8 c)}$$

Here η is the free surface elevation, D is the total water depth given as the sum of the still water depth d and the free surface elevation $D = d + \eta$. P and Q represent the horizontal components of the volume flux, and τ_ψ and τ_φ are the bottom friction terms, in ψ and φ direction. φ and ψ represent the latitude and longitude, respectively.

2.4. Manning's formula to evaluate of the bottom friction terms

The Manning's formula to evaluate the friction terms to simulate bottom friction in different bottom roughness conditions is written as

$$\tau_x = \frac{gn^2}{D^{\frac{7}{3}}} P\sqrt{P^2 + Q^2} \ , \qquad \text{(A2.9 a)}$$

$$\tau_y = \frac{gn^2}{D^{\frac{7}{3}}} Q\sqrt{P^2 + Q^2} \ , \qquad \text{(A2.9 b)}$$

where n is the empirical Manning coefficient to simulate different bottom roughness conditions. D is the total water depth given as the sum of the still water depth d and the free surface elevation $D = d + \eta$ and P and Q represent the horizontal components of the volume flux.

2.5. The discrete staggered leap-frog scheme for linear SWEs used in NSWING

The discrete leap-frog finite difference scheme excluding friction terms and Coriolis parameter is written as,

$$\frac{\eta_{i,j}^{n+\frac{1}{2}}-\eta_{i,j}^{n-\frac{1}{2}}}{\Delta t}+\frac{P_{i+\frac{1}{2},j}^{n}-P_{i-\frac{1}{2},j}^{n}}{\Delta x}+\frac{Q_{i+\frac{1}{2},j}^{n}-Q_{i-\frac{1}{2},j}^{n}}{\Delta x}=-\frac{d_{i,j}^{n+\frac{1}{2}}-d_{i,j}^{n-\frac{1}{2}}}{\Delta t} \tag{A2.10 a}$$

$$\frac{P_{i+1/2,j}^{n}-P_{i-1/2,j}^{n}}{\Delta t}+gd_{i+1/2,j}\frac{\eta_{i+1,j}^{n+1/2}-\eta_{i,j}^{n-1/2}}{\Delta x}=0 \tag{A2.10 b}$$

$$\frac{Q_{i+1/2,j}^{n}-Q_{i-1/2,j}^{n}}{\Delta t}+gd_{i+1/2,j}\frac{\eta_{i+1,j}^{n+1/2}-\eta_{i,j}^{n-1/2}}{\Delta y}=0 \tag{A2.10 c}$$

NSWING evaluates the free surface elevation η at each centre point (i,j) of the grid cell at the time step $n-1/2$ with the continuity equation (2.5 a). Then, volume flux P and Q are computed using the momentum equations (2.5 b and 2.5 c) at the n-th time step at the surrounding points of (i,j), which are in the centre of the adjoining grid cell borders. This process is shown exemplarily in the reference frame in figure 2.3. The computation is explicit; thus, each time step depends on evaluating the previous time step. At $t=0$ the initial condition (a grid containing the free surface deformation η) previously defined by the user launches the numerical simulation.

2.6. The discrete staggered leap-frog scheme including a second-order upwind scheme for non-linear SWEs in NSWING

The discretization of the nonlinear SWEs applies the finite staggered leap-frog scheme, but a second-order upwind scheme evaluates the momentum equation's nonlinear convective terms.

These discretization terms yield,

$$\frac{\partial}{\partial x}\frac{P^2}{D}=\frac{1}{\Delta x}\left[\lambda_{11}\frac{\left(P_{i+3/2,j}^{n}\right)^2}{D_{i+3/2,j}^{n}}+\lambda_{12}\frac{\left(P_{i+1/2,j}^{n}\right)^2}{D_{i+1/2,j}^{n}}+\lambda_{13}\frac{\left(P_{i-1/2,j}^{n}\right)^2}{D_{i-1/2,j}^{n}}\right], \tag{A2.11 a}$$

$$\frac{\partial}{\partial y}\frac{PQ}{D}=\frac{1}{\Delta y}\left[\lambda_{21}\frac{(PQ)_{i+1/2,j+1}^{n}}{D_{i+1/2,j+1}^{n}}+\lambda_{22}\frac{(PQ)_{i+1/2,j}^{n}}{D_{i+1/2,j}^{n}}+\lambda_{23}\frac{(PQ)_{i+1/2,j-1}^{n}}{D_{i+1/2,j-1}^{n}}\right], \tag{A2.11 b}$$

$$\frac{\partial}{\partial x}\frac{PQ}{D}=\frac{1}{\Delta x}\left[\lambda_{31}\frac{(PQ)_{i+1/2,j+1}^{n}}{D_{i+1,j+1/2}^{n}}+\lambda_{32}\frac{(PQ)_{i+1/2,j}^{n}}{D_{i,j+1/2}^{n}}+\lambda_{33}\frac{(PQ)_{i+1/2,j-1}^{n}}{D_{i-1,j+1/2}^{n}}\right], \tag{A2.11 c}$$

$$\frac{\partial}{\partial y}\frac{Q^2}{D} = \frac{1}{\Delta y}\left[\lambda_{41}\frac{\left(Q_{i,j+3/2}^n\right)^2}{D_{i,j+3/2}^n} + \lambda_{42}\frac{\left(Q_{i,j+1/2}^n\right)^2}{D_{i,j+1/2}^n} + \lambda_{43}\frac{\left(Q_{i,j-1/2}^n\right)^2}{D_{i,j-1/2}^n}\right],\qquad\text{(A2.11 d)}$$

and the coefficients λ are defined as,

$$\begin{cases}\lambda_{11} = 0, & \lambda_{12} = 1, & \lambda_{13} = -1, & if \ P_{i+1/2,j}^n \geq 0 \\ \lambda_{11} = 1, & \lambda_{12} = -1, & \lambda_{13} = 0, & if \ P_{i+1/2,j}^n < 0\end{cases}$$

$$\begin{cases}\lambda_{21} = 0, & \lambda_{22} = 1, & \lambda_{23} = -1, & if \ Q_{i+1/2,j}^n \geq 0 \\ \lambda_{21} = 1, & \lambda_{22} = -1, & \lambda_{23} = 0, & if \ Q_{i+1/2,j}^n < 0\end{cases}$$

$$\begin{cases}\lambda_{31} = 0, & \lambda_{32} = 1, & \lambda_{33} = -1, & if \ P_{i,j+1/2}^n \geq 0 \\ \lambda_{31} = 1, & \lambda_{32} = -1, & \lambda_{33} = 0, & if \ P_{i,j+1/2}^n < 0\end{cases}$$

$$\begin{cases}\lambda_{41} = 0, & \lambda_{42} = 1, & \lambda_{43} = -1, & if \ Q_{i,j+1/2}^n \geq 0 \\ \lambda_{41} = 1, & \lambda_{42} = -1, & \lambda_{43} = 0, & if \ Q_{i,j+1/2}^n < 0\end{cases}$$

2.7. Discretization of the bottom friction terms

Discretization of the bottom friction terms yield,

$$\tau_x = \nu_x\left(P_{i+1/2,j}^{n+1} + P_{i+1/2,j}^n\right) \qquad\text{(A2.12 a)}$$

$$\tau_y = \nu_y\left(Q_{i,j+1/2}^{n+1} + Q_{i,j+1/2}^n\right) \qquad\text{(A2.12 b)}$$

where ν_x and ν_y are defined as,

$$\nu_x = \frac{1}{2}\frac{gn^2}{\left(D_{i+1/2,j}^n\right)^{\frac{7}{3}}}\sqrt{\left[\left(P_{i+1/2,j}^n\right)^2 + \left(Q_{i+1/2,j}^n\right)^2\right]} \qquad\text{(A2.12 a)}$$

$$\nu_y = \frac{1}{2}\frac{gn^2}{\left(D_{i,j+1/2}^n\right)^{\frac{7}{3}}}\sqrt{\left[\left(P_{i,j+1/2}^n\right)^2 + \left(Q_{i,j+1/2}^n\right)^2\right]}. \qquad\text{(A2.12 b)}$$

2.8. Analytical solution

Aydın and Kânoğlu (2017) solution is based on Kânoğlu (2004). He proposes that a waveform of any kind can be transformed linearly in the hodograph space for the spatial coordinate to evaluate the nonlinear time histories of the given initial waveform. That method results in simpler integrals for the shoreline motion and velocity. Later, Aydın and Kânoğlu (2017) present

an efficient computational framework for Kânoğlu's (2004) approach by employing eigenfunction expansions to solve the NSW equations.

The one-plus-one dimensional nonlinear SWE describe the propagation of a wave in a water body with water depth,

$$u_t + uu_x + \eta_x = 0, \tag{A2.13 a}$$

$$[u(d + \eta)]_x + \eta_t = 0 \tag{A2.13 b}$$

Where $u(x,t)$ and $\eta(x,t)$ are the horizontal depth-averaged velocity and free surface elevation, respectively. The origin of the coordinate system is at the initial shoreline, and x is increasing towards the seaward direction with $\tilde{d}(\tilde{x}) = \tilde{x} * \tan\beta$, where β is the beach angle. Kânoğlu (2004) defines the dimensionless variables with the arbitrary reference length $\tilde{l}$, as $x = \tilde{x}/\tilde{l}$, $d = \tilde{d}/(\tilde{l}\tan\beta)$, $\eta = \tilde{\eta}/(\tilde{l}\tan\beta)$, $u = \tilde{u}/(\tilde{g}\tilde{l}\tan\beta)^{1/2}$ and $t = \tilde{t}(\tilde{g}\tan\beta/\tilde{l})^{1/2}$ where $\tilde{g}$ is the gravitational acceleration. Carrier and Greenspan's (1958) use the hodograph transformation defining the new set of independent variables (σ, λ) that reduced the nonlinear SWE to a single second-order linear equation, using the Riemann invariants of the hyperbolic system (A2.13 a and b).

$$\sigma\phi_{\lambda\lambda} - (\sigma\phi_\sigma)_\sigma = 0 \tag{A2.14}$$

Then, Kânoğlu (2004) introduces the potential $\phi(\sigma, \lambda)$ as $u = \phi_\sigma/\sigma$ and presents a bounded solution at the shoreline with the initial conditions $\lambda = 0$, $u = 0$ and a wave profile in (σ, λ)-space. The transformation according to Carrier and Greenspan (1958) also defines the shoreline to be at $\sigma = 0$ in the hodograph (σ, λ)-space. When $\phi(\sigma, \lambda)$ is known, the following hodograph transformation provide the solution in (x, t)-space:

$$u = \frac{\phi_\sigma}{\sigma} \tag{A2.15 a}$$

$$\eta = \frac{1}{4}\phi_\lambda - \frac{1}{2}u^2 \tag{A2.15 b}$$

$$x = \frac{1}{16}\sigma^2 - \frac{1}{4}\phi_\lambda + \frac{1}{2}u^2 \tag{A2.15 c}$$

$$t = u - \frac{1}{2}\lambda \tag{A2.15 d}$$

To overcome the difficulty of including realistic profiles in terms of geophysical scales, Kânoğlu (2004) uses the linearized form of the hodograph transformation for the spatial

variable $x \cong \frac{1}{16}\sigma^2$ to define the initial waveform in the (σ, λ)-space, $\eta\left(\frac{1}{16}\sigma^2, 0\right)$. Consequently, $\phi(\sigma, \lambda)$ can be obtained through integration, as demonstrated in Kânoğlu (2004). Thus, it is possible to investigate in any realistic waveform such as Gaussian and N-wave shapes.

If we consider an initial waveform $\eta(x, 0)$, the evolution of the water-surface elevation is now given by $\eta(\sigma, \lambda) = \frac{1}{4}\phi_\lambda - \frac{1}{2}u^2$. This equation can be integrated numerically to obtain the water-surface elevation given for a time t^* or a position x^* using the Newton-Raphson iteration algorithms (Synolakis, 1987). Considering this work, we are interested in shoreline motion and velocity. Then the equation can be rewritten concerning the shoreline position that also allows obtaining the shoreline velocity u_s.

$$\eta_s(\lambda) = \eta(0, \lambda) = \frac{1}{4}\phi_\lambda - \frac{1}{2}u_s^2 \qquad (A2.16)$$

Kânoğlu (2004) presents the four cases previously suggested by Carrier et al. (2003). However, the method is applicable to any initial waveform.

Alternatively, to the integral solution techniques, Aydın and Kânoğlu (2017) then consider an initial-boundary value problem and use the most general eigenfunction expansion. Since the solution needs to be bounded everywhere, they use a Dirichlet (first-type) and a Neumann (second-type) boundary condition and express it through eigenfunction expansion. They figured out that independent of the boundary type, the wave is reflected at the seaward boundary, and thus physical dimension must be chosen with care when estimating the runup.

They obtain the series expansion for the potential function. The series expansion for the potential function is then resolved for the given initial and boundary conditions. They also present a solution for the shoreline velocities demonstrating how to treat singularities. Once the potential and the velocity are evaluated in the hodograph-space, the results in the physical space can be obtained with the following expressions,

$$\eta = \varphi - \frac{u^2}{2} \qquad (2.14\ a)$$

$$x = \sigma^2 - \eta \qquad (2.14\ b)$$

$$t = \lambda + u. \qquad (2.14\ c)$$

And then, the time histories of the shoreline position are computed using $\sigma = 0$, and

$$x_s(\lambda) = \frac{u_s^2(\lambda)}{2} - \varphi(0, \lambda), \qquad (2.15\ a)$$

$$t_s(\lambda) = \lambda + u_s(\lambda). \tag{2.15 b}$$

Again, the application of the Newton-Raphson iteration algorithms allows computing η and u at any location x and time t.

3. Brief history of tsunamigenic earthquakes in the North-East Atlantic

The following section lists tsunamigenic earthquakes in the North-East Atlantic (Galbis Rodríguez 1932, Baptista and Miranda 2009, Kaabouben et al. 2009). Baptista and Miranda (2009) tsunami catalogue lists 21 tsunami events but excluded six events due to unreliability.

3.1. The 218 BC tsunami

A high energy event of 218 BC included in Galbis Rodríguez (1932) catalogue is not included here. Sedimentary deposits have been identified for this event on the Valedelagrana Spit Bar close to Cadiz by Luque et al. (2002), who conclude that the deposit has a similar signature as a deposit found for the November 1, 1755 tsunami. Vizcaino et al. (2006) found a matching debris flow signature in the Marques de Pombal core. Both signatures dated in the same eras of about 2200-2300 yr BP and thus agreed with Galbis Rodríguez (1932). This event was estimated with a M>8 magnitude, but the generating source is unknown.

3.2. The 60 BC Portugal and Galicia tsunmi

An earthquake with an estimated 8.5 magnitude generated the Portugal/Galicia tsunami dated 60 BC and is the oldest event considered in Portuguese catalogues (LNEC 1986, Martins and Mendes Victor 2001). Sousa (1678) presents a description of the earthquake and tsunami, stating that it ruined many places, and the sea left its ordinary limits occupying land in some places and uncovering in other places.

3.3. The 382 AD Cape Vincent tsunami

The Roman writer Amiano Marcellino (in Brito 1597) describes that this event caused significant morphological changes close to Cape St. Vincent. He wrote that an island disappeared and the formation of new islets. Martins and Mendes Victor (2001) catalogue attributes a Magnitude of M ~ 7.5.

3.4. The January 26, 1531, Tagus estuary tsunami

Between 4 and 5 a.m., a strong earthquake was felt in the LTV and Lisbon. The earthquake caused heavy destruction in Lisbon and surrounding with about 1000 casualties (Vogt and Levret 1985; Justo and Salwa, 1998). The Tagus River flooded downtown Lisbon and dwellings along the estuary. The tsunami deposited ships that anchored in the harbour above the waterline. Henriques et al. (1988) compiled Portuguese descriptions of the 1531 earthquake. The maximum macroseismic intensity is X (MSK), and approximate coordinates of the epicentre considering the macroseismic field are 38.9 N, 9.0 W (Martins and Mendes-Victor 2001). Baptista et al. (2014) point out that the population of Lisbon was already aware of the possible connection of the inundation with the earthquake. Baptista et al. (2014) reevaluate the event with the epicentre at 39.00 N, 8.9 W and a magnitude close to M = 6.6. These authors also present a tectonic structure for the event and consider the NNE to SSW extending and East dipping Vila Franca de Xira fault as earthquake and tsunami source.

3.5. The December 27, 1722, Tavira tsunami

On December 27, 1722, an earthquake struck Tavira between 5 and 6 p.m. This earthquake was felt from Cape St. Vincent to the Spanish border (Mendonça 1758). Some inundations in Tavira are documented, and Baptista et al. (2007) used numerical tsunami modelling and interpretation of multichannel seismic profiles to estimate the earthquake source. They propose an epicentre close to 37.02 N, 7.82 W and that the earthquake with a magnitude of about M ~ 6.5 generated a local tsunami.

3.6. The November 1, 1755, transatlantic tsunami

On November 1, 1755, at around 9:40 a.m., a massive Mw=8.5±0.3 earthquake (Martínez Solares and Arroyo, 2004) struck Portugal. The shakings were felt all over Europe as far as Hamburg, the Azores and Cape Verde Islands, but the strongest ones all over the Iberian Peninsula especially close to Cape St. Vincente (Pereira de Sousa, 1919; Martínez Solares et al., 1979). It devastated the Iberian and North Morocco coasts, causing enormous damage and casualties. This event is the strongest in modern European history. Numerous compilations and historical accounts document the occurrences that happened that day. Tsunami descriptions state 10-15m high waves at Cape St. Vincente. Baptista et al. (1998a) estimate about 900 casualties exclusively to the tsunami in Lisbon, where the water penetrated about 250 m landward. The tsunami was observed on the North Atlantic coasts and in Central and South America. Kaabouben et al.

(2009) summarize Tsunami observations for the 1755 event in Morocco. In Portugal description of the Tsunami are available for many locations among them, Lisbon, Cascais, Setúbal, Porto, Figueira da Foz, Lagos, Albufeira, Faro, Tavira, Castro Marim, Lagoa, Madeira and Porto Santo (Mendonça 1758, Pereira de Sousa 1919, Baptista et al. 1998a, b, Baptista et al. 2003, Santos and Koshimura 2015, Wronna et al. 2017). This cataclysm caused intense throughout history; already, Kant and Voltaire explained the catastrophe as natural phenomena (Mendes-Victor et al. 2008 and Gupta and Gahalaut, 2013). The 1755 earthquake epicentre was somewhere south-west of Portugal in the SWIM, according to ray backtracing methods. Several proposals for the tectonic source of the earthquake were presented, discussed and disputed (Baptista et al. 1998 a,b , Zitellini et al. 1999, 2001, Baptista et al. 2003, Vilanova et al. 2003, Gutscher et al. 2002, Matias et al. 2005, Thiebot and Gutscher 2006, Gutscher et al. 2006, Barkan et al. 2009, Carvalho et al. 2009, Ribeiro et al. 2009). However, the quest for the exact earthquake source is still a matter of debate, led to the intense investigation revealing a significant knowledge about the tectonic structures in the SWIM.

3.7. The November 16, 1755, La Coruna tsunami

Mendonça (1758) describes an explosion on November 16, 1755, at half-past three, that caused damage and flux and reflux of the sea in Santiago de Compostella and Coruña. Perrey (1847) reports that in Lisbon, the land subsided and that the sea inflated.

3.8. The March 29, 1756, Lisbon tsunami

Perrey (1847) describes a violent shock in Lisbon and the agitation of the water in the Tagus river. The original source of this description of the event is the Journal Historique (1756). Neither Mendonça (1758) mentions this event, nor Martins and Mendes-Victor (2001) include this event in their catalogue. Baptista and Miranda (2009) list the event considering a source in the Tagus estuary but attribute low reliability.

3.9. The March 31, 1761, transatlantic tsunami

On March 31, 1761, around noon, an earthquake that lasted about 3 min was felt in Lisbon. Several walls collapsed in Lisbon, but damages had been worse in Setúbal, Vila Franca de Xira, and Porto. A systematic inquiry was commissioned by the president of Royal and Supreme Council of Castilla) also bishop of Cartagena, Diego de Rojas y Contreras in Spain. This inquiry delivers the most extensive dataset on this event. Rodríguez de la Torre (1997) presents a review

of this data and an assessment of macroseismic intensities. People felt the earthquake from Morocco, the Iberian Peninsula, France until the Netherlands, the UK, and Ireland. In Lisbon, about 1 hour and 15 minutes later, the tsunami with an estimated amplitude of 8 feet was observed (Molloy, 1761). Observations of the tsunami exist in the northeast Atlantic in Cadiz, Madeira, Azores Islands, the UK, Ireland, and the Caribbean in Barbados. Baptista et al. (2006) summarizes the earthquake and tsunami observations and conclude for a magnitude of about 8.5 and locate the earthquake 34.5 N, 13 W using macroseismic analysis and tsunami backward raytracing.

3.10. The December 18, 1926, Lisbon tsunami

On December 18, 1926, an earthquake of unknown shook Lisbon at 14:45, lasting a couple of seconds. Martins and Mendes-Victor (2001) locate the epicentre at 38.7 N, 9.2 W. There is an instrumental record in Coimbra, and the newspapers report several observations of agitation in the Tagus river. However, Baptista and Miranda (2009) do not identify a clear tsunami signal at the Cascais tide gauge.

3.11. The May 8, 1939, North Atlantic tsunami

On May 8, 1939, at 1:47, a magnitude 7.1 earthquake generated a small tsunami (0.3m maximum peak to peak amplitude) at the Azores archipelago with an epicentre located at 37.4 N, 23,9 W (Buforn et al. 1988, Cabral 2020). Baptista and Miranda (2009) do not identify a tsunami signal at the tide gauges on mainland Portugal. Reis et al. (2017) use numerical tsunami modelling and compare it to the tide gauge signal and conclude a similar source proposed by Buforn et al. (1988) with a predominant strike-slip mechanism.

3.12. The November 25, 1941, North Atlantic tsunami

At 17:04 of November 25, 1941, a strong magnitude earthquake occurred between the Portuguese mainland and the Azores archipelago. Martins and Mendes-Victor (2001) estimate the magnitude with 8.2 and locate the epicentre at 37.42 N, 19.01 W, approximately 790 km offshore mainland Portugal. The shakings were felt in the Azores, the Iberian Peninsula, Morocco, Switzerland, the UK, the USA, and the tide gauges in mainland Portugal, Madeira, Azores, Morocco, and the UK registered a small tsunami. Portuguese newspapers report the observations in the Tagus and Douro estuaries (Baptista and Miranda 2009). The tide station in Essaouria, Morocco (0.45m, peak to peak) recorded the maximum peak to peak amplitude of 0.45m

(Kaabouben et al. 2009). Baptista et al. (2016) used the empirical Green functions to invert the tsunami source and conclude for rupture length of approximately 160 km with a considerable thrust component. These authors discussed the possibility of a landslide as a secondary tsunami source offshore Morocco, referring to reports of damaged submarine cables (Debrach 1946, and Rothé 1951).

3.13. The February 28, 1969, Horseshoe tsunami

At 2:40 on February 28, 1969, a strong magnitude (M~7.9) earthquake struck Portugal. A vessel navigating offshore Sines observed the seaquake, and a 32k ton ship navigating close to the Horseshoe Abyssal Plane was structurally damaged, forcing it to return to Lisbon (Ambraseys, 1985, Baptista and Miranda 2009). Fukao (1973) locates the epicentre southwest of Iberia in the Horseshoe Abyssal Plain at 22 km depth proposing a SE dipping thrust fault with a small strike-slip component. This rupture mechanism generated a tsunami that was recorded in the tide stations in mainland Portugal, Spain, Azores, Morocco and in the Canary Islands (Baptista et al. 1992, Heinrich et al. 1994, Gjevik et al. 1997, Rabinovich et al. 1998) with the maximum amplitude 0.9 m in Casablanca (Kaabouben et al. 2009). Baptista et al. (1992) uses a maximum entropy analysis and concludes for wave heights up to 1 m along the coast of Portugal.

3.14. The May 26, 1975, Gloria Fault tsunami

On May 26, 1975, at about 8:15 local time, another Gloria fault-related earthquake occurred in the NE Atlantic close to 35.9 N, 17.5 W. However, the epicentre was 200 km south of the Gloria fault (Buforn et al. 1988; Lynnes and Ruff 1985). The earthquake excited a small amplitude tsunami recorded in Portugal, Spain, Azores, and Ceuta (Kaabouben et al. 2009). In Lagos, the tide gauge registered a 0.3 m maximum amplitude and in Horta (Faial islands, Azores), a maximum peak to peak amplitude of 0.76 m (Baptista and Miranda 2009, Kaabouben et al. 2009). Kaabouben et al. (2008) presented a reanalyzes for the 1975 Gloria tsunami and concluded for a source in the Tydeman Fracture zone which is approximately parallel to the Gloria fault. These authors also used numerical tsunami modelling and concluded that the modelled tsunami amplitudes are in good agreement with the observations when considering a fault plane solution by Lynnes and Ruff (1985).

3.15. The January 1, 1980, Azores tsunami

A strong earthquake occurred on January 1, 1980, at 16:43 local time. The epicentre was between Terceira and São Jorge Island at 38.81 N, 27.78 W (Baptista and Miranda 2009). This strike-slip event had a 7.2 magnitude and was the strongest earthquake in the Azores Archipelago in the 20th Century (Cabral 2020). In Angra do Heroísmo (Terceira), the tide station recorded a small tsunami with a 0.3 m maximum peak to peak amplitude. Baptista and Miranda (2009) checked the tide gauges in mainland Portugal and did not identify a tsunami signal.

4. The September 28th, 2018, tsunami in Palu-Sulawesi, Indonesia: A post-event field survey

Omira, R., Dogan, G.G., Hidayat, R., Husrin S., Prasetya G., Annunziato A., Proietti C., Probst P., Paparo M.A., Wronna M., Zaytsev A., Pronin P., Giniyatullin A., Putra P.S., Hartanto D., Ginanjar G., Kongko W., Pelinovsky E., Yalciner A.C. (2019). The September 28th, 2018, Tsunami In Palu-Sulawesi, Indonesia: A Post-Event Field Survey. Pure Appl. Geophys. 176, 1379–1395 (2019). https://doi.org/10.1007/s00024-019-02145

▌Pure and Applied Geophysics

The September 28th, 2018, Tsunami In Palu-Sulawesi, Indonesia: A Post-Event Field Survey

R. Omira,[1,2] G. G. Dogan,[3] R. Hidayat,[4] S. Husrin,[5] G. Prasetya,[6] A. Annunziato,[7] C. Proietti,[7] P. Probst,[7] M. A. Paparo,[8] M. Wronna,[2] A. Zaytsev,[9] P. Pronin,[10] A. Giniyatullin,[10] P. S. Putra,[11] D. Hartanto,[12] G. Ginanjar,[12] W. Kongko,[13] E. Pelinovsky,[14] and A. C. Yalciner[3]

Abstract—On September 28th, 2018, a powerful earthquake (M_w 7.5) struck the Island of Sulawesi in Indonesia. The earthquake was followed by a destructive and deadly tsunami that hit the Bay of Palu. A UNESCO international tsunami survey team responded to the disaster and surveyed 125 km of coastline along the Palu Bay up to the earthquake epicentre region. The team performed 78 tsunami runup and inundation height measurements throughout the surveyed coastline. Measured values reached 9.1 m for the runup height and 8.7 m for the inundation height, both at Benteng village. The survey team also identified ten large coastal sectors that collapsed into the sea of Palu Bay after the earthquake. The distribution of the measured tsunami data within Palu Bay exhibits a clear localised impact suggesting the contribution of secondary non-seismic local sources to the generation of the tsunami. Findings of the field reconnaissance are discussed to provide an insight into the remaining debated source of the Palu tsunami.

Key words: Tsunami, runup height, inundation height, coastal damage, landslides, Palu-Sulawesi, Indonesia.

1. Introduction

Population exposure to tsunami along the Indonesian coast is the third highest in the world (Løvholt et al. 2014). The tsunami threat in Indonesia is mainly associated with large earthquakes often occurring within the surrounding seismogenic zones (Horspool et al. 2014). Before the December 26th, 2004 Indian Ocean earthquake and tsunami, the east of the Indonesian archipelago, with the highest frequency of tsunamis, was considered as the most tsunami hazardous zone of Indonesia (Prasetya et al. 2001). Eastern Indonesia lies within a plate triple junction where the Pacific-Philippine and the India–Australia Plates subduct underneath the Eurasian (or Sunda) Plate at rates of 75 and 90 mm/yr, respectively (Socquet et al. 2006; Spencer 2011) (Fig. 1). In this geodynamic context, the seismic activity is high and the presence of several microplates generating motions that accommodate the convergence between the main plates results in complex tectonics (Nishimura and Suparka 1990) (Fig. 1). Major collisional orogenies, subduction zones, rift systems, and rapidly slipping transform faults often take place within the boundaries between these microplates (Socquet et al. 2006).

[1] Portuguese Institute for Sea and Atmosphere (IPMA), Lisbon, Portugal. E-mail: omirarachid10@yahoo.fr

[2] Dom Luiz Institute (IDL), Faculty of Sciences, University of Lisbon, Lisbon, Portugal.

[3] Department of Civil Engineering, Ocean Engineering Research Center, Middle East Technical University, Ankara, Turkey.

[4] Coordinating Ministry for Maritime Affairs (CMMA-RI), Jakarta, Indonesia.

[5] Ministry of Maritime Affairs and Fisheries (MMAF-RI), Jakarta, Indonesia.

[6] Indonesian Tsunami Scientific Community (IATsI), Jakarta, Indonesia.

[7] Joint Research Centre, European Commission, Ispra Site, Ispra, Italy.

[8] Department of Physics and Astronomy, University of Bologna, Bologna, Italy.

[9] Special Research Bureau for Automation of Marine Researches, Nizhny Novgorod, Russia.

[10] Nizhny Novgorod State Technical University n.a. R.E. Alekseev, Nizhny Novgorod, Russia.

[11] Indonesian Institute of Science (LIPI), Jakarta, Indonesia.

[12] Meteorology, Climatology, and Geophysical Agency (BMKG), Jakarta, Indonesia.

[13] Agency for the Assessment and Application of Technology (BPPT), Jakarta, Indonesia.

[14] Institute of Applied Physics, Nizhny Novgorod, Russia.

166
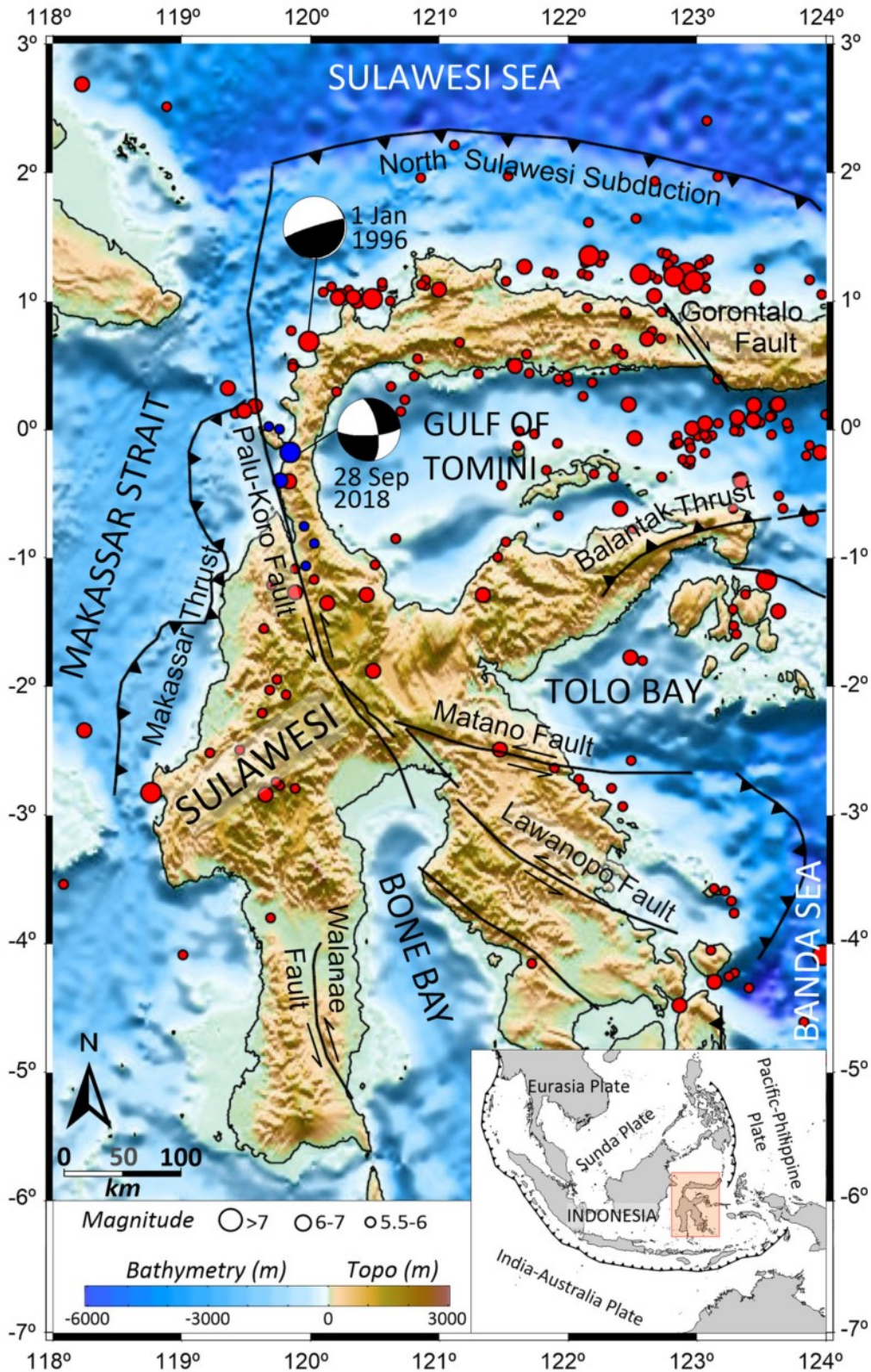
Tectonic setting and seismicity of the Sulawesi Island, Eastern Indonesia. Solid red circles are instrumental M > 5.5 seismicity from IRIS (1970–2018), and solid blue circles are epicentres from the M 7.5 earthquake sequence (with M > 5.5). The focal mechanisms, beach balls, for both the September 2018 and the January 1996 are from the USGS. Major active tectonic structures and faults are plotted in bold black lines. Bathymetric and topographic data are from GEBCO 30arc-sec

Sulawesi Island, located within the triple junction of east Indonesia, is obliquely crossed by one of the main fault systems, the left-lateral Central Sulawesi Fault System (CSFS), limiting the Eurasian Plate to the east (Bellier et al. 2001) (Fig. 1). The CSFS comprises two transform faults, the Palu-Koro and Matano, that connect the North Sulawesi subduction zone to the Banda Sea domain (Bellier et al. 2001) (Fig. 1). Within the Palu-Koro Fault, a strike-slip left-lateral fault with a slip rate of 42 mm/yr (Socquet et al. 2006), large shallow earthquakes are likely to occur (Watkinson and Hall 2016). The events of 1996 (M_w 7.7) and 1998 (M_w 6.6) took place close to the fault zone but they did not clearly lie on the active Palu–Koro Fault, and none had a focal mechanism indicating left-lateral slip along the Palu–Koro trend (Watkinson and Hall 2016).

Sulawesi has a long history of earthquake-inducing tsunamis. In the period between 1820 and 1982, fourteen tsunamis have been reported around the Sulawesi Island (Prasetya et al. 2001). Most of these events have involved the main active tectonic structures of the region, namely the Palu-Koro Fault and the north Sulawesi subduction zone. Palu-Koro Fault was responsible for causing at least two tsunamigenic earthquakes, on December 1st, 1927 and on August 14th, 1968 at the Bay of Palu (Prasetya et al. 2001). The most recent tsunami in the region, 2–4 m wave height, occurred on January 1st, 1996 after an M_w 7.8 normal faulting earthquake (Pelinovsky et al. 1997; Gomez et al. 2000) (Fig. 1).

At 10:02:45 UTC (local time 6:02:45 pm), on September 28th, 2018, a magnitude M_w 7.5 earthquake took place in the Island of Sulawesi in Indonesia. The US Geological Survey (USGS) located the event epicentre at 0.256°S and 119.846°E, northern Donggala District (Fig. 1). The earthquake
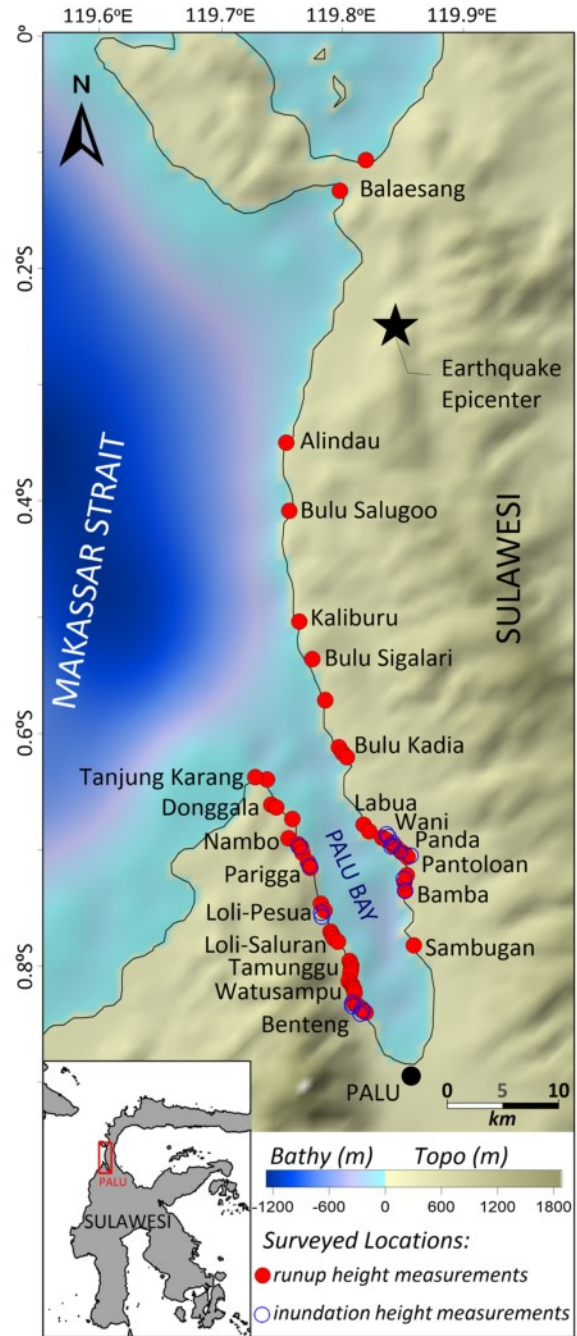

Figure 2
Locations where the team performed the post-tsunami survey and measured the runup heights (solid red circles) and the inundations heights (blue circles). Bathymetric and topographic data are from GEBCO 30arc-sec

resulted from a shallow strike-slip faulting with a focal depth estimated at 13.5 km by the USGS (Fig. 1). Few minutes after the earthquake a massive
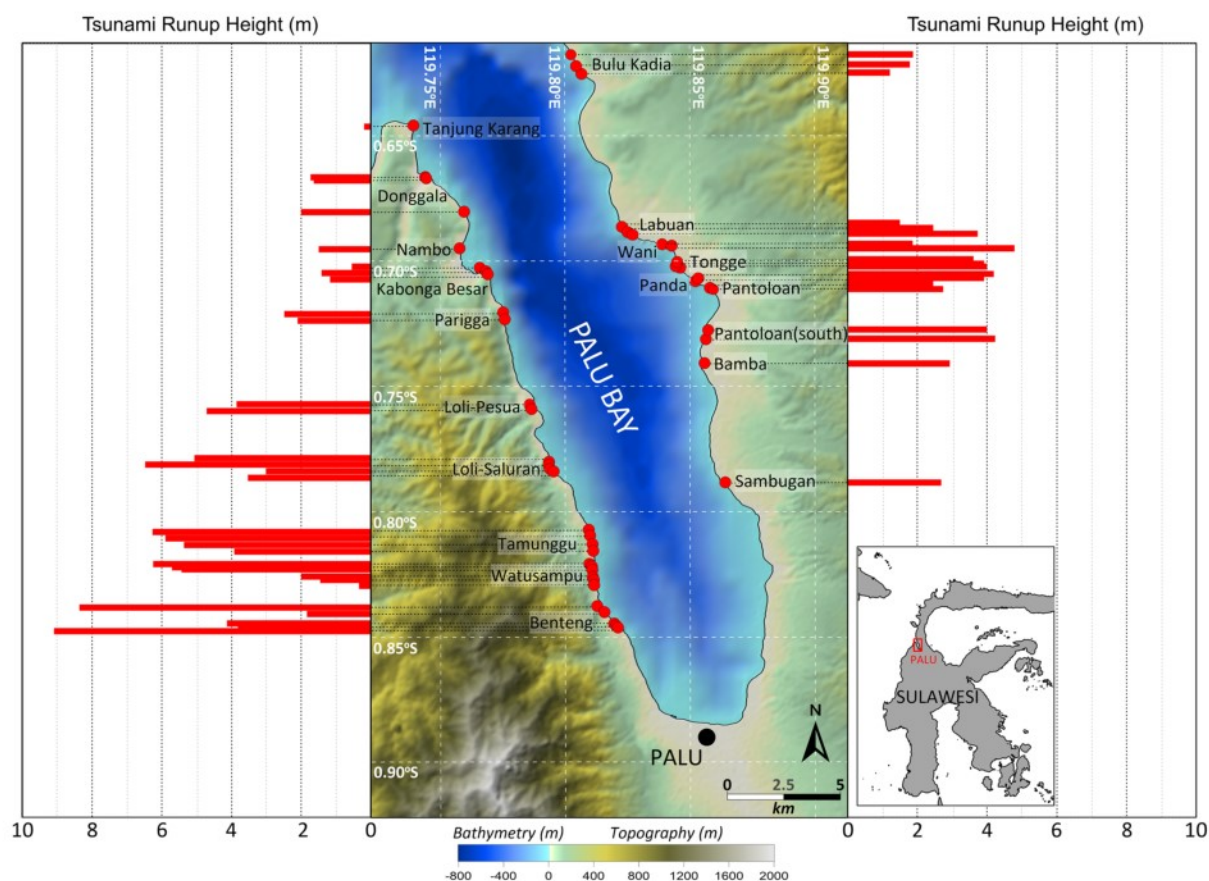
Figure 3
Tsunami runup heights measured along the coastline of Palu Bay. Bathymetric data are from BIG (Badan Informasi Geospasial, Indonesia) and topographic data are from Shuttle Radar Topography Mission (SRTM)

tsunami hit the Bay of Palu. Pantoloan tide gauge recorded the tsunami signal with a maximum amplitude of 1.9 m and a period of ∼ 3.5 min according to the sea level data available from the Agency for Geo-spatial Information Indonesia (BIG) (http://tides.big.go.id), but the tsunami by far exceeded this recorded height along several other coastal zones. The earthquake and tsunami caused substantial destruction of property and loss of life with more than 2000 fatalities (ASEAN 2018). A tsunami of such size surprised the scientific community as it followed an earthquake with a strike-slip rupture mechanism unlikely to produce destructive tsunamis.

In this article, we present the results of a field reconnaissance conducted by a UNESCO international survey team to collect the tsunami data following the September 28th Palu event. Results include runup and inundation measurements in addition to coastal damage observations and landslides occurrence. Furthermore, we discuss the survey findings attempting to provide an insight into the tsunami source that remains a matter of a heated scientific debate.

2. Post-Tsunami Field Measurements

The post-tsunami survey of the September 28th, 2018 event took place on November 2018 between 7 and 11. The survey consisted of measuring the tsunami characteristics and used the conventional methods described in the UNESCO-IOC ITST Post-Tsunami Survey Field Guide 2nd Edition (UNESCO-ITST 2014). The team also took into consideration
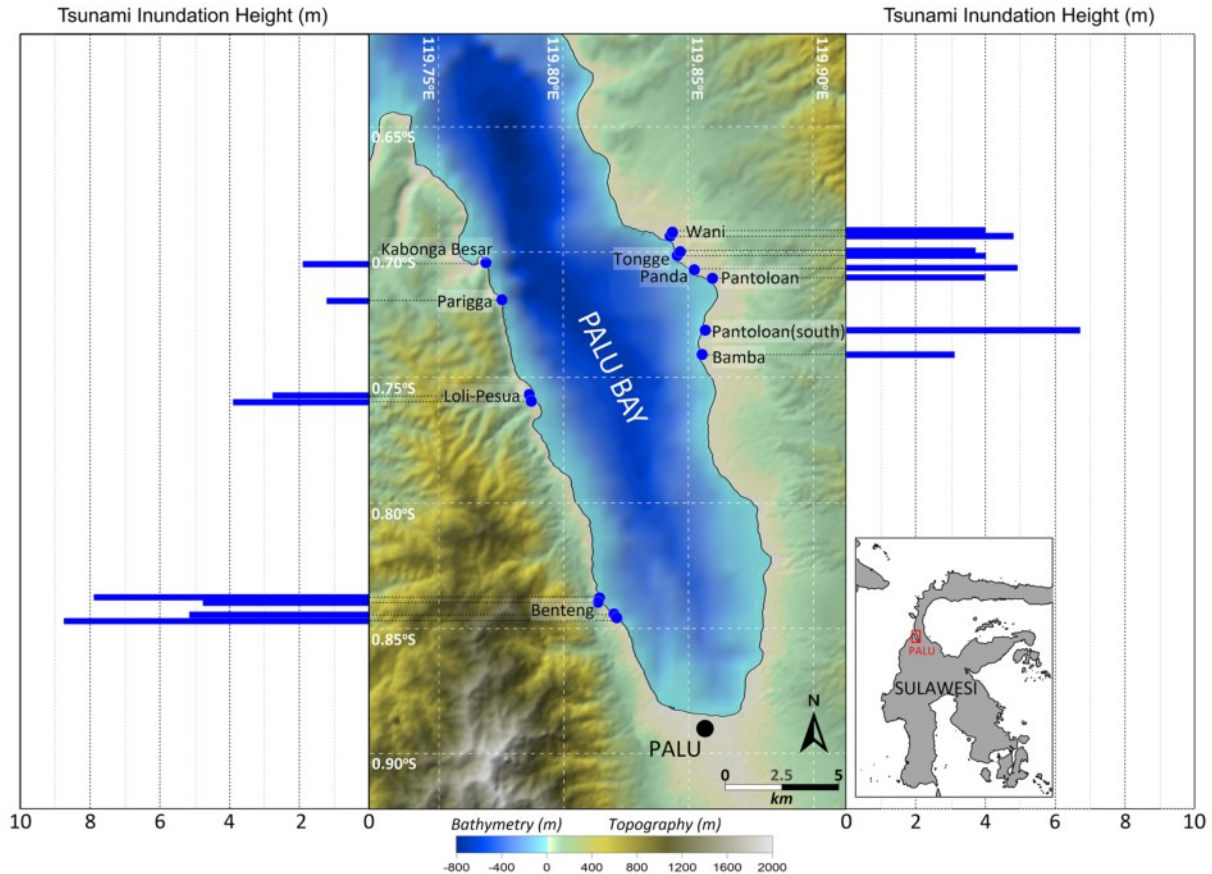
Figure 4
Tsunami inundation heights measured along the coastline of Palu Bay. Bathymetric data are from Badan Informasi Geospasial, Indonesia (BIG) and topographic data are from Shuttle Radar Topography Mission (SRTM)

the findings of the previous surveys carried out in the region (Muhari et al. 2018) and, accordingly, focussed their field reconnaissance on coastal zones less covered.

The survey covered about 125 km of coastline, from Tanjung Karang cape west up to the earthquake epicentre region northeast (Fig. 2). The team collected tsunami data after identifying the inland waves penetration from deposited evidence (debris, watermarks left on structures, etc.), from the extent of destruction (on vegetation and constructions), and from the testimony of witnesses that survived the tsunami. Optical level, GPS station and laser ruler instruments were employed to take the measurements of runup and inundation heights.

The survey team documented the tsunami runup heights at 62 locations and the inundation heights at 16 locations (Fig. 2). We first collected the data with respect to the sea level at the time of each measurement. Then we adjusted all the measured values to the sea level upon which the tsunami reached the surveyed coast. This processing was feasible using the signal recorded at the Pantoloan Port tide gauge and assuming no significant variations on the sea level inside Palu Bay. Results of the survey are depicted in Figs. 3 and 4 and summarised in the Annex A. Runup heights distribution at surveyed locations shows values varying from 0 m (no tsunami) up to 9.1 m (Fig. 3). The expected errors in

Figure 5
Observed tsunami damage on the surveyed coastal village of Wani, eastern side of Palu Bay coast: **a** overview of the coastal destruction; **b** boat and car swept up by the waves; **c** remaining foundation of a destroyed house

field runup measurements are normally in the range of ± 30 cm according to Heidarzadeh et al. (2018a).

2.1. Runup and inundation heights inside Palu Bay

Inside Palu Bay, between 0.90°S and 0.61°S, the team measured the maximum value of runup height (9.1 m) in Benteng, at the western side of the Bay (Fig. 3). At this location, the slope of coastal land area is steep, reaching values up to 20°. Here, we also noticed a local variability of tsunami impact as, few meters to the north, we measured runup heights in the range of 4 m. Further north, towards the western entrance of the Bay, the tsunami runup significantly decreases, heights less than 2 m. At Tanjung Karang, Donggala Regency, we measured a small runup of 0.2 m height at coastal zones with a slope less than 5°, while about 2 km southward, at Donggala city,

the tsunami runup was as high as 1.7 m at a gentle slope coast of about 2.5°. Between Watusampu south and Nambo north, the runup height varies from 0.3 to 6.4 m, being maximum at Loli-Saluran village.

Along the eastern coastal side of Palu Bay, the team focussed their reconnaissance surrounding the Pantoloan Port, up to Labuan north and Bamba south (Fig. 3). At this coastline transect, we took 17 runup measurements with heights ranging from 1.5 to 4.8 m. We measured the maximum runup in Wani with 4.8 m height. Here, the coastal land area has a gently slope of about 4°. The runup heights also gradually decrease towards the bay entrance where the runup values remain below 1.9 m in height at Bulu Kadia (Fig. 3).

Inundation heights at surveyed locations range from 1.2 to 8.7 m (Fig. 4). We measured the maximum height of 8.7 m in Benteng village, at the

Figure 6
Observed tsunami damage on the surveyed coastal village of Panda, eastern side of Palu Bay coast: **a** overview of the coastal destruction; **b** tree removed by the tsunami; **c** remaining foundation of a destroyed house

western coastline of Palu Bay (Fig. 4). Northward, there is a significant decrease of tsunami inundation, with heights remained below 4.0 m at Loli-Pesua village, Parigga, and Kagomba Besar (Fig. 4). At the eastern coast of Palu Bay, the team measured inundation heights at 8 locations surrounding the Pantoloan port (Fig. 4). Here, the inundation reached the height of 4.8 m in Wani, 4.0 m in Tongge, 4.9 m in Panda, 4.0 m in Pantoloan and 3.1 m in Bamba (Fig. 4). We obtained the maximum inundation height of 6.7 m in Pantoloan (south) (Fig. 4).

2.2. Runup heights outside Palu Bay

Outside Palu Bay, from the Bay entrance up to the earthquake epicentre region, the measured runup height varies from 0 to 0.9 m (Table 2). Along this stretch of coastline, we collected the maximum height of 0.9 m in Bulu Sigalari (Fig. 2, for location). However, further north, at Balaesang (Fig. 2, for location), no tsunami impact was observed despite the occurrence of a noticeable inundation. At these locations, eyewitnesses described a slow increase of sea level that led to flood their houses, which repeated for three successive days after the earthquake. We interpreted the described inundation as a result of the co-seismic subsidence leading to inland water penetration at high tide.

3. Observations of Tsunami Coastal Impact

During the survey of the affected coastline, besides measuring the physical parameters of the

Figure 7
Observed tsunami damage on the surveyed coastal village of Benteng, western side of Palu Bay coast: **a** overview of the coastal destruction; **b** damage in structures and vegetation; **c** heavily damaged house

tsunami, the team explored the tsunami effects on both natural and man-made environments. We observed massive destruction in several low-lying coasts, where houses were severally damaged and coastal vegetation suffered dramatic impact.

The penetration of the tsunami at Wani village, located within the eastern coastline of Palu Bay, caused a major destruction (Fig. 5a). The incident waves swept up boats and cars before crushing them against the houses, resulting in dramatic damage (Fig. 5b). Here, the tsunami waves washed away several sea-facing houses and only their foundations remained (Fig. 5c). Tsunami survivors reported that three successive waves hit Wani, the second was the largest, that followed a leading depression wave. They also mentioned that the direction of the incoming waves was from southwest of Wani.

Between Wani north and Pantoloan Port south, we carried out a reconnaissance of the tsunami impact in Panda (Fig. 2, for location), the village that was severely devastated by the waves (Fig. 6a). Here, eyewitnesses reported more than 100 tsunami fatalities. We noticed that both constructions and coastal vegetation suffered heavy tsunami impact (Fig. 6b, c). The tsunami left several trees removed (Fig. 6b) and houses destroyed (Fig. 6c).

We also examined the tsunami damage along the western coastline of Palu Bay. At Benteng village (Fig. 2, for location), even though the tsunami inundation resulted in short extent distance, the coast has experienced a substantial property damage (Fig. 7a). We witnessed significant damage in both structures and vegetation (Fig. 7b). In this village, several houses collapsed and those that withstood the tsunami

Figure 8
Observed tsunami damage on the surveyed coastal village of Loli-Saluran, Western side of Palu Bay coast: **a** overview of the coastal destruction; **b** debris left by the tsunami; **c** heavily damaged sea-facing houses

impact were heavily damaged and would require extensive repairs or complete reconstruction to be habitable again (Fig. 7c).

Further north, the bay at Loli-Saluran village (Fig. 2, for location) was massively damaged by the tsunami (Fig. 8a). Here, a large amount of tsunami debris was visible along the shoreline (Fig. 8b). This debris was composed of a mixture of material from damaged and destroyed houses, personal belongings from within the houses and uprooted vegetation (Fig. 8b). The tsunami destroyed several sea-facing houses, and the remaining ones require a complete reconstruction for further use (Fig. 8c).

In addition to the damage observations presented here for four selected coastal sites, the team has prepared a complete reconnaissance report where

details on the tsunami impact at other surveyed sites can be found. The report is available on the UNESCO-ITIC website (http://itic.ioc-unesco.org/images/stories/itst_tsunami_survey/itst_palu/ITST-Nov-7-11-Short-Survey-Report-due-on-November-23-2018.pdf).

4. Coastal Landslides

Throughout the surveyed coast, we observed evidence of several coastal landslides that collapsed into Palu Bay. We identified ten of such slope failures on both western and eastern sides of the bay (Fig. 9). To obtain useful information on the size of the collapsed sectors, we carried out a GPS tracking of the
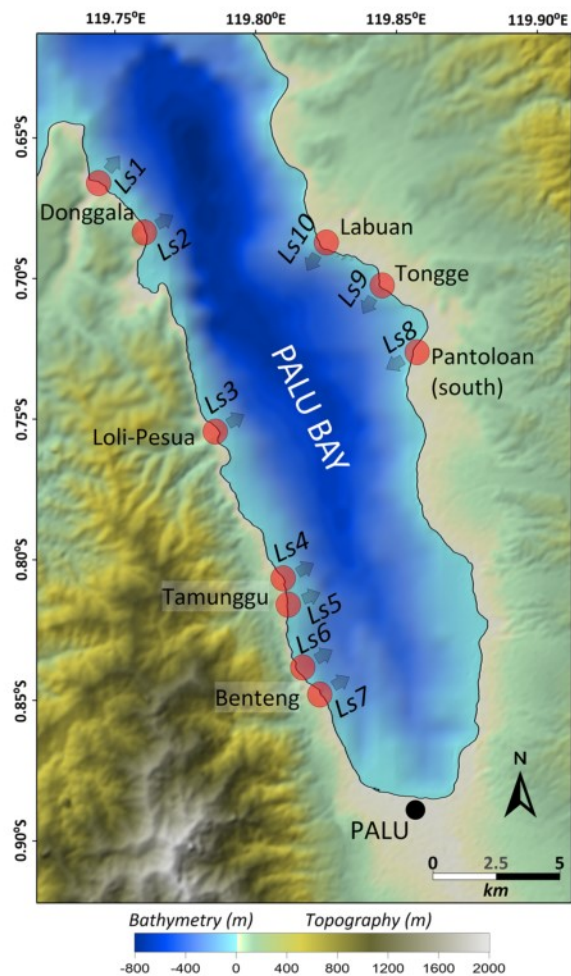
Figure 9
Locations of the coastal landslides (Ls1 to 10) identified by the survey team

rim of the head-scarp and measured the height of the main scarp of the identified landslides.

To search for the coastal landslides, we first analysed of the amateur videos taken for the tsunami event (Sources: https://www.instagram.com/p/BoRttnsn5po/?taken-by=icoze_ricochet; and https://www.youtube.com/watch?time_continue=2&v=61ItBglP-YM). The available videos show the formation of several point-source tsunami waves at the western coast of Palu Bay following the earthquake occurrence (Fig. 10a). After analysing these videos and identifying the locations of these point-sources, the team conducted an in situ reconnaissance that led to find evidence of coast retreat corresponding to the collapse of significant amount of material into the

sea. Figure 10b shows the surveyed coastal landslide at Benteng location, where the team performed a GPS tracking of the rim of the head-scarp and measured the height of the main scarp. Comparison of pre- and post-event satellite images also supports our findings as they clearly indicate a sector of the coast that vanished into the sea (Fig. 10c).

We discovered other coastal collapses after interviewing the eyewitnesses (Fig. 11a). At the impacted coast of Loli-Pesua, the tsunami survivors pointed out coastal point-source of the incident waves, where the survey revealed the presence of signs of coastal landslide occurrence (Fig. 11a). For this event, the team tracked the rim of the head-scarp and measured the height of the main scarp (Fig. 11b). Pre- and post-earthquake satellite images side-by-side also show the coastal sectors collapsed into the sea (Fig. 11c).

Along the coastline between Benteng south and Loli-Pesua north, the team identified two additional coastal landslides in Tamunggu (Fig. 9 for location). Further north, we surveyed the coastal subsidence in Donggala where a part of the city and the port collapsed into the sea (Fig. 9 for location).

At the eastern coastline of Palu Bay, where no video recording the wave generation is available, the testimonies of eyewitnesses were crucial for the identification of the coastal sectors that collapsed into the sea. Following the description of the eyewitnesses, we found three landslides located along the stretch of coastline between Pantoloan south and Labuan north (Fig. 9, for location). The locations of these identified landslides are consistent with the descriptions provided by the tsunami survivors in what regards the directions of the incident waves at Wani and Panda.

Arikawa et al. (2018) also conducted a field survey that focussed on identifying coastal subsidence occurred following the Sulawesi earthquake. They reported a total of seven locations of potential coastal subsidence, five of them are located inside Palu bay. Among the coastal landslides we identified in our survey, three were also observed by Arikawa et al. (2018) in Donggala, Tamunggu and Labuan (Fig. 9, for location). Our findings, on the other hand, show seven additional landslide locations inside Palu Bay
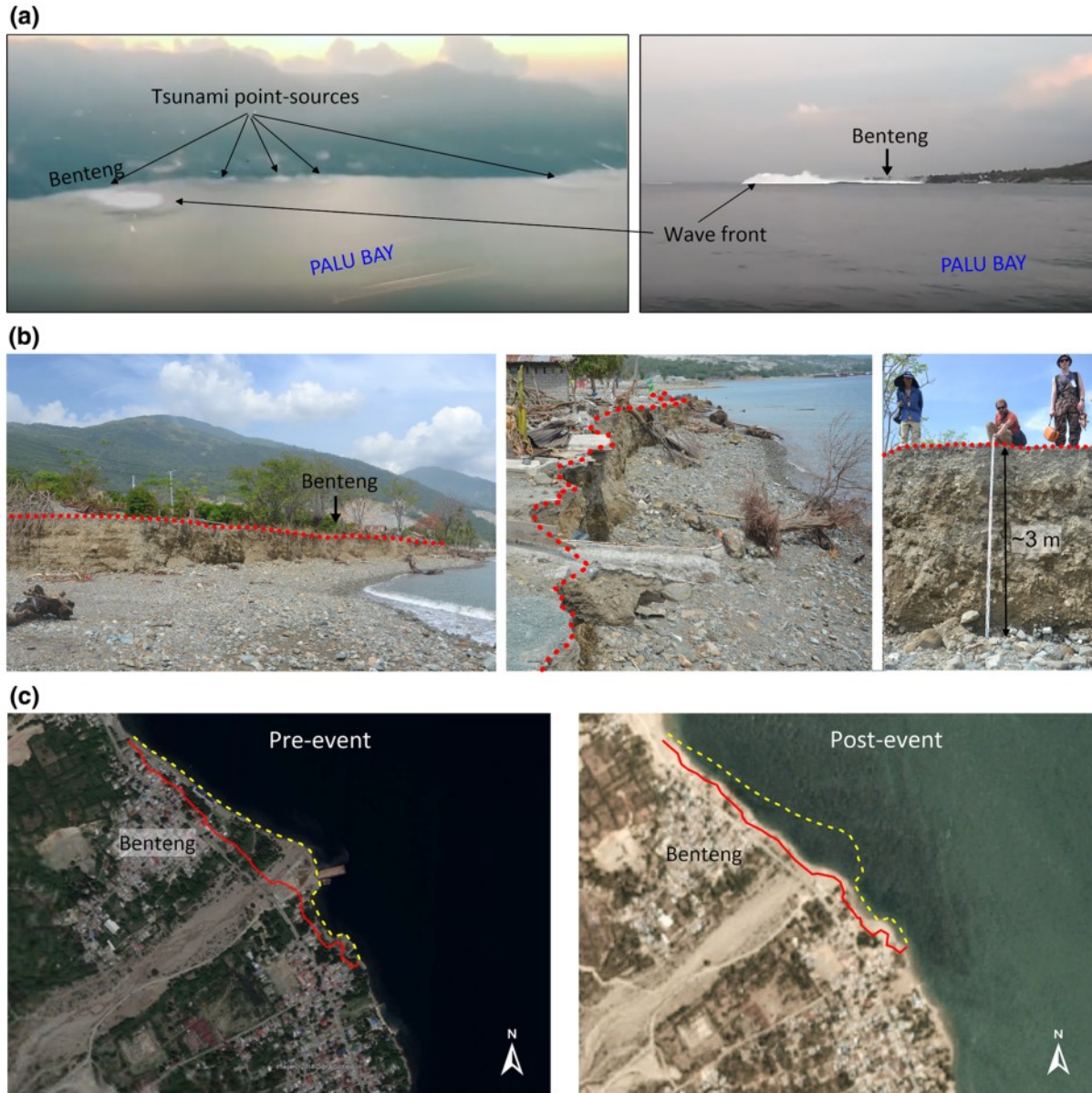
175

Figure 10

Benteng's coastal sector that collapsed into the sea: **a** photos captured from videos that recorded point-source waves generation following the earthquake; **b** survey of the collapse including GPS tracking of the rim of the head-scarp and measurement of the height of the main scarp **c** comparison of satellite images (google earth images) before and after the earthquake, red line marks the landslide scarp and the yellow dashed line marks the pre-event coastline

and therefore provide information completing the previous surveys.

In Table 1, we provide information on the identified landslides' locations and measured characteristics. The mission report also presents further details and description of the identified sector collapses and landslides (http://itic.ioc-unesco.org/images/stories/itst_tsunami_survey/itst_palu/ITST-Nov-7-11-Short-Survey-Report-due-on-November-23-2018.pdf).
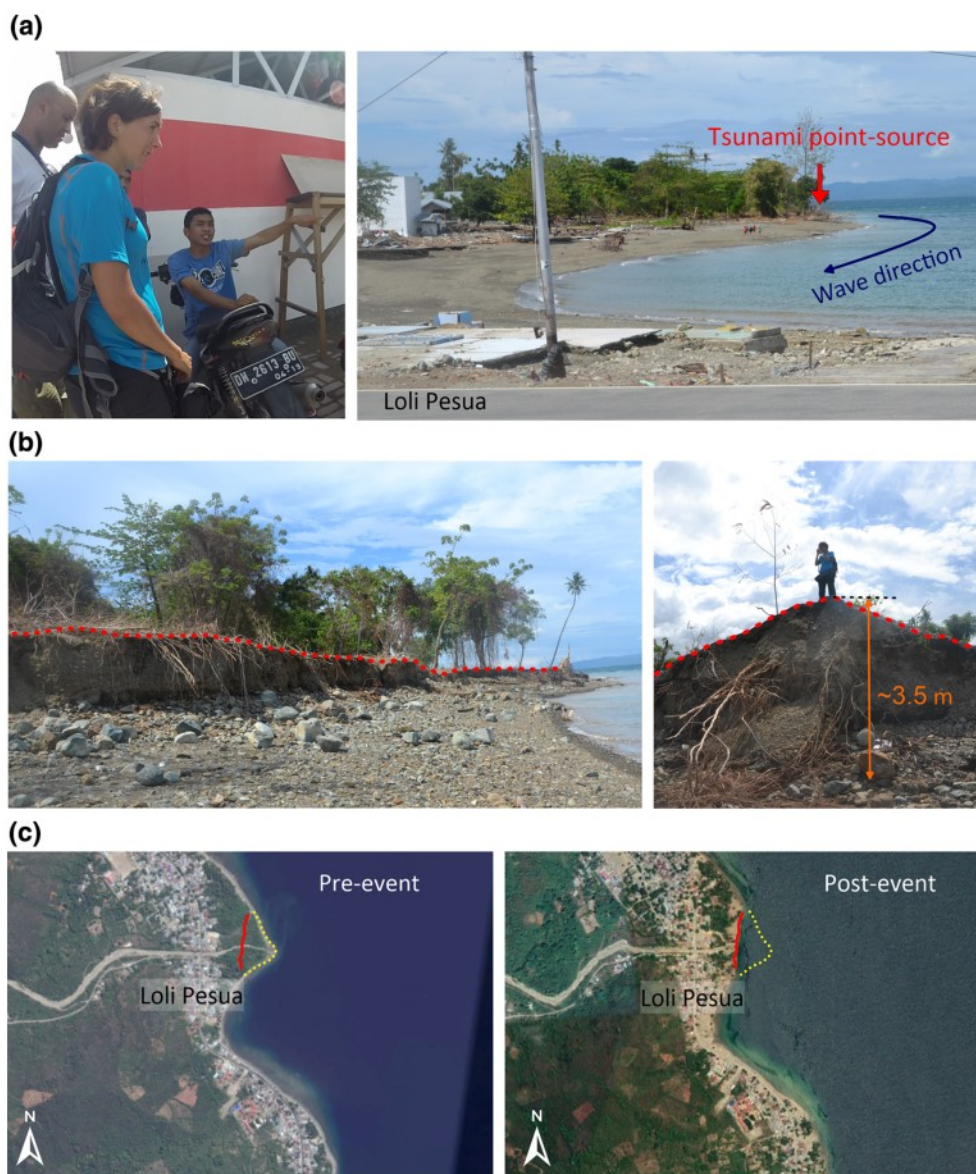
Figure 11

Loli-Pesua's coastal sector that collapsed into the sea: **a** survey team interviewing eyewitness that indicated the location of the incident tsunami wave; **b** identification of the landslide and GPS tracking of its rim of the head-scarp and measurement of the height of its main scarp; **c** comparison of satellite image (google earth images) before and after the earthquake, red line marks the landslide scarp and the yellow dashed line marks the pre-event coastline

5. Discussion and Conclusions

The tsunami that followed the September 28th, 2018, M_w 7.5 earthquake has shown the potential of strike-slip events in generating major sea waves. Nevertheless, it raised a heated scientific debate on the real source of the observed tsunami. In this sense, field surveys aiming to collect the tsunami data are of crucial importance to contribute to the understanding of the sources that led to a such surprizing tsunami.

In this work, the collected tsunami runup and inundation heights along the shore of Palu Bay

Table 1

Identified coastal landslides (Ls1 to 10), their locations, measured length of the rim of the head-scarp and height of the main scarp

Coastal landslide	Location	Length of the rim of the head-scarp (m)	Max. height of the main scarp (m)
Ls1	Donggala (western side of Palu Bay)	∼ 500	8
Ls2	Donggala (western side of Palu Bay)	∼ 300	–
Ls3	Loli-Pesua (western side of Palu Bay)	∼ 250	3.5
Ls4	Tamunggu (western side of Palu Bay)	∼ 400	1.5
Ls5	Tamunggu (western side of Palu Bay)	∼ 300	2.0
Ls6	Benteng (western side of Palu Bay)	∼ 700	–
Ls7	Benteng (western side of Palu Bay)	∼ 1000	3.0
Ls8	Pantoloan (eastern side of Palu Bay)	∼ 800	2.0
Ls9	Tongge (eastern side of Palu Bay)	∼ 500	2.0
Ls10	Labuan (eastern side of Palu Bay)	∼ 800	2.0

confirm the extreme effects of the tsunami and the impacts on coastal communities and infrastructures. The analysis of these data indicates a clear localised impact in different transects of the coast. This fact favours the hypothesis that local point-sources have likely contributed to the tsunami, but without ruling out here the possible contribution of the earthquake co-seismic deformation to the generation of the observed waves. The hypothesis of a multiple-source tsunami was also raised for the very similar event of August 7th, 1999 that resulted in high runup height in Izmit Bay (Turkey) after an M_w 7.4 strike-slip earthquake (Altinok et al. 1999, 2001; Yalciner et al. 2000; Tinti et al. 2006). Multiple-source for Palu

Figure 12
Tsunami evacuation sign indicating the route to follow in case of wave threat

tsunami is reinforced by our findings that indicate the occurrence of several coastal sectors and their collapse into the sea. Some of the localisations of the identified coastal landslides correspond to the places where various amateur videos captured the tsunami waves. Moreover, the investigation of Palu tsunami using numerical modelling, recently published by Heidarzadeh et al. (2018b), also suggests the contribution of additional secondary sources to the observed tsunami.

In various locations along the shore of Palu Bay, the survey results show heavily damaged houses and property. While in these locations the level of destruction was very high, we found that the inundation extended for short distances, for only tens of meters in some cases. We can explain this fact by high wave heights and short wave periods. Such waves are characteristics of non-tectonic sources as landslide-induced tsunamis.

Despite the massive destruction, it is worth to mention that the number of tsunami victims was very

low or even nil in some coastal locations. Our interviews of eyewitnesses revealed a high tsunami education and awareness of coastal population that self-evacuated after feeling the earthquake shaking or observing anomalous sea activity. Moreover, we noticed the presence of tsunami evacuation signs indicating the routes to follow in case of waves arrival (Fig. 12). Their presence and the people awareness could be one of the most critical factors that contributed to a successful tsunami self-evacuation in some heavily impacted coastal areas.

In conclusion, during the post-tsunami field survey we covered about 125 km long coastline and surveyed tens of coastal locations. The results of our survey constitute a database of 62 runup and 16 inundation measured heights. The collected runup and inundation heights reached maximum values of 9.1 m and 8.7 m, respectively, both at Benteng village. Our survey also led to identify ten coastal sectors that collapsed into the sea in locations where amateur videos recorded the generation of local waves and/or pointed out by the survivors as tsunami point-sources. Observation of tsunami consequences on impacted coasts showed massive damage both on property and natural environment. The analysis of collected data, testimonies of eyewitnesses, recorded videos and distribution of damage suggests the contribution of local non-seismic sources to the September 28th tsunami.

Appendix

See Table 2.

Table 2

List of locations and measurement results of Palu Tsunami field survey

Area	E/W	Point#	Point ID	Lat	Lon	Measurement-detided (m)	Type (RH = runup height, IH = inundation height, other)
Alindau	E	1	E01.01	− 0.35395	119.76194	–	–
Bulu Salugoo	E	2	E02.01	− 0.41283	119.76123	–	–
Kaliburu	E	3	E03.01	− 0.50688	119.76654	–	–
Bulu Sigalari	E	4	E04.01	− 0.54152	119.77979	0.9	RH
Enu	E	5	E05.01	− 0.576	119.79038	–	–
Bulu Kadia	E	6	E06.01	− 0.61711	119.80202	1.9	RH
Bulu Kadia	E	6	E06.02	− 0.62206	119.80442	1.8	RH
Bulu Kadia	E	6	E06.03	− 0.62508	119.80626	1.2	RH
Labuan	E	7	E07.01	− 0.68803	119.82413	1.5	RH
Labuan	E	7	E07.02	− 0.68846	119.82472	2.4	RH

Table 2 *continued*

Area	E/W	Point#	Point ID	Lat	Lon	Measurement-detided (m)	Type (RH = runup height, IH = inundation height, other)
Labuan	E	7	E07.03	− 0.68888	119.82536	3.7	RH
North Ngapa	E	8	E08.01	− 0.69341	119.83815	1.8	RH
North Ngapa	E	8	E08.02	− 0.69341	119.83815	1.9	RH
Ngapa (Wani)	E	9	E09.01	− 0.69345	119.84258	4.7	RH
Ngapa (Wani)	E	9	E09.02	− 0.69345	119.84258	4.8	RH
Ngapa (Wani)	E	9	E09.03	− 0.69396	119.84213	4.0	IH
Ngapa (Wani)	E	9	E09.05	− 0.69400	119.84205	4.8	IH
Tongge	E	10	E10.01	− 0.70052	119.84512	3.6	RH
Tongge	E	10	E10.02	− 0.70131	119.84492	3.7	IH
Tongge	E	10	E10.03	− 0.70137	119.84438	3.9	RH
Tongge	E	10	E10.04	− 0.70140	119.84438	4.0	IH
Tongge	E	10	E10.05	− 0.701933	119.845994	4.0	RH
Panda	E	11	E11.01	− 0.70707	119.85292	3.9	RH
Panda	E	11	E11.02	− 0.7072	119.85204	4.3	RH
Panda	E	11	E11.03	− 0.70724	119.85160	4.9	IH
Pantoloan	E	12	E12.01	− 0.71065	119.85852	2.4	RH
Pantoloan	E	12	E12.02	− 0.71069	119.85892	4.0	IH
Pantoloan	E	12	E12.03	− 0.710718	119.858905	2.7	RH
Pantoloan	E	12	E12.04	− 0.71101	119.85819	2.4	RH
Pantoloan (South)	E	13	E13.01	− 0.7275	119.85716	4.0	RH
Pantoloan (South)	E	13	E13.02	− 0.73141	119.85616	4.2	RH
Pantoloan (South)	E	13	E13.03	− 0.73141	119.85616	6.7	IH
Bamba	E	14	E14.01	− 0.7406	119.85586	2.9	RH
Bamba	E	14	E14.03	− 0.74087	119.8548	3.1	IH
Sambugan	E	15	E15.01	− 0.78863	119.86406	2.7	RH
Tanjungkarang	W	1	W01.01	− 0.644865	119.730361	−	−
Tanjungkarang	W	1	W01.02	− 0.64576	119.73892	0.2	RH
Donggala	W	2	W02.01	− 0.66646	119.74395	1.6	RH
Donggala	W	2	W02.02	− 0.66648	119.74395	1.7	RH
Donggala Kota Wisata, Ujung	W	3	W03.02	− 0.67972	119.75997	2.0	RH
Nambo	W	3	W03.03	− 0.69457	119.75741	1.5	RH
Kabonga Besar	W	4	W04.01	− 0.70263	119.76599	0.4	RH
Kabonga Besar	W	4	W04.02	− 0.70400	119.76805	1.4	RH
Kabonga Besar	W	4	W04.03	− 0.70450	119.76836	1.9	IH
Kabonga Besar	W	4	W04.04	− 0.70491	119.76864	1.2	RH
Parigga	W	5	W05.01	− 0.71933	119.77466	1.2	IH
Parigga	W	5	W05.02	− 0.72029	119.77517	2.1	RH
Parigga	W	5	W05.03	− 0.72056	119.77511	2.4	RH
Loli-Pesua	W	6	W06.01	− 0.75721	119.78611	2.7	IH
Loli-Pesua	W	6	W06.02	− 0.75774	119.78524	3.9	RH
Loli-Pesua	W	6	W06.03	− 0.75837	119.78547	4.7	RH
Loli-Pesua	W	6	W06.04	− 0.75883	119.78643	3.9	IH
Lolisaluran	W	7	W07.01	− 0.78036	119.79317	5.1	RH
Lolisaluran	W	7	W07.02	− 0.78113	119.79318	6.4	RH
Lolisaluran	W	7	W07.03	− 0.78303	119.79373	3.0	RH
Lolisaluran	W	7	W07.04	− 0.78408	119.79532	3.5	RH
Tamunggu	W	8	W08.01	− 0.80727	119.80934	6.2	RH
Tamunggu	W	8	W08.03	− 0.809486	119.80981	5.9	RH
Tamunggu	W	8	W08.04	− 0.80987	119.80996	5.3	RH
Tamunggu	W	8	W08.05	− 0.81330	119.81055	5.4	RH
Tamunggu	W	8	W08.07	− 0.81558	119.81068	3.9	RH
Watusampu	W	9	W09.01	− 0.8216	119.8099	6.3	RH

Table 2 *continued*

Area	E/W	Point#	Point ID	Lat	Lon	Measurement-detided (m)	Type (RH = runup height, IH = inundation height, other)
Watusampu	W	9	W09.02	− 0.82207	119.81024	5.7	RH
Watusampu	W	9	W09.03	− 0.8222	119.81013	5.4	RH
Watusampu	W	9	W09.04	− 0.82511	119.81090	1.5	RH
Watusampu	W	9	W09.05	− 0.82513	119.81087	2.0	RH
Watusampu	W	9	W09.06	− 0.82648	119.81115	0.3	RH
North Benteng	W	10	W10.03	− 0.83772	119.81371	7.9	IH
North Benteng	W	10	W10.05	− 0.83782	119.81317	4.7	IH
North Benteng	W	10	W10.06	− 0.83784	119.8125	8.3	RH
North Benteng	W	10	W10.07	− 0.83997	119.81594	1.8	RH
Benteng	W	11	W11.01	− 0.84491	119.81947	4.2	RH
Benteng	W	11	W11.02	− 0.84514	119.82011	5.2	IH
Benteng	W	11	W11.03	− 0.84562	119.82067	8.7	IH
Benteng	W	11	W11.04	− 0.84591	119.82061	3.8	RH
Benteng	W	11	W11.05	− 0.84642	119.82117	9.1	RH

REFERENCES

Altinok, Y., Alpar, B., Ersoy, S., & Yalciner, A. C. (1999). Tsunami generation of the Kocaeli earthquake (August 17, 1999) in the Izmit Bay: Coastal observations, bathymetry, and seismic data. *Turkish Journal of Marine Sciences (Institute of Marine Sciences and Management, University of Istanbul), 5*(3), 130–144.

Altinok, Y., Tinti, S., Alpar, B., Yalciner, A. C., Ersoy, Ş., Bortolucci, E., et al. (2001). The tsunami of August 17, 1999 in Izmit bay, Turkey. *Natural Hazards, 24*(2), 133–146.

Arikawa, T., Muhari, A., Okumura, Y., Dohi, Y., Afriyanto, B., Sujatmiko, K., & Imamura, F. (2018). Coastal Subsidence Induced Several Tsunamis During the 2018 Sulawesi Earthquake. J. Disaster Res., Vol.13 Sci. Comm., sc20181204.

ASEAN (2018). ASEAN-Coordinating Centre for Humanitarian Assistance on disaster: Situation Update No. 12 M 7.4 Earthquake & Tsunami Sulawesi, Indonesia. https://asean.org/storage/2018/10/AHA-Situation_Update-no12-Sulawesi-EQ-rev.pdf. Last access: 18 December 2018.

Bellier, O., Sébrier, M., Beaudouin, T., Villeneuve, M., Braucher, R., Bourles, D., et al. (2001). High slip rate for a low seismicity along the Palu-Koro active fault in central Sulawesi (Indonesia). *Terra Nova, 13*(6), 463–470.

Gomez, J. M., Madariaga, R., Walpersdorf, A., & Chalard, E. (2000). The 1996 earthquakes in Sulawesi, Indonesia. *Bulletin of the Seismological Society of America, 90*(3), 739–751.

Heidarzadeh, M., Muhari, A., & Wijanarto, A. B. (2018a). Insights on the source of the 28 September 2018 Sulawesi tsunami, Indonesia based on spectral analyses and numerical simulations.

Pure and Applied Geophysics. https://doi.org/10.1007/s00024-018-2065-9.

Heidarzadeh, M., Teeuw, R., Day, S., & Solana, C. (2018b). Storm wave runups and sea level variations for the September 2017 Hurricane Maria along the coast of Dominica, eastern Caribbean Sea: evidence from field surveys and sea level data analysis. *Coastal Engineering Journal.*. https://doi.org/10.1080/21664250.2018.1546269.

Horspool, N., Pranantyo, I., Griffin, J., Latief, H., Natawidjaja, D. H., Kongko, W., et al. (2014). A probabilistic tsunami hazard assessment for Indonesia. *Natural Hazards and Earth System Sciences, 14*(11), 3105–3122.

Løvholt, F., Glimsdal, S., Harbitz, C. B., Horspool, N., Smebye, H., De Bono, A., et al. (2014). Global tsunami hazard and exposure due to large co-seismic slip. *International journal of disaster risk reduction, 10,* 406–418.

Muhari, A., Imamura, F., Arikawa, T., Hakim, A., & Afriyanto, B. (2018). Solving the Puzzle of the September 2018 Palu, Indonesia, Tsunami Mystery: Clues from the Tsunami Waveform and the Initial Field Survey Data. *Journal of Disaster Research, 13,* sc20181108.

Nishimura, S., & Suparka, S. (1990). Tectonics of east Indonesia. *Tectonophysics, 181*(1–4), 257–266.

Pelinovsky, E., Yuliadi, D., Prasetya, G., & Hidayat, R. (1997). The 1996 Sulawesi tsunami. *Natural Hazards, 16*(1), 29–38.

Prasetya, G. S., De Lange, W. P., & Healy, T. R. (2001). The makassar strait tsunamigenic region, Indonesia. *Natural Hazards, 24*(3), 295–307.

Socquet, A., Simons, W., Vigny, C., McCaffrey, R., Subarya, C., Sarsito, D., Ambrosius, B. & Spakman, W. (2006). Microblock rotations and fault coupling in SE Asia triple junction (Sulawesi, Indonesia) from GPS and earthquake slip vector data. Journal of Geophysical Research: Solid Earth, 111(B8).

Spencer, J. E. (2011). Gently dipping normal faults identified with Space Shuttle radar topography data in central Sulawesi, Indonesia, and some implications for fault mechanics. *Earth and Planetary Science Letters, 308*(3–4), 267–276.

Tinti, S., Armigliato, A., Manucci, A., Pagnoni, G., Zaniboni, F., Yalciner, A. C., et al. (2006). The generating mechanisms of the August 17, 1999 Izmit bay (Turkey) tsunami: regional (tectonic)

and local (mass instabilities) causes. *Marine Geology, 225*(1–4), 311–330.

UNESCO (2014). International Tsunami Survey Team (ITST) Post-Tsunami Survey Field Guide. 2nd Edition. IOC Manuals and Guides No.37, Paris: UNESCO 2014 (English).

Watkinson, I. M., & Hall, R. (2016). Fault systems of the eastern Indonesian triple junction: evaluation of Quaternary activity and implications for seismic hazards. *Geological Society, London,* *Special Publications, 441*(1), 71–120. https://doi.org/10.1144/SP441.8.

Yalciner, A. C., Altinok, Y., & Synolakis, C. E. (2000). Tsunami Waves in Izmit Bay after the Kocaeli Earthquake. Earthquake Spectra, Kocaeli, Turkey Earthquake of August 17, 1999 Reconnaissance Report. *Special Issue Supplement to Professional Journal of Earthquake Engineering Research Institute, 16,* 55–62.

182